Sampling Time-resolved Phenomena

by

Ayush Bhandari

S.M., Massachusetts Institute of Technology (2014)

Submitted to the the Program in Media Arts and Sciences,
in partial fulfillment of the requirements for the degree of

Doctor of Philosophy

at the

MASSACHUSETTS INSTITUTE OF TECHNOLOGY

September 2018

Author . . . . . .
Program in Media Arts and Sciences
August 10, 2018

Certified by . . . . . .
Ramesh Raskar
Associate Professor
Thesis Supervisor

Accepted by . . . . . .
Tod Machover
Professor of Media Arts and Sciences,
Academic Head, Program in Media Arts and Sciences

Sampling Time-resolved Phenomena
by
Ayush Bhandari

Submitted to the the Program in Media Arts and Sciences,
on August 10, 2018, in partial fulfillment of the
requirements for the degree of
Doctor of Philosophy

Abstract

Broadly speaking, time-resolved phenomena refers to three dimensional capture of a scene based on the time-of-flight principle. Since speed and and time are proportional quantities, knowing time-of-flight allows one to estimate distances. This time-of-flight may be attributed to a pulse of light or a wave packet of sound. Depending on the sub-band of the electromagnetic spectrum, the interaction of waves or pulses with the scene of interest results in measurements and based on this proxy of the physical world, one is interested in inferring physical properties of the scene. This may be something simple as depth, or something more involved such as fluorescence lifetime of a biological sample or the diffusion coefficient of turbid/scattering medium.

The goal of this work is to develop a unifying approach to study time-resolved phenomena across various sub-bands of the electromagnetic spectrum, devise algorithms to solve for the corresponding inverse problems and provide fundamental limits. Sampling theory, which deals with the interplay between the discrete and the continuous realms, plays a critical role in this work due to the continuous nature of physical world and the discrete nature of its proxy, that is, the time-resolved measurements.

Thesis Supervisor: Ramesh Raskar
Title: Associate Professor

Sampling Time-resolved Phenomena
by
Ayush Bhandari

This doctoral thesis has been examined by the following thesis reader.

Thesis Reader . . . . . .

Laurent Demanet
Associate Professor of Applied Mathematics
Department of Mathematics
Massachusetts Institute of Technology

Sampling Time-resolved Phenomena
by
Ayush Bhandari

This doctoral thesis has been examined by the following thesis reader.

Thesis Reader . . . . . .

Felix Krahmer
Assistant Professor of Optimization and Data Analysis
Department of Mathematics
Technical University of Munich

Sampling Time-resolved Phenomena
by
Ayush Bhandari

This doctoral thesis has been examined by the following thesis reader.

Thesis Reader . . . . . .

Laurent Daudet
Professor of Physics
Langevin Institute for Waves and Images (LOA)
Université Paris Diderot–Paris 7

Preface

A Confluence of Imaging and Harmonic Analysis

This thesis is titled "Sampling Time-resolved Phenomena." As the name suggests, this work is at the confluence of two themes: time-resolved imaging and harmonic analysis. The goal of this work is to study key problems in the the field of time-resolved imaging through the lens of harmonic analysis, and in particular, sampling theory. In some way, this line of work also "samples" various inverse problems in the context of time-resolved imaging. Although it was not planned in any way, interestingly, both these topics are deeply rooted in the history of the academic institution where this work was done. Claude Shannon conceived the idea of the "digital" realm and *sampling theory* was born. In the same way, the use of "time" information in the context of imaging traces its roots back to the historical experiments conducted by Harold Edgerton.

In the conventional sense, any imaging sensor leads to a *photograph* which is simply the amount of photons collected per-pixel. An abstraction of the two-dimensional *photograph* is the plenoptic function which describes light recorded at all possible locations, orientations, wavelengths and times. For a fixed orientation and co-ordinates, by marginalizing the time information one records the photograph. Beyond the optical context of this idea, the key aspect that is investigated in this work is: Can we retain the time-information in the process of sensing? We refer to any information as a function of time as time-resolved information. For instance, plenoptic function with time information is referred to as the time-resolved image. In contrast to the classical imaging which produces a two dimensional image (or matrix), the time-resolved image is a three dimensional tensor where each pixel contains a time-profile corresponding to the scene.

Modern day consumer-grade electronic sensing technology allows for sensing information at different time scales; microsecond, nanosecond and picosecond. For instance, optical sensors such as the Microsoft Kinect allow for imaging at time scale of the order of tens of nanoseconds[1]. Since time and speed[2] are proportional quantities, knowing how much time it has taken for a pulse or wave of light to backscatter from an object allows to calculate the depth of the object; thus resulting in a three dimensional image, also known as the *depth image*.

Regardless of the modality used for the task of sensing, ultimately, the measurements are stored in a digital format as a countable set of measurements. While physical phenomena such as depth, fluorescence lifetime and constants of scattering media are defined on the continuum, measurements can only be discrete and finitely many, and thus they are only a proxy of the underlying continuous phenomena. A central question that arises is: When do the discrete measurements uniquely describe a continuous phenomenon? This is where *sampling theory* finds its way in this thesis.

The first part of this thesis develops harmonic analysis related tools and algorithms. These developments are then used in the context of applications which constitute the second part of the thesis.

On the theoretical front, our first result extends the notion of "bandwidth." Classically, when a signal or function is bandlimited, the de facto idea is that the signal or function is compactly supported in the Fourier domain. Here, we develop a more general sampling theory which goes beyond the Fourier domain. Three specific signal classes are discussed: bandlimited signals, smooth signals (shift-invariant subspaces)

[1]Light travels at approximately one foot in one nanosecond.

[2]We generally consider the notion of speed in context of waves in a given medium. In context of optical imaging, this refers to the speed of light in vacuum.

and sparse signals. This work is a result of collaboration with Ahmed Zayed and Yonina Eldar. Our second result introduces the *unlimited sensing* framework which is a novel, non-linear sensing architecture that allows for recovery of an arbitrarily high dynamic range, continuous-time signal from its low dynamic range, digital measurements or "samples". The key idea here is to inject modulo non-linearity in the sensing process which limits the range of amplitudes of the recorded signal. In this context, we develop a theory which considers two important cases; global and local reconstruction. The global reconstruction scheme leads to a version of the Shannon's sampling theorem and is useful for dealing with bandlimited functions. The local reconstruction scheme deals with parametric signals (such as spikes and sum of sinusoids) where finitely many samples characterize the whole signal. This line of work was developed in collaboration with Felix Krahmer. The last result in the theoretical part of this thesis deals with sampling theory of rational functions which arises in the context of fluorescence lifetime imaging. Interestingly, it can be shown experimentally that the Fourier transform in this case amounts to a sum of modulated rational functions which related to delay and lifetime parameters in imaging. The key ideas leading to the results were developed during discussions with Thierry Blu.

The second part of this thesis deals with applications where conceptual ideas are verified with experimental analysis. In this direction, our first result applied the theory of sparse sampling and super-resolution to the problem of time-resolved imaging. Although results related to a specific class of time-resolved sensors are included in this part, overall, the experimental work has benefitted from the inputs provided by Achuta Kadambi, Refael Whyte, Andrew Wallace, Shahram Izadi and Jamie Schiel. Our second result demonstrates applicability of low-cost time-resolved imaging sensors for fluorescence lifetime imaging. Fluorescence lifetime imaging (FLI) is a popular method for extracting useful information that is otherwise unavailable from a conventional intensity image. Here, we present a generalized time-based, cost-effective method for estimating lifetimes by repurposing a consumer-grade time-of-flight sensor. By developing mathematical theory that unifies time- and frequency-domain approaches, we can interpret a time-based signal as a combination of multiple frequency measurements. We show that we can estimate lifetimes without knowledge of the illumination signal and without any calibration. Experimental aspects of this work have benefited from a collaboration with Christopher Barsi. Our next result demonstrates recovery of time-resolved images without assuming the knowledge of the sampling instants or the sampling rate. This problem is closely tied to the problem of sparse phase retrieval. Aurélien Bourquard has contributed to the algorithmic aspects of this work. Our final result in the context of experimental verification deals with the problem of photoacoustic or PA tomography. We reformulate the PA imaging problem as a time-of-flight super-resolution problem. Based on the PA wave equations, we show that the problem reduces to estimation of sparse cellular features from a set of finite trigonometric moments. For this purpose, we develop a super-resolution algorithm which achieves near exact performance (in context of maximum likelihood estimation) when working with experimental data. This work has been made possible due to inputs from Eric Strohm and Michael Kolios.

Acknowledgments

The work presented in this thesis is an attempt towards achieving my research goal of striking a synergistic balance between theory and practice. Many of the results could not make it to the thesis partly because the experiments could not be explained by theory and partly because the theory could not be made practicable. Nonetheless, all that worked out is indeed a culmination of a number of enriching collaborations. I feel extremely fortunate to have come in contact with a number of individuals who have not only added to my scientific pursuit but also progressively helped me become a better version of myself.

In capacity of being my advisor at MIT, Ramesh Raskar has contributed in several unconventional ways which have empowered me to become an independent researcher and sustain a career while doing what I enjoy the most! In the conventional sense of things, I could have continued on the research path paved by Ramesh and churned enough papers to call it a thesis. However this is not the case here. During the course of years, Ramesh has provided me with unprecedented research freedom to select topics of my choice while giving invaluable inputs and creative twists that would enhance the context of the problem. Collaborations across disciplines has never been a problem both because of Ramesh's broad curiosity and generous funding support. I will always be thankful to Ramesh for instilling the confidence that is needed for working with experimental data. When I leave MIT, I will be taking two things with me, "all simulations are doomed to succeed" and "magic will happen at the last moment."

Before moving to MIT and even during my stay here, there is one individual who has been a constant source of encouragement and inspiration. I take this opportunity to thank Thierry Blu who has helped me navigate through various subtleties linked with the art and craft of signal processing and, applied mathematics in general. My several visits to Hong Kong and his stay at Harvard has led to a number of interesting discussions and unfinished drafts. I look forward to many more years of inspiration and interesting collaborations. Beyond work, Thierry's advises have helped me shape my vision of a research career. Thanks for taking all those calls and helping me sort out things.

Michael Unser was my starting point for sampling theory. Thank you for helping me set my foot in the topic and for the time at EPFL.

Ahmed Zayed has introduced me to the world of generalized Fourier analysis. This has helped me explore various approximation theoretic problems in the context of phase space representations and harmonic analysis. I thank him for sharing his mathematical expertise and ideas.

Yonina Eldar has helped me extend and refine ideas in the context of super-resolution and sparse recovery. It has been a wonderful collaboration that has led to a whole new class of problems. In fact, our meeting today at MIT has put forth a seed for interesting future work. Thanks for all the help and encouragement and also for sharing your thoughts and perspectives!

"Unlimited Sensing" has blossomed into a beautiful reality and an interesting class of inverse problems. This has been made possible due to the joint work with Felix Krahmer. Our discussions in Munich and Tallinn together with hours and hours of long calls have led to some of the most exciting results and many more in the pipeline. Thank you Felix for being an ideal collaborator, friend, teacher and more!

On the experimental side, much of the time-resolved imaging work was possible due to the joint work with three talented individuals; Achuta Kadambi, Christopher Barsi and Refael Whyte. What a journey it has been! Thank you for all the discussions and painstaking hours that have led to our papers.

Over the course of years, Achuta and I have collaborated on several fronts; research, travel, outings but

our most exciting adventure is going to be the book we are authoring. Achuta is perhaps the only person with whom I have interacted on a daily basis during the Boston years. Despite our almost antithetical perspectives, I have always learnt something. Thank you!

Experimental work has also benefited from contributions outside of our lab. Andrew Wallace has helped with the super-resolution experiments that were based on time-correlated single photon counting sensors. Shahram Izadi, together with his research group at Microsoft Research, modified the Kinect which helped us verify our theoretical models in context of multi-bounce imaging. Thank you all for the joint work.

During all these years, I have had the great fortune of being hosted by a number of research groups that have influenced my research directions and trained me as a scientist. I would like to thank Frédéric Bimbot for the time spent at INRIA-Rennes, Pina Marziliano and Chong Meng Samson See for the Singapore stay, Thierry Blu for several stays at CUHK, Martin Vetterli and Michael Unser for a wonderful year at EPFL, Anders Hansen for hosting me at the DAMTP, University of Cambridge and Ron Kimmel at the Technion. I also thank colleagues at University College London and Imperial College London for their hospitality during the UK visit in 2016.

TU Munich has been a natural stop in the last two years. I would like to thank Felix Krahmer and Holger Boche for hosting me in Munich. It has been fantastic! I also thank Ullrich Mönich for discussions at MIT and elsewhere, and his warm hospitality at TU Munich. Luckily, Hans Feichtinger was also at TU Munich during my stays over there. Thank you for sharing your expertise in harmonic analysis and your views and philosophy on the subject of teaching. Outside of work, Munich has been enjoyable because of my friends. Thank you Pouya Tafti, Michael Rübsamen, Constanze Hoensbroech and Philipp Witzleben.

Beyond scientific advise, both Laurent Daudet and Laurent Demanet have helped me figure out various things about research life. Laurent Daudet has been helpful on critical aspects ranging from advise on research career to introducing me to other scientists in the field. I have benefitted immensely from his suggestions tailored towards my situation. Thank you for going that extra mile and making time for impromptu phone calls! I met Laurent Demanet during my first week at MIT and since then he has participated in several research discussions that have shaped my doctoral trajectory. His foresight with problems and encouragement are deeply appreciated. His teaching style will be a benchmark for my future life. Together with Felix Krahmer, Laurent Daudet and Laurent Demanet were also committee members for my doctoral thesis. I feel fortunate to have all of you on my committee and I look forward to our continuing collaborations.

During the last leg of my stay, I was an external member in Alan Oppenheim's group. Thank you for having me in all those sparking group meetings. I also thank Petros Boufounos, Sefa Demirtas and Tom Baran for our discussions in and out of the group meetings. Thanks to the DSPG, the "Big Apple Circus" would have never happened for me.

During a tough phase in life, Michael Bronstien's timely advise on carving an academic career has worked wonders for me. Thank you Michael! I look forward to working with you! Laurent Jacques and Joe Paradiso, thank you for your help and support as well.

There are a few individuals who started out as co-workers but the lines quickly blurred and we became good friends. Who knew we would come this far! Simon Arberet, Aurélien Bourquard, Xiaowen Dong, Gemma Roig, Thomas Heinis, Chris Gilliam, Sunny Jolly, Luboš Omelina and Dima Batenkov deserve a special vote of thanks.

Adrien Clidière, Magnus Andermo, Aurélien Bourquard, Xiaowen Dong and Sven Januszek, the word "thank you" is not enough for you!

I thank all the past and current members of Ramesh Raskar's lab for making the stay enjoyable. This includes Achuta Kadambi, Nikhil Naik (and Priya), Otkrist Gupta, Guy Satat, Anshuman Das, Tristan Swedish, Dan Raviv, Barmak Heshmat, Tomohiro Maeda, Chris Barsi, Aydin Arpa, Kshitij Marwah, Micha Feigin, Albert Redo-Sanchez, Jamie Schiel, Refael Whyte, Gordon Wetzstein, Annette Mossel, Luboš Omelina, Karin Roesch and Pratik Shah. My apologies in advance if I missed out someone.

Steve Otis has helped us file tens of patents and his thought provoking questions have been a source of inspiration. Thank you Steve for the tireless hours of work you have put into all the patent applications. Collaborating with you has been a great experience!

Jermey Matthews from MIT Press has made our book project come to life. Thanks for your help with the process.

Thank you Maggie Church and Maggie Cohen! You have gone beyond your call of duty to help me with the administrative aspects of lab life. Linda Peterson and Keira Horowitz, thank you, thank you and thank you! You have kept my boat sailing.

Finally, with each year passing by, I have a deeper sense of appreciation for what my parents have done for me (and others). Words can not describe the ways in which they have helped me carve my life, find my passion and yet be grounded in certain values which keep one going.

Last one year has been tumultuous and excruciating. My parents have been a tremendous source of support and life force during this time. They have helped me stay positive and focused. My close friends (you all know who you are) have taken our camaraderie to another level; your selflessness is exemplary. Thank you all for being there! My collaborators have patiently waited for me to cope up and supported my career goals by actively helping me when I was low. All of this will last a lifetime!

Massachusetts Institute of Technology
August 09, 2018.

Contents

Sampling Time-resolved Phenomena **24**

1 Introduction and Roadmap **25**
1.1 Overview . . . 25
1.2 Roadmap of this Thesis . . . 29
1.3 Technical Context . . . 33
1.3.1 Variations on a Theme . . . 35

Theoretical Contributions **38**

2 Sampling and Super-resolution: A Generalized Approach **39**
2.1 Sampling Theory and Approximation . . . 39
2.1.1 Sampling Theory of Smooth Signals . . . 39
2.1.2 Sampling Theory of Sparse Signals . . . 43
2.1.3 Sampling Theory Beyond Fourier Domain . . . 45
2.1.4 Overview of Contributions . . . 46
2.1.5 Notation . . . 47
2.1.6 Roadmap of this Chapter . . . 48
2.2 The Special Affine Fourier Transform . . . 48
2.2.1 Forward Transform . . . 49
2.2.2 Inverse Transform . . . 50
2.2.3 Geometry of the Special Affine Fourier Transform . . . 51
2.3 Convolution and Product Theorems . . . 55
2.3.1 Comparison and Alternative Results . . . 59
2.3.2 Summary of Results . . . 60
2.4 Sampling Theory of Smooth Functions . . . 60
2.4.1 Bandlimited Subspaces of the SAFT . . . 60
2.4.2 Shift-Invariant Subspaces of the SAFT . . . 63
2.4.2.1 Reconstruction with Arbitrary Basis Functions . . . 66
2.4.2.2 Application: Fractional Delay Filtering . . . 67
2.5 Sampling and Super-resolution of Sparse Signals . . . 71
2.5.0.1 Special Affine Fourier Series (SAFS) . . . 71
2.5.0.2 Sparse Signals and Arbitrary Bandlimited Kernels . . . 74
2.5.0.3 Generalization to Arbitrary Bandlimited Sampling Kernels . . . 76
2.5.0.4 Special cases of the SAFT domain result . . . 76
2.5.0.5 Sparse Signals and Smooth Time-limited Kernels . . . 78
2.5.0.6 Sparse Signals and the Gabor Transform Kernel . . . 81

3 The Unlimited Sensing Framework **84**
3.1 Introduction and Overview . . . 84
3.1.1 Shannon's Sampling Theory and a Practical Bottleneck . . . 85
3.1.2 A Solution via Modular Arithmetic . . . 86
3.1.2.1 Practical Context: Analog-to-Digital Converters . . . 86
3.1.2.2 Theoretical Context: Generalized Linear Model for Inverse Problems 87
3.1.3 Contributions . . . 91
3.2 Modulo Mapping . . . 92
3.2.1 Modulo Operator and Phase Unwrapping: The Case of One Dimensional Recovery 93
3.2.2 Modulo Operator and Imaging: The Case of Two Dimensional Recovery . . . 97
3.2.2.1 Acquisition Devices and Application Areas . . . 97
3.2.2.2 Recovery Algorithms . . . 99
3.2.3 Modulo Operations in Higher Dimensions . . . 100
3.2.4 Summary . . . 100
3.3 Unlimited Sampling of Bandlimited Signals . . . 101
3.3.1 A Sufficiency Condition and a Sampling Theorem . . . 102
3.3.1.1 Main Result: The Unlimited Sampling Theorem . . . 102
3.3.2 Numerical Demonstration . . . 109
3.4 Unlimited Sampling of Sparse Signals . . . 110
3.4.0.1 Sampling and Recovery of Sparse Signals in Practice . . . 111
3.4.1 Problem Setup . . . 112
3.4.2 Localized Reconstruction from Unlimited Sampling . . . 113
3.4.3 A Sufficiency Condition for Recovering Sparse Signals . . . 115
3.4.4 Numerical Demonstration . . . 115
3.5 Unlimited Sampling of Sparse Sinusoidal Mixture . . . 116
3.5.1 Coding Theory, Spectral Estimation and Sinusoids . . . 116
3.5.2 Sampling Sparse Mixtures of Sinusoids . . . 118
3.5.3 Sufficiency Condition for Recovery of Sparse Mixtures of Sinusoids . . . 118
3.5.4 Numerical Demonstration . . . 119

4 Sampling Parametric Functions of the Rational Family **121**
4.1 Introduction to the Sampling Problem . . . 121
4.1.1 Special Case: Single Exponential . . . 122
4.1.2 General Case: K Exponential Functions . . . 123

Applications and Experimental Demonstration **127**

5 Super-resolved Multi-bounce Imaging **128**
5.1 Introduction . . . 128
5.2 ToF Image Formation Model . . . 130
5.2.1 A General Model for ToF Sensors . . . 130
5.2.2 ToF Sensors and Sampling Theory . . . 131
5.2.3 Lidar Based ToF Imaging . . . 131
5.3 Super–Resolved ToF Imaging . . . 132
5.3.1 Bandlimited Approximation of Sampling Kernel . . . 132

5.3.2 Super-Resolution via FRI Principles . . . 134
5.3.3 Experimental Results and Performance Evaluation . . . 136
5.4 Summary . . . 137

6 Fluorescence Lifetime Imaging: A Blind and Calibration-free Approach 139
6.1 Introduction . . . 139
6.1.1 Roadmap for this Chapter . . . 140
6.2 ToF Image Formation Model . . . 140
6.2.1 Time-Domain ToF Imaging (TD-ToF) . . . 142
6.2.2 Frequency-Domain ToF Imaging (FD-ToF) . . . 144
6.3 Fluorescence Lifetime Imaging with Time-of-Flight Sensors . . . 145
6.3.1 Time-Domain ToF FLI: Theory and Experiments . . . 146
6.3.1.1 Theoretical Modeling . . . 146
6.3.1.2 Experimental Verification of TD-ToF-FLI . . . 148
6.3.2 Frequency-Domain ToF FLI: Theory and Experiments . . . 151
6.3.2.1 Experimental Verification of FD-ToF-FLI . . . 152
6.4 Discussion . . . 154
6.4.1 ToF Sensors for Microscopy . . . 154
6.4.2 Nanosecond Range Lifetime Sensing . . . 154
6.4.3 Experimental and Computational Precision . . . 156
6.5 Summary of Results . . . 157

7 Sampling without Time Information: Phase-retrieval in Time-resolved Imaging 159
7.1 Introduction . . . 159
7.1.1 Contributions . . . 161
7.1.2 Role of Temporal Phase Retrieval . . . 161
7.2 Problem Formulation . . . 162
7.3 Sampling Echoes of Light . . . 164
7.3.1 Bandlimited Approximation of Probing Function . . . 164
7.3.2 Sampling Theory Context . . . 164
7.4 Reconstruction via Phase Retrieval . . . 165
7.5 Experimental Validation . . . 166
7.5.1 Simulation . . . 166
7.5.2 Practical Validation . . . 166
7.6 Extension to Frequency Domain Time-resolved Imaging . . . 168
7.6.1 Estimating Fourier Transform from Measurements . . . 168
7.6.2 Direct Measurement of Fourier Magnitude Information . . . 170
7.6.3 Reconstruction via Frequency Estimation . . . 171
7.6.4 Revisiting the case of $K = 2$: Estimating $\{\Gamma_k\}$ from $\{\gamma_k\}$ . . . 172
7.6.5 Higher-Order Settings . . . 173
7.6.6 Experimental Results . . . 173
7.7 Summary of Results . . . 175

8 Photo-acoustic Time-resolved Tomography 176
8.1 Introduction . . . 176
8.2 Problem Setup: Photoacoustic ToF Imaging . . . 180

8.2.1 ToF Imaging Pipeline 180
8.2.2 From PA Wave Equations to Time-of-Flight 182
8.2.3 Tomographic Measurements for Geometric Estimation 183
8.3 Inverse Problem: Estimating Time-of-Flight 184
8.4 Photoacoustic ToF Imaging: Experimental Verification 186
8.4.1 ToF Estimation of RBCs 186
8.4.2 ToF Estimation of Melanoma Cells 187
8.5 Summary 187

Looking Ahead **189**

9 Conclusion **190**

List of Figures

1-1 3D images via time-resolved measurements. We show amplitude image (or the conventional digital image), depth image based on time-delays and 3D images seen from multiple viewpoints. 27
1-2 The role of diversity in imaging. 28
1-3 The Special Affine Fourier Transform (SAFT) which parametrically generalizes a number of well known unitary transforms linked with signal processing and optics. 31
1-4 Image formation model for time-resolved sensing. 34

2-1 Sampling and approximation procedure in shift-invariant subspaces. 42
2-2 K-sparse signals (a) on a real line and (b) periodized version of (a) on a circle. 44
2-3 Comparison of complex exponentials or $e^{\jmath\omega t}$ (Fourier basis function) with polynomial basis functions $e^{\jmath\phi(t)}$ where $\phi(t)$ is a quadratic function, $\phi(t) = a_2t^2 + a_1t + a_0$ for some $\{a_k\}_{k=0}^{3} \in \mathbb{R}$. 46
2-4 Fourier transform is cyclic on a group of 4, that is, $\mathscr{T}_{\mathbf{\Lambda}_{\mathsf{FT}}}^{(k+4)} = \mathscr{T}_{\mathbf{\Lambda}_{\mathsf{FT}}}^{(k)}$, $k \in \mathbb{Z}^+$ as described in (2.21). The Fractional Fourier transform allows for fractionalization of k so that a version of the Fourier transform may be defined on an arbitrary point on the circle. We denote such as transform by $\mathscr{T}_{\mathbf{\Lambda}_\theta}[f]$ where θ takes real values. 52
2-5 The SAFT maps one convex enclosure into another while preserving area since the transformation matrix $\mathbf{\Lambda}_{\mathsf{L}} \in \mathsf{SL}_2(\mathbb{R})$. The action of $\mathbf{\Lambda}_{\mathsf{L}}$ on a time-frequency co-ordinate $\mathbf{r} \in \mathbb{R}^2([0,1])$ results in $\widehat{\mathbf{r}} = \mathbf{\Lambda}_{\mathsf{L}}\mathbf{r}$. (a) For the FrFT, $\mathbf{\Lambda}_{\mathsf{L}} = \mathbf{\Lambda}_\theta$ implements rotation. The inverse transform corresponds to $\mathbf{\Lambda}_\theta^{-1} = \mathbf{\Lambda}_\theta^\top$. (b) For the Fresnel transform, $\mathbf{\Lambda}_{\mathsf{L}} = \mathbf{\Lambda}_{\mathsf{Fr}}$ implements shear. The inverse transform corresponds to $\mathbf{\Lambda}_{\mathsf{Fr}}^{-1}$. (c) For the Linear Canonical Transform (LCT), $\mathbf{\Lambda}_{\mathsf{L}}$ deforms a unit square into an arbitrary parallelogram. The inverse transform corresponds to $\mathbf{\Lambda}_{\mathsf{L}}^{-1}$. (d) For the SAFT, presence of an offset $\lambda = [p \;\; q]^\top$ results in an affine transform. Consequently, the inverse transform is given by $\mathbf{r} = \mathbf{\Lambda}_{\mathsf{L}}^{-1}\widehat{\mathbf{r}} - \mathbf{\Lambda}_{\mathsf{L}}^{-1}\lambda$. 53
2-6 Block diagram for SAFT convolution. We use the usual definition of the convolution operation in conjunction with chirp modulation to define the SAFT convolution operation. The gain factor $K_b = K_{\mathbf{\Lambda}_{\mathsf{S}}}$. 56
2-7 Defining low-pass projections in the SAFT sense. 62

2-8 Fractional Delay Filtering of signals in SAFT domain using the shift–invariant signal model. We show equidistant samples of the real part of the signal $g_{\mathsf{sig}}(t)$. The signal is characterized by coefficient and frequency vectors $\boldsymbol{\alpha}$ and $\boldsymbol{\omega}$ taking values $[35, 18, 10]$ and $[0.77, 0.31, 0.25]$, respectively. The SAFT parameter vector is set to be $[a_0, b_0, c_0, d_0, p_0, q_0]$ taking values [7, 2, 0.6, 0.3143, 2.5, 1], respectively. We use power cosine function $\nu(t) = (2/3)\cos^4(\pi t/4)\,\mathbb{1}_{[-2,+2]}(t)$ as the generator of shift–invariant subspace, we estimate the τ–delayed samples $g^{\tau}(kT)$, $k \in \mathbb{Z}$ and compare it with the analytical samples $g^{\tau}_{\mathsf{sig}}(kT)$, $k \in \mathbb{Z}$. Given $g_{\mathsf{sig}}(kT)$, the choice $\tau = 0$ amounts to reconstruction/interpolation the signal (see (2.45,2.50). For other choices of $\tau = 0.1T, 0.3T$ and $0.5T$, we reconstruct shifted versions of the $g_{\mathsf{sig}}(t)$. (Inset) Comparison between shift–invariant model for SAFT using ν in (2.54) and the classical Shannon's sampling method using $\nu = \text{sinc}$. The comparison metric is chosen to be peak–signal–to–noise ratio. The shift–invariant model for SAFT proves to be a better solution. 70

3-1 Usual ADC compared with self-reset ADC. (a) Whenever the input signal f_{In} voltage exceeds a certain threshold λ, the output signal f_{Out} in any conventional ADC saturates to λ and this results in clipping. In contrast, whenever $|f_{\mathsf{In}}| > \lambda$, the self-reset ADC folds f_{In} such that f_{Out} is always in the range $[-\lambda, \lambda]$. In this way, the self-reset configuration circumvents clipping but introduces discontinuities. (b) Images obtained with prototype self-reset ADC (b1) Image obtained with a self-reset ADC shows folded amplitudes. (b2) For each pixel, the "reset count map" shows the number of times the image amplitude has undergone folding. (b3) Unfolded image based on reset count map. (b4) Image obtained using an optical microscope. 86
3-2 Standard approaches for regularizing linear inverse problems. 88
3-3 Decomposition of a smooth signal into a modulo part and a piecewise constant part. . . 94
3-4 Recovery from modulo operator with $\lambda = 1/50$. (Left figure) Recovery procedure that exploits higher order finite-differences. (Right figure) Classical unwrapping algorithm which works with first order conditions fails in this case. 96
3-5 Classification of acquisition schemes and algorithms in context of two dimensional modulo operation. 98
3-6 SR-ADC architecture for obtaining modulo samples. 101
3-7 For a prototype low-pass filtered data $g = f * \psi$ (in ——) we plot the continuous version of the modulo-ADC $\mathscr{M}_{\lambda}(g(t))$ (in ——) together with uniform samples y_k (in —•). We plot the continuous time residual $\varepsilon_g(t) = g(t) - \mathscr{M}_{\lambda}(g(t))$ (in ——) and its sampled version $\{\varepsilon_{\gamma} = \gamma_k - y_k\}$ (in —•). 103
3-8 Higher order differences commute with the modulo operation. After applying the amplitude folding (via modulo operation) to the derivative (and difference of modulo samples, respectively), one obtains the same output as if one had started with g_k instead of y_k. That in turn will allow for recovery if the higher order finite differences of the samples or g_k's are so small that the amplitude folding has no effect. 105
3-9 Modulo sampling of bandlimited functions. (a) Randomly generated bandlimited function $g \in \mathcal{B}_{\pi}$, its modulo samples y_k acquired with $\lambda = 1/20$ and $T \approx 1/2\pi e$, as well as reconstructed samples $\widetilde{\gamma}_k$ with $N = 5$. The mean squared error between $\gamma_k = g(kT)$ and reconstructed samples, $\widetilde{\gamma}_k$ was 1.6×10^{-33}. (b) We plot $\varepsilon_g(t) = g(t) - y(t)$ and compare the ground truth ε_{γ} with its reconstructed version $\widetilde{\varepsilon}_{\gamma}$. The mean squared error between ε_{γ} and $\widetilde{\varepsilon}_{\gamma}$ was of the order of machine precision, 1.5×10^{-33}. 109

3-10 Two practical scenarios for amplitude limited sampling. (a) Ultra-wide band signal undergoes saturation. (b) Data from ultrasonic sensor reveals that the dominant reflection is clipped or saturated as it exceeds the maximum recordable voltage of the ADC. In this case, exact calibration of ψ is not possible. 111
3-11 Unlimited sampling of sparse signals with $K = 2$. We plot low-pass filtered data g (cf. (3.27), the folded function $\mathscr{M}_\lambda(g)$ as well as modulo samples y_n in (3.8). 112
3-12 Sparse signal recovery via local reconstruction of modulo samples with $\beta_g = 3.2511$ and $\lambda = 0.25$. (a) We plot K–sparse signal $s_K(t)$ with $K = 3$ and $\tau = 10$, the low-pass filtered signal $g = s_K * \psi$ where $\psi(t) = \text{sinc}(t)$ as well as modulo samples $y_n = \mathscr{M}_\lambda(g_n)$ with $T = 0.0485$. Note that $\psi \in \mathcal{B}_\pi$. (b) Using Algorithm 1, we estimate unfolded samples $\widetilde{g}_n$ from $N = 99$ modulo samples of y_n. For this purpose $L = 3$. The reconstruction is observed to be exact (upto machine precision). Given $2K+1$ of $\widetilde{g}_n$, the spikes are estimated using Algorithm 2. 116
3-13 (a) Sampled version of a sinusoidal mixture with $K = 3$. These samples are obtained using time-resolved imaging sensor [209] where each sinusoidal frequency is related to an echo of light. (b) Conventional ADCs saturate or clip with the input signal exceeds the maximum recordable voltage of the ADC. (c) Sampling with *unlimited sensing framework* results in low dynamic range, scrambled samples. This is based on a new ADC design which non-linearly folds the amplitudes of the signal. In this way, entire dynamic range of the input signal is encoded in folded samples. 117
3-14 Unlimited sampling and recovery of sinusoidal mixtures (a) Sinusoidal mixture with $K = 3$. We plot g together with unlimited samples $\{y_n\}_{n=0}^{N-1}$ where N is chosen in accordance with Theorem 12. (b) Using modulo samples y_n, we estimate unfolded samples $\widetilde{g}_n$. The estimated samples match the oracle valued samples, g_n up to machine precision. (c) We use spectral estimation [67] to estimate unknowns $\widetilde{c}_k$ and $\widetilde{\nu}_k$ which are used to synthesize $\widetilde{g}(t)$ using (3.36). The estimated signal matches the original. The mean squared error between g and $\widetilde{g}$ is noted to be 1.3191×10^{-15}. 120

5-1 Illustration of the time–of–flight (ToF) principle. (a) The sensor emits a signal and the reflected signal is time delayed version of the emitted signal. The time delay is proportional to the distance of the object form the sensor. (b) ToF principle in complex environment which suffers from multiple reflected echoes. (c) Challenging case of super-resolution of multiple overlapping echoes. (d) Lidar ToF data corresponding to (b). (e) Lidar ToF data corresponding to the super-resolution problem in (c). 129
5-2 Instrument response function for LiDAR ToF system. (a) Observed time profile and its Fourier Series approximation (5.15) with $L = 25$ ns and $M_0 = 80$. (b) Fourier spectrum together with Fourier Series coefficients $\{\widehat{\phi}_m\}_{|m| \leqslant M_0 = 80}$ (5.15). With $f_0 = \omega_0/2\pi = 40.0195$ MHz, the maximum frequency used for approximation of $\phi(t)$ is $M_0 f_0$. . . . 133
5-3 LiDAR based Super-resolution ToF Imaging. (a) The experiment consists of two retro-reflecting cubes at distance of 330 m from the sensor. We show the recovery of reflectors with inter-reflector separation $\delta d_{\ell_1} = 1.7$ cm. We also plot the result due to Orthogonal Matching Pursuit [229]. (b) We conduct experiments with various separations and plot the results on log–log scale. Our method outperforms previously reported results on the same data in [64]. 136

5-4 (a) We setup experiments with separation distances $\delta d = 1.74$, 3.20 and 18.21 cm, respectively and plot the log-MSE as a function of signal–to–noise ratio or the SNR (in dB). (b) We use the IRF to estimate the SNR. The observed SNR for the system is 43.18 dB. (c) We compare computational times for OMP and matrix pencil method. The average of all trials is marked in the figure. In contrast, the RJMCMC method due to [64] requires about a second per pixel. 138

6-1 Depth or range imaging based on time-of-flight (ToF) principles and its link with fluorescence lifetime imaging. For the choice of scene response function (SRF) $h(t,x) = \rho\delta(t - x - 2d/c)$ (a) and (b) compare time and frequency based methods for depth imaging based on ToF principles. (a) Probing and reflected signal for time-domain time-of-flight (TD–ToF) setup. The time delay is proportional to distance d. (b) Probing and reflected signal for frequency-domain time-of-flight (FD–ToF) setup. The phase is proportional to distance d and modulation frequency ω_0. For the SRF $h(t,x) = h_{\mathsf{Depth}}(t,x) + h_{\mathsf{Sample}}(t,x)$ in (6.13), (c) and (d) compare time and frequency based methods for fluorescence lifetime imaging based on ToF principles. (c) Probing and reflected signal for time-domain time-of-flight (TD–ToF) setup. The time delay is proportional to distance d and the waveform shape is linked with lifetime τ. (b) Probing and reflected signal for frequency-domain time-of-flight (FD–ToF) setup. The phase is proportional to distance d, modulation frequency ω_0 and lifetime τ. (e) Experimental setup for fluorescence lifetime estimation using ToF sensors. 143

6-2 Experimental cross-correlated probing function Eq. (6.8) (– –) and its Fourier series approximation (–•–), Eq. (6.9), with $N_0 = 30$. Since the time-domain signal $\mathsf{C}_{p,\overline{p}}$ lasts for $\Delta = 309.902$ ns, the corresponding fundamental Fourier harmonic is $\omega_0/2\pi = 3.2268$ MHz. Consequently, Fourier coefficient $N_0 = 30$ corresponds to ~ 96.80 MHz. Inset: Fourier series coefficients $\widehat{\phi}_n, n = -N_0, \ldots, N_0$. 144

6-3 TD-ToF-FLI measurements. (a) Time profile of measurements $m_k = m(kT_s), T_s = 7.8120$ ps based on $K = 3968$ samples. These measurements result from convolving cross-correlation of the probing function with the SRF, Eq. (6.17). (b) Phase measurements computed using $\angle\widehat{\mathbf{h}} = \angle\mathbf{V}^{+}\mathbf{m}$ with $N_0 = 15, \Delta = 309.9$ ns. We estimate the distance $\widetilde{d}$ and lifetime $\widetilde{\tau}$ parameter using nonlinear least squares fitting, which results in the fitted curve. The fitted result is marked in —. The estimated phase contribution Eq. (6.19) due to distance $\theta_{\widetilde{d}}$ and lifetime $\theta_{\widetilde{\tau}}$ is also plotted. 149

6-4 FD-ToF-FLI measurements of a 61×66 pixel patch of 120×160 pixel sensor image. The size of the scene is approximately 2.3 in^2. (a) Multi-frequency measurements of $\tau = 32$ ns quantum dot based fluorescent sample. We show phase and amplitude images, that is, $\{\angle z(10f_0), \angle z(20f_0), \angle z(30f_0), \angle z(40f_0)\}$ (in radians, $[0, 2\pi]$) and $\{|z(10f_0)|, |z(20f_0)|, |z(30f_0)|, |z(40f_0)|\}$ (in decibels), respectively. The base modulation frequency for the experiment is $f_0 = \omega_0/2\pi = 1$ MHz. The phase at the background pixel is recorded to be $\angle z_{(x_b,y_b)}(40f_0) = 4.1625$ radians which amounts to a depth of 2.48 m which is consistent with the experimental setup. At the location of the fluorescent sample, we recored a higher phase value $\angle z_{(x_f,y_f)}(40f_0) = 5.5822$ which is attributed to the fluorescence phenomenon. (b) Multi–frequency, raw phase measurements $\{\angle z_{(x,y)}(kf_0)\}_{k=1}^{K=40}$ for four pixels. The measurements confirm with the theoretical hypothesis of Eq. (6.19) as well as the fitted phase obtained by Eq. (6.34). The estimated phase contribution Eq. (6.19) due distance $\theta_{\widetilde{d}}$ and lifetime $\theta_{\widetilde{\tau}}$ is also plotted. . 153

6-5 Estimation accuracy of $\tau_1 = 4$ ns and $\tau_2 = 32$ ns. (a) We plot 2000 estimated values of lifetime as a function of SNR ranging from 0–60 dB. As the SNR increases, the estimates cluster around the oracle estimate of $\tau = 4$ ns and $\tau = 32$ ns, respectively. (b) We plot the $\sqrt{\mathsf{MSE}_\tau}$ on log scale as a function of SNR. After 15 dB, we note a consistent linear relationship Eq. (6.35) between SNR and the $\log\left(\sqrt{\mathsf{MSE}_\tau}\right)$. 155

6-6 Measured phase as a function of the modulation frequency. We plot the measured phase corresponding to a 120 pixel cross-section of the 160×120 ToF sensor image for modulation frequencies $f = \{10,\ 20,\ 30,\ 40\}$ MHz. The first 50 phase measurements are due to the background pixel which is at a depth $d = 2.5$ m. The dashed line marks the average phase value over first 50 pixels. The average phase value for each modulation frequency leads to a distance estimate: $d = \{2.56,\ 2.52,\ 2.47,\ 2.48\}$ in meters. 157

7-1 Reflection from semi-reflective surfaces. The Memorial Church can be seen imprinted on the glass facade of the Harvard University Science Center. 160

7-2 Time-aware imaging. (a) Exemplary setting for imaging through semi-reflective media. (b) Corresponding time-aware image at pixel $\mathbf{r}_0 = (x_0, y_0)^\top$. 160

7-3 Bandlimited approximation $\widetilde{\varphi} \approx \mathcal{C}[p]$ with $L = 25$ (red curves) and its cyclic auto-correlation $\mathcal{C}[\widetilde{\varphi}]$ (blue curve). Shown are the spatial-domain signals (top) and the corresponding Fourier-domain magnitudes in log scale (bottom). 163

7-4 Experimental results on acquisition and reconstruction of echoes of light in a scene. (a) Single pixel, time-stamped samples $y = \mathcal{C}[p] * \overline{h}_2$ serve as our ground truth because the phase information is known. We also plot the estimated, 2-sparse SRF (7.5) in red ink. (b) Fourier domain frequency samples of the SRF, $\widehat{h}_2(\ell\omega_0)$ with $L = [-20, 20]$ and $\omega_0 = 2\pi/\Delta, \Delta = 70$ ps. We plot the measured data in green and the fitted data in black. The frequencies are estimated using Cadzow's method. (c) Same pixel, time-stampless, low-pass filtered, auto-correlated samples (7.9) together with the estimated, auto-correlated SRF $\mathcal{C}[h_2]$ in red ink. (d) Fourier domain samples $\widehat{s}(\ell\omega_0)$ (7.11) and its fitted version (black ink). (e) Ground truth images for the experiment. (f) Estimated images using temporal phase retrieval. 167

7-5 Phase Retrieval in Setting $K = 3$. This measurement corresponds to pixel $(20, 20)$ of the synthetic experiment in Section 7.6.6. (a) Complex–valued $\widehat{s}(\omega)$ with the real and imaginary parts together with the envelope $\pm|\widehat{s}(\omega)|$. (b) Phase–less $|\widehat{s}(\omega)|^2$ with $s_n = |\widehat{s}(n\omega_0)|^2, \omega_0 = 5$. (c) Decomposition of s_n into terms of $\{\gamma_k, \nu_k\}_{|k|\leqslant K_0}$ as in (7.22). 171

7-6 (a) Experimental results for simulated data with $K = 3$. The images on the top are spatial maps of the available magnitude multi-frequency measurements $|\hat{s}(2n\omega_0 + 1)|^2, n = 1, \ldots, 8$. For $K = 3$ we show the ground truth which consists of distinct layers constituting the scene as well as the reconstruction from the phase-less data with $N = 1+(K^2-K)/2 = 4$ measurements. We list the PNSR value indicating reconstruction up to machine precision. (b) Performance analysis of the Cadzow's CMPA algorithm [275] for $K = 2$ for the noisy case. We show the effect of over–sampling, that is $N = \kappa(K+1)$ samples, on mean squared error (MSE) as a function of signal–to–noise ratio (SNR). As can be seen, when $\kappa = 2$ or we have $2N$ samples of s_n, the CMPA algorithm has a stabilizing effect on MSE. For the case of $16x$ oversampling, the MSE decreases linearly with increase in SNR. This effect happens as early as SNR $= 3$ (dB) for the CMPA algorithm. We also compare the LSE method with the CMPA method for different over–sampling factors. (c) Scene setup for experiment for $K = 2$ with Microsoft Kinect. (d) Schematic representation of the constituent images. (e) We reconstruct the assuming that we measure $\widehat{s}(nf_0), n = 50, \ldots, 100$ with $f_0 = 1$ MHz. (f) Reconstruction via phase retrieval using $|\widehat{s}(nf_0)|^2, n = 50, \ldots, 100$ with $f_0 = 1$ MHz. 174

8-1 Conceptual explanation of the *photoacoustic effect* which is the conversion or transformation of electromagnetic energy into acoustic energy. This phenomenon that was first observed by Alexander Graham Bell in 1880 [279]. In this example, a pulse of light excited a cell which in turn releases acoustic energy. The *ultrasonic* acoustic signature was acquired experimentally. 177

8-2 Photoacoustic measurements of single RBC. The cross-section of the biconcave RBC is shown in blue ink. The arrow shows the direction of wave/pulse propagation. (a) Horizontal configuration with minimal spread in time-domain. (b) Vertical configuration with a larger spread in time-domain. The red bars mark the approximate time-spread of the pulses. Also see Fig. 8-5. 178

8-3 Power spectrum of low-pass measurements: $\widehat{B}_h(\omega) = \widehat{S}_h(\omega)\, b(\omega)$ where $b(\omega)$ is the frequency response of the low-pass measurement device. With $\Delta_2 < \Delta_1$, no spectral minima occur in the bandwidth $\omega \in [-\Omega_m, \Omega_m]$. 179

8-4 Photoacoustic waves in layered media. All figures should be understood in sense of negative time. (a) Geometrical setup with K reflecting boundaries or layers. The first reflective surface marked in blue is virtual. Optical excitation causes thermo elastic expansion resulting in sound waves and $t = z/\nu$ is the instant at which sound waves travel to the source. There on, sound waves are reflected from each layer at $t = z_k/\nu$. (b) Corresponding scene respond function. Here, each reflecting boundary results in a round trip travel time of $t_k = 2z_k/\nu$. (c) We plot the propagating wave, $\mathsf{P}(z, t)$ in the case of optical excitation $\mathsf{H}(z, t) = \delta(z - z_T)\, p(t)$, where the probing function $p(t)$ is chosen to be a Gabor pulse. (d) Time-domain waves reflected towards the source at $z = 0$. 181

8-5 Tomography of RBCs. At each θ, reflections from the cell walls (layered media) result in a distinct time-of-flight, $\Delta_\theta = |z_1 - z_0|$. Note that Δ_θ encodes the geometric properties of the enclosure which may be RBC, WBC or CMC. 183

8-6 Optical images of RBCs at various orientations ranging from horizontal to vertical. Optical images are used to register with corresponding PA measurements. 187

8-7 (a) Photoacoustic measurements $\{m_{\theta_\ell}(nT)\}_{\ell,n}$ with $T = 0.125$ ns, $N = 311$ and θ_ℓ ranging from vertical to horizontal orientation in 108 steps. (a_1) to (a_4) We plot PA measurements for four orientations. In the inset, we plot the optical image of the single cell RBC together with an approximate orientation angle. The measured data in blue ink (—). Super–resolved SRF specified by $\{|\gamma_k^{(\theta)}|, t_k^{(\theta)}\}_{k=0,1}$ in (8.6) and (8.8) is marked in red ink (—•). Based on the estimates $\{|\widetilde{\gamma}_k^{(\theta)}|, \widetilde{t}_k^{(\theta)}\}_{k=0,1}$, the reconstructed data $\widetilde{m}_\theta$ (8.8) is plotted in red ink (- - -). Reconstruction quality metric, the PSNR and the ToF are also annotated in the inset. Finally, we show the result of maximum likelihood estimation (exhaustive search) with blue spikes (—▶). (b) PA measurements of melanoma cells (CTC). We show the data in gray ink (—). Super–resolved SRF, $\{|\gamma_k^{(\theta)}|, t_k^{(\theta)}\}_{k=0,3}$ is marked in red ink (—•) and the reconstructed data is plotted in red ink (- - -). 188

List of Tables

1.1 Summary of Theoretical Contributions and Relevant Chapters/Sections. 30

2.1 Comparison of Approximation Schemes 42
2.2 Roadmap of Key Sampling Theory Results Linked with the SAFT Domain 48
2.3 SAFT, Transformations and Operations 49

3.1 Generalized Linear Model for Sparse Signal Recovery 89

5.1 Different Modalities for Optical Time-of-Flight Sensor Based Depth Imaging 131

6.1 Time and Frequency Domain Time-of-Flight Depth Imaging 142
6.2 Time and Frequency Domain Time-of-Flight Fluorescence Lifetime Imaging 146
6.3 Time Domain ToF FLI ($\tau = 32$ ns and $d = 1.05$ m). 150
6.4 Frequency Domain ToF FLI ($\tau = 32$ns and $d = 2.5$ m). 154

8.1 Estimates of Cell Size 187

To my parents.

Introduction to Time-resolved Sensing and Imaging

पावका नः सरस्वती वाजेभिर्वाजिनीवती ।
यज्ञं वष्टु धियावसुः ॥

चोदयित्री सूनृतानां चेतन्ती सुमतीनाम ।
यज्ञं दधे सरस्वती ॥

महो अर्णः सरस्वती पर चेतयति केतुना ।
धियो विश्वा वि राजति ॥

"Her great flood does Sarasvatī reveal with her beacon. She rules over all insights." [1]

— Rigveda (Mandala I, §3, ¶ 10–12)

1 Introduction and Roadmap

1.1 Overview

"A picture is worth a thousand words."

Throughout the past several centuries, this immemorial phrase has pushed development of photography from analog to digital, accelerated by breakthrough advancements in sensor technology. The digital revolution created a necessity for sophisticated signal processing algorithms tailored for image enhancement, storage and compression. Shannon's sampling theory was the pathway for analog-to-digital image conversion. The classical Weiner filter was used for image enhancement. Transform-domain coding utilizing discrete cosine and wavelet transforms played a pivotal role in JPEG compression. Over the last few decades, with the advent of the *wavelet transform* and *compressed sensing* theory, the field of signal processing has undergone a philosophical reformation. A field that once relied heavily on smoothness assumptions now uses principles inspired by the notion of sparsity. Until the last decade or so, the fields of image sensor technology and signal processing ran in parallel to one another with minimal interaction or exchange of know-how. However, there has recently been a growing trend towards the coherent co-design of sensors and algorithms: This is the theme of the emerging area of *Computational Imaging* [2].

Practitioners of this computational imaging/photography ideology have devised many solutions which were previously not possible when individually adding functionality to the sensor architecture or using a more sophisticated processing algorithm. For example, consider the problem of motion deblurring that arises in conventional imaging. Whenever an object moves during sensor exposure, it causes pixels to

smear across the frame resulting in a blurred image. In the context of signal processing, this is an ill-posed problem that has been well-explored within the theme of deconvolution. The key problem is that the exposure time defines a temporal filter, which is essentially a box filter that annihilates any high-pass, spatial information. Consequently, algorithmic sophistication alone is not enough. Blurring may be avoided by a shorter exposure time, but this comes at the expense of low signal-to-noise ratio. It is clear that neither deconvolution nor the sensor level adaptation in itself suffice for a solution to the deblurring problem. The distinct role of computational imaging emerges when one considers the so-called *Flutter–Shutter* approach [3]. This approach involves a co-design of sensor and algorithms: in contrast to traditional imaging methods which require the shutter to be fully open during the exposure time, the flutter–shutter method flutters the shutter on and off in a binary, pseudo-random sequence. This sequence converts the non-invertible box-filter into an invertible one and, based on the choice of pseudo-random sequence, the corresponding deconvolution filter may be devised. Beyond deblurring in consumer imaging, the flutter–shutter approach is also useful in bio-imaging [4] where the imaging sensor may not be fast enough to capture flowing structures such as blood cells. Other notable examples of the computational imaging philosophy include,

- High dynamic range imaging [5].
- Light-field imaging [6, 7].
- Single pixel imaging [8].
- Fourier ptychographic microscopy [9].
- Non-line-of-sight imaging [10].

For the most part, image sensor design, signal/image processing and computational imaging have largely been restricted to two dimensional scenes. However, a true and richer representation of the environment around us lives in a three dimensional or 3D space. Capturing 3D information of a scene offers unparalleled benefits in accuracy and capabilities and is surely the future in many areas. This necessitates development of imaging modalities capable of recording 3D images.

A number of methods have been developed for the purpose of 3D imaging. This involves triangulation, interferometry and time-of-flight approaches. Of all the 3D capture techniques, the time-resolved approach based on the Time-of-Flight (ToF) method has arguably attracted the most commercial and scientific interest in the last couple of years; there has been a surge of research towards improving both the sensor design as well as the algorithms used for processing 3D images. Time-resolved imaging is the theme of this work around which new theoretical developments and applications are reported in this thesis.

The ToF principle, which is at the heart of all time-resolved imaging systems, exploits the idea that distance and time are proportional quantities. As the name suggests, ToF is the round trip time between the source and the destination taken by a particle or a wave, in a given medium. Hence, knowing one entity is equivalent to knowing the other. Nature is replete with examples that rely on the ToF principle. Bats, dolphins and visually impaired human beings use the ToF principle for navigational purposes.

Chronologically, the use of sound waves superseded the use of electromagnetic waves. Humans have used stones to estimate the depth of wells for millennia. The earliest work on using light waves for measuring ToF dates back to an experiment conducted by Galileo who was interested in estimating the speed of light. Unfortunately, his choice of distance (separation between two hills) did not lead to a conclusive result. The Danish astronomer Ole Rømer overcame this difficulty by using planetary distances. About two hundred years later, French physicist Hippolyte Fizeau was the first to estimate the speed of light precisely.

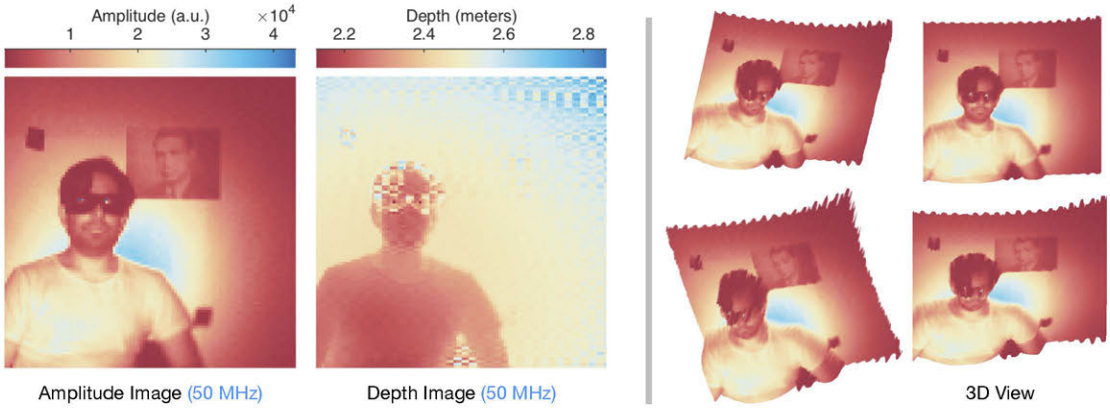

Figure 1-1: 3D images via time-resolved measurements. We show amplitude image (or the conventional digital image), depth image based on time-delays and 3D images seen from multiple viewpoints.

Through the discovery of the photoelectric effect by Albert Einstein in the 1900s and the development of the electronic imaging sensors (CCD/CMOS), we are now at a point where the accumulated research efforts in the area of photonics and electronics have culminated in mass producible optical ToF sensors.

Contrary to conventional imaging sensors such as digital cameras that produce 2D images $I(x, y)$, ToF sensors capture 3D images, $I(x, y, z)$. The unique ToF sensor produces two images per exposure: an amplitude image and a depth/delay image. The amplitude image is the standard 2D photograph, $I(x, y)$. Each pixel on the depth image represents the corresponding distance in the scene which is an equivalent of the *time-delay*[1]. The combination of the amplitude and the depth image produces the 3D image. We show the amplitude, depth and resulting 3D images in Fig. 1-1.

ToF based 3D imaging allows for applications that were previously unexplored. One of the first results demonstrated non–line–of–sight imaging capability [10]. This result—in parallel to "Doc" Edgerton's famous *Bullet Through Apple*[2] image—lead to ultrafast imaging of light packets at an exorbitant frame rate of one trillion frames per second. A flurry of follow up work lead to results that allowed imaging through scattered media [11], light–in–flight imaging [12, 13] and 3D imaging in extremely low light [14].

Early scientific instrumentation for computational imaging based on ToF principle required high quality equipment often fragile, prohibitively expensive and constrained to controlled laboratory environment. This is because fundamental to the ToF principle is the fact that the speed of light, that is, 3×10^8 m/s, is assumed to finite. This, in practice, is achievable only when electro-optical elements of the imaging system are extremely precise. However, in context of gaming and entertainment industry, a number of consumer companies such as Mesa Imaging, Microsoft and PMDtec have developed consumer-grade ToF sensors that are not only affordable but also alleviate all the issues associated with their expensive and sensitive counterparts—custom designed scientific hardware.

With the advent of 3D sensing technology (most notably, the Microsoft Kinect XBox One) we can now replace room sized apparatus [10], moving sensors, and raster scan systems [14] by *miniaturized, cost–effective, real–time, and full-frame* ToF systems. Computational ToF imaging has already found a plethora of applications in, for example, ultra–fast imaging [15, 16], non line–of–sight imaging [17], imaging

[1]For distances in meters, the time-delay is on the order of nanoseconds.

[2]`http://edgerton-digital-collections.org/galleries/iconic\#hee-nc-64002`

through scattering media, [18] and colored ToF imaging [19]. Outside of the computational imaging and human–computer interaction communities, an important application area is health care technology [20] and bio-imaging [21].

ToF sensors motivate a demand for forward models and algorithms that can handle this new wave of data. A handful of algorithms inspired by the signal processing community have been used to tackle inverse problems in optical ToF, but significant and numerous challenges still remain. Current efforts are directed at establishing empirical results with a rare discussion on design of *efficient algorithms*, *fundamental limits* or *performance bounds*. Another question that remains is: Can mathematics motivate new sensing architectures in this context?

While optical ToF sensors are a recent phenomenon, other systems centered around time-resolved measurements such as ultrasound, seismic and radar technology have been around for decades. The knowledge transfer between optical and other ToF systems is far from reality. Each ToF modality has its own idiosyncratic constraints which stem from the physics of the problem. However, there are commonalities that are shared by all of these systems.

Beyond the conventional sense, time-resolved sensors open a whole new dimension in the context of sensing and imaging—the *time* dimension. View-point diversity and illumination diversity are well established ideas that are frequently used in applications ranging from microscopy to computer vision. While the former relies on taking more measurements from different viewpoints, the latter approach typically keeps the imaging sensor fixed while illuminating the scene from different perspectives. This is explained in Fig. 1-2. In this context, exploiting *time diversity*, that is, acquiring an image at different time-scales poses new questions at various levels; both in the direction of theory and applications.

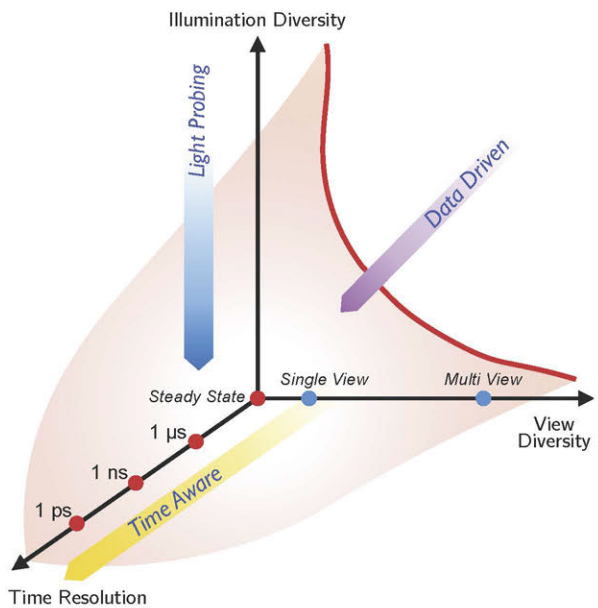

Figure 1-2: The role of diversity in imaging.

To systematically dissect this idea, consider the *plenoptic function* [22] which is a function of time and parameters such as viewpoints (three dimensional co-ordinates and orientation), wavelength, and polarization. Typically, such a function is captured by marginalizing the time information which leads to a *photograph* or *how many photons are collected at a given pixel?* On the other hand, if we have access to the time information, as pointed out by Velten *et al.* [10], even non-line-of-sight information may be captured. The time scales at which information can be captured depends on the hardware and the modality. In the same way as *spatial resolution* is connected to conventional imaging, the idea of *time resolution* is tied to the extent to which a time-resolved sensor can capture information at different time scales. In either case, the end product, which is a measurement, is a discrete quantity. However, imaging parameters such as time-delays (or depth) and fluorescence lifetimes are defined on the continuum. This is where sampling theory and harmonic analysis finds its way in this thesis.

This thesis is based on a collection of chapters which strives to achieve a synergistic balance between

theory and applications. Tools based on theory are used to devise new algorithms or tailor existing ones to push the state-of-the-art in context of practice. Inspiration from practice and experiments is used to carve new mathematical hypotheses leading to new results in theory.

1.2 Roadmap of this Thesis

The topics covered in this thesis are categorized into theoretical and applied contributions. Although the development of chapters presented in this work was a result of a cyclic process between theory and experiments, for readability of the same, theoretical contributions precede practical demonstrations. An overview of the roadmap is below which also shows interdependencies between the results covered in various chapters. Furthermore, a chapter-wise summary of theoretical contributions and their context is presented in 1.1.

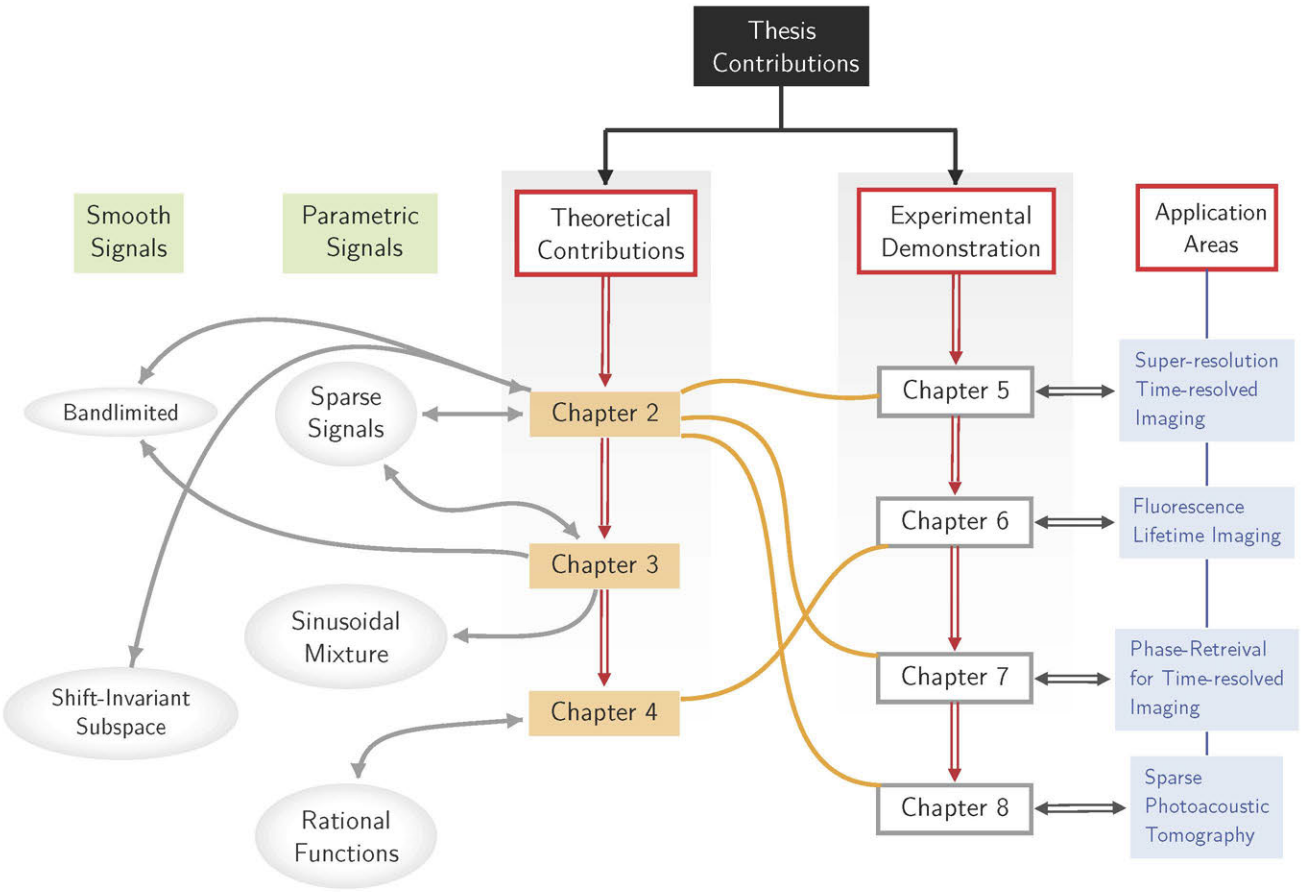

Table 1.1: Summary of Theoretical Contributions and Relevant Chapters/Sections.

	Section	Result	Context
Chapter 2	Section 2.3	Theorem 2	Convolution and product theorem for the SAFT domain.
	Section 2.3.1	Theorem 3	Alternative version of convolution and product theorem.
	Section 2.4.1	Theorem 4	Sampling Theorem for SAFT domain.
	Section 2.4.2	Theorem 5	Riesz basis criteria for SAFT domain.
	Section 2.5	Theorem 6	Series representation for sparse signals.
	Section 2.5.0.2	Theorem 7	Sparse Sampling with bandlimited kernels
	Section 2.5.0.2	Theorem 8	Exact recovery condition for super-resolution.
	Section 2.5.0.2	Proposition 1	Sparse representation with arbitrary bandlimited kernels.
	Section 2.5.0.5	Proposition 2	Sparse representation with time-limited kernels.
	Section 2.5.0.5	Proposition 3	Smoothness and decay in the SAFT domain.
Chapter 3	Section 3.3	Theorem 9	Unlimited sampling of bandlimited functions.
	Section 3.4	Theorem 10	Local reconstruction theorem.
	Section 3.4	Theorem 11	Unlimited sampling sparse signals.
	Section 3.5	Theorem 12	Unlimited sampling sparse mixture of sinusoids.
Chapter 4	Section 4.1.2	Theorem 13	Parametric sampling of modulated rational functions.

Summary of Results

1. **Theoretical Contributions**

   - Chapter 2 Sampling and Super-resolution: A Generalized Approach

     As mentioned earlier, scene related parameters lie on a continuum while (digital) measurements can only be discrete. For this purpose, we start our discussion with *sampling theory*. This approximation theoretic result is at the heart of analog-to-digital conversion and states that a function bandlimited in the Fourier domain is completely characterized by its discrete measurements obtained at uniform time instants that are at least separated by an interval inversely proportional to twice the maximum frequency. This result has been extended far and wide. Two recurrent themes ask the following questions:

     Q. 1 Can we recover non–bandlimited signals?

     Q. 2 What if the domain of investigation is something other than the Fourier Transform?

     In this chapter, we take sampling theory beyond the Fourier Transform. Bandlimited functions are de-facto associated with compact support in the Fourier domain, however, in many interesting applications, this may not be a suitable choice. For instance, in holography, a natural choice of translation is the Fresnel transform.

     For this purpose, we consider the Special Affine Fourier Transform (SAFT) which parametrically generalizes a number of well known unitary transforms linked with signal processing and optics (cf. Fig. 1-3). We first derive a version of Shannon's sampling theory based on

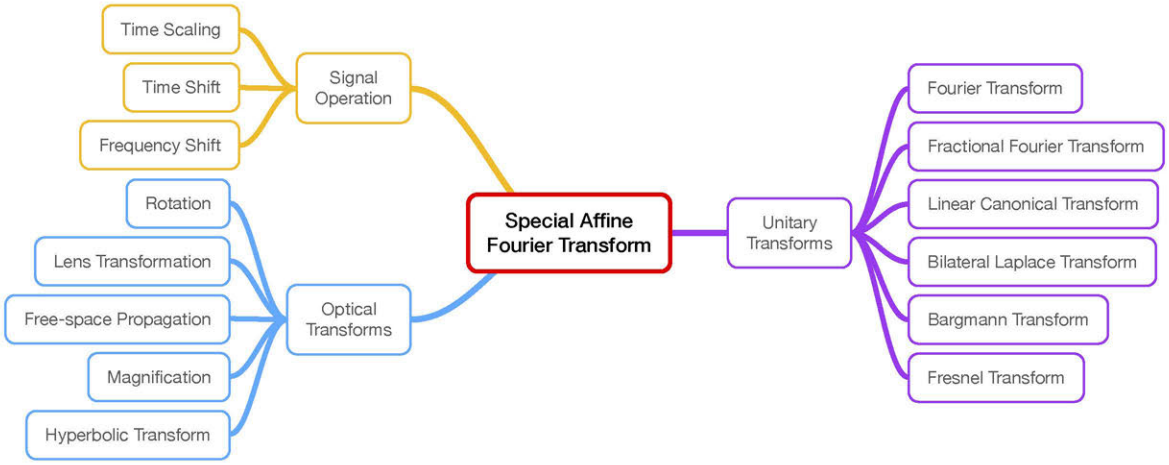

Figure 1-3: The Special Affine Fourier Transform (SAFT) which parametrically generalizes a number of well known unitary transforms linked with signal processing and optics.

---

the convolution structure tailored for the SAFT domain. Having identified the subspace of SAFT–bandlimited functions, we extend the results to shift-invariant subspaces. There on, we use various harmonic analysis related tools for studying recovery of sparse signals from low-pass projections in the SAFT domain. The chapter therefore provides a unified view of sampling theory for a large class of disparately studied operations. All of the results developed in this chapter are backward compatible with the Fourier domain results.

A summary of main theorems and their corresponding context is presented in 1.1.

- Chapter 3 The Unlimited Sensing Framework

  This chapter introduces the *unlimited sensing* framework that allows for recovery of arbitrarily high dynamic range signals from a constant factor oversampling of its low dynamic range samples. Remarkably, the oversampling factor is independent of the maximum recordable voltage.

  Conventional sensing systems such as the analog-to-digital convertor saturate or clip whenever the signal crosse the maximum recordable voltage. In contrast, the unlimited sensing strategy is based on a radically new sampling architecture and comes with recovery guarantees.

  In analogy to Shannon's sampling theorem, our first result, the *Unlimited Sampling Theorem* proves that a bandlimited signal can be recovered from modulo samples provided that a certain sampling density criterion, that is independent of the ADC threshold, is satisfied. In this way, our result allows for perfect recovery of a bandlimited function whose amplitude exceeds the ADC threshold by orders of magnitude. Next, we consider the inverse problem of recovering a sparse signal from its low-pass filtered version. This problem frequently arises in several areas of science and engineering and in context of signal processing, it is studied in several flavors, namely, sparse sampling, super-resolution and sparse deconvolution. We develop a sampling theory for modulo sampling of low- pass filtered spikes. Our main result consists of a new *local reconstruction theorem* and an algorithm which stably recovers a K–sparse signal

from low-pass, modulo samples. The local reconstruction theorem is then used for studying classical spectral estimation methods for estimation of sinusoidal mixtures.

As will be seen later in Chapters 5, 7 and 8, both sparse signals and sinusoidal mixture models are very relevant to the context of time-resolved imaging.

A summary of main theorems and their corresponding context is presented in 1.1.

- Chapter 4 Sampling Parametric Functions of the Rational Family

  Inspired by application of tim-resolved sensing in context of fluorescence lifetime imaging, we consider the problem of recovery of delays and lifetimes in Chapter 4. We model such functions as a parametric class of modulated, rational functions and derive sampling bounds for the same. This line of work leads to efficient algorithms for recovery of fluorescence lifetimes.

2. **Applied Contributions**

- Chapter 5 Super-resolved Multi-bounce Imaging

  Optical time-resolved (or time-of-flight) sensors can measure scene depth accurately by projection and reception of an optical signal. The range to a surface in the path of the emitted signal is proportional to the delay time of the light echo or the reflected signal. In practice, a diverging beam may be subject to multi-echo backscatter, and all these echoes must be resolved to estimate the multiple depths. In this chapter, we propose a method for super-resolution of optical ToF signals. Our contributions are twofold. Starting with a general image formation model common to most ToF sensors, we draw a striking analogy of ToF systems with sampling theory. Based on our model, we reformulate the ToF super-resolution problem as a parameter estimation problem pivoted around the sparse sampling framework. In particular, we show that super–resolution of multi-echo backscattered signal amounts to recovery of Dirac impulses from low-pass measurements. Our theory is corroborated by analysis of data collected from a photon counting, LiDAR sensor, showing the effectiveness of our non-iterative and computationally efficient algorithm.

- Chapter 6 Fluorescence Lifetime Imaging: A Blind and Calibration-free Approach

  This chapter demonstrates applicability of low-cost time-resolved imaging sensors for fluorescence lifetime imaging. Fluorescence lifetime imaging (FLI) is a popular method for extracting useful information that is otherwise unavailable from a conventional intensity image. Usually, however, it requires expensive equipment, is often limited to either distinctly frequency- or time-domain modalities, and demands calibration measurements and precise knowledge of the illumination signal. Here, we present a generalized time-based, cost-effective method for estimating lifetimes by repurposing a consumer-grade time-of-flight sensor. By developing mathematical theory that unifies time- and frequency-domain approaches, we can interpret a time-based signal as a combination of multiple frequency measurements. We show that we can estimate lifetimes without knowledge of the illumination signal and without any calibration. We experimentally demonstrate this blind, reference-free method using a quantum dot solution and discuss the method's implementation in FLI applications.

- Chapter 7 Sampling without Time Information: Phase-retrieval in Time-resolved Imaging

  This chapter considers the problem of sampling and reconstruction of a continuous-time sparse signal without assuming the knowledge of the sampling instants or the sampling rate. This topic has its roots in the problem of recovering multiple echoes of light from its low-pass filtered and auto-correlated, time-domain measurements. This application is closely related to the topic of sparse phase retrieval and in this context, we discuss the advantage of phase-free measurements. While this problem is ill-posed, cues based on physical constraints allow for its appropriate regularization. We validate our theory with experiments based on customized, optical time-of-flight imaging sensors. What singles out our approach is that our sensing method allows for temporal phase retrieval as opposed to the usual case of spatial phase retrieval. Preliminary experiments and results demonstrate a compelling capability of our phase-retrieval based imaging device.

- Chapter 8 Photo-acoustic Time-resolved Tomography

  Photoacoustic or PA waves, generated from blood cells, create distinct spectral features in the Fourier domain, for example, maxima and minima. In this way, high-frequency PA signals can be used to identify and distinguish blood cells. However, due to finite bandwidth of physical systems, many interesting Fourier features are invisible within the observed bandwidth. To overcome this challenge, we reformulate the PA imaging problem as a time-of-flight super-resolution problem. Based on the PA wave equations, we show that the problem reduces to estimation of sparse cellular features from a set of finite trigonometric moments. For this purpose, we develop a super-resolution algorithm which achieves near exact performance (in context of maximum likelihood estimation) when working with experimental data. Hence, our work alleviates an important bottleneck in PA imaging linked with classification of cellular features.

1.3 Technical Context

Since time-resolved or ToF imaging is the theme of this work, here we will briefly touch upon the imaging framework which motivates the results in this thesis.

ToF sensors are active illumination devices consisting of an illumination unit capable of probing a scene with an amplitude modulated light that is not necessarily coherent. We call this amplitude modulated waveform the *probing function* or $p(x, y, t)$ where (x, y) are the spatial co-ordinates and t is the continuous time variable. For simplicity of exposition, we will consider per-pixel processing and simply write $p(t)$. The probing function interacts with the *scene response function* (SRF). This interaction results in the *reflected signal* $r(t)$. The reflected signal is observed at the ToF sensor, which is characterized by its transfer function that we refer to as the *instrument response function* (IRF). The IRF models the sensor's electro-optical assembly. For example, the IRF for a digital camera is the point spread function of the lens. The interaction between the reflected signal and the ToF sensor results in the measured signal $m(t)$. The measured signal then undergoes a transformation $\mathscr{T}$ and is converted to digital samples $y_n = y(t)|_{t=nT}$. The time-resolved imaging/sensing pipeline is shown in Fig. 1-4.

Explicit relation between the elements of the ToF sensing pipeline is follows:

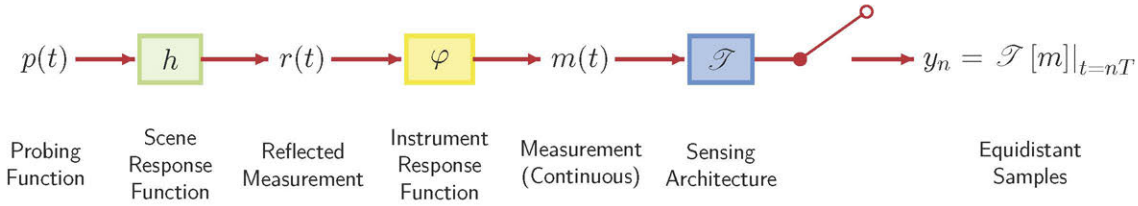

Figure 1-4: Image formation model for time-resolved sensing.

1) Probing Function denoted by $p(t)$ represents the waveform emitted by the ToF sensor's illumination unit. The probing function may be a time-localized pulse or a continuous wave. In either case, it is chosen to be a periodic function of form $p(t) = p(t + T_p), T_p > 0$.

2) Scene Response Function or SRF denoted by $h(t, \tau)$ models the transfer function of the scene. For example, for an object with reflection coefficient Γ and at a depth d meters away from the sensor, the SRF takes form of, $h(t, \tau) = \Gamma\delta(t - \tau - 2d/c)$. Here c is the speed of light. The SRF may also be characterized as the Green's function of a differential equation that models some physical phenomenon such as fluorescence emission, diffusion or scattering.

3) Reflected Function denoted by $r(t)$ is the result of interaction between the probing signal and the SRF. The reflected signal is modeled as a Volterra/Fredholm integral,

$$r(t) = \int_{\Omega_1} p(\tau)\, h(t, \tau)\, d\tau.$$

Whenever the SRF is a shift-invariant kernel, i.e., $h_{\mathsf{SI}}(t, \tau) = h(t - \tau)$, the reflected signal is simply a convolution/filtering operation between the probing function and the SRF, $r(t) = (p * h)(t)$.

4) Instrument Response Function or the IRF denoted by $\varphi(t, \tau)$ models the transfer function of the electro-optical elements of the ToF sensor. For example, in conventional digital cameras, the spatial IRF is the point spread function of the lens.

5) Measurements denoted by $m(t)$ are a result of sensing the reflected signal via the electro-optical elements of the ToF sensor. Continuous-time measurements are modeled as,

$$m(t) = \int_{\Omega_2} r(\tau)\, \varphi(t, \tau)\, d\tau.$$

6) The measured signal undergoes transformation $\mathscr{T}$ and results in,

$$y(t) = \mathscr{T}[m](t).$$

7) The ToF sensor stores discrete measurements by sampling continuous-time signal $y(t)$ and this results in the discrete sequence $y_n = y(nT)|_{t=nT, k\in\mathbb{Z}}$ where $T > 0$ is the sampling interval.

In many practical cases of interest, both the SRF and the IRF are shift-invariant. In that case, the

measurements can be written as a convolution product, $m(t) = (p * h * \varphi)(t)$. Whenever the IRF is a function of form $\varphi(t, \tau) = \varphi(t + \tau)$, the measurements amount to $m(t) = (r \otimes \varphi)(t)$ where $\otimes$ denotes cross–correlation operation. Equivalently, we may write $m(t) = (\overline{r} * p)(t)$ where $*$ denotes convolution and $\overline{r}(t) = r(-t)$.

A distinct feature of the consumer ToF sensors is their use of the lock-in principle [23] which implements the cross-correlation operation. From a mathematical standpoint, and in the absence of noise and distortion, this translates to the fact that,

$$\varphi(t, \tau) = p(\tau + t).$$

1.3.1 Variations on a Theme

Based on the ToF image formation model parameters, $\{p, h, \varphi, \mathscr{T}\}$, one may now define the specific inverse problem at hand. This is also true of other wave-based ToF modalities—radar, sonar, ultrasound, terahertz, and others. As is the case in practice, it is convenient to model the functions $\{p, h, \varphi\}$ to be shift-invariant, in which case, we have,

$$y(t) = \mathscr{T}\underbrace{[p * h * \varphi]}_{m}(t) \xrightarrow{\text{Sampling}} y_n = y(t)|_{t=nT}.$$

This flexible model is at the heart of several applications within and beyond the time-resolved imaging context. Furthermore, here, we have only emphasized on the time-resolved aspect of measurements. More generally, one may assume y to be a plenoptic function where space, orientation, wavelength and polarization information may also be considered for further generalization.

The contributions in this thesis are based on variations on the above model. Below, we summarize this aspect by providing the technical link with each chapter.

1. In Chapter 2 we set $\mathscr{T}$ to be identity and investigate the recovery of $y(t)$ from y_n when $y(t)$ is bandlimited in the Special Affine Fourier Transform (SAFT) domain. We then generalize this result to the case of shift-invariant spaces. Lastly, with a sampling theorem in place, we study the problem of recovering K-sparse signals,

$$h(t) = \sum_{k=0}^{K-1} c_k \delta(t - t_k)$$

when p and φ are bandlimited in the sense of the SAFT domain. All of the results are backward compatible with the Fourier domain.

2. Chapter 3 focuses on the case when $\mathscr{T}$ is a modulo operator. All of the results are developed for Fourier domain. The key question that is addressed is: How to recover $m(t)$ from sampled measurements, $y_n = y(t)|_{t=nT}$ where,

$$\begin{aligned} y_n &= \mathscr{T}[m](nT) \\ &= \text{mod}_\lambda(m(nT)) \end{aligned}$$

and where mod is the modulo operation that forces the range of $y \in [0, \lambda)$. Our result allows

for recovery of arbitrarily high dynamic range signal, that is $|m(t)| \gg \lambda$ from a constant factor oversampling of its low dynamic range samples y_n.

In the context of time-resolved sensing, we extend this result for the case when p and φ are bandlimited in Fourier domain and,

- $h(t)$ is a K-sparse signal,

$$h(t) = \sum_{k=0}^{K-1} c_k \delta(t - t_k).$$

- $h(t)$ is a K-sparse mixture of sinusoids,

$$h(t) = \sum_{k=0}^{K-1} c_k e^{\jmath \nu_k t}.$$

3. In Chapter 4, we consider the problem of recovery of $2K+1$ unknowns, $\left\{t_0, \{\mu_k, \tau_k\}_{k=0}^{K-1}\right\}$ from measurements, $y_n = \widehat{m}(\omega_n), \quad \omega_n = n\omega_0 \quad \omega_0 > 0, \quad n = 0, \ldots, N-1$ where,

$$\widehat{m}(\omega) = \left(\Gamma + \sum_{k=0}^{K-1} \frac{\mu_k}{\frac{1}{\tau_k} + \jmath\omega}\right) e^{-\jmath\omega t_0}$$

is the Fourier transform of transfer function related to the fluorescence lifetime imaging problem. As it will be demonstrated experimentally in Chapter 6, such measurements are related to a scene response function of the form

$$h(t) = \underbrace{\Gamma\delta(t - t_0)}_{\text{Pulse Echo}} + \underbrace{\mu \exp\left(-\frac{t - t_0}{\tau}\right) \Pi(t - t_0)}_{\text{Decaying Echo}}$$

and can be directly acquired in Fourier domain.

4. Chapter 5 focuses on experimental demonstration of super-resolution. This is case, the scene response function is a K–sparse signal in time domain and $\{p, \varphi\}$ are smooth pulses that can be calibrated experimentally.

5. Continuing along the lines of Chapter 5, Chapter 7 studies the problem of phase retrieval. In this case, the scene response function is a K–sparse signal in time domain. However, unlike the case of super-resolution where we considered $\mathscr{T}$ to be identity, in case of **phase retrieval**,

   - $\mathscr{T}[m] = m * \overline{m}$ (auto-correlation) when p is a smooth pulse.

     This is the case of *time-domain* formulation.

   - $\mathscr{T}[m] = |m|^2$ (absolute value) when p is a sinusoid/continuous wave.

     This is case of *frequency-domain* formulation.

In either case, we study the results with experimental validation.

6. Chapter 8 studies super-resolution in context of photoacoustic tomography where h is a 2–sparse signal and $\{p, \varphi\}$ approximate the solution to the differential equation. Assuming approximate shift-invariance, we are able to model the measurements as a sum of overlapping Gabor pulses whose parameters are unknown. We use experimental data to validate our results.

Theoretical Contributions

दिवस कण्वास इन्दवो वसु सिन्धूनां पदे ।
सवं वव्रिं कुह धित्सथः ॥

अभूदु भा उ अंशवे हिरण्यं परति सूर्यः ।
वयख्यज्जिह्वयासितः ॥

अभूदु पारमेतवे पन्था रतय्स साधुया ।
अदर्शि वि सरुतिर्दिवः ॥

"And the path of truth has come into being to lead right to the far shore.
The course of heaven has appeared." [1]

— Rigveda (Mandala I, §46, ¶ 09–11)

2

Sampling and Super-resolution: A Generalized Approach

2.1 Sampling Theory and Approximation

At the heart of many disciplines of science and engineering, and in particular, signal processing and approximation theory is a mathematical model of the form,

$$y(t) = \sum_{k \in \mathcal{K}} c_k \phi(t - t_k), \tag{2.1}$$

where t is the continuous-time variable and $\mathcal{K}$ is some set. This deceptively simple model is in fact a concise representation of a rich class of problems. We elaborate on this aspect by considering two antithetical variations.

2.1.1 Sampling Theory of Smooth Signals

Let $\mathcal{K}$ to be the set of integers with $t_k = kT$ and where T is some positive constant. Whenever ϕ is chosen to be the re-scaled sinc function[1], $\text{sinc}_T(t) \stackrel{\text{def}}{=} \text{sinc}(t/T)$, (2.1) takes form of the widely studied Shannon's sampling theorem [24]. This theorem is the bridge between the continuous and the discrete world and the statement of the theorem is as follows:

[1]We define the sinc function as $\text{sinc}(t) = \frac{\sin(\pi t)}{\pi t}$.

Theorem 1 (Shannon [24]). *If a continuous function y contains no frequencies higher than Ω_m (in radians per second), it is completely determined by giving its ordinates at a series of points spaced $T = \pi/\Omega_m$ apart.*

The series representation in (2.1) is exact provided that the maximum frequency content of y obeys the Nyquist condition,

$$\Omega_m \leqslant \frac{\pi}{T} \qquad \text{(Nyquist Rate).}$$

Whenever this is not the case, that is to say that the function is non-band-limited, one obtains a band-limited approximation of y. This is because of an orthogonal projection operator inherent to the choice of functions $\{\text{sinc}_T(t-kT)\}_{k\in\mathcal{K}}$. This family of functions forms an orthonormal basis [25]. Thanks to the orthogonality property, the weights or coefficients $\{c_k\}_{k\in\mathcal{K}}$ in (2.1) can be obtained by computing the orthogonal projection (or the inner-product) between y and component-wise basis functions $\phi(t-kT)$ [26]. This operation embodies the "pre-filtering with anti-aliasing filter" step in context of sampling theory and the resultant coefficients $c_k = y(kT)$ are the uniform samples of the signal [27, 28]. Unlike other orthonormal systems, such as the Fourier series and the wavelet expansion, the coefficients of expansion, $\{c_k\}_{k\in\mathcal{K}}$, are explicitly specified a series of numbers on the function y itself, that is, $c_k = y(kT)$. This remarkable feature is due to the choice of basis functions in (2.1) and links the continuous function $y(t)$ with a sequence of discrete numbers $y(kT)$. In view of Theorem 1 which requires equidistant sampling ($t_k = kT$), the sampling result is also valid for the case of non-equidistant samples. However, this requires an appropriate adjustment of the Nyquist frequency, more generally known as the *sampling density*. One of the earliest results in this direction is due to Kadec [29].

The choice of $\phi(t) = \text{sinc}_T(t)$ is rather constraining. A more flexible signal model that is particularly befitting our discussion, consists of *shift-invariant subspaces* (or the SIS) [30, 31, 27, 32, 28] which constitute a much larger class of signals when compared to their band-limited counterparts. The advent of wavelets and multiresolution analysis [33] led to design of such basis functions for multi-scale approximation. The mathematical ideas that were pivotal to the multiresolution analysis could be repurposed for shift-invariant approximation which are less constrained in the sense that they are devoid of the multiresolution requirement [34]. What this meant is that a stronger band-limitedness constraint of the classical sampling theory could be replaced by a flexible set of wavelet–inspired rules for the shift-invariant model. These basic rules guarantee stability, uniqueness and approximation capability of representation in (2.1).

Shift-invariant spaces have been the focus of many research papers in recent years because of their close connection with sampling theory [27, 32, 35] and wavelets and multiresolution analysis [34, 36, 37]. They have many applications in signal and image processing (cf. Table I in [38], [39]). For example, in many signal processing applications, it is of interest to represent a signal as a linear combination of shifted versions of some basis function φ, called the generators of the space, that generates a stable basis for a space. More precisely, we consider spaces of the form,

$$\mathsf{V}_{\mathsf{SIS}} = \text{span}\{\varphi(t-n)\}_{n\in\mathbb{Z}}. \tag{2.2}$$

For instance, with $\varphi = \text{sinc}$, one obtains the shift-invariant subspace spanned by the sinc functions—the bandlimited subspace, that is,

$$\mathsf{V}_{\mathsf{BL}} = \text{span}\left\{\frac{1}{\sqrt{T}}\text{sinc}_T(t-nT)\right\}_{n\in\mathbb{Z}}, \qquad \text{sinc}_T(t) \stackrel{\text{def}}{=} \text{sinc}\left(\frac{t}{T}\right). \tag{2.3}$$

Any finite-energy function $f \in L_2$ can be represented as,

$$f(t) = \sum_{n \in \mathbb{Z}} c_n \varphi(t-n),$$

where,

- φ is a pre-specified kernel which may be carefully designed or fixed.
- $\{c_n\}_{n \in \mathbb{Z}}$ are the coefficients of representation (not necessarily pointwise samples). For stability purposes, it is required that the coefficients c_n are square-summable, that is to say $c \in \ell_2$ or $\sum\limits_{n \in \mathbb{Z}} |c_n|^2 < \infty$.

When $c_n \in \mathbb{R}$, (2.2) defines a vector space, $\mathsf{V}_{\mathsf{SIS}}$. The space $\mathsf{V}_{\mathsf{SIS}}$ is shift-invariant in the sense that,

$$\forall f \in \mathsf{V}_{\mathsf{SIS}} \Rightarrow f(t-k) \in \mathsf{V}_{\mathsf{SIS}}, \quad k \in \mathbb{Z}.$$

This is because,

$$f(t-k) = \sum_{n \in \mathbb{Z}} c_n \varphi(t-n-k) = \sum_{n \in \mathbb{Z}} c_n \varphi(t-(n+k)) = \sum_{m \in \mathbb{Z}} c_{m-k} \varphi(t-m)$$

and the shifted function $f(t-k), k \in \mathbb{Z}$ can be obtained by shifting each coefficient by k. Another example of such a space is that of polynomial functions of fixed degree, say K. In this case, shifts of polynomials span the same space. This is a property that will be useful in the study of parametric sampling of rational functions discussed in Section 4.1.2 of Chapter 4.

For the generator φ to be a well-defined subspace of the square-integrable function and to provide a stable and unique representation in terms of coefficients, it is required that the family of functions $\{\varphi(t-n)\}_{n \in \mathbb{Z}}$ forms a Riesz basis [40]. Equivalently, there exist two positive constants associated with the generator φ, $0 < \eta_1^{\varphi}, \eta_2^{\varphi} < +\infty$, such that

$$\forall c \in \ell_2, \quad \eta_1^{\varphi} \|c\|_{\ell_2}^2 \leqslant \left\| \sum_{n \in \mathbb{Z}} c_n \varphi(t-n) \right\|_{L_2}^2 \leqslant \eta_2^{\varphi} \|c\|_{\ell_2}^2 \tag{2.4}$$

where, as before, ℓ_2 is the space of all square-summable sequences and $\|c\|_{\ell_2}^2$ is the squared ℓ_2-norm of the sequence. Recall, the Fourier domain equivalent of (2.4) is

$$\eta_1^{\varphi} \leqslant \sum_{n \in \mathbb{Z}} |\widehat{\varphi}(\omega - 2\pi n)|^2 \leqslant \eta_2^{\varphi}. \tag{2.5}$$

where the quantity in the center,

$$\mathsf{G}_{\varphi}(\omega) = \sum_{n \in \mathbb{Z}} |\widehat{\varphi}(\omega - 2\pi n)|^2 \tag{2.6}$$

is also known as the Grammian. The ratio $\rho_{\varphi} = \eta_2^{\varphi} / \eta_1^{\varphi}$ is called the *condition number* of the Riesz basis. The basis is shift-orthonormal[2] or a tight frame if $\rho_{\varphi} = 1$. A function that satisfies (2.5) is known as the

[2]Shift-orthonormality means that $\langle \varphi, \varphi(\cdot - k) \rangle = \delta_k$ where $\langle f, g \rangle = \int_{-\infty}^{+\infty} f(t) g^*(t) \, dt$ is the L_2-inner product and

Table 2.1: Comparison of Approximation Schemes

Approximation Scheme	Analysis Function	Synthesis Function	Fourier Condition
Interpolation [24]	$\widetilde{\varphi}(t) = \delta(t)$	$\varphi(t)\|_{t=k,k\in\mathbb{Z}} = \delta_k$	$\sum_{n\in\mathbb{Z}} \widehat{\varphi}(\omega - 2\pi n) = 1$
Quasi Interpolation [41]	$\widetilde{\varphi}(t) = \delta(t)$	$\widehat{\varphi}(\omega - 2\pi n) = \delta_n + O(\omega^L)$	
L_2 Optimal [42, 31]	$\widetilde{\varphi}(t) \in \mathsf{V}_{\mathsf{SIS}}(\varphi)$	$\varphi(t)$	$\widehat{\widetilde{\varphi}}(\omega) = \frac{\widehat{\varphi}(\omega)}{\mathsf{G}_{\varphi}(\omega)}$ (cf. (2.6))
L_2 Projection [43]	$\langle \widetilde{\varphi}(t-k), \varphi(t)\rangle = \delta_k$	$\varphi(t)$	

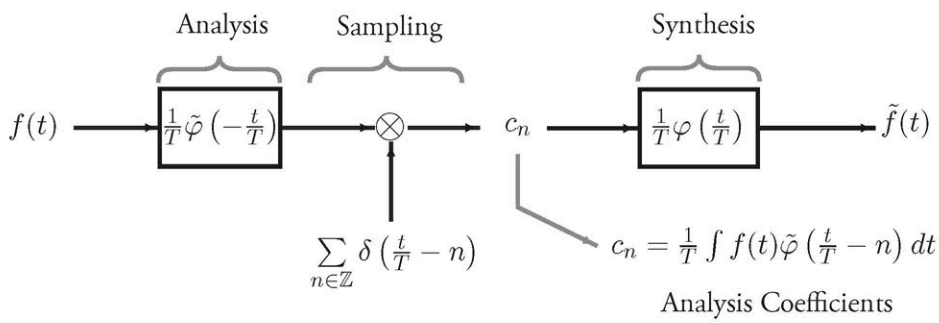

Figure 2-1: Sampling and approximation procedure in shift-invariant subspaces.

generator of $\mathsf{V}_{\mathsf{SIS}}$.

In order to obtain a reasonable approximation of f, we must specify the coefficients $\{c_n\}_{n\in\mathbb{Z}}$ in a way that the error between the function f and its approximation can be controlled. This amounts to including a pre-filtering step before sampling and in analogy to the case bandlimited functions, this step ensures that f admits a suitable representation in $\mathsf{V}_{\mathsf{SIS}}$. Mathematically, the coefficients can thus be evaluated as,

$$c_n = \frac{1}{T}\int f(t)\widetilde{\varphi}\left(\frac{t}{T} - n\right) dt, \tag{2.7}$$

where $\widetilde{\varphi}$ is the *analysis* or the *sampling* kernel. The approximation method for shift-invariant subspaces is schematically described in Fig. 2-1. Given generator φ, several approximation schemes have been investigated in the literature that discuss design principles for evaluation of the sampling kernel. We list the most common ones in Table 2.1.

The SIS model linked with the sampling theory has been extended to several interesting directions including non-uniform sampling [32], time-warped sampling [44], consistent sampling [45] and non-linear sampling [46]. However, it must be emphasized that all of the results linked with Shannon's sampling theory and shift-invariant approximation are pivoted on the theme of *subspaces of smooth functions*. That is to say, the function or signal to be approximated belongs to a subspace of smooth functions. In this context, band-limitedness [35] and regularity [26] are established measures of smoothness.

Alternatively, in many practical cases, the subspace structure as well as the smoothness assumptions

$\delta_k = \begin{cases} 1, & \text{if } k = 0 \\ 0, & \text{if } k \neq 0 \end{cases}$ denotes the Kronecker delta.

may fall short of capturing the true features in the signal of interest. Sparse signals [47] are quintessential examples of a setting where smooth subspace based approximation would be a suboptimal approach. This brings us to our next example—the case of sparse signals.

2.1.2 Sampling Theory of Sparse Signals

In this case, we set $\mathcal{K}$ to be a set of K contiguous integers and $\{c_k, t_k\}_{k\in\mathcal{K}}$ are arbitrary, real-valued numbers. Now we may re-write (2.1) as,

$$y(t) = \sum_{k=0}^{K-1} c_k \phi(t - t_k). \tag{2.8}$$

Given a sampled sequence or discrete measurements of form $y(nT), n = 0, \ldots, N-1$, one is interested in estimating $2K+1$ unknowns, $\left\{K, \{c_k, t_k\}_{k=0}^{K-1}\right\}$. In order to ensure a unique representation, in most cases it is assumed that K and ϕ are known a-priori. From a practical standpoint, ϕ may be,

- ▶ an excitation pulse used in a time-of-flight imaging system such as radar, sonar, lidar and ultrasound.
- ▶ a low-pass filter that is an approximation of:
  - ○ the point spread function of an optical instrument such as a lens, microscope or a telescope.
  - ○ transfer function of an electronic sensor such as an antenna or a microphone.
  - ○ Green's function of some partial differential equation that represents a physical process (for example, diffusion or fluorescence lifetime imaging).
  - ○ beampattern of a sensor array.
- ▶ spectral line shape in spectroscopy (often assumed to be a Cauchy, Gaussian or a Voigt distribution).

Depending on the choice of ϕ, estimating $\{c_k, t_k\}_{k\in\mathcal{K}}$ in the above variation of model in (2.1) is a classical problem that ubiquitously occurs in several fields of science and engineering. Some well known signal processing centric examples include: (a) source localization[48], (b) resolution of signals/echoes [49, 50, 51], (c) seismic imaging [52], (d) time-delay estimation [53, 54, 55, 56], (e) sparse deconvolution [57], (f) super-resolution [58, 59, 60], (g) multipath channel estimation [61, 62, 63] and (h) time-of-flight imaging [64, 65, 66].

As disparate as these applications may seem on a first glance, they all share the same fundamental attribute: *"How can one recover a signal with broadband features from a given set of narrowband measurements?"*

This qualitative statement is best understood in the Fourier domain. Thanks to the convolution-multiplication duality,

$$\phi(t) * \sum_{k=0}^{K-1} c_k \delta(t - t_k) \xrightarrow{\text{Fourier}} \widehat{\phi}(\omega) \sum_{k=0}^{K-1} c_k e^{\jmath\omega t_k},$$

where '$*$' denotes the convolution/filtering operation and $\widehat{\phi}$ is Fourier transform of ϕ. Due to low-pass nature of $\widehat{\phi}$, clearly, observing data $\{y(nT)\}_n$, amounts to observing a narrowband version of the Fourier

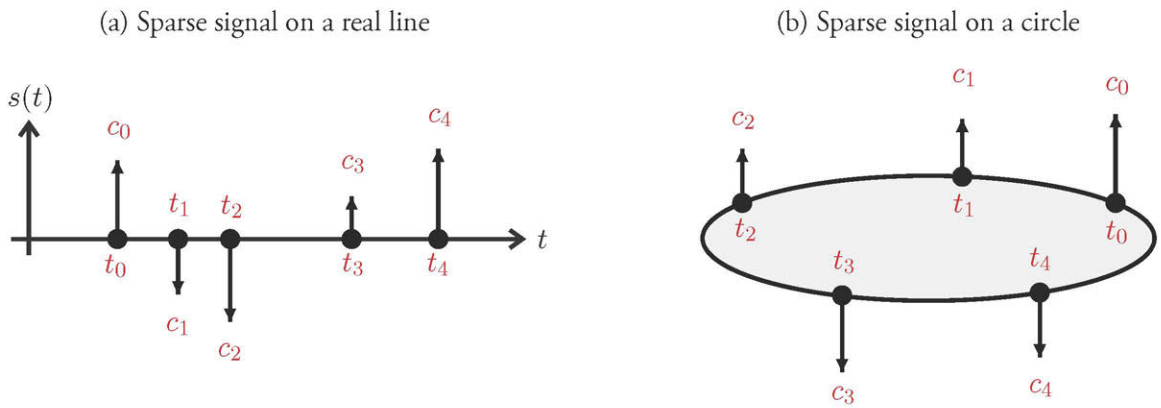

Figure 2-2: K-sparse signals (a) on a real line and (b) periodized version of (a) on a circle.

spectrum of $\sum_{k=0}^{K-1} c_k e^{\jmath\omega t_k}$ which is broadband in the sense that it occupies all frequencies. While the goal of recovering spikes parameterized by $\{c_k, t_k\}_{k\in\mathcal{K}}$ is very different from that of the previous section, the analogy across sampling theory remains intact.

Note that the data $\{y(nT)\}_n$, are projections of spikes onto space spanned by $\left\{\overline{\phi}(t-nT)\right\}_{n=0}^{N-1}$, where $\overline{\phi}(t) = \phi(-t)$. This is because of the mathematical equivalence,

$$y(nT) = \underbrace{\int s(t)\,\overline{\phi}(t-nT)\,dt}_{\text{Projection}} \equiv \underbrace{(s*\phi)(t)|_{t=nT}}_{\text{Convolution}}, \tag{2.9}$$

where s is the sparse signal,

$$s(t) = \sum_{k=0}^{K-1} c_k \delta(t-t_k). \tag{2.10}$$

Alternatively, a sparse signal may also be represented on a circle (via periodization) which leads to the following representation,

$$s_{\text{per}}(t) = \sum_{n\in\mathbb{Z}} \sum_{k=0}^{K-1} c_k \delta(t-t_k-nT). \tag{2.11}$$

A prototype sparse signal on a real line and a circle is shown in Fig. 2-2 (a) and (b), respectively. Here the sparsity level is $K=5$.

Unlike band-limited or smooth signals which follow a linear recovery principle [27], sparse signals rely on non-linear principles mainly because of the non-linear nature functional dependence of y on $\{t_k\}_{k\in\mathcal{K}}$. Hence sparse signals follow a different recovery procedure outlined as follows: assuming that $y(t)$ and K are known, and ϕ is a band-limited function,

1) **Deconvolution:** Estimate $\widehat{s}(\omega) = \widehat{y}(\omega)/\widehat{\phi}(\omega)$ for all contiguous frequencies such that $|\widehat{\phi}(\omega)| > 0$.

2) **Extrapolation:** Estimate $\{c_k, t_k\}_{k\in\mathcal{K}}$ by solving for,

$$\underset{\{c_k,t_k\}_{k\in\mathcal{K}}}{\arg\min} \left| \widehat{s}(\omega) - \sum_{k=0}^{K-1} c_k e^{\jmath\omega t_k} \right|^2 .$$

The above procedure may be easily adapted to the case of sampled signal, that is, $y(nT), n = 0, \ldots, N-1$, by using discrete Fourier transform and is outlined in Algorithm 2 in Section 3.4.

Although the problem of estimation of $\{t_k\}_{k\in\mathcal{K}}$ is a non-linear one, remarkably, it can be completely decoupled from the estimation of $\{c_k\}_{k\in\mathcal{K}}$. This is a very well studied problem in the area of high resolution spectral estimation and we refer the readers to [67] and [68] for a first hand introduction.

Finite Rate of Innovation Signals: Despite the prevalence of the problem setup in (2.8) across several fields (cf. Table I and Table II in [54], [55] as well as [57]), the link to sampling theory was established only recently by Vetterli [69], Blu[70] and co-workers in their study of *finite rate of innovation* or FRI signals. These are signals which are described by countable degrees of freedom or *innovations*.

While the sparse signal (2.10) is certainly an FRI signal with $2K$ innovations, the advantage of the FRI framework is that it defines a class of signals that is much richer than sparse signals specified in (2.10). For example, any signal which can be mapped to (2.10) via some invertible mapping/transformation is an FRI signal. To see this principle in effect, a sum of exponentials with unknown amplitudes and frequencies can be mapped to (2.10) via the Fourier transform. Similarly, piecewise polynomials and splines can be mapped to (2.10) via the derivative operator [69]. More generally, let $\mathcal{L}$ denote some linear, invertible operator such as a derivative or an integral, then,

$$y(t) = (\phi * \mathcal{L}[s])(t), \quad s(t) = \sum_{k=0}^{K-1} c_k \delta(t - t_k) \tag{2.12}$$

is an FRI signal since it has countable degrees of freedom. When $\mathcal{L}$ is an identity operator, the above takes form of the sparse signal defined in (2.8).

Due to this flexibility in modeling a wide class of signals, the FRI model has been extended in a number of interesting directions such as ECG compression [71], channel estimation [72], time-resolved imaging [66, 73], image feature detection [74, 75, 76], medical imaging [77, 78, 79] and tomography [80].

2.1.3 Sampling Theory Beyond Fourier Domain

Equidistant sampling and band-limitedness are essential ingredients that are at the core of sampling theory. While most sampling devices utilize uniform sampling architecture, the choice of Fourier domain for defining band-limitedness may be a restrictive. In practice, many systems and physical phenomena are modeled as linear and time-varying/non-stationary. On the other hand, complex exponentials—that are constituent components of Fourier transform—are the eigen functions of linear systems. As a result, the choice of Fourier domain may not be suitable from a general perspective.

Polynomial phase models [81] that generalize complex exponentials are often used as an alternative basis for modeling time-varying systems. Such models are specified by basis functions of form $e^{\jmath\varphi(t)}$.

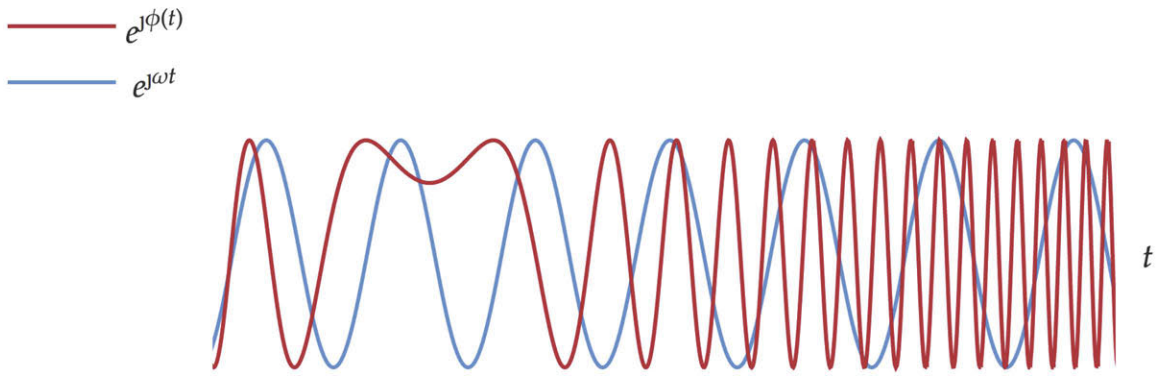

Figure 2-3: Comparison of complex exponentials or $e^{\jmath\omega t}$ (Fourier basis function) with polynomial basis functions $e^{\jmath\phi(t)}$ where $\phi(t)$ is a quadratic function, $\phi(t) = a_2t^2 + a_1t + a_0$ for some $\{a_k\}_{k=0}^{3} \in \mathbb{R}$.

One notable example of this class is quadratic chirps which are specified by $\varphi(t) = a_2t^2 + a_1t + a_0$ (cf. Fig. 2-3). Due to their wide applicability, chirp based transformations [82], multi-scale orthonormal bases and frames [83] as well as dictionary based pursuit algorithms [84] have been devised in literature. Active imaging systems such as radar [85] and sonar [86] use chirps for probing the environment. In [87], Martone demonstrates the effectivity of polynomial phase basis functions of the fractional Fourier transform for multicarrier communication with time-frequency selective channels. Harms *et al.* [88] use chirps for identification of linear time-varying systems. Fresnel transforms [89] use polynomial phase for digital holography [90] and Fresnel diffraction. Other applications of polynomial phase functions include time-frequency representations [91], sensor array processing [92], ghost imaging [93], image encryption [94] and quantum physics [95].

Independent of the applications and work dating back to Norbert Weiner [96], polynomial phase representations were studied in context of phase space and mathematical physics. This led to development of unitary transformations such as the fractional Fourier transform (FrFT) [97] and the Linear Canonical Transform (LCT) [98]. These transformations generalize the Fourier transform in the same way polynomial phase $e^{\jmath\varphi(t)}$ generalizes the complex exponentials, that is, $e^{\jmath\omega t}$.

In the area of signal processing, Almeida first introduced the fractional Fourier transform (FrFT) as a tool for time-frequency representations [99]. Following [99], a number of papers have extended the Shannon's sampling theorem to the FrFT domain (cf.[100] and [38] and references there in). In [38], Bhandari and Zayed developed the shift-invariant model for the FrFT domain which was later generalized in [101].

Interestingly, all of the aforementioned transformations and corresponding basis functions are specific cases of the Special Affine Fourier Transform (SAFT).

2.1.4 Overview of Contributions

In this chapter, our goal is to extend sampling and approximation theory of both *smooth* and *sparse* signals beyond the Fourier domain. We do so by considering the Special Affine Fourier Transform (SAFT) which is a parametric transformation that subsumes a number of well known unitary transformations used in

signal processing and optics.

Key contributions are listed as follows:

1. **Convolution Structures**

   The Fourier *convolution theorem* states that convolution of two functions amounts to multiplication in the transform domain. However, this is not the case for several transformations linked with polynomial phase kernels. Here we develop convolution structures which enforce multiplication in the transform domain. This property is very relevant for classical operations such as filtering.

2. **Sampling Theory of Smooth Functions**

   A key aspect of this work is to develop sampling and approximation procedures for both bandlimited and shift-invariant subspaces. Here, we prove results related with sampling theory in the context of the Special Affine Fourier Transform (SAFT).

3. **Sampling and Super-resolution of Sparse Signals**

   Having developed sampling theory linked with bandlimited subspaces of the Special Affine Fourier Transform (SAFT), we study the problem of super-resolution and its draw parallels with existing literature. We derive sampling theorems for sparse signals with three distinct flavors:

   1) Sampling with arbitrary, bandlimited kernels.
   2) Sampling with smooth, time-limited kernels.
   3) Sparse signal recovery from Gabor transform measurements linked with the SAFT domain.

   For this purpose, we introduce two mathematical tools:

   - the Special Affine Fourier Series (a generalization of the Fourier Series) for representing time-limited functions.
   - the Gabor transform associated with the SAFT (a generalization of the usual Gabor transform).

2.1.5 Notation

Throughout this chapter, set of integers, reals and complex numbers is denoted by $\mathbb{Z}$, $\mathbb{R}$, and $\mathbb{C}$, respectively and $\mathbb{Z}^+$ denotes a set of positive integers. Continuous-time functions are denoted by $f(t), t \in \mathbb{R}$ while $f[m], m \in \mathbb{Z}$ are used for their discrete counterparts. We use script fonts for operators, that is, $\mathscr{O} f$. For instance, $\mathscr{P}$ denotes the projection operator and the derivative operator of order k is written as $\mathscr{D}^k f = f^{(k)}$. Function/operator composition is denoted by $\circ$. We use boldface font for representing vectors and matrices, for example $\mathbf{x}$ and $\mathbf{X}$, respectively, and $\mathbf{X}^\top$ is the matrix transpose. We use $\mathbf{I}$ to denote an identity matrix. A characteristic function on domain $\mathcal{D}$ is denoted by $\mathbb{1}_{\mathcal{D}}$. Dirac distribution is represented by $\delta(t), t \in \mathbb{R}$. All operations linked with δ are treated in terms of distributions. The Kronecker delta is represented by $\delta[m], m \in \mathbb{Z}$. The space of square-integrable and absolutely integrable functions is denoted by L_2 and L_1, respectively and $\langle f, g \rangle = \int f g^*$ is the L_2 inner-product. We use $\overline{(\cdot)}$ to denote time-reversal.

Table 2.2: Roadmap of Key Sampling Theory Results Linked with the SAFT Domain

	Section	Result	Context
Chapter 2	Section 2.3	Theorem 2	Convolution and product theorem for the SAFT domain.
	Section 2.3.1	Theorem 3	Alternative version of convolution and product theorem.
	Section 2.4.1	Theorem 4	Sampling Theorem for SAFT domain.
	Section 2.4.2	Theorem 5	Riesz basis criteria for SAFT domain.
	Section 2.5	Theorem 6	Series representation for sparse signals.
	Section 2.5.0.2	Theorem 7	Sparse Sampling with bandlimited kernels
	Section 2.5.0.2	Theorem 8	Exact recovery condition for super-resolution.
	Section 2.5.0.2	Proposition 1	Sparse representation with arbitrary bandlimited kernels.
	Section 2.5.0.5	Proposition 2	Sparse representation with time-limited kernels.
	Section 2.5.0.5	Proposition 3	Smoothness and decay in the SAFT domain.

2.1.6 Roadmap of this Chapter

The results in this chapter are organized as follows.

- In Section 2.2, we define the SAFT and its inverse and study its various properties.
- Section 2.3 is devoted to the development of convolution and product theorems for the SAFT domain.
- Section 2.4 discussed the case of smooth functions. In this context,
  - In Section 2.4.1, we study the sampling theorem for bandlimited functions associated with the SAFT domain.
  - In Section 2.4.2, we study sampling theory for shift-invariant subspaces associated with the SAFT domain.
- Section 2.5 is devoted to the study of several results linked with the topic of sparse sampling.

To ease navigation of results through this chapter, main theorems and their corresponding sections are listed in Table 2.2.

2.2 The Special Affine Fourier Transform

The Special Affine Fourier Transform or the SAFT was introduced by Abe and Sheridan [102] as a generalization of the FrFT. The SAFT can be thought of as a versatile transformation which parametrically generalizes a number of well known unitary and non-unitary transformations as well as mathematical and optical operations. In Table 2.3 we list its parameters together with the associated mappings.

Table 2.3: SAFT, Transformations and Operations

SAFT Parameters ($\mathbf{\Lambda}_{\mathsf{S}}$)	Corresponding Transform
$\left[\begin{array}{cc\|c} 0 & 1 & 0 \\ -1 & 0 & 0 \end{array}\right] = \mathbf{\Lambda}_{\mathsf{FT}}$	**Fourier Transform (FT)**
$\left[\begin{array}{cc\|c} 0 & 1 & p \\ -1 & 0 & q \end{array}\right] = \mathbf{\Lambda}_{\mathsf{FT}}^{\mathsf{O}}$	**Offset Fourier Transform**
$\left[\begin{array}{cc\|c} \cos\theta & \sin\theta & 0 \\ -\sin\theta & \cos\theta & 0 \end{array}\right] = \mathbf{\Lambda}_{\theta}$	**Fractional Fourier Transform (FrFT)**
$\left[\begin{array}{cc\|c} \cos\theta & \sin\theta & p \\ -\sin\theta & \cos\theta & q \end{array}\right] = \mathbf{\Lambda}_{\theta}^{\mathsf{O}}$	**Offset Fractional Fourier Transform**
$\left[\begin{array}{cc\|c} a & b & 0 \\ c & d & 0 \end{array}\right] = \mathbf{\Lambda}_{\mathsf{L}}$	**Linear Canonical Transform (LCT)**
$\left[\begin{array}{cc\|c} 1 & b & 0 \\ 0 & 1 & 0 \end{array}\right] = \mathbf{\Lambda}_{\mathsf{Fr}}$	**Fresnel Transform**
$\left[\begin{array}{cc\|c} 0 & \jmath & 0 \\ \jmath & 0 & 0 \end{array}\right] = \mathbf{\Lambda}_{\mathsf{LT}}$	**Laplace Transform (LT)**
$\left[\begin{array}{cc\|c} \jmath\cos\theta & \jmath\sin\theta & 0 \\ \jmath\sin\theta & -\jmath\cos\theta & 0 \end{array}\right]$	**Fractional Laplace Transform**
$\left[\begin{array}{cc\|c} 1 & \jmath b & 0 \\ \jmath & 1 & 0 \end{array}\right]$	**Bilateral Laplace Transform**
$\left[\begin{array}{cc\|c} 1 & -\jmath b & 0 \\ 0 & 1 & 0 \end{array}\right], b \geq 0$	**Gauss–Weierstrass Transform**
$\frac{1}{\sqrt{2}}\left[\begin{array}{cc\|c} 0 & e^{-\jmath\pi/2} & 0 \\ -e^{-\jmath\pi/2} & 1 & 0 \end{array}\right]$	**Bargmann Transform**
SAFT Parameters ($\mathbf{\Lambda}_{\mathsf{S}}$)	**Corresponding Signal Operation**
$\left[\begin{array}{cc\|c} 1/\alpha & 0 & 0 \\ 0 & \alpha & 0 \end{array}\right] = \mathbf{\Lambda}_{\alpha}$	**Time Scaling**
$\left[\begin{array}{cc\|c} 1 & 0 & \tau \\ 0 & 1 & 0 \end{array}\right] = \mathbf{\Lambda}_{\tau}$	**Time Shift**
$\left[\begin{array}{cc\|c} 1 & 0 & 0 \\ 0 & 1 & \xi \end{array}\right] = \mathbf{\Lambda}_{\xi}$	**Frequency Shift/Modulation**
SAFT Parameters ($\mathbf{\Lambda}_{\mathsf{S}}$)	**Corresponding Optical Operation**
$\left[\begin{array}{cc\|c} \cos\theta & \sin\theta & 0 \\ -\sin\theta & \cos\theta & 0 \end{array}\right] = \mathbf{\Lambda}_{\theta}$	**Rotation**
$\left[\begin{array}{cc\|c} 1 & 0 & 0 \\ \tau & 1 & 0 \end{array}\right] = \mathbf{\Lambda}_{\tau}$	**Lens Transformation**
$\left[\begin{array}{cc\|c} 1 & \eta & 0 \\ 0 & 1 & 0 \end{array}\right] = \mathbf{\Lambda}_{\eta}$	**Free Space Propagation**
$\left[\begin{array}{cc\|c} e^{\beta} & 0 & 0 \\ 0 & e^{-\beta} & 0 \end{array}\right] = \mathbf{\Lambda}_{\beta}$	**Magnification**
$\left[\begin{array}{cc\|c} \cosh\alpha & \sinh\alpha & 0 \\ \sinh\alpha & \cosh\alpha & 0 \end{array}\right] = \mathbf{\Lambda}_{\eta}$	**Hyperbolic Transformation**

2.2.1 Forward Transform

Mathematically, the SAFT of a signal $f(t)$ is a mapping, $\mathscr{T}_{\text{SAFT}} : f \to \widehat{f}_{\mathbf{\Lambda}_{\mathsf{S}}}$ which is defined by an integral transformation parameterized by a matrix $\mathbf{\Lambda}_{\mathsf{S}}$

$$\mathscr{T}_{\mathbf{\Lambda}_{\mathsf{S}}}[f] = \widehat{f}_{\mathbf{\Lambda}_{\mathsf{S}}}(\omega) = \begin{cases} \left\langle f, \kappa_{\mathbf{\Lambda}_{\mathsf{S}}}(\cdot, \omega) \right\rangle & b \neq 0 \\ \sqrt{d} e^{\jmath \frac{cd}{2}(\omega - p)^2 + \jmath\omega q} f\left(d\left(\omega - p\right)\right) & b = 0. \end{cases} \tag{2.13}$$

When $b \neq 0$, the matrix $\mathbf{\Lambda}_{\mathsf{S}}^{(2\times 3)}$ is the SAFT parameter matrix,

$$\mathbf{\Lambda}_{\mathsf{S}} = \left[\begin{array}{cc|c} a & b & p \\ c & d & q \end{array}\right] \equiv \left[\begin{array}{c|c} \mathbf{\Lambda}_{\mathsf{L}} & \lambda \end{array}\right], \tag{2.14}$$

which is obtained by concatenating the Linear Canonical Transform or the LCT matrix,

$$\mathbf{\Lambda}_{\mathsf{L}} = \begin{bmatrix} a & b \\ c & d \end{bmatrix}, \quad |\mathbf{\Lambda}_{\mathsf{L}}| = 1 \text{ or } ad - bc = 1 \tag{2.15}$$

(see Table 2.3 and [98]), and, an offset vector, $\lambda = [p \;\; q]^{\top}$ with elements p and q that represent displacement and modulation, respectively. Let $\mathbf{r} = [t \;\; \omega]^{\top}$ denote the time-frequency co-ordinates. The function $\kappa_{\mathbf{\Lambda}_{\mathsf{S}}}(\mathbf{r})$ in (2.13) is the parametric SAFT kernel based on a complex exponential of quadratic form,

$$\kappa_{\mathbf{\Lambda}_{\mathsf{S}}}(\mathbf{r}) = K^{*}_{\mathbf{\Lambda}_{\mathsf{S}}} \exp\left(-\jmath\left(\mathbf{r}^{\top}\mathbf{U}\mathbf{r} + \mathbf{v}^{\top}\mathbf{r}\right)\right) \tag{2.16}$$

where,

$$\mathbf{U} = \frac{1}{2b}\begin{bmatrix} a & -1 \\ -1 & d \end{bmatrix}, \quad \mathbf{v} = \frac{1}{b}\begin{bmatrix} p \\ bq - dp \end{bmatrix} \quad \text{and} \quad K_{\mathbf{\Lambda}_{\mathsf{S}}} = \frac{1}{\sqrt{\jmath 2\pi b}} \exp\left(\jmath\frac{dp^2}{2b}\right).$$

Both $\mathbf{U}$ and $\mathbf{v}$ are parameterized by $\mathbf{\Lambda}_{\mathsf{S}}$ and hence the SAFT kernel is also parameterized by $\mathbf{\Lambda}_{\mathsf{S}}$. The exponential part of the kernel is explicitly written as,

$$\exp\left(-\jmath\left(\mathbf{r}^{\top}\mathbf{U}\mathbf{r} + \mathbf{v}^{\top}\mathbf{r}\right)\right) = \exp\left(-\frac{\jmath}{2b}\left(at^2 + d\omega^2 + 2t\left(p - \omega\right) - 2\omega\left(dp - bq\right)\right)\right).$$

Note that $\mathbf{\Lambda}_{\mathsf{L}}$ has 3 free parameters $\{a, b, d\}$ and c is constrained by $|\mathbf{\Lambda}_{\mathsf{L}}| = 1$. Due to this concatenation of the LCT matrix with a vector, the SAFT is also referred to as the *Offset Linear Canonical Transform* or the OLCT [103]. The matrix $\mathbf{\Lambda}_{\mathsf{S}}$ arises naturally in applications involving optics and imaging. We refer the reader to the books [104, 105] for further details on the intuitive meaning of such a matrix representation.

The SAFT of the Dirac distribution is calculated by,

$$\begin{aligned} \widehat{\delta}_{\mathbf{\Lambda}_{\mathsf{S}}}(\omega) &\overset{(2.13)}{=} \left\langle \delta, \kappa_{\mathbf{\Lambda}_{\mathsf{S}}}(\cdot, \omega)\right\rangle \\ &= \kappa^{*}_{\mathbf{\Lambda}_{\mathsf{S}}}(t, \omega)\big|_{t=0} \\ &= K_{\mathbf{\Lambda}_{\mathsf{S}}} \exp\left(\frac{\jmath}{2b}\left(d\omega^2 - 2\omega\left(dp - bq\right)\right)\right), \end{aligned} \tag{2.17}$$

and is non-bandlimited. Furthermore, $|\widehat{\delta}_{\mathbf{\Lambda}_{\mathsf{S}}}(\omega)| = \frac{1}{\sqrt{2\pi b}}$.

2.2.2 Inverse Transform

In order to define the inverse-SAFT, we first note that the SAFT satisfies the following composition property,

$$\left(\mathscr{T}_{\mathbf{\Lambda}_{\mathsf{S}_2}} \circ \mathscr{T}_{\mathbf{\Lambda}_{\mathsf{S}_1}}\right)[f] = z_0 \mathscr{T}_{\mathbf{\Lambda}_{\mathsf{S}_3}}[f] \tag{2.18}$$

where z_0 is a complex number (phase offset). The elements of the resultant SAFT parameter matrix are specified by,

$$\mathbf{\Lambda}_{\mathsf{S}_3} = \left[\; \mathbf{\Lambda}_{\mathsf{L}_3} \;\middle|\; \lambda_3 \;\right] = \left[\; \mathbf{\Lambda}_{\mathsf{L}_2}\mathbf{\Lambda}_{\mathsf{L}_1} \;\middle|\; \mathbf{\Lambda}_{\mathsf{L}_2}\lambda_2 + \lambda_1 \;\right].$$

In the context of phase space, the physical significance of the SAFT parameter matrix is that it maps

time-frequency co-ordinates $\mathbf{r} = [t \;\; \omega]^\top$ into its affine transformed version,

$$\begin{bmatrix} t \\ \omega \end{bmatrix} \xrightarrow{\mathsf{SAFT}} \begin{bmatrix} a & b \\ c & d \end{bmatrix} \begin{bmatrix} t \\ \omega \end{bmatrix} + \begin{bmatrix} p \\ q \end{bmatrix} \equiv \mathbf{r} \xrightarrow{\mathsf{SAFT}} \mathbf{\Lambda}_{\mathsf{L}}\mathbf{r} + \lambda.$$

Hence, the inverse-SAFT is defined by some affine transform that allows for the mapping,

$$\begin{bmatrix} at + bp + p \\ ct + d\omega + q \end{bmatrix} \xrightarrow{\mathsf{Inverse\ SAFT}} \begin{bmatrix} t \\ \omega \end{bmatrix}.$$

Thanks to the composition property (2.18), setting,

$$\begin{aligned} \mathbf{\Lambda}_{\mathsf{S}_3} &= \begin{bmatrix} \mathbf{\Lambda}_{\mathsf{L}_3} & \lambda_3 \end{bmatrix} = \begin{bmatrix} \mathbf{I} & \mathbf{0} \end{bmatrix} \qquad \text{(Identity Operation)} \\ &\Rightarrow \mathbf{\Lambda}_{\mathsf{L}_2} = \mathbf{\Lambda}_{\mathsf{L}_1}^{-1} \quad \text{and} \quad \lambda_2 = -\mathbf{\Lambda}_{\mathsf{L}_2}\lambda_1, \end{aligned}$$

results in the inverse parameter matrix defining inverse-SAFT which is equivalent to an SAFT with matrix $\mathbf{\Lambda}_{\mathsf{S}}^{\mathsf{inv}}$,

$$\mathbf{\Lambda}_{\mathsf{S}}^{\mathsf{inv}} = \left[\begin{array}{cc|c} +d & -b & bq - dp \\ -c & +a & cp - aq \end{array}\right] = \begin{bmatrix} \mathbf{\Lambda}_{\mathsf{L}}^{-1} & -\mathbf{\Lambda}_{\mathsf{L}}^{-1}\lambda \end{bmatrix} \tag{2.19}$$

where $c = \frac{ad-1}{b}$. Thus, the inverse transform (iSAFT) is defined as an SAFT with matrix $\mathbf{\Lambda}_{\mathsf{S}}^{\mathsf{inv}}$ in (2.19),

$$\mathscr{T}_{\mathbf{\Lambda}_{\mathsf{S}}^{\mathsf{inv}}}[\widehat{f}] = f(t) = K_{\mathbf{\Lambda}_{\mathsf{S}}^{\mathsf{inv}}} \left\langle \widehat{f}_{\mathbf{\Lambda}_{\mathsf{S}}}, \kappa_{\mathbf{\Lambda}_{\mathsf{S}}^{\mathsf{inv}}}(\cdot, t) \right\rangle \tag{2.20}$$

where $\kappa_{\mathbf{\Lambda}_{\mathsf{S}}^{\mathsf{inv}}}(\omega, t) = \kappa^*_{\mathbf{\Lambda}_{\mathsf{S}}}(t, \omega)$ and,

$$K_{\mathbf{\Lambda}_{\mathsf{S}}^{\mathsf{inv}}} = \exp\left(\frac{\jmath}{2}\left(cdp^2 + abq^2 - 2adpq\right)\right).$$

2.2.3 Geometry of the Special Affine Fourier Transform

An intriguing property of the SAFT is its geometrical interpretation in the context of time-frequency representations and the fact that the parameter matrix belongs to a class of area preserving matrices—the ones whose determinant is unity. We elaborate on these aspects starting with the cyclic property of the Fourier transform [97].

Let $\mathscr{T}^{(0)}_{\mathbf{\Lambda}_{\mathsf{FT}}} = \mathrm{I}$ be the identity operation that is, $\mathscr{T}^{(0)}_{\mathbf{\Lambda}_{\mathsf{FT}}}[f] = f$ which we use to define the Fourier operator composition:

$$\mathscr{T}^{(k)}_{\mathbf{\Lambda}_{\mathsf{FT}}} = \mathscr{T}^{(k-1)}_{\mathbf{\Lambda}_{\mathsf{FT}}} \circ \mathscr{T}_{\mathbf{\Lambda}_{\mathsf{FT}}} = \underbrace{\mathscr{T}_{\mathbf{\Lambda}_{\mathsf{FT}}} \circ \cdots \circ \mathscr{T}_{\mathbf{\Lambda}_{\mathsf{FT}}}}_{k-\mathsf{times}}, \quad k \in \mathbb{Z}^+. \tag{2.21}$$

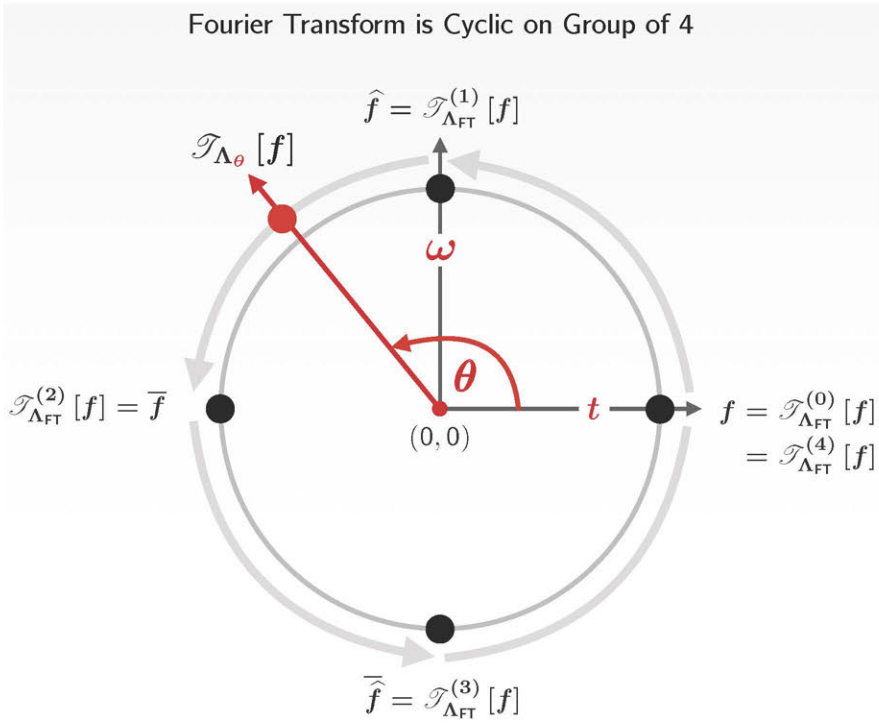

Figure 2-4: Fourier transform is cyclic on a group of 4, that is, $\mathscr{T}^{(k+4)}_{\mathbf{\Lambda}_{\mathsf{FT}}} = \mathscr{T}^{(k)}_{\mathbf{\Lambda}_{\mathsf{FT}}}, k \in \mathbb{Z}^+$ as described in (2.21). The Fractional Fourier transform allows for fractionalization of k so that a version of the Fourier transform may be defined on an arbitrary point on the circle. We denote such as transform by $\mathscr{T}_{\mathbf{\Lambda}_\theta}[f]$ where θ takes real values.

Note that:

$$\begin{aligned} \widehat{f} &= \mathscr{T}^{(1)}_{\mathbf{\Lambda}_{\mathsf{FT}}}[f] & \overline{f} &= \mathscr{T}^{(2)}_{\mathbf{\Lambda}_{\mathsf{FT}}}[f] \\ \overline{\widehat{f}} &= \mathscr{T}^{(3)}_{\mathbf{\Lambda}_{\mathsf{FT}}}[f] & \underbrace{f = \mathscr{T}^{(4)}_{\mathbf{\Lambda}_{\mathsf{FT}}}[f] \equiv \mathscr{T}^{(0)}_{\mathbf{\Lambda}_{\mathsf{FT}}}[f]}_{\text{Identity Operation}}. \end{aligned}$$

From the last equality, $\mathscr{T}^{(4)}_{\mathbf{\Lambda}_{\mathsf{FT}}}[f] = \mathscr{T}^{(0)}_{\mathbf{\Lambda}_{\mathsf{FT}}}[f]$, we conclude that the Fourier operator is periodic with $N = 4$. Due to this periodic structure, the Fourier operator can be represented on a circle as shown in Fig. 2-4.

Unitary mappings that can be continuously defined on the circle (as opposed to $k \in \mathbb{Z}^+$) were first identified by Condon [97]. This is known as the fractional Fourier transform (FrFT). Qualitatively, the FrFT "fractionalizes" the Fourier transform in the sense that $\mathscr{T}^{(k)}_{\mathbf{\Lambda}_{\mathsf{FT}}}[f], k \in \mathbb{Z}^+$ can be defined for an arbitrary point on the circle through $\theta = k\pi/2, k \in \mathbb{Z}$ by the transformation $\mathscr{T}_{\mathbf{\Lambda}_\theta}[f], \theta \in \mathbb{R}$. We compare the Fourier transform with the FrFT in Fig. 2-4. As shown in Fig. 2-5(a), the action of the FrFT on the time-frequency co-ordinates $\mathbf{r} = [t \;\; \omega]^\top, \mathbf{r} \in \mathbb{R}([0,1]^2)$ results in rotation of the time-frequency plane [106] due to $\widehat{\mathbf{r}} = \mathbf{\Lambda}_\theta \mathbf{r}, \theta \in \mathbb{R}$—an intrinsic property of the FrFT. This is explained by the co-ordinate transformation matrix—the rotation matrix $\mathbf{\Lambda}_\theta$ in case of the FrFT (cf. Table 2.3).

The submatrix $\mathbf{\Lambda}_{\mathsf{L}}$ of $\mathbf{\Lambda}_{\mathsf{S}}$ may be decomposed in several ways. One interesting decomposition relates

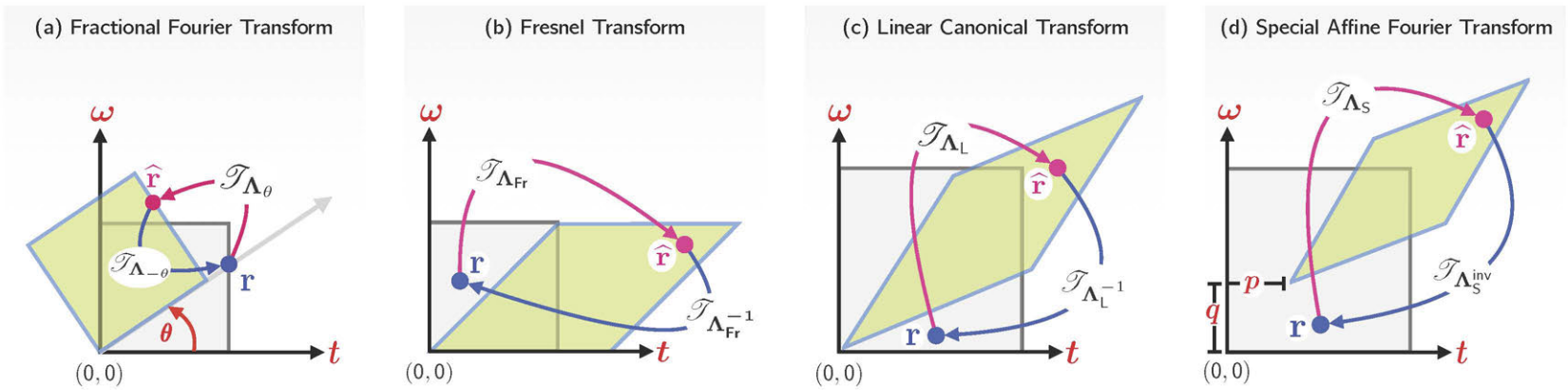

Figure 2-5: The SAFT maps one convex enclosure into another while preserving area since the transformation matrix $\mathbf{\Lambda}_{\mathsf{L}} \in \mathsf{SL}_2(\mathbb{R})$. The action of $\mathbf{\Lambda}_{\mathsf{L}}$ on a time-frequency co-ordinate $\mathbf{r} \in \mathbb{R}^2([0,1])$ results in $\widehat{\mathbf{r}} = \mathbf{\Lambda}_{\mathsf{L}}\mathbf{r}$. (a) For the FrFT, $\mathbf{\Lambda}_{\mathsf{L}} = \mathbf{\Lambda}_\theta$ implements rotation. The inverse transform corresponds to $\mathbf{\Lambda}_\theta^{-1} = \mathbf{\Lambda}_\theta^\top$. (b) For the Fresnel transform, $\mathbf{\Lambda}_{\mathsf{L}} = \mathbf{\Lambda}_{\mathsf{Fr}}$ implements shear. The inverse transform corresponds to $\mathbf{\Lambda}_{\mathsf{Fr}}^{-1}$. (c) For the Linear Canonical Transform (LCT), $\mathbf{\Lambda}_{\mathsf{L}}$ deforms a unit square into an arbitrary parallelogram. The inverse transform corresponds to $\mathbf{\Lambda}_{\mathsf{L}}^{-1}$. (d) For the SAFT, presence of an offset $\lambda = [p \;\; q]^\top$ results in an affine transform. Consequently, the inverse transform is given by $\mathbf{r} = \mathbf{\Lambda}_{\mathsf{L}}^{-1}\widehat{\mathbf{r}} - \mathbf{\Lambda}_{\mathsf{L}}^{-1}\lambda$.

$\mathbf{\Lambda}_{\mathsf{L}}$ to the Fourier transform such that $\mathbf{\Lambda}_{\mathsf{L}} = \mathbf{M}_1 \mathbf{\Lambda}_{\mathsf{FT}} \mathbf{M}_2$ where

$$\mathbf{M}_1 = \begin{bmatrix} b & 0 \\ d & 1/b \end{bmatrix} \quad \text{and} \quad \mathbf{M}_2 = \begin{bmatrix} 1 & 0 \\ a/b & 1 \end{bmatrix}$$

are modulation matrices[3]. This decomposition implies that the SAFT can be implemented as a Fourier transform using the following sequence of steps,

$$\begin{aligned} f_1(x) &\overset{\text{def}}{=} \mathscr{T}_{\mathbf{M_2}|\mathbf{0}}[f](x) \overset{(2.13)}{=} e^{\jmath \frac{a}{2b} x^2} f(x), \\ \widehat{f_1}(\xi) &= \mathscr{T}_{\mathbf{\Lambda}_{\mathsf{FT}}}[f_1](\xi) = \int f_1(x) e^{-\jmath \xi x} dx, \\ \widehat{f_1}(\omega) &\overset{\text{def}}{=} \mathscr{T}_{\mathbf{M_1}|\boldsymbol{\lambda}}[\widehat{f_1}](\omega) \overset{(2.13)}{=} \frac{1}{\sqrt{b}} e^{\jmath \omega q + \jmath \frac{d}{2b}(\omega - p)^2} \widehat{f_1}\left(\frac{\omega - p}{b}\right). \end{aligned}$$

By simplifying $\widehat{f_1}(\omega)$, we observe that it is indeed the SAFT of $f(t)$. In this way, we generalize the previously known result of Zayed [107] that links the FrFT to the Fourier Transform.

An alternative decomposition relates the SAFT with the FrFT and the Fresnel transform via the elegant Iwasawa Decomposition,

$$\mathbf{\Lambda}_{\mathsf{L}} = \mathbf{\Lambda}_{\theta} \begin{bmatrix} \Gamma & 0 \\ 0 & \Gamma^{-1} \end{bmatrix} \underbrace{\begin{bmatrix} 1 & u \\ 0 & 1 \end{bmatrix}}_{\text{Fresnel Transform}}, \quad \begin{aligned} \Gamma &= \sqrt{a^2 + c^2} \\ u &= (ab + cd)/\Gamma^2 \end{aligned}.$$

In fact, rotation is a special operation of a class of matrices that belong to the special linear group $\mathsf{SL}_2(\mathbb{R})$ where,

$$\mathsf{SL}_2(\mathbb{R}) = \left\{ \mathbf{A} = \begin{bmatrix} a_1 & a_2 \\ a_3 & a_4 \end{bmatrix}, \quad \{a_k\}_{k=1}^4 \in \mathbb{R} \text{ and } |\mathbf{A}| = 1 \right\}.$$

With the exception of the Laplace, Gauss and Bargmann transforms in Table 2.3, all other operations can be explained by $\mathbf{\Lambda}_{\mathsf{L}} \in \mathsf{SL}_2(\mathbb{R})$ which entails that $ad - bc = 1$. Since the basis vectors of $\mathbf{\Lambda}_{\mathsf{L}}$ form a parallelogram in $\mathbb{R}^2$, its enclosed area must always be unity or the area must be preserved under application of $\mathbf{\Lambda}_{\mathsf{L}}$. This aspect has important consequences in ray optics where $\mathbf{\Lambda}_{\mathsf{L}}$ models paraxial optics [102, 104]. In Figs. 2-5(b), 2-5(c) and 2-5(d) we describe the deformation on $\mathbf{r}$ due to $\mathbf{\Lambda}_{\mathsf{S}}$ for the Fresnel transform ($\mathbf{\Lambda}_{\mathsf{S}} = \mathbf{\Lambda}_{\mathsf{Fr}}$), the LCT ($\mathbf{\Lambda}_{\mathsf{S}} = \mathbf{\Lambda}_{\mathsf{L}}$) and the SAFT.

Geometrically, the inverse transform relies on specification of $\mathbf{\Lambda}_{\mathsf{S}}^{\mathsf{inv}}$ which undoes the effect of $\mathbf{\Lambda}_{\mathsf{S}}$. For the FrFT, the Fresnel transform and the LCT, the operation is simply the inverse of the matrix, that is $\mathbf{\Lambda}_{\mathsf{S}}^{\mathsf{inv}} = \mathbf{\Lambda}_{\mathsf{S}}^{-1}, \mathbf{\Lambda}_{\mathsf{S}} = \{\mathbf{\Lambda}_{\theta}, \mathbf{\Lambda}_{\mathsf{Fr}}, \mathbf{\Lambda}_{\mathsf{L}}\}$ (cf. Table 2.3). The case of the SAFT is unique because it implements an affine transform as opposed to the usual case of a linear transform (cf. compare Fig. 2-5(b,c) and Fig. 2-5(d)). The presence of an offset $\lambda = [p \;\; q]^{\top}$ in (2.14) warrants an adjustment by $-\mathbf{\Lambda}_{\mathsf{L}}^{-1}\lambda$ (2.19) for the SAFT.

[3]We refer to $\mathbf{M}_1$ and $\mathbf{M}_2$ as modulation matrices because whenever $b = 0$ in (2.14), the SAFT in (2.13) amounts to modulation of the function f.

2.3 Convolution and Product Theorems

Let $\mathscr{T} : f \to \widehat{f}$ be a unitary, integral operator which maps f to its transform domain representation $\widehat{f}$. For example, if $\mathscr{T}$ is the Fourier operator, that is,

$$\mathscr{T}_{\mathbf{\Lambda}_{\mathsf{FT}}}[f](\omega) \stackrel{\text{def}}{=} \widehat{f}(\omega) = \frac{1}{\sqrt{2\pi}} \int_{\mathbb{R}} f(t)\, e^{-\jmath\omega t} dt, \tag{2.22}$$

then $\widehat{f}$ is identified as the frequency domain of f. Furthermore, let $*$ denote the standard convolution operator defined by

$$(f * g)(t) = \frac{1}{\sqrt{2\pi}} \int_{\mathbb{R}} f(x) g(t-x) dx.$$

It is well known that for some functions f and g, and $\mathscr{T} = \mathscr{T}_{\mathbf{\Lambda}_{\mathsf{FT}}}$, we have,

$$\mathscr{T}_{\mathbf{\Lambda}_{\mathsf{FT}}}[f * g](\omega) = \underbrace{\mathscr{T}_{\mathbf{\Lambda}_{\mathsf{FT}}}[f](\omega)\, \mathscr{T}_{\mathbf{\Lambda}_{\mathsf{FT}}}[g](\omega)}_{\text{Product in Transform Domain}}. \tag{2.23}$$

This result is known as the Fourier *convolution theorem*.

In context of signal processing theory, Almeida first studied the fractional Fourier Transform (FrFT) domain representation of convolution and product operators [108]. Unfortunately, Almeida's formulation did not conform with the classical Fourier convolution–multiplication property. That is to say, the convolution of functions in time domain did not result in multiplication of their respective FrFT spectrums. As a follow up, Zayed formulated the convolution operation for the FrFT which resulted in an elegant convolution–multiplication property in FrFT domain [109]. Recently, Xiang and Qin [110] introduced a new convolution operation that is more suitable for the SAFT and by which the SAFT of the convolution of two functions is the product of their SAFTs and a phase factor. However, their convolution structure does not work well with the inverse transform in so far as the inverse transform of the product of two functions is not equal to the convolution of the transforms.

In this section we introduce a new convolution operation that works well with both the SAFT and its inverse leading to an analogue of the convolution and product formulas for the Fourier transform. Furthermore, we introduce a second convolution operation that leads to the elimination of the phase factor in the convolution formula obtained in [110]. Later, these properties will be used in the context of sampling theory as convolution structures allow us to define filtering operations and low-pass projections in the SAFT domain.

Before we define the convolution operation in the SAFT domain, let us introduce the chirp modulation operation.

Definition 1 (Chirp Modulation). *Let* $\mathbf{A} = [a_{j,k}]$ *be a* 2×2 *matrix. We define the modulation function,*

$$m_{\mathbf{A}}(t) \stackrel{\text{def}}{=} \exp\left(\jmath \frac{a_{11}}{2a_{12}} t^2\right). \tag{2.24}$$

Furthermore, for a given function f*, we define its chirp modulated functions associated with the matrix* $\mathbf{A}$ *as,*

$$\overrightarrow{f}(t) \stackrel{\text{def}}{=} m_{\mathbf{A}}(t) f(t) \quad \textit{and} \quad \overleftarrow{f}(t) \stackrel{\text{def}}{=} m^*_{\mathbf{A}}(t) f(t), \tag{2.25}$$

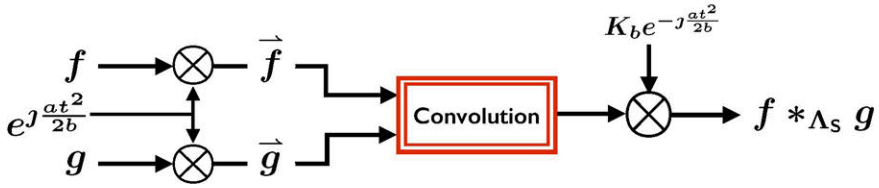

Figure 2-6: Block diagram for SAFT convolution. We use the usual definition of the convolution operation in conjunction with chirp modulation to define the SAFT convolution operation. The gain factor $K_b = K_{\mathbf{\Lambda}_\mathsf{S}}$.

---

respectively. Note that $\|\vec{f}(t)\|_{L_2}^2 = \|f(t)\|_{L_2}^2$.

For example, let $\mathbf{A} = \mathbf{\Lambda}_\mathsf{S}$, then, we have,

$$\vec{f}(t) = m_{\mathbf{\Lambda}_\mathsf{S}} f(t) = e^{\jmath\frac{at^2}{2b}} f(t).$$

For the case when $\mathbf{A} = \mathbf{\Lambda}_\mathsf{S}^{\mathsf{inv}}$, we get, $\vec{f}(t) = m_{\mathbf{\Lambda}_\mathsf{S}^{\mathsf{inv}}}(t) f(t) = e^{-\jmath\frac{dt^2}{2b}} f(t)$. Next we define the SAFT convolution operator.

Definition 2 (SAFT Convolution)**.** *Let $*$ denote the usual convolution operator. Given functions f and g, the SAFT convolution operator denoted by $*_{\mathbf{\Lambda}_\mathsf{S}}$, is defined as*

$$h(t) = \left(f *_{\mathbf{\Lambda}_\mathsf{S}} g\right)(t) \stackrel{\text{def}}{=} K_{\mathbf{\Lambda}_\mathsf{S}} m_{\mathbf{\Lambda}_\mathsf{S}}^{*}(t) \left(\vec{f} * \vec{g}\right)(t), \tag{2.26}$$

where $\vec{f}(t) = m_{\mathbf{\Lambda}_\mathsf{S}}(t) f(t) \stackrel{(2.25)}{=} e^{\jmath\frac{at^2}{2b}} f(t)$*; the same applies to the function g.*

In Fig. 2-6, we explain the SAFT convolution operation defined in (2.26). Note that the SAFT convolution operation is based on the usual convolution of pre-modulated functions $\vec{f}(t)$ and $\vec{g}(t)$. This operation, also known as *chirping*, is a standard procedure in optical information processing [111] and analog processing where it is implemented via mixing circuits (cf. Fig. 6(a) in [88]). Similarly, in the field of holography, such operations are used for defining Fresnel transforms (cf. (10) in [90]). Pre- and post-modulations are critical in our context and enforce the convolution-multiplication property. A formal statement of this result is as follows:

Theorem 2 (SAFT Convolution and Product Theorem)**.** *Let f and g be any two given functions for which the convolution $*_{\mathbf{\Lambda}_\mathsf{S}}$ exists and set,*

$$h(t) = \left(f *_{\mathbf{\Lambda}_\mathsf{S}} g\right)(t).$$

Furthermore, let $\widehat{f}_{\mathbf{\Lambda}_\mathsf{S}}(\omega), \widehat{g}_{\mathbf{\Lambda}_\mathsf{S}}(\omega)$ and $\widehat{h}_{\mathbf{\Lambda}_\mathsf{S}}(\omega)$ be the SAFT of f, g and h, respectively. Then we have,

$$h(t) = \left(f *_{\mathbf{\Lambda}_\mathsf{S}} g\right)(t) \xrightarrow{\mathsf{SAFT}} \widehat{h}_{\mathbf{\Lambda}_\mathsf{S}}(\omega) = \Phi_{\mathbf{\Lambda}_\mathsf{S}}(\omega)\, \widehat{f}_{\mathbf{\Lambda}_\mathsf{S}}(\omega)\, \widehat{g}_{\mathbf{\Lambda}_\mathsf{S}}(\omega),$$

where $\Phi_{\mathbf{\Lambda}_{\mathsf{S}}}(\omega) = e^{\jmath\frac{\omega}{b}(dp-bq)}e^{-\jmath\frac{d\omega^2}{2b}}$. *Moreover, let,*

$$h(t) = \Phi_{\mathbf{\Lambda}_{\mathsf{S}}^{inv}}(t)\, f(t)\, g(t) \;\; \textit{with}\; \Phi_{\mathbf{\Lambda}_{\mathsf{S}}^{inv}}(t) = e^{\jmath\frac{at^2}{2b}}e^{-\jmath\frac{t}{b}(ap_0+bq_0)},$$

then, we have, $\widehat{h}_{\mathbf{\Lambda}_{\mathsf{S}}}(\omega) = K_{\mathbf{\Lambda}_{\mathsf{S}}^{inv}}\left(\widehat{f} *_{\mathbf{\Lambda}_{\mathsf{S}}^{inv}} \widehat{g}\right)(\omega)$.

Proof. We begin with computing the SAFT of h,

$$\begin{aligned}
\widehat{h}_{\mathbf{\Lambda}_{\mathsf{S}}}(\omega) &\overset{(2.13)}{=} \left\langle h(t), \kappa_{\mathbf{\Lambda}_{\mathsf{S}}}(t,\omega)\right\rangle \\
&= \int_{\mathbb{R}} h(t)\,\kappa^*(t,\omega)\,dt \\
&\overset{(2.26)}{=} \int_{\mathbb{R}}\left(K_{\mathbf{\Lambda}_{\mathsf{S}}} m^*_{\mathbf{\Lambda}_{\mathsf{S}}}(t)\int_{\mathbb{R}}\vec{f}(z)\,\vec{g}(t-z)\,dz\right)\kappa^*(t,\omega)\,dt \\
&= \underbrace{K^2_{\mathbf{\Lambda}_{\mathsf{S}}} e^{\jmath\frac{d\omega^2}{2b}} e^{-\jmath\frac{\omega}{b}(dp-bq)}}_{=K^2_{\mathbf{\Lambda}_{\mathsf{S}}}\Phi^*_{\mathbf{\Lambda}_{\mathsf{S}}}}\int_{\mathbb{R}} e^{\jmath\frac{t}{b}(p-\omega)}\boxed{m_{\mathbf{\Lambda}_{\mathsf{S}}}(t)}\left(\boxed{m^*_{\mathbf{\Lambda}_{\mathsf{S}}}(t)}\int_{\mathbb{R}}\vec{f}(z)\,\vec{g}(t-z)\,dz\right)dt.
\end{aligned}$$

In the above development, note that the items in the box cancel one another because $m^*_{\mathbf{\Lambda}_{\mathsf{S}}} m_{\mathbf{\Lambda}_{\mathsf{S}}} = 1$ (see Definition 1). Setting $t - z = v$ and using (2.25), we obtain an integral of separable form, that is, $\widehat{h}_{\mathbf{\Lambda}_{\mathsf{S}}}(\omega) = I_f(\omega)\, I_g(\omega)$ because,

$$\underbrace{K^2_{\mathbf{\Lambda}_{\mathsf{S}}}\Phi^*_{\mathbf{\Lambda}_{\mathsf{S}}}(\omega)\iint_{\mathbb{R}} f(x)\, m_{\mathbf{\Lambda}_{\mathsf{S}}}(x)\, g(v)\, m_{\mathbf{\Lambda}_{\mathsf{S}}}(v)\, e^{\jmath\frac{v+x}{b}(p-\omega)}dxdv}_{\widehat{h}_{\mathbf{\Lambda}_{\mathsf{S}}}(\omega)} = I_f(\omega)\, I_g(\omega) = \widehat{h}_{\mathbf{\Lambda}_{\mathsf{S}}}(\omega), \tag{2.27}$$

where, for a given function f, we define,

$$I_f(\omega) \overset{\text{def}}{=} K_{\mathbf{\Lambda}_{\mathsf{S}}}\sqrt{\Phi^*_{\mathbf{\Lambda}_{\mathsf{S}}}(\omega)}\int_{\mathbb{R}} f(z)\, m_{\mathbf{\Lambda}_{\mathsf{S}}}(z)\, e^{\jmath\frac{z}{b}(p-\omega)}dz. \tag{2.28}$$

Indeed, using (2.28) and (2.13), it is easy to see that,

$$I_f(\omega) = \sqrt{\Phi^*_{\mathbf{\Lambda}_{\mathsf{S}}}(\omega)}\Phi_{\mathbf{\Lambda}_{\mathsf{S}}}(\omega)\,\widehat{f}_{\mathbf{\Lambda}_{\mathsf{S}}}(\omega) \tag{2.29}$$

and this result extends to $I_g(\omega)$ by symmetry. We conclude,

$$\begin{aligned}
\widehat{h}_{\mathbf{\Lambda}_{\mathsf{S}}}(\omega) &\overset{(2.27)}{=} I_f(\omega)\, I_g(\omega) \\
&\overset{(2.29)}{=} \sqrt{\Phi^*_{\mathbf{\Lambda}_{\mathsf{S}}}(\omega)}\Phi_{\mathbf{\Lambda}_{\mathsf{S}}}(\omega)\,\widehat{f}_{\mathbf{\Lambda}_{\mathsf{S}}}(\omega)\cdot\sqrt{\Phi^*_{\mathbf{\Lambda}_{\mathsf{S}}}(\omega)}\Phi_{\mathbf{\Lambda}_{\mathsf{S}}}(\omega)\,\widehat{g}_{\mathbf{\Lambda}_{\mathsf{S}}}(\omega) \\
&= \Phi_{\mathbf{\Lambda}_{\mathsf{S}}}(\omega)\,\widehat{f}_{\mathbf{\Lambda}_{\mathsf{S}}}(\omega)\,\widehat{g}_{\mathbf{\Lambda}_{\mathsf{S}}}(\omega)
\end{aligned}$$

which is the statement of part I of Theorem 2.

Now we establish the product theorem for the SAFT,

$$\Phi_{\mathbf{\Lambda}_{\mathsf{S}}^{\mathsf{inv}}}(t)\, f(t)\, g(t) \xrightarrow{\mathsf{SAFT}} K_{\mathbf{\Lambda}_{\mathsf{S}}^{\mathsf{inv}}}\left(\widehat{f} *_{\mathbf{\Lambda}_{\mathsf{S}}^{\mathsf{inv}}} \widehat{g}\right)(\omega)\,.$$

Since the inverse–SAFT is the SAFT of a function with $\mathbf{\Lambda}_{\mathsf{S}} = \mathbf{\Lambda}_{\mathsf{S}}^{\mathsf{inv}}$ in (2.19), we have,

$$\begin{aligned} h(t) =& K_{\mathbf{\Lambda}_{\mathsf{S}}^{\mathsf{inv}}} K_{\mathbf{\Lambda}_{\mathsf{S}}}^{*} \int_{\mathbb{R}} \widehat{h}_{\mathbf{\Lambda}_{\mathsf{S}}}(\omega)\, e^{-\jmath \frac{\left(at^2+d\omega^2\right)}{2b}} e^{-\jmath \frac{\omega}{b}(p_0-t)} e^{\jmath \frac{t}{b}(ap_0+bq_0)} d\omega \\ =& K_{\mathbf{\Lambda}_{\mathsf{S}}^{\mathsf{inv}}} K_{\mathbf{\Lambda}_{\mathsf{S}}}^{*} \Phi_{\mathbf{\Lambda}_{\mathsf{S}}^{\mathsf{inv}}}^{*}(t) \int_{\mathbb{R}} \widehat{h}_{\mathbf{\Lambda}_{\mathsf{S}}}(\omega)\, e^{-\jmath \frac{d\omega^2}{2b}} e^{-\jmath \frac{\omega(p_0-t)}{b}} d\omega. \end{aligned}$$

By setting,

$$\begin{aligned} \widehat{h}_{\mathbf{\Lambda}_{\mathsf{S}}}(\omega) &= K_{\mathbf{\Lambda}_{\mathsf{S}}^{\mathsf{inv}}}\left(\widehat{f} *_{\mathbf{\Lambda}_{\mathsf{S}}^{\mathsf{inv}}} \widehat{g}\right)(\omega) \\ &= K_{\mathbf{\Lambda}_{\mathsf{S}}^{\mathsf{inv}}} K_{\mathbf{\Lambda}_{\mathsf{S}}}^{*} m_{\mathbf{\Lambda}_{\mathsf{S}}^{\mathsf{inv}}}^{*}(\omega) \left(\vec{\widehat{f}}(\omega) * \vec{\widehat{g}}(\omega)\right), \end{aligned}$$

where, for $\mathbf{\Lambda}_{\mathsf{S}} = \mathbf{\Lambda}_{\mathsf{S}}^{\mathsf{inv}}$ (see (2.19)), we have,

$$m_{\mathbf{\Lambda}_{\mathsf{S}}^{\mathsf{inv}}}(\cdot) = e^{-\jmath \frac{d(\cdot)^2}{2b}} \text{ and } \vec{f}(\omega) = m_{\mathbf{\Lambda}_{\mathsf{S}}^{\mathsf{inv}}}(\omega)\, f(\omega)\,.$$

Upon simplification, we obtain the separable integrals,

$$\begin{aligned} h(t) &= \left(K_{\mathbf{\Lambda}_{\mathsf{S}}^{\mathsf{inv}}} K_{\mathbf{\Lambda}_{\mathsf{S}}}^{*}\right)^2 \Phi_{\mathbf{\Lambda}_{\mathsf{S}}^{\mathsf{inv}}}^{*}(t) \iint \widehat{f}(\nu)\, m_{\mathbf{\Lambda}_{\mathsf{S}}^{\mathsf{inv}}}(\nu)\, \widehat{g}(\omega-\nu)\, m_{\mathbf{\Lambda}_{\mathsf{S}}^{\mathsf{inv}}}(\omega-\nu)\, d\nu e^{-\jmath \frac{\omega(p_0-t)}{b}} d\omega \\ &= \int \vec{\widehat{f}}(\nu)\, e^{-\jmath \frac{\nu(p_0-t)}{b}} d\nu \int \vec{\widehat{g}}(\omega)\, e^{-\jmath \frac{\omega(p_0-t)}{b}} d\omega \\ &= I_f(t)\, I_g(t)\,, \end{aligned}$$

where,

$$\begin{aligned} I_f(t) &= K_{\mathbf{\Lambda}_{\mathsf{S}}^{\mathsf{inv}}} K_{\mathbf{\Lambda}_{\mathsf{S}}}^{*} \sqrt{\Phi_{\mathbf{\Lambda}_{\mathsf{S}}^{\mathsf{inv}}}^{*}(t)} \int_{\mathbb{R}} \vec{f}(\omega) e^{-\jmath \frac{\omega(p_0-t)}{b}} d\omega. \\ &= \sqrt{\Phi_{\mathbf{\Lambda}_{\mathsf{S}}^{\mathsf{inv}}}^{*}(t)} \Phi_{\mathbf{\Lambda}_{\mathsf{S}}^{\mathsf{inv}}}(t)\, f(t)\,. \end{aligned}$$

As a result, we have,

$$\begin{aligned} h(t) &= I_f(t)\, I_g(t) \\ &= \sqrt{\Phi_{\mathbf{\Lambda}_{\mathsf{S}}^{\mathsf{inv}}}^{*}(t)} \Phi_{\mathbf{\Lambda}_{\mathsf{S}}^{\mathsf{inv}}}(t)\, f(t) \cdot \sqrt{\Phi_{\mathbf{\Lambda}_{\mathsf{S}}^{\mathsf{inv}}}^{*}(t)} \Phi_{\mathbf{\Lambda}_{\mathsf{S}}^{\mathsf{inv}}}(t)\, g(t) \\ &= \Phi_{\mathbf{\Lambda}_{\mathsf{S}}^{\mathsf{inv}}}(t)\, f(t)\, g(t) \end{aligned}$$

which is the desired result. ■

2.3.1 Comparison and Alternative Results

In this section we compare our results with those of [110]. We show that our approach is not only easier to derive, but also provides more symmetric formulas to implement. Our convolution formula is the same as the one given in [110], both assert that the SAFT of the convolution of two functions is the product of their SAFT and a phase factor given by $\Phi_{\mathbf{\Lambda}_\mathsf{S}}(\omega)$. But our product formula is different from that in [110] which states that the SAFT of the product of two functions f and g is,

$$\left(K_{\mathbf{\Lambda}_\mathsf{S}} K^*_{\mathbf{\Lambda}_\mathsf{S}}\right) \Phi^*_{\mathbf{\Lambda}_\mathsf{S}}(\omega) \left(\widehat{f}_{\mathbf{\Lambda}_\mathsf{S}}(\omega)\, \Phi_{\mathbf{\Lambda}_\mathsf{S}}(\omega) * \widehat{g}_{\mathbf{\Lambda}_\mathsf{FT}}\left(\frac{\omega}{b}\right)\right). \tag{2.30}$$

The reason our convolution and product formulas are more symmetric and simpler goes back to our definition of the chirp modulation, see Definition 1 , which uses the adaptive matrix $\mathbf{\Lambda}_\mathsf{S}$ that accommodates both the forward and backward SAFT.

Furthermore, we will now derive another convolution for SAFT which eliminates the phase factor $\Phi_{\mathbf{\Lambda}_\mathsf{S}}$ from the convolution formula.

Definition 3 (Phase–free SAFT Convolution)**.** *Let f and g be two given functions and $*$ denote the usual convolution operation. The second SAFT convolution $\star$ is defined by,*

$$h(t) = (f \star g)(t) \stackrel{\text{def}}{=} \sqrt{2} K_{\mathbf{\Lambda}_\mathsf{S}} m^*_{\mathbf{\Lambda}_\mathsf{S}}(t) \left(\vec{f}(\cdot) * \vec{g}(\cdot)\right)(\sqrt{2}t).$$

In view of this SAFT–convolution, we have the following theorem.

Theorem 3. *Let $h(t) = (f \star g)(t)$. Then, we have,*

$$\widehat{h}_{\mathbf{\Lambda}_\mathsf{S}}(\omega) = \widehat{f}_{\mathbf{\Lambda}_1}\left(\frac{\omega}{\sqrt{2}}\right) \widehat{g}_{\mathbf{\Lambda}_1}\left(\frac{\omega}{\sqrt{2}}\right)$$

where $\widehat{f}_{\mathbf{\Lambda}_1}$ denotes the SAFT of f with respect to the matrix $\mathbf{\Lambda}_1 = \left[\mathbf{\Lambda} \mid \lambda/\sqrt{2}\right]$ (cf. (2.14)).

Proof. Let $\Omega_0 = bq - dp$. We have,

$$\widehat{h}_{\mathbf{\Lambda}_\mathsf{S}}(\omega) = \sqrt{2} K^2_{\mathbf{\Lambda}_\mathsf{S}} e^{-\frac{\jmath a t^2}{2b}} \int_{\mathbb{R}} e^{\frac{\jmath}{2b}\left(at^2 + d\omega^2 + 2tp - 2t\omega + 2\omega\Omega_0\right)} dt \int_{\mathbb{R}} f(\tau) e^{\frac{\jmath a t^2}{2b}} g(\sqrt{2}t - \tau) e^{\frac{\jmath a}{2b}(\sqrt{2}t - \tau)^2} d\tau.$$

Setting $x = \sqrt{2}t - \tau$ and simplifying the integrals, we obtain,

$$\begin{aligned}
\widehat{h}_{\mathbf{\Lambda}_\mathsf{S}}(\omega) &= K^2_{\mathbf{\Lambda}_\mathsf{S}} \Phi^*_{\mathbf{\Lambda}_\mathsf{S}}(\omega) \int_{\mathbb{R}} e^{\frac{\jmath a \tau^2}{2b}} f(\tau) d\tau \int_{\mathbb{R}} g(x) e^{\frac{\jmath}{2b}\left(ax^2 + 2(p-\omega)(x+\tau)/\sqrt{2}\right)} dx \\
&= K^2_{\mathbf{\Lambda}_\mathsf{S}} \Phi^*_{\mathbf{\Lambda}_\mathsf{S}}(\omega) \int_{\mathbb{R}} e^{\frac{\jmath}{2b}\left(a\tau^2 + 2(p-\omega)\tau/\sqrt{2}\right)} f(\tau) d\tau \int_{\mathbb{R}} g(x) e^{\frac{\jmath}{2b}\left(ax^2 + 2(p-\omega)x/\sqrt{2}\right)} dx \\
&= K^2_{\mathbf{\Lambda}_\mathsf{S}} \Phi^*_{\mathbf{\Lambda}_\mathsf{S}}(\omega) \int_{\mathbb{R}} e^{\frac{\jmath}{2b}\left(a\tau^2 + \sqrt{2}p\tau - \sqrt{2}\tau\omega\right)} f(\tau) d\tau \int_{\mathbb{R}} e^{\frac{\jmath}{2b}\left(ax^2 + \sqrt{2}px - \sqrt{2}x\omega)\right)} g(x) dx.
\end{aligned}$$

But since,

$$\Phi^*_{\mathbf{\Lambda}_\mathsf{S}}(\omega) = e^{\jmath \frac{1}{2b}\left(2d\left(\frac{\omega}{\sqrt{2}}\right)^2 + 2\sqrt{2}\Omega_0 \frac{\omega}{\sqrt{2}}\right)},$$

it follows, that $\widehat{h}_{\mathbf{\Lambda}_{\mathsf{S}}}(\omega) = I_f(\omega) I_g(\omega)$, where

$$I_f(\omega) = K_{\mathbf{\Lambda}_{\mathsf{S}}} \int_{\mathbb{R}} e^{\frac{j}{2b}\left(a\tau^2 + d\left(\frac{\omega}{\sqrt{2}}\right)^2 + \sqrt{2}p\tau - \sqrt{2}\tau\omega + \sqrt{2}\Omega_0\left(\frac{\omega}{\sqrt{2}}\right)\right)} f(\tau) d\tau$$

and similar expression for $I_g(\omega)$. But it is easy to see that

$$I_f(\omega) = \widehat{f}_{\mathbf{\Lambda}_1}\left(\frac{\omega}{\sqrt{2}}\right),$$

and this completes the proof. ■

Relation to Convolution theory of LCTs: In the special case where $p = q = 0 \Leftrightarrow \mathbf{\Lambda}_{\mathsf{S}} = \mathbf{\Lambda}_{\mathsf{LCT}}$, the SAFT reduces to the LCT and the last convolution theorem takes the simple form

$$\mathscr{T}_{\mathsf{LCT}}[f \star g](\omega) = \mathscr{T}_{\mathsf{LCT}}[f]\left(\frac{\omega}{\sqrt{2}}\right) \mathscr{T}_{\mathsf{LCT}}[g]\left(\frac{\omega}{\sqrt{2}}\right).$$

2.3.2 Summary of Results

In this section, we introduced two definitions of convolution operation that establish the convolution–product theorem for the Special Affine Fourier Transform (SAFT) introduced by Abe and Sheridan [102, 112]. Our result is quite general in that our convolution–product theorem is applicable to all the listed unitary transformations in Table 2.3. Furthermore, we also presented a product theorem for the SAFT which establishes the fact that the product of functions in time amounts to convolution in SAFT domain. We conclude that our construction of the convolution structure for the SAFT domain establishes the SAFT duality principle, that is, convolution in one domain amounts to multiplication in the transform domain and vice–versa.

2.4 Sampling Theory of Smooth Functions

For brevity, several computations and variations that were developed in [113] have been omitted here. For further details on computations involved with the proofs, we refer the reader to [113].

2.4.1 Bandlimited Subspaces of the SAFT

In order to set the ground for sampling of sparse signals in subsequent sections, we begin by developing the sampling theorem for SAFT bandlimited signals. The notion of bandlimitedness has a de facto association with the Fourier domain. Below, we consider a more general definition.

Definition 4 (Bandlimited Functions)**.** *Let f be a square-integrable function. We say that f is Ω_m–bandlimited and write,*

$$f \in \mathcal{B}_{\Omega_m}^{\mathbf{\Lambda}_{\mathsf{S}}} \Leftrightarrow f(t) = K_{\mathbf{\Lambda}_{\mathsf{S}}^{inv}} \int_{-\Omega_m}^{+\Omega_m} \widehat{f}_{\mathbf{\Lambda}_{\mathsf{S}}}(\omega) \kappa^*_{\mathbf{\Lambda}_{\mathsf{S}}^{inv}}(\omega) d\omega.$$

With $\mathbf{\Lambda}_{\mathsf{S}} = \mathbf{\Lambda}_{\mathsf{FT}}$, we obtain the standard case when f is Ω_m–bandlimited in the Fourier domain.

Shannon's sampling theorem (cf. Theorem 1) is restricted to Fourier transforms. In that case, $\mathbf{\Lambda}_{\mathsf{S}} = \mathbf{\Lambda}_{\mathsf{FT}}$ and any $f \in \mathcal{B}_{\Omega_m}^{\mathbf{\Lambda}_{\mathsf{FT}}}$ can be uniquely recovered from samples $f(kT), k \in \mathbb{Z}$ provided that $T \leq \pi/\Omega_m$. For bandlimited signals in the SAFT sense, the statement of Shannon's sampling theorem is follows.

Theorem 4 (Shannon's Sampling Theorem for the SAFT Domain)**.** *Let f be an Ω_m–bandlimited function in the SAFT domain, that is, $f \in \mathcal{B}_{\Omega_m}^{\mathbf{\Lambda}_{\mathsf{S}}}$. Then, we have,*

$$f(t) = e^{-\jmath\frac{at^2}{2b}} \sum_{n\in\mathbb{Z}} \vec{f}(nT)\, e^{-\jmath p\frac{t-nT}{b}} \operatorname{sinc}_T(t-nT). \tag{2.31}$$

A detailed proof of this theorem that is based on reproducing kernel Hilbert spaces is given our [113]. Here, we will briefly outline the key steps. The associated computations will be useful in the context of sampling sparse signals.

It is well known that the sampling theorem for the Fourier domain can be interpreted as an orthogonal projection of f onto the subspace of bandlimited functions [28], V_{BL} in (2.3). Thanks to the projection theorem,

$$\mathscr{P}_{\mathsf{V}_{\mathsf{BL}}} f = \arg\min_{g\in\mathsf{V}_{\mathsf{BL}}} \|f-g\|_{L_2}^2 \ , \ f \in \mathcal{B}_{\Omega_m}^{\mathbf{\Lambda}_{\mathsf{FT}}} \Leftrightarrow f = \mathscr{P}_{\mathsf{V}_{\mathsf{BL}}} f. \tag{2.32}$$

In the spirit of the Fourier domain result, we derived the subspace of bandlimited functions linked with the SAFT domain which take the form of,

$$\phi_n(t) = \frac{e^{-\jmath\frac{p}{b}(t-nT)}}{\sqrt{T}} m_{\mathbf{\Lambda}_{\mathsf{S}}}^*(t)\, m_{\mathbf{\Lambda}_{\mathsf{S}}}(nT) \operatorname{sinc}_T(t-nT). \tag{2.33}$$

The family $\{\phi_n(t)\}_{n\in\mathbb{Z}}$ is an orthonormal basis for the subspace of bandlimited functions in the SAFT domain. Indeed, $\phi_0 \in \mathcal{B}_{\Omega_m}^{\mathbf{\Lambda}_{\mathsf{S}}}$ with $\Omega_m = \pi b/T$ since,

$$n=0, \quad \widehat{\phi}_{\mathbf{\Lambda}_{\mathsf{S}}}(\omega) = \sqrt{T} K_{\mathbf{\Lambda}_{\mathsf{S}}} \Phi_{\mathbf{\Lambda}_{\mathsf{S}}}^*(\omega) \underbrace{\mathbb{1}_{[-\Omega_m,\Omega_m]}(\omega)}_{\text{Bandlimited}} \qquad \Omega_m = \frac{\pi b}{T}.$$

Let us denote the subspace of bandlimited functions associated with the SAFT domain by,

$$\mathsf{V}_{\mathsf{BL}}^{\mathbf{\Lambda}_{\mathsf{S}}} = \operatorname{span}\{\phi_n(t)\}_{n\in\mathbb{Z}} \overset{(2.33)}{=} \operatorname{span}\left\{ \frac{e^{-\jmath\frac{p}{b}(t-nT)}}{\sqrt{T}} m_{\mathbf{\Lambda}_{\mathsf{S}}}^*(t)\, m_{\mathbf{\Lambda}_{\mathsf{S}}}(nT) \operatorname{sinc}_T(t-nT) \right\}_{n\in\mathbb{Z}} \tag{2.34}$$

Thanks to the orthonormality and the bandlimitedness properties, the implication of the projection theorem (cf. (2.32)) is that $f \in \mathcal{B}_{\Omega_m}^{\mathbf{\Lambda}_{\mathsf{S}}} \Leftrightarrow f = \mathscr{P}_{\mathsf{V}_{\mathsf{BL}}^{\mathbf{\Lambda}_{\mathsf{S}}}} f$ and by developing this further, we obtain,

$$\begin{aligned} \mathscr{P}_{\mathsf{V}_{\mathsf{BL}}^{\mathbf{\Lambda}_{\mathsf{S}}}} f &= \sum_{n\in\mathbb{Z}} \langle f, \phi_n \rangle \phi_n(t) \\ &= e^{-\jmath\frac{at^2}{2b}} \sum_{n\in\mathbb{Z}} \vec{f}(nT)\, e^{-\jmath p\frac{t-nT}{b}} \operatorname{sinc}_T(t-nT). \end{aligned} \tag{2.35}$$

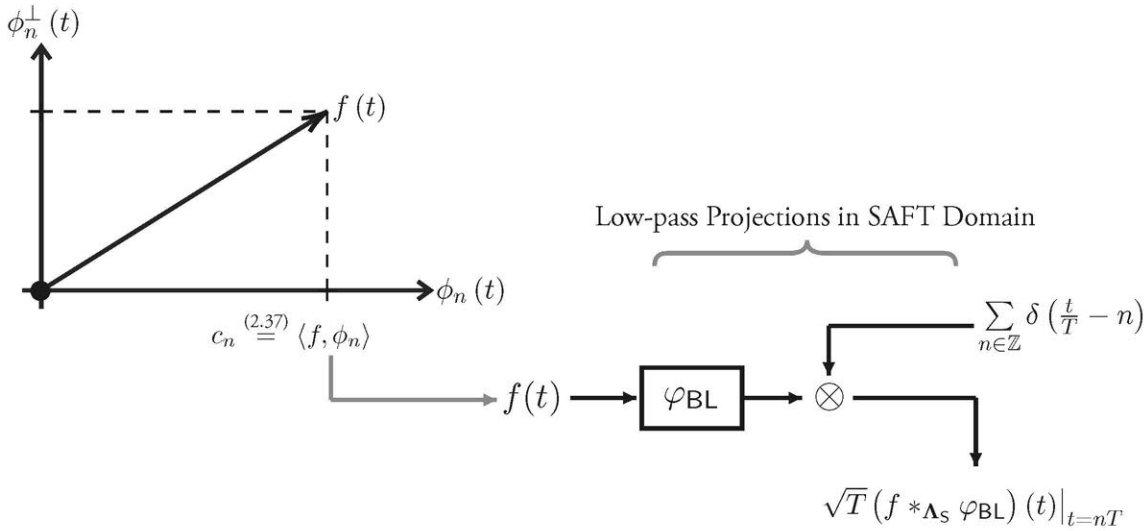

Figure 2-7: Defining low-pass projections in the SAFT sense.

As in the classical case, the coefficients $c_n = \langle f, \phi_n \rangle$ are equivalent to low-pass filtering in the SAFT domain followed by uniform sampling. To make this link clear, consider the kernel,

$$\varphi_{\mathsf{BL}}(t) = \frac{1}{\sqrt{T} K_{\mathbf{\Lambda}_{\mathsf{S}}}} m^*_{\mathbf{\Lambda}_{\mathsf{S}}}(t)\, e^{-\jmath \frac{p}{b} t} \mathrm{sinc}_T(-t)\,, \tag{2.36}$$

which is the amplitude scaled version of ϕ_0 and hence $\varphi_{\mathsf{BL}} \in \mathcal{B}^{\mathbf{\Lambda}_{\mathsf{S}}}_{\Omega_m}$.

$$\begin{aligned}
\langle f, \phi_n \rangle &= \int f(x) \phi^*_n(x)\, dx \\
&= \frac{1}{\sqrt{T}} \int f(x)\, e^{+\jmath \frac{p}{b}(x-nT)} m_{\mathbf{\Lambda}_{\mathsf{S}}}(x)\, m^*_{\mathbf{\Lambda}_{\mathsf{S}}}(nT)\, \mathrm{sinc}_T(x - nT)\, dx \\
&= \frac{m^*_{\mathbf{\Lambda}_{\mathsf{S}}}(nT)}{\sqrt{T}} \int \underbrace{f(x)\, m_{\mathbf{\Lambda}_{\mathsf{S}}}(x)}_{\overset{(2.25)}{=} \vec{f}(x)} \underbrace{e^{+\jmath \frac{p}{b}(x-nT)} \mathrm{sinc}_T(x - nT)}_{g(x-nT)}\, dx \\
&\overset{(a)}{=} \frac{m^*_{\mathbf{\Lambda}_{\mathsf{S}}}(nT)}{\sqrt{T}} \left(\vec{f} * \overline{g}\right)(t)\Big|_{t=nT, n\in\mathbb{Z}} \\
&\overset{(b)}{=} \sqrt{T}\left(f *_{\mathbf{\Lambda}_{\mathsf{S}}} \varphi_{\mathsf{BL}}\right)(t)\big|_{t=nT, n\in\mathbb{Z}}
\end{aligned}$$

where in (a) we have used $\overline{g}(t) = e^{-\jmath \frac{p}{b} t} \mathrm{sinc}_T(-t)$ and in (b) follows from (2.36). Hence, to conclude, we have,

$$\langle f, \phi_n \rangle = \sqrt{T}\left(f *_{\mathbf{\Lambda}_{\mathsf{S}}} \varphi_{\mathsf{BL}}\right)(t)\big|_{t=nT}, \quad \varphi_{\mathsf{BL}}(t) = K_{\mathbf{\Lambda}_{\mathsf{S}}} \phi_0(t)\,. \tag{2.37}$$

This equivalence is summarized in Fig. 2-7. Whenever $f \in \mathcal{B}^{\mathbf{\Lambda}_{\mathsf{S}}}_{\Omega_m}$ the convolution-product duality in

Theorem 2 implies that the expansion coefficients in (2.35) are indeed the pointwise samples. When $f \notin \mathcal{B}_{\Omega_m}^{\mathbf{\Lambda}_\mathsf{S}}$, the projection $c_n^\perp = \langle f, \phi_n^\perp \rangle$ is non-zero and corresponds to the out-of-band energy and $\phi_n^\perp(t)$ corresponds to the high-pass filter which is specified by,

$$\widehat{\phi}_{\mathbf{\Lambda}_\mathsf{S}}^\perp(\omega) = \sqrt{T} K_{\mathbf{\Lambda}_\mathsf{S}} \Phi_{\mathbf{\Lambda}_\mathsf{S}}^*(\omega) \underbrace{\left(1 - \mathbb{1}_{[-\Omega_m, \Omega_m]}(\omega)\right)}_{\text{High Pass Filter}} \qquad \Omega_m = \frac{\pi b}{T}.$$

in the SAFT domain.

Remark 1 (Generalization of Shannon's Sampling Theory)**.** *An immediate consequence of Theorem 4 is that it applies to all the transforms listed in Table 2.3.*

The sampling theorems for the Fresnel Transform [89], fractional Fourier transform [107, 114, 38] and the linear canonical transform [100, 101] are all now a straight–forward consequence of Theorem 4. For example, the sampling formula for the LCT can be easily obtained from our sampling theorem by setting $p = 0$ to yield

$$f(t) = e^{-\jmath \frac{at^2}{2b}} \sum_{n \in \mathbb{Z}} \vec{f}(nT) \operatorname{sinc}_T(t - nT).$$

2.4.2 Shift-Invariant Subspaces of the SAFT

In view of the sampling formula for the SAFT domain given by (2.31), we would like to approximate a function $f \in L_2$ using the shift-invariant model for SAFT domain,

$$\begin{aligned} f(t) &= e^{-\jmath \frac{a}{2b} t^2} \sum_{n \in \mathbb{Z}} \underbrace{\left(c_n e^{\jmath \frac{a}{2b} n^2}\right)}_{\overset{(2.25)}{=} \vec{c}_n} \underbrace{e^{\jmath \frac{a}{2b}(t-n)^2} \varphi(t-n)}_{\vec{\varphi}(t-n)} \\ &= e^{-\jmath \frac{a}{2b} t^2} \sum_{n \in \mathbb{Z}} \vec{c}_n \vec{\varphi}(t-n). \end{aligned} \tag{2.38}$$

This calls for a generalization of the definition of shift-invariant subspaces and the structure of the approximation space that follows is,

$$\mathsf{V}_{\mathsf{SIS}}^{\mathbf{\Lambda}_\mathsf{S}} = \operatorname{span}\left\{\vec{\varphi}(t-n)\right\}_{n \in \mathbb{Z}}. \tag{2.39}$$

Since (2.38) can be interpreted as a convolution[4] between a sequence $\{c_n\}$ and modulated kernel φ, we will develop two mathematical tools to study the SAFT domain equivalent of Riesz basis condition in (2.5). The first of the two tools is the semi-discrete convolution operator for the SAFT domain.

Definition 5 (Semi-discrete SAFT Convolution)**.** *Let $*$ denote the usual convolution operator. Given a square-summable sequence $\{c_n\}_{n \in \mathbb{Z}}$ and a function $g \in L_2$, the semi-discrete SAFT convolution operator denoted by $*'_{\mathbf{\Lambda}_\mathsf{S}}$, is defined as*

$$h(t) = \left(c *'_{\mathbf{\Lambda}_\mathsf{S}} g\right)(t) \overset{\text{def}}{=} K_{\mathbf{\Lambda}_\mathsf{S}} m_{\mathbf{\Lambda}_\mathsf{S}}^*(t) \sum_{n \in \mathbb{Z}} \vec{c}_n \vec{g}(t-n) \tag{2.40}$$

[4]In the sense of the SAFT discussed in Section 2.3.

where $\vec{g}(t) = m_{\mathbf{\Lambda}_{\mathsf{S}}}(t)\, g(t) \overset{(2.25)}{=} e^{\jmath \frac{at^2}{2b}} g(t)$*; the same applies to the function* c_n*.*

In dealing with sequence representation, we next define a version of the discrete time Fourier transform for the SAFT domain which we will refer to as the discrete time SAFT or DT-SAFT.

Definition 6 (Discrete Time SAFT (DT-SAFT))**.** *Let* $\{c_n\}_{n\in\mathbb{Z}}$ *be a square-summable sequence. We define the discrete time SAFT of this sequence as,*

$$\widehat{\mathrm{C}}_{\mathbf{\Lambda}_{\mathsf{S}}}(\omega) = \sum_{n\in\mathbb{Z}} c_n \kappa^*_{\mathbf{\Lambda}_{\mathsf{S}}}(n,\omega), \tag{2.41}$$

where the kernel $\kappa^*_{\mathbf{\Lambda}_{\mathsf{S}}}(n,\omega)$ *is defined in* (2.16)*.*

Based on the above definition of the DT-SAFT, we next use a result[5] which establishes that semi-discrete convolution between a sequence and a function amounts to multiplication in the SAFT domain. This lemma will later be used for studying Riesz basis condition for the $\vec{\varphi}$ to form an admissible generator of $\mathsf{V}^{\mathbf{\Lambda}_{\mathsf{S}}}_{\mathsf{SIS}}$ in (2.39).

Lemma 1 ([113])**.** *The SAFT of* h *defined in* (2.40) *is given by,*

$$\widehat{h}_{\mathbf{\Lambda}_{\mathsf{S}}}(\omega) = \Phi_{\mathbf{\Lambda}_{\mathsf{S}}}(\omega)\, \widehat{\mathrm{C}}_{\mathbf{\Lambda}_{\mathsf{S}}}(\omega)\, \widehat{\varphi}_{\mathbf{\Lambda}_{\mathsf{S}}}(\omega) \tag{2.42}$$

where, $\Phi_{\mathbf{\Lambda}_{\mathsf{S}}}(\omega) = e^{\jmath \frac{\omega}{b}(dp-bq)} e^{-\jmath \frac{d\omega^2}{2b}}$ *and* $\widehat{\mathrm{C}}_{\mathbf{\Lambda}_{\mathsf{S}}}(\omega)$ *is defined in* (2.41)*. Furthermore,* $\left|\widehat{\mathrm{C}}_{\mathbf{\Lambda}_{\mathsf{S}}}(\omega)\right|$ *is a periodic function with period* $2\pi b$*.*

By using this Lemma, In the next theorem we give a necessary and sufficient condition for a function $\varphi(t)$ to be a generator for a shift-invariant space associated with the SAFT domain. This result generalizes the result associated with the Fourier domain and can be extended to several unitary transforms listed in Table 2.3.

Theorem 5. *Let* $\varphi \in L_2$ *be a kernel of* $\mathsf{V}^{\mathbf{\Lambda}_{\mathsf{S}}}_{\mathsf{SIS}}$ *in* (2.39)*. Then,* $\vec{\varphi}(t)$ *is a Riesz basis for* $\mathsf{V}^{\mathbf{\Lambda}_{\mathsf{S}}}_{\mathsf{SIS}}$ *if and only if there are two positive constants such that,*

$$\eta_1^{\varphi} \leqslant \sum_{n\in\mathbb{Z}} \left|\widehat{\varphi}_{\mathbf{\Lambda}_{\mathsf{S}}}(\omega - 2\pi bn)\right|^2 \leqslant \eta_2^{\varphi}. \tag{2.43}$$

Proof. Any $f \in \mathsf{V}^{\mathbf{\Lambda}_{\mathsf{S}}}_{\mathsf{SIS}} \subset L_2$ can be written as $f(t) \overset{(2.38)}{=} \left(c *'_{\mathbf{\Lambda}_{\mathsf{S}}} \varphi\right)(t)$. By using the result of Lemma 1, we have,

$$\widehat{f}_{\mathbf{\Lambda}_{\mathsf{S}}}(\omega) = \Phi_{\mathbf{\Lambda}_{\mathsf{S}}}(\omega)\, \widehat{\mathrm{C}}_{\mathbf{\Lambda}_{\mathsf{S}}}(\omega)\, \widehat{\varphi}_{\mathbf{\Lambda}_{\mathsf{S}}}(\omega)$$

where $\widehat{\mathrm{C}}_{\mathbf{\Lambda}_{\mathsf{S}}}(\omega)$ is the DT–SAFT of the sequence $\{c_n\}_n$ given in (2.41). Since $\Phi_{\mathbf{\Lambda}_{\mathsf{S}}}(\omega) = e^{\jmath \frac{\omega}{b}(dp-bq)} e^{-\jmath \frac{d\omega^2}{2b}}$ (an all-pass transfer function), we have,

$$\left|\widehat{f}_{\mathbf{\Lambda}_{\mathsf{S}}}(\omega)\right|^2 = \left|\widehat{\mathrm{C}}_{\mathbf{\Lambda}_{\mathsf{S}}}(\omega)\, \widehat{\varphi}_{\mathbf{\Lambda}_{\mathsf{S}}}(\omega)\right|^2.$$

By integrating on both sides, we have,

$$\left\|\widehat{f}_{\mathbf{\Lambda}_{\mathsf{S}}}(\omega)\right\|^2_{L_2} = \int \left|\widehat{\mathrm{C}}_{\mathbf{\Lambda}_{\mathsf{S}}}(\omega)\, \widehat{\varphi}_{\mathbf{\Lambda}_{\mathsf{S}}}(\omega)\right|^2 d\omega.$$

[5] We proved this result in [113]. We will however omit the proof for brevity.

Now since $\left|\widehat{\mathrm{C}}_{\mathbf{\Lambda}_{\mathsf{S}}}(\omega)\right| = \left|\widehat{\mathrm{C}}_{\mathbf{\Lambda}_{\mathsf{S}}}(\omega + T_b)\right|, T_b = 2\pi b$ (according to Lemma 1), we can further simplify the above integral,

$$\begin{aligned}
\int_{-\infty}^{+\infty} \left|\widehat{\mathrm{C}}_{\mathbf{\Lambda}_{\mathsf{S}}}(\omega)\,\widehat{\varphi}_{\mathbf{\Lambda}_{\mathsf{S}}}(\omega)\right|^2 d\omega &= \int_{-\infty}^{+\infty} \left|\widehat{\mathrm{C}}_{\mathbf{\Lambda}_{\mathsf{S}}}(\omega)\right|^2 \left|\widehat{\varphi}_{\mathbf{\Lambda}_{\mathsf{S}}}(\omega)\right|^2 d\omega \\
&= \sum_{k\in\mathbb{Z}} \int_{kT_b}^{(k+1)T_b} \left|\widehat{\mathrm{C}}_{\mathbf{\Lambda}_{\mathsf{S}}}(\omega)\right|^2 \left|\widehat{\varphi}_{\mathbf{\Lambda}_{\mathsf{S}}}(\omega)\right|^2 d\omega \\
&= \sum_{k\in\mathbb{Z}} \int_{0}^{T_b} \left|\widehat{\mathrm{C}}_{\mathbf{\Lambda}_{\mathsf{S}}}(\omega + kT_b)\right|^2 \left|\widehat{\varphi}_{\mathbf{\Lambda}_{\mathsf{S}}}(\omega + kT_b)\right|^2 d\omega \\
&= \int_{0}^{T_b} \left|\widehat{\mathrm{C}}_{\mathbf{\Lambda}_{\mathsf{S}}}(\omega)\right|^2 \underbrace{\sum_{k\in\mathbb{Z}} \left|\widehat{\varphi}_{\mathbf{\Lambda}_{\mathsf{S}}}(\omega + kT_b)\right|^2}_{\text{Grammian}} d\omega \\
&= \int_{0}^{T_b} \left|\widehat{\mathrm{C}}_{\mathbf{\Lambda}_{\mathsf{S}}}(\omega)\right|^2 \mathsf{G}_{\varphi}^{\mathbf{\Lambda}_{\mathsf{S}}}(\omega)\, d\omega,
\end{aligned}$$

where $\mathsf{G}_{\varphi}^{\mathbf{\Lambda}_{\mathsf{S}}}(\omega)$, similar to (2.6), is the Grammian defined for the SAFT of φ, that is,

$$\mathsf{G}_{\varphi}^{\mathbf{\Lambda}_{\mathsf{S}}}(\omega) = \sum_{k\in\mathbb{Z}} \left|\widehat{\varphi}_{\mathbf{\Lambda}_{\mathsf{S}}}(\omega + kT_b)\right|^2.$$

Hence, we conclude that,

$$\left\|\widehat{f}_{\mathbf{\Lambda}_{\mathsf{S}}}(\omega)\right\|_{L_2}^2 = \int_{0}^{T_b} \left|\widehat{\mathrm{C}}_{\mathbf{\Lambda}_{\mathsf{S}}}(\omega)\right|^2 \mathsf{G}_{\varphi}^{\mathbf{\Lambda}_{\mathsf{S}}}(\omega)\, d\omega.$$

Furthermore, note that,

$$\begin{aligned}
\int_{0}^{T_b} \left|\widehat{\mathrm{C}}_{\mathbf{\Lambda}_{\mathsf{S}}}(\omega)\right|^2 d\omega &= \int_{0}^{T_b} \sum_{k,l\in\mathbb{Z}} c_k c_l^* \kappa_{\mathbf{\Lambda}_{\mathsf{S}}}^*(k,\omega)\, \kappa_{\mathbf{\Lambda}_{\mathsf{S}}}(l,\omega)\, d\omega \\
&= \frac{1}{K_{\mathbf{\Lambda}_{\mathsf{S}}}^2} \int_{0}^{T_b} \sum_{k,l\in\mathbb{Z}} c_k c_l^* \exp\left(\frac{\jmath}{2b}\left[a\left(k^2 - l^2\right) - 2\omega\left(k - l\right) + 2p\left(k - l\right)\right]\right) d\omega.
\end{aligned}$$

The above is further simplified based on the observation that $K_{\mathbf{\Lambda}_{\mathsf{S}}}^2 T_b = 1$ and,

$$\int_0^{T_b} e^{-\jmath \frac{\omega}{b}(k-l)} d\omega = b \int_0^{2\pi} e^{-\jmath \nu (k-l)} d\nu = T_b \delta_{k-l}.$$

And hence,

$$\left\| \widehat{\mathrm{C}}_{\mathbf{\Lambda}_{\mathsf{S}}}(\omega) \right\|_{L_2[0,T_b]}^2 = \int_0^{T_b} \left| \widehat{\mathrm{C}}_{\mathbf{\Lambda}_{\mathsf{S}}}(\omega) \right|^2 d\omega = \sum_{n \in \mathbb{Z}} |c_n|^2 = \|c\|_{\ell_2}^2 .$$

Since,

$$0 < \eta_1^{\varphi} \leqslant \mathsf{G}_{\varphi}^{\mathbf{\Lambda}_{\mathsf{S}}}(\omega) \leqslant \eta_2^{\varphi} < \infty$$

and $\|c\|_{\ell_2}^2 = ||\vec{c}||_{\ell_2}^2$, we have,

$$\eta_1^{\varphi} \left\| \widehat{\mathrm{C}}_{\mathbf{\Lambda}_{\mathsf{S}}}(\omega) \right\|_{L_2[0,T_b]}^2 = \eta_1^{\varphi} \|c\|_{\ell_2}^2 \leq \left\| \widehat{f}_{\mathbf{\Lambda}_{\mathsf{S}}}(\omega) \right\|_{L_2}^2 \leq \eta_2^{\varphi} \|c\|_{\ell_2}^2 = \eta_2^{\varphi} \left\| \widehat{\mathrm{C}}_{\mathbf{\Lambda}_{\mathsf{S}}}(\omega) \right\|_{L_2[0,T_b]}^2$$

which proves the result. ■

For the L_2 optimal approximation scheme listed in Table 2.1, the analysis kernel is simply the dual of φ, which in the context of the SAFT domain is given by,

$$\widehat{\widetilde{\varphi}}_{\mathbf{\Lambda}_{\mathsf{S}}}(\omega) = \frac{\widehat{\varphi}_{\mathbf{\Lambda}_{\mathsf{S}}}(\omega)}{\mathsf{G}_{\varphi}^{\mathbf{\Lambda}_{\mathsf{S}}}(\omega)} = \frac{\widehat{\varphi}_{\mathbf{\Lambda}_{\mathsf{S}}}(\omega)}{\sum_{k \in \mathbb{Z}} \left| \widehat{\varphi}_{\mathbf{\Lambda}_{\mathsf{S}}}(\omega + kT_b) \right|^2}.$$

2.4.2.1 Reconstruction with Arbitrary Basis Functions

In many cases of interest and for practical purposes, one is interested in the expansion of some function f (not necessarily SAFT–bandlimited) in terms of some basis functions,

$$\psi(t) = \frac{1}{K_{\mathbf{\Lambda}_{\mathsf{S}}}} m_{\mathbf{\Lambda}_{\mathsf{S}}}^*(t) e^{-\jmath \frac{p}{b} t} \nu(t) \tag{2.44}$$

which are parameterized by $\nu(t)$. For instance, when $\nu(t) = \mathrm{sinc}_T(t)$, we end up with the approximation space corresponding to SAFT bandlimited functions since $\psi \in \mathcal{B}_{\Omega_m}^{\mathbf{\Lambda}_{\mathsf{S}}}$ (cf. (2.36)). In view of Theorem 5, we assume that the basis functions generated by ψ form a Riesz basis. More precisely, we consider expansions of form,

$$f(t) = e^{-\jmath \frac{at^2}{2b}} \sum_{k \in \mathbb{Z}} \vec{c}_k e^{-\jmath p \frac{(t-k)}{b}} \nu(t-k) \Leftrightarrow \left(c *'_{\mathbf{\Lambda}_{\mathsf{S}}} \psi \right), \tag{2.45}$$

which generalizes the representation in (2.31). Indeed, for the case of sampling series in SAFT domain, we have $c_k = f(t)|_{t=k, k \in \mathbb{Z}}$ and $\nu = \mathrm{sinc}$. In order to compute the proxy of Shannon's samples, that is

the weights $\{c_k\}_k$ relative to the basis functions ν, we discretize (2.45) and obtain,

$$f(k) = c_k *'_{\mathbf{\Lambda}_\mathsf{S}} \left(\frac{1}{K_{\mathbf{\Lambda}_\mathsf{S}}} m^*_{\mathbf{\Lambda}_\mathsf{S}}(t)\, e^{-\jmath \frac{p}{b} t} \nu(t) \right) \equiv \left(c *'_{\mathbf{\Lambda}_\mathsf{S}} \psi \right)_k . \tag{2.46}$$

Now, assume that there exists a sequence $\{\vartheta_k\}$ such that,

$$c_k = \left(f(k) *_{\mathbf{\Lambda}_\mathsf{S}} \frac{1}{K_{\mathbf{\Lambda}_\mathsf{S}}} m^*_{\mathbf{\Lambda}_\mathsf{S}}(k)\, e^{-\jmath \frac{p}{b} k} \vartheta_k \right). \tag{2.47}$$

Back substituting weights c_k from (2.47) in (2.45) results in,

$$f(t) = e^{-\jmath \frac{at^2}{2b}} \sum_{k \in \mathbb{Z}} f(k)\, e^{\jmath \frac{ak^2}{2b}} e^{-\jmath p \frac{(t-k)}{b}} \underbrace{(\vartheta * \nu)(t-k)}_{\text{New Basis Functions}} . \tag{2.48}$$

Hence the representation of $f(t)$ in the basis $\nu(t)$ is equivalent to interpolation of samples of f with new basis functions

$$\psi_{\mathsf{new}}(t) = \frac{1}{K_{\mathbf{\Lambda}_\mathsf{S}}} m^*_{\mathbf{\Lambda}_\mathsf{S}}(t)\, e^{-\jmath \frac{p}{b} t} (\nu * \vartheta)(t), \tag{2.49}$$

and therefore,

$$f(t) \overset{(2.45)}{=} \left(c *'_{\mathbf{\Lambda}_\mathsf{S}} \psi \right)(t) \Leftrightarrow \left(f *'_{\mathbf{\Lambda}_\mathsf{S}} \psi_{\mathsf{new}} \right)(t). \tag{2.50}$$

The relation between the sequence ϑ and the basis functions ν is obtained by sampling (2.48),

$$f(t)|_{t=m} = e^{-\jmath \frac{am^2}{2b}} \sum_{k \in \mathbb{Z}} f(k)\, e^{\jmath \frac{ak^2}{2b}} e^{-\jmath p \frac{(m-k)}{b}} (\vartheta * \nu)(m-k),$$

which amounts to the interpolation condition, that is,

$$\begin{aligned} (\vartheta * \nu)(m-k) &= \delta_{m,k} \quad \text{(Interpolation Condition)} \\ &\Rightarrow f(t)|_{t=m} = e^{-\jmath \frac{am^2}{2b}} \sum_{k \in \mathbb{Z}} f(k)\, e^{\jmath \frac{ak^2}{2b}} e^{-\jmath p \frac{(m-k)}{b}} \delta(m-k) \\ &= f(m). \end{aligned} \tag{2.51}$$

The impulse response of the inverse discrete filter ϑ is related to the basis functions ν by a simple Fourier condition,

$$(\vartheta * \nu)(m) \overset{(2.51)}{=} \delta_m \Leftrightarrow \widehat{\vartheta}\left(e^{j\omega}\right) \sum_{k \in \mathbb{Z}} \widehat{\nu}(\omega + 2\pi k) = 1. \tag{2.52}$$

The existence of a stable sequence ϑ is guaranteed because we assume that ψ (and hence ν) generates Riesz basis and hence for all $\omega \in \mathbb{R}$, $\sum_{k \in \mathbb{Z}} \widehat{\nu}(\omega + 2\pi k) \neq 0$.

2.4.2.2 Application: Fractional Delay Filtering

Fractional Delay Filters (FDF) have found applications in a wide range of problems linked with signal processing [115, 116]. The FDF problem can be described as follows: Given samples of some finite–energy signal $f(t)$, how can one estimate the samples of τ–delayed version of f, that is $f^\tau(nT) \overset{\text{def}}{=}$

$f(t-\tau)|_{t=nT}, n \in \mathbb{Z}, \tau \in [0,T]$? For the shift–invariant subspace model linked with SAFT domain, we have,

$$f^{\tau}(t) \overset{(2.45)}{=} \left(c *'_{\mathbf{\Lambda}_{\mathsf{S}}} \psi\right)(t-\tau) \overset{(2.50)}{=} \left(f *'_{\mathbf{\Lambda}_{\mathsf{S}}} \psi_{\mathsf{new}}\right)(t-\tau). \tag{2.53}$$

Since the samples of f are readily available, one option is to set $\nu = \text{sinc}$ which leads to $c_k = f(kT), k \in \mathbb{Z}$. Hence, if f is a SAFT–bandlimited signal, re–samling τ–delayed version of interpolated samples of f leads to desired solution. That said, infinite support and slow–decay of the sinc filter make this solution impractical for cases when finite number of samples are available or f is not strictly bandlimited. For this purpose, we model f as a shift–invariant signal in SAFT–domain (2.45). Consequently, we propose to estimate,

$$f^{\tau}(mT) = \left(c *'_{\mathbf{\Lambda}_{\mathsf{S}}} \psi\right)(mT-\tau) \approx f(mT-\tau), m \in \mathbb{Z}.$$

This is a three step procedure:

1. Once we set $\nu(t)$ and hence, $\psi(t)$ in (2.44), we compute the inverse discrete filter ϑ.
2. Starting with samples $f(mT)$, we compute c_m using (2.47).
3. Then, we compute $\left(c *'_{\mathbf{\Lambda}_{\mathsf{S}}} \psi\right)(mT-\tau)$ to estimate delayed signal, $f(mT-\tau)$.

The sequence of operations is summarized as follows,

$$f(mT) \rightarrow \boxed{\vartheta} \overset{(2.47)}{\rightarrow} c \rightarrow \boxed{\psi(mT-\tau)} \overset{(2.53)}{\rightarrow} \left(c *'_{\mathbf{\Lambda}_{\mathsf{S}}} \psi\right)(mT-\tau).$$

Next, we present an example of FDF in SAFT domain.

Design Example: Power Cosine Filters for FDF in SAFT domain

Let $\psi(t)$ be defined in (2.44) and,

$$\nu(t) = \left(\frac{2}{3}\right)\cos^4\left(\frac{\pi t}{4}\right)\mathbb{1}_{[-2,+2]}(t). \tag{2.54}$$

Let $\widehat{\nu}(\omega)$ be for the Fourier Transform of $\nu(t)$. The SAFT of ψ is given by,

$$\widehat{\psi}_{\mathbf{\Lambda}_{\mathsf{S}}}(\omega) = e^{\jmath\left(\frac{d\omega^2}{2b} + \frac{bq-dp}{b}\omega\right)}\widehat{\nu}\left(\frac{\omega}{b}\right).$$

For a unique, stable representation of f in shift–invariant subspace, generated by ψ, to exist, the basis functions must form a Riesz basis for SAFT (see Theorem 5). To that end, we must show that,

$$\mathsf{G}_{\psi}^{\mathbf{\Lambda}_{\mathsf{S}}}(\omega) = \sum_{k\in\mathbb{Z}}\left|\widehat{\psi}_{\mathbf{\Lambda}_{\mathsf{S}}}(\omega + kT_b)\right|^2 = \sum_{k\in\mathbb{Z}}\widehat{\nu}\left(\frac{\omega}{b} + 2\pi k\right)$$

is bounded from below and above. This is indeed the case. Notice that $\widehat{\nu}(\omega) = \sum_{|k|\leqslant 2}\rho_k \,\text{sinc}(2\omega - k\pi)$ with $\rho_k = 4/(2+k)!\,(2-k)!$. Let $\mathsf{G}_{\nu}(\omega) = \sum_k |\widehat{\nu}(\omega + 2\pi k)|^2$. Since $\mathsf{G}_{\nu}(\omega)$ is an even symmetric, periodic function, to prove that $\mathsf{G}_{\nu} > 0$ (compare (2.5)), it suffices to show that $\forall\omega \in [0,\pi]$, $\eta_1^{\nu} =$

$\inf \mathsf{G}_\nu > 0$ or equivalently,

$$\eta_1^\nu = \inf_\omega \left(\left|\widehat{\nu}(\omega)\right|^2 + \left|\widehat{\nu}(\omega - 2\pi)\right|^2 \right), \quad \forall \omega \in [0, \pi].$$

Now since $\widehat{\nu}(\omega)$ is a monotonically decreasing function on $[0, \pi]$ and for $\omega = \pi$, $\operatorname{sinc}(2(\omega + 2\pi m) - k\pi) = 0, \forall m \in \mathbb{Z} - \{1\}$, we deduce that $\inf_\omega \mathsf{G}_\nu$ occurs at $\omega = \pi$. As a result, we have, $\eta_1^\nu = \mathsf{G}_\nu(\pi) = 2\left(\frac{(2!)^2}{4}\right)^2$. Using similar argument, we conclude that $\eta_2^\nu = \sup_\omega \mathsf{G}_\nu(\omega)$ is computed at $\omega = 0$ which results in $\eta_2^\nu = 1$.

In order to compute the inverse discrete filter ϑ, we use the previously developed property in (2.52). With $\nu(k) = \frac{1}{6}(\delta_{k-1} + 4\delta_k + \delta_{k+1}), k \in \mathbb{Z}$, the transfer function of the filter ϑ results in,

$$\vartheta(e^{\jmath\omega}) = \frac{6}{e^{+\jmath\omega} + 4 + e^{-\jmath\omega}}.$$

Similar to the cubic spline [116], the impulse response of such a filter is given by,

$$\vartheta_k = -\left(\frac{6\mu}{1-\mu^2}\right)\mu^{|k|}, k \in \mathbb{Z} \text{ with } \mu = \sqrt{3} - 2.$$

Unlike most prevalent approaches in literature which discuss finite impulse response filters or FIR filters (cf. [115]), note that our design is pivoted around infinite response filters or IIR filters.

Experimental Verification For experimental verification, we assume uniform samples $\{g_{\mathsf{sig}}(kT)\}_k$ of a truncated harmonic signal,

$$g_{\mathsf{sig}}(t) = \begin{cases} e^{-j\left(\frac{a_0}{2b_0}t^2 + \frac{p_0}{b_0}t\right)} \sum\limits_{m=1}^{m=3} \alpha_k \cos(2\pi\omega_k t) & t \in [-2.6180, 2.6120] \\ 0 & \text{otherwise} \end{cases}$$

with weight vector $\boldsymbol{\alpha} = [35, 18, 10]$ and frequency vector $\boldsymbol{\omega} = [0.77, 0.31, 0.25]$. This represents a common place practical example where finitely many samples of a signal are given (such as an audio signal). The SAFT parameter vector for the experiment is chosen to be $[a_0, b_0, c_0, d_0, p_0, q_0] = [7, 2, 0.6, 0.3143, 2.5, 1]$ which verifies $ad - bc = 1$ in (2.15) and the sampling rate is set to be $T = \pi b_0/60$. This sampling rate is not set according to the sampling theorem for the SAFT because g_{sig} is non-bandlimited. Instead, the sampling rate is to be considered in the spirit of approximation theory in that the truncated signal $g_{\mathsf{sig}} \in L_2(\mathbb{R})$ and we would like to approximate g_{sig} from its samples [26]. Note that as $T \to 0$, the approximation error between g_{sig} and its approximation shrinks to zero. For details on this topic, we refer to the work of Blu and Unser [26].

In the context of FDF, using (2.53), we estimate the samples $g^\tau(kT)$ of the function $g_{\mathsf{sig}}^\tau(t) = g_{\mathsf{sig}}(t - \tau)$ for $\tau = \frac{mT}{10}, m = 1, \ldots, 5$. We compare the shift–invariant model for SAFT domain with the traditional Shannon's sampling series for SAFT ($\nu = \operatorname{sinc}, \vartheta[k] = \delta_k$). As before, [38], the metric for

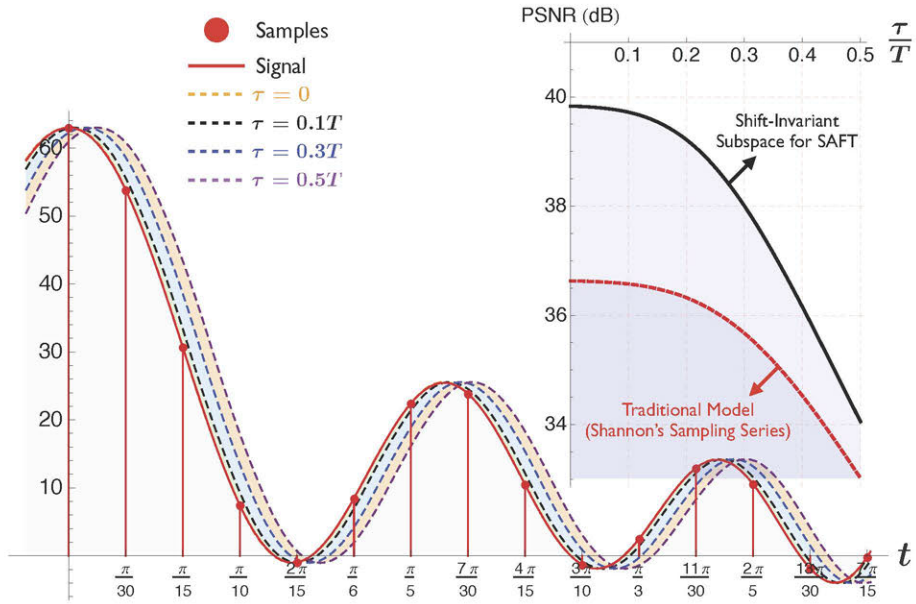

Figure 2-8: Fractional Delay Filtering of signals in SAFT domain using the shift–invariant signal model. We show equidistant samples of the real part of the signal $g_{\mathsf{sig}}(t)$. The signal is characterized by coefficient and frequency vectors $\boldsymbol{\alpha}$ and $\boldsymbol{\omega}$ taking values $[35, 18, 10]$ and $[0.77, 0.31, 0.25]$, respectively. The SAFT parameter vector is set to be $[a_0, b_0, c_0, d_0, p_0, q_0]$ taking values $[7, 2, 0.6, 0.3143, 2.5, 1]$, respectively. We use power cosine function $\nu(t) = (2/3)\cos^4(\pi t/4)\,\mathbb{1}_{[-2,+2]}(t)$ as the generator of shift–invariant subspace, we estimate the τ–delayed samples $g^{\tau}(kT)$, $k \in \mathbb{Z}$ and compare it with the analytical samples $g^{\tau}_{\mathsf{sig}}(kT)$, $k \in \mathbb{Z}$. Given $g_{\mathsf{sig}}(kT)$, the choice $\tau = 0$ amounts to reconstruction/interpolation the signal (see (2.45,2.50). For other choices of $\tau = 0.1T, 0.3T$ and $0.5T$, we reconstruct shifted versions of the $g_{\mathsf{sig}}(t)$. (Inset) Comparison between shift–invariant model for SAFT using ν in (2.54) and the classical Shannon's sampling method using $\nu = \text{sinc}$. The comparison metric is chosen to be peak–signal–to–noise ratio. The shift–invariant model for SAFT proves to be a better solution.

---

measuring distortion is set to be peak–signal–to–noise ratio (PSNR),

$$\mathsf{PSNR} = 10\log_{10}\left(\frac{\max\left\{|g^{\tau}_{\mathsf{sig}}(kT)|^2\right\}}{\mathsf{E}\left\{|g^{\tau}(kT) - g^{\tau}_{\mathsf{sig}}(kT)|^2\right\}}\right), \quad \text{(in dB)}$$

where $\mathsf{E}\{\cdot\}$ is the usual expectation operator. Figure 2-8 summarizes the result of experimentation. For several choices of $\tau \in [0, T]$, the shift–invariant model for SAFT outperforms the traditional method of filtering. This is because shift-invariant subspaces encompass a larger class of functions as compared to subspace of bandlimited functions. Now since g_{sig} is non-bandlimited in the SAFT domain, it still holds that $g_{\mathsf{sig}} \in L_2(\mathbb{R})$ in which case shift-invariant model for the SAFT domain is applicable.

2.5 Sampling and Super-resolution of Sparse Signals

In this section, we revisit the signal models described in Section 2.1.2. In view of the model in (2.8), we will be working with kernel or pulse φ. When φ is bandlimited in the Fourier domain, the super-resolution problem boils down to estimating $\{c_k\}$'s and $\{t_k\}$'s from measurements $y(nT), T > 0$ of,

$$y(t) = \sum_{k=0}^{K-1} c_k \varphi(t - t_k).$$

This problem can be restated as that of sampling spikes or sparse functions given a bandlimited sampling kernel, φ because of the equivalence in (2.9).

In the previous section, we discussed sampling theory of bandlimited signals in the SAFT domain. By considering sparse signals specified in (2.10) (instead of bandlimited functions), the measurements in context of the SAFT domain amount to,

$$s \to \boxed{\varphi} \to \underbrace{s *_{\mathbf{\Lambda}_{\mathsf{S}}} \varphi = y}_{\text{Pre-Filtering}} \to \underbrace{\otimes_{\delta_{nT}} \to y(nT)}_{\text{Sampling}}, \tag{2.55}$$

where $\otimes_{\delta_{nT}}$ denotes the sampling operation or modulation with a T-periodic impulse train. As shown in (2.35), whenever $s \in \mathcal{B}_{\Omega_m}^{\mathbf{\Lambda}_{\mathsf{S}}}$, samples $y(nT)$ uniquely characterize s provided that $T \leq \pi b/\Omega_m$.

Next, we turn our attention to the problem of recovering a sparse signal from low-pass projections defined in (2.37). In particular, we will discus three variations on this theme where low-pass projections are attributed to:

1) Arbitrary, bandlimited sampling kernels.

2) Smooth, time-limited sampling kernels.

3) Gabor functions associated with the SAFT domain.

The first two results rely on the architecture of (2.55). The last result generalizes the recent work of Aubel *et al.* [117] and can be extended to the case of phase-retrieval [118, 119, 120] and wavelets.

Since sparse signals are time-limited, their periodic extension allows for a Fourier series representation. That said, the basis functions of the SAFT kernel are aperiodic. As a result, before discussing the recovery of sparse signals, we introduce mathematical tools that allow for Fourier series-like representation of time-limited signals.

2.5.0.1 Special Affine Fourier Series (SAFS)

It is well known that the family of functions $\left\{e^{\jmath k\omega_0 t}\right\}_{k\in\mathbb{Z}}$, with fundamental harmonic $\omega_0 = 2\pi/T_h$, constitutes an orthonormal basis of $L_2([-\pi/T_h, \pi/T_h])$. These basis functions are used for representing T_h-periodic functions. Let $\mathsf{V}_{\mathsf{FS}} = \text{span}\left\{e^{\jmath k\omega_0 t}\right\}_{k\in\mathbb{Z}}$. Due to the orthonormality and completeness properties, it follows that, for every $f(t) = f(t + T_h)$,

$$\mathscr{P}_{\mathsf{V}_{\mathsf{FS}}} f = \sum_{n\in\mathbb{Z}} c_n e^{\jmath k\omega_0 t}, \quad c_n = \left\langle f, e^{\jmath k\omega_0 t} \right\rangle. \tag{2.56}$$

Inspired by the Fourier series representation, here, we develop a parallel for the SAFT domain which is useful for the task of representing time-limited signals including sparse signals.

In order to determine the basis functions associated with the Special Affine Fourier Series or the SAFS, we first identify the candidate functions and then enforce the orthonormality property. Note that a spike at frequency $\omega = n\omega_0$ in the SAFT domain results in the time domain function

$$\left\langle \delta\left(\omega - n\omega_0\right), \kappa_{\mathbf{\Lambda}_{\mathsf{S}}^{\mathsf{inv}}}\left(\omega, t\right)\right\rangle \overset{(2.20)}{=} \kappa^*_{\mathbf{\Lambda}_{\mathsf{S}}^{\mathsf{inv}}}\left(n\omega_0, t\right). \tag{2.57}$$

With the above as our prototype basis function, we would like to represent a time-limited signal $s\left(t\right),\ t \in [0, T_h)$ as

$$s\left(t\right) = \sum_{n\in\mathbb{Z}} \widehat{s}_{\mathbf{\Lambda}_{\mathsf{S}}}\left[n\right] \kappa^*_{\mathbf{\Lambda}_{\mathsf{S}}^{\mathsf{inv}}}\left(n\omega_0, t\right), \tag{2.58}$$

which mimics (2.56), and where the SAFS coefficients are

$$\widehat{s}_{\mathbf{\Lambda}_{\mathsf{S}}}\left[n\right] = \left\langle s, \kappa_{\mathbf{\Lambda}_{\mathsf{S}}}\left(\cdot, n\omega_0\right)\right\rangle_{[0,T_h]}. \tag{2.59}$$

To enable a representation in the form (2.59), we enforce orthogonality on the candidate basis functions,

$$\left\langle \kappa_{\mathbf{\Lambda}_{\mathsf{S}}}\left(t, n\omega_0\right), \kappa_{\mathbf{\Lambda}_{\mathsf{S}}^{\mathsf{inv}}}\left(k\omega_0, t\right)\right\rangle_{[0,T_h]} \equiv \underbrace{I_{\omega_0} = w_0\delta_{n-k}}_{\text{Orthogonality}},$$

for an appropriate w_0. Computing the inner-product explicitly yields,

$$\begin{aligned} I_{\omega_0} &= \left|K_{\mathbf{\Lambda}_{\mathsf{S}}}\right|^2 \mu \int_0^{T_h} e^{\jmath\frac{\omega_0(k-n)}{b}t} dt \\ &= \left|K_{\mathbf{\Lambda}_{\mathsf{S}}}\right|^2 \begin{cases} T_h & k = n, \\ -\mu\frac{\jmath b}{(k-n)\omega_0}\left(1 - e^{-\jmath\frac{\omega_0 T_h}{b}(k-n)}\right) & k \neq n, \end{cases} \end{aligned}$$

where for brevity we denoted,

$$\mu = \left(e^{-\jmath\frac{\omega_0(k-n)}{2b}(2bq + d\omega_0(k+n) - 2dp)}\right).$$

Therefore, the orthogonality property will hold, if,

$$1 - e^{-\jmath\frac{\omega_0 T_h}{b}(k-n)} = 0 \Leftrightarrow \omega_0 = 2\pi b/T_h.$$

In the above, $w_0 = T_h K^2_{\mathbf{\Lambda}_{\mathsf{S}}}$ is the scaling constant which orthonormalizes the basis functions and we assume that $1/\sqrt{w_0}$ is absorbed into the definition of the SAFS basis functions, $\{\kappa^*_{\mathbf{\Lambda}_{\mathsf{S}}^{\mathsf{inv}}}\left(n\omega_0, t\right)\}_{n\in\mathbb{Z}}$. We consolidate our result in the following definition.

Definition 7 (Special Affine Fourier Series)**.** *Let s be a time-limited signal supported on the interval $[0, T_h)$. The Special Affine Fourier Series representation of s is defined in (2.58) and (2.59) where $\omega_0 = 2\pi b/T_h$.*

In case of $\mathbf{\Lambda}_{\mathsf{S}} = \mathbf{\Lambda}_{\mathsf{FT}}$, the SAFS reduces to the Fourier series. To see this, let us substitute the

parameters of $\mathbf{\Lambda}_{\mathsf{FT}}$, from Table 2.3, in $\mathbf{\Lambda}_{\mathsf{S}}$. Then, we have, $\kappa^*_{\mathbf{\Lambda}_{\mathsf{S}}^{\mathsf{inv}}}(n\omega_0, t) = e^{\jmath n\omega_0 t}$ which are indeed the basis functions for the Fourier Series (upto a constant, $K_{\mathbf{\Lambda}_{\mathsf{S}}}$). Similarly, with $\mathbf{\Lambda}_{\mathsf{S}} = \mathbf{\Lambda}_\theta$, the SAFS reduces to Fractional Fourier series (cf. (10) in [121]).

Based on the definition of the SAFS for time-limited functions, we now develop an alternative representation of sparse signals defined in (2.10) that are supported on the interval

$$T_h = \left|\max\{t_k\}_{k=0}^{K-1} - \min\{t_k\}_{k=0}^{K-1}\right|.$$

For periodic signals, T_h can be interpreted as the length of the circle shown in Fig. 2-2.

With T_h above and $\epsilon > 0$, we compute the SAFS coefficients,

$$\begin{aligned}\widehat{s}_{\mathbf{\Lambda}_{\mathsf{S}}}[n] &\overset{(2.59)}{=} \left\langle s, \kappa_{\mathbf{\Lambda}_{\mathsf{S}}}(t, n\omega_0)\right\rangle = \int_{\epsilon}^{\epsilon+T_h} s(t)\,\kappa^*_{\mathbf{\Lambda}_{\mathsf{S}}}(t, n\omega_0)\,dt \\ &= \sum_{k=0}^{K-1} c_k \kappa^*_{\mathbf{\Lambda}_{\mathsf{S}}}(t_k, n\omega_0), \quad \omega_0 = 2\pi b/T_h. \end{aligned} \tag{2.60}$$

From (2.58) we obtain the SAFT series,

$$s(t) \overset{(2.58)}{=} \sum_{n\in\mathbb{Z}} \sum_{k=0}^{K-1} c_k \kappa^*_{\mathbf{\Lambda}_{\mathsf{S}}}(t_k, n\omega_0) \kappa^*_{\mathbf{\Lambda}_{\mathsf{S}}^{\mathsf{inv}}}(n\omega_0, t). \tag{2.61}$$

Using (2.16) we have,

$$\kappa^*_{\mathbf{\Lambda}_{\mathsf{S}}}(t_k, n\omega_0)\,\kappa^*_{\mathbf{\Lambda}_{\mathsf{S}}^{\mathsf{inv}}}(n\omega_0, t) \overset{(2.16)}{=} e^{-\jmath(\mathsf{Q}(t)-\mathsf{Q}(t_k))} e^{\jmath\frac{\omega_0 n}{b}(t-t_k)} \tag{2.62}$$

where $\mathsf{Q}(t)$ is a quadratic polynomial,

$$\mathsf{Q}(t) \overset{\text{def}}{=} \frac{at^2 + 2pt}{2b}. \tag{2.63}$$

Substituting into (2.61) leads to,

$$\begin{aligned} s(t) &= e^{-\jmath\mathsf{Q}(t)} \sum_{n\in\mathbb{Z}} \sum_{k=0}^{K-1} \underbrace{c_k e^{\jmath\mathsf{Q}(t_k)}}_{c'_k} \underbrace{e^{-\jmath\frac{\omega_0 n t_k}{b}}}_{u_k^n} e^{\jmath\frac{\omega_0 n t}{b}} \\ &= e^{-\jmath\mathsf{Q}(t)} \sum_{n\in\mathbb{Z}} \widehat{h}[n]\, e^{\jmath\frac{\omega_0 n t}{b}} = e^{-\jmath\mathsf{Q}(t)} h(t), \end{aligned} \tag{2.64}$$

where $\widehat{h}[n]$ is a sum of complex exponentials:

$$\widehat{h}[n] = \sum_{k=0}^{K-1} c_k e^{\jmath\mathsf{Q}(t_k)} e^{-\jmath\frac{\omega_0 n}{b} t_k} = \sum_{k=0}^{K-1} c'_k u_k^n. \tag{2.65}$$

By arranging (2.64), we may rewrite,

$$\underbrace{s(t)\, e^{\jmath \mathsf{Q}(t)}}_{h(t)} = \underbrace{\sum_{n\in\mathbb{Z}} \widehat{h}[n]\, e^{\jmath \frac{2\pi}{T} nt}}_{\text{Fourier Series}} \equiv h(t), \tag{2.66}$$

with $\widehat{h}[n]$ given in (2.65). We have thus shown that a modulated version of the sparse signal $s(t)$ is equivalent to another sparse signal,

$$h(t) = \sum_{n\in\mathbb{Z}} \sum_{k=0}^{K-1} c'_k \delta\left(t - t'_k - nT\right) \tag{2.67}$$

where unknowns $\{c'_k, t'_k\}_{k=0}^{K-1}$ of $h(t)$ are related to the unknowns of the sparse signal we seek to recover

$$c'_k = c_k e^{\jmath \mathsf{Q}(t_k)} \quad \text{and} \quad t'_k = t_k.$$

Due to this link between $s(t)$ in (2.10) and $h(t)$ in (2.67), their Fourier series coefficients are also related to one another as in (2.66). We formally state this result as a theorem.

Theorem 6 (SAFS of Sparse Signals)**.** *Let $s(t)$ be the sparse signal defined in (2.10). Then, the Special Affine Fourier Series representation of $s(t)$ is given by,*

$$s(t) = e^{-\jmath \mathsf{Q}(t)} \sum_{n\in\mathbb{Z}} \widehat{h}[n]\, e^{\jmath \frac{\omega_0 nt}{b}},$$

where $\widehat{h}[n] = \sum_{k=0}^{K-1} c_k e^{\jmath \mathsf{Q}(t_k)} e^{-\jmath \frac{\omega_0 n}{b} t_k}$ *and* $\mathsf{Q}(t)$ *is defined in* (2.63).

This re-parameterization of the sparse signal $s(t)$ in form of the Fourier series coefficients of $h(t)$ is key to studying sparse sampling theorems in the SAFT domain.

2.5.0.2 Sparse Signals and Arbitrary Bandlimited Kernels

Consider the setting in which the sampling kernel $\varphi = \varphi_{\mathsf{BL}}(t)$ (2.36). In this case, the low-pass filtered measurements are given by $y(t) = \left(s *_{\mathbf{\Lambda}_{\mathsf{S}}} \varphi_{\mathsf{BL}}\right)(t)$. The measurements can be expressed in terms of low-pass, orthogonal projections (2.37) as given in the following proposition.

Proposition 1 (Bandlimited Case)**.** *Let s be the sparse signal defined in (2.10) and the bandlimited sampling kernel $\varphi_{\mathsf{BL}}(t)$ be defined in (2.36). Then, the measurements simplify to*

$$y(t) = \sqrt{T} e^{-\jmath \mathsf{Q}(t)} \sum_{|m|\leqslant M} \widehat{h}[m]\, e^{\jmath \frac{\omega_0 mt}{b}}, \quad M = \left\lfloor \frac{T_h}{2T} \right\rfloor, \tag{2.68}$$

where Q *is defined in (2.63) and* $\widehat{h}[n]$ *is defined in (2.65).*

Proof. Here, we will prove a more general result. Let ψ be an arbitrary function with a well defined Fourier transform and let $\varphi(t) = \left(TK^2_{\mathbf{\Lambda}_{\mathsf{S}}}\right)^{-1/2} m^*_{\mathbf{\Lambda}_{\mathsf{S}}}(t)\, e^{-\jmath \frac{p}{b} t} \psi(t)$. By using the definition of the

SAFT-convolution (2.26), we have

$$\begin{aligned} y(t) &= K_{\mathbf{\Lambda}_{\mathsf{S}}} m^*_{\mathbf{\Lambda}_{\mathsf{S}}}(t) \left(\vec{s} * \vec{\varphi}\right)(t) \\ &\overset{(a)}{=} \frac{1}{\sqrt{T}} m^*_{\mathbf{\Lambda}_{\mathsf{S}}}(t) \left(e^{\jmath \frac{p}{b} t} h(t) * e^{\jmath \frac{p}{b} t} \psi(t)\right) \\ &\overset{(b)}{=} \frac{1}{\sqrt{T}} m^*_{\mathbf{\Lambda}_{\mathsf{S}}}(t) e^{\jmath \frac{p}{b} t} \left(h(t) * \psi(t)\right) \\ &\overset{(c)}{=} \frac{1}{\sqrt{T}} e^{-\jmath \mathsf{Q}(t)} \sum_{m \in \mathbb{Z}} \widehat{h}[m] \widehat{\psi}\left(\frac{\omega_0 m}{b}\right) e^{\jmath \frac{\omega_0 m}{b} t}, \end{aligned} \tag{2.69}$$

where (a) is due to (2.26), (b) is due to invariance of complex exponentials under convolution operation (eigen-function property) and (c) is because h is a T_h-periodic function (2.67). Here, $y(t)$ is completely characterized by the Fourier series coefficients of h and ψ. With $\psi(t) = \mathrm{sinc}_T(t)$, we have,

$$\widehat{\psi}(\omega) = T \mathbb{1}_{\left[-\frac{\pi}{T}, \frac{\pi}{T}\right]}(\omega)$$

where $\omega = \omega_0 m/b$ and since $\widehat{\psi}(m\omega_0 \Delta/b) = 0, m > T_h/2T$, (2.68) holds. ■

Next, we state the main result linked with sampling of sparse signals in the SAFT domain.

Theorem 7 (Sparse Sampling with Bandlimited Kernel)**.** *Let $s(t)$ be a continuous–time, sparse signal (2.10) and let φ_{LP} be the low–pass filter defined in (2.36) with $T = \pi b/\Omega_m$. Suppose that we observe low–pass filtered samples $y(nT) = \left(s *_{\mathbf{\Lambda}_{\mathsf{S}}} \varphi_{\mathsf{LP}}\right)(nT), n = 0, \ldots, N-1$. Provided that K and $\mathbf{\Lambda}_{\mathsf{S}}$ are known and $N \geq T_h/T + 1$, the low-pass filtered samples $y(nT)$, $n = 0, \ldots, N-1$ are a sufficient characterization of the sparse signal $s(t)$ in (2.10).*

Proof. To show that this statement holds, we start with the observation that modulating the low-pass samples results in the Fourier series of the sparse signal in (2.67). More precisely,

$$g_n = \frac{y(nT)}{\sqrt{T}} e^{\jmath \mathsf{Q}(nT)} \overset{(2.68)}{=} \sum_{|m| \leqslant f_c = M} \widehat{h}[m] e^{\jmath \frac{\omega_0 m}{b} nT}. \tag{2.70}$$

Also, from (2.65), the Fourier coefficients $\widehat{h}[m]$ are a linear combination of complex exponentials. In vector-matrix notation, we have, $\mathbf{g} = \mathbf{V}\widehat{\mathbf{h}}$,

$$\begin{bmatrix} g_0 \\ \vdots \\ g_{N-1} \end{bmatrix} = \begin{bmatrix} 1 & \cdots & 1 & \cdots & 1 \\ e^{-\jmath \frac{2\pi}{T} f_c} & \ddots & 1 & \ddots & e^{+\jmath \frac{2\pi}{T} f_c} \\ \vdots & \ddots & 1 & \ddots & \vdots \\ e^{-\jmath \frac{2\pi}{T} f_c (N-1)} & \cdots & 1 & \cdots & e^{+\jmath \frac{2\pi}{T} f_c (N-1)} \end{bmatrix} \begin{bmatrix} \hat{h}[-f_c] \\ \vdots \\ \hat{h}[f_c] \end{bmatrix} \equiv \mathbf{g} = \mathbf{V}\widehat{\mathbf{h}} \tag{2.71}$$

From (2.70), we estimate $\widehat{h}[m]$ using the inverse Fourier transform, that is, $\widehat{\mathbf{h}} = \mathbf{V}^+ \mathbf{g}$ where $(\cdot)^+$ denotes the matrix pseudo-inverse. A unique solution to this system of equations exists provided that

$$N \geq 2f_c + 1, \quad f_c = \left\lfloor \frac{T_h}{2T} \right\rfloor. \tag{C67}$$

Having computed $\widehat{\mathbf{h}}$, we are now left with the task of estimating $\{c'_k, t'_k\}_{k=0}^{K-1}$ associated with the sparse signal in (2.67). In spectral estimation theory [67], it is well known that the sum of complex exponentials in (2.65) admits an autoregressive form which allows us to write,

$$\widehat{h}[m] + \sum_{k=1}^{K} r[k]\,\widehat{h}[m-k] = 0. \tag{2.72}$$

The K–tap filter defined by $\{r[k]\}$ is known as the *annhilating filter* [67, 69] which is used to estimate the non-linear unknowns $\{t'_k\}_{k=0}^{K-1}$ provided that $\{t'_k\}_{k=0}^{K-1}$ are distinct and $\widehat{h}[m], m \in [-K, K]$ is known, thus implying,

$$f_c \geqslant K. \tag{C68}$$

By combining conditions (C1) and (C2), we finally obtain,

$$N \geqslant T_h/T + 1. \tag{2.73}$$

Whenever (2.73) holds, a recovery procedure from the FRI literature [69, 70] can be directly applied. To this end, (2.73) guarantees that we can estimate the filter r in (2.72) which is then used for constructing a polynomial of degree K, $\mathsf{R}(z) = \sum_{k=0}^{K} r[k]\, z^{-k}$. The K–roots of this polynomial, that is, $u_k = e^{-\jmath\omega_0 t_k/b}$, encode the information about $\{t_k\}_{k=0}^{K-1}$. Let $\widetilde{t}_k$ denote the estimate of t_k. Then, by factorizing $\mathsf{R}(z)$, we estimate the roots $\widetilde{u}_k$ which is used to estimate $\widetilde{t}_k = (b/\omega_0)\,\angle\widetilde{u}_k$. To determine $\{c_k\}_{k=0}^{K-1}$ in (2.10), we first construct the quadratic polynomial $\mathsf{Q}\left(\widetilde{t}_k\right) = \left(a\widetilde{t}_k^2 + 2p\widetilde{t}_k\right)/2b$. There on, we estimate $\widetilde{c}_k$ by solving the least–squares problem since c_k's in (2.65) linearly depend on known quantities. ■

2.5.0.3 Generalization to Arbitrary Bandlimited Sampling Kernels

For the same recovery condition (cf. (2.73)), our result straight-forwardly generalizes to any arbitrary, bandlimited sampling kernel of the form,

$$\psi \in \mathcal{B}_{\Omega_m}^{\mathbf{\Lambda}_{\mathsf{FT}}},\ \varphi_{\mathsf{BL}}(t) = \frac{1}{\sqrt{T}K_b} m^*_{\mathbf{\Lambda}_{\mathsf{S}}}(t)\, e^{-\jmath\frac{p}{b}t}\psi\left(\frac{t}{T}\right) \tag{2.74}$$

provided that $\psi \in \mathcal{B}_{\Omega_m}^{\mathbf{\Lambda}_{\mathsf{FT}}}$ and the Fourier transform of ψ does not vanish in the interval $[-\Omega_m, \Omega_m]$. This is a consequence of a generalized version of Proposition 1. Arbitrary bandlimited kernels result in a version of (2.70),

$$g_n = \sum_{|m|\leqslant f_c} \widehat{h}[m]\,\widehat{\psi}\left(\frac{\omega_0 m T}{b}\right) e^{\jmath\frac{\omega_0 m}{b}nT} \Leftrightarrow \mathbf{g} = \mathbf{V}\mathbf{D}\widehat{\mathbf{h}},$$

where $\mathbf{D}$ is a diagonal matrix composed of Fourier series coefficients of ψ, that is, $\{\widehat{\psi}(T\omega_0 m/b)\}_{|m|\leqslant f_c}$. Given ψ, $\widehat{\mathbf{h}}$ can be "deconvolved" using $\widehat{\mathbf{h}} = \mathbf{D}^{-1}\mathbf{V}^{+}\mathbf{g}$ (cf. Section 2.1.2).

2.5.0.4 Special cases of the SAFT domain result

By appropriately selecting the parameter matrix $\mathbf{\Lambda}_{\mathsf{S}}$, we can directly derive results for any of the operations described in Table 2.3. Next, we revisit some examples in the literature which are special cases of the SAFT

domain.

Sparse or FRI Sampling in Fourier Domain

The FRI sampling result which was derived in context of Fourier domain [69] is a special case of Theorem 7. By setting,

$$\mathbf{\Lambda}_{\mathsf{S}} = \left[\begin{array}{cc|c} 0 & 1 & 0 \\ -1 & 0 & 0 \end{array}\right] \equiv \mathbf{\Lambda}_{\mathsf{FT}},$$

we note that $\mathsf{Q}(t) = 0$ and $s(t) = h(t)$ in (2.66). In this case the sampling rate is $T = \pi/\Omega_m$ and provided that $N \geq T_h/T + 1$, the sparse signal can be recovered from low-pass projections in the Fourier domain.

Sparse Sampling in Fractional Fourier Domain

Sparse sampling in context of the fractional Fourier domain was discussed in [114]. As above, this is a special case of Theorem 7. By setting,

$$\mathbf{\Lambda}_{\mathsf{S}} = \left[\begin{array}{cc|c} \cos\theta & \sin\theta & 0 \\ -\sin\theta & \cos\theta & 0 \end{array}\right] \equiv \mathbf{\Lambda}_{\boldsymbol{\theta}},$$

we note that $\mathsf{Q}(t) = \frac{t^2}{2}\cot\theta$ and as shown in [114], $s(t)$ is given by,

$$s(t) \overset{(2.66)}{=} e^{-\jmath\frac{t^2}{2}\cot\theta} \sum_{n\in\mathbb{Z}} \sum_{k=0}^{K-1} c'_k u_k^n e^{\jmath\frac{2\pi}{T_h}nt},$$

where $c'_k = c_k e^{\jmath\frac{t_k^2}{2}\cot\theta}$. In this case the sampling rate is $T = \pi\sin\theta/\Omega_m$ and provided that $N \geq T_h/T + 1$, the sparse signal can be recovered from low-pass projections in the Fractional Fourier domain.

Link with Super-resolution via Convex Programming

Our work is directly related to recent results on super-resolution based on convex-programming [60]. Let,

$$\|s\|_{\mathsf{TV}} = \sum_{k=0}^{K-1} |c_k| \tag{2.75}$$

denote the TV–norm of the sparse signal s (2.10). Also note that, $\|s\|_{\mathsf{TV}} = \|h\|_{\mathsf{TV}}$. Given sampled measurements $\{y(nT)\}_{n=0}^{N-1}$ (2.68) we first obtain $\{g_n\}_{n=0}^{N-1}$ from (2.70). We then estimate $\widehat{\mathbf{h}} = \mathbf{V}^{+}\mathbf{g}$. As a result, we may recast our sparse recovery problem as a minimization problem of the form,

$$\min_h \|h\|_{\mathsf{TV}} \text{ with } \left\{\widehat{h}[m] = \int_0^{T_h} h(t)\, e^{\jmath\omega_0 mt} dt\right\}_{|m|\leqslant f_c}. \tag{2.76}$$

Theorem 7 assumes knowledge of K—a proxy for *sparsity* or the *rate of innovation*. Accordingly, the sampling criterion (2.73) is based on a counting principle: the kernel bandwidth should be at least equal to the number of unknowns (cf. (C2)). With K known, in the absence of perturbations, the un-

knowns $\{t_k\}_{k=0}^{K-1}$ can be arbitrarily close. In contrast, (2.76) avoids any assumptions on K but relies on a minimum separation principle [60].

Let $\mathbb{T}_K = \{t_k\}_{k=0}^{K-1}$ denote the support of s and let us define the minimum separation between any two entries of $\mathbb{T}_K$ by,

$$\delta_{\min}(\mathbb{T}_K) \stackrel{\text{def}}{=} \inf_{\mathbb{T}_K : t_k \neq t_\ell} |t_k - t_\ell| .$$

We can now repurpose our generalized result in the context of super-resolution [60]. The formal result is as follows.

Theorem 8 (Exact Recovery based on Minimum Separation Principle)**.** *Let $\mathbb{T}_K = \{t_k\}_{k=0}^{K-1}$ be the support set of the sparse signal s and $f_c = \lfloor T_h/2T \rfloor$ be the cut-off frequency of the sampling kernel defined in (2.36). If $\delta_{min}(\mathbb{T}_K) f_c \geqslant 2$ then h (and hence s) is a unique solution to (2.76).*

The proof of this theorem follows from [60]. Even though our discussion is quite general (due to Table 2.3), extension to [60] comes at no extra cost—the computational complexity and the exact recovery principle remain the same. A similar parallel can be drawn with the work on atomic norms [122].

2.5.0.5 Sparse Signals and Smooth Time-limited Kernels

In the previous section, we focused on sampling kernels which were bandlimited (2.74). However, in applications, the sampling kernels may be pulses or echoes that are time-limited [64, 65, 66, 73, 78, 21]. In this case, we can model such a sampling kernel as a SAFS (2.58),

$$\begin{aligned}\psi(t) &\stackrel{(2.58)}{=} \sum_{n\in\mathbb{Z}} \widehat{\psi}_{\mathbf{\Lambda}_\mathsf{S}}[n]\, \kappa^*_{\mathbf{\Lambda}_\mathsf{S}^{\mathsf{inv}}}(n\omega_0, t), \quad \psi(t) = 0, t \notin [0, T_h] \\ &= \sum_{n\in\mathbb{Z}} \widehat{\psi}_{\mathbf{\Lambda}_\mathsf{S}}[n]\, e^{-\jmath \mathsf{Q}(t)} \Phi_{\mathbf{\Lambda}_\mathsf{S}}(n\omega_0)\, e^{\jmath \frac{n\omega_0 t}{b}}, \end{aligned} \tag{2.77}$$

where $\Phi_{\mathbf{\Lambda}_\mathsf{S}}(\omega) = e^{\jmath \frac{\omega}{b}(dp-bq)} e^{-\jmath \frac{d\omega^2}{2b}}$ and $\mathsf{Q}(t)$ is defined in (2.63). As usual, the filtered spikes are given by $y(t) = \left(s *_{\mathbf{\Lambda}_\mathsf{S}} \psi\right)(t)$. A further simplification of the measurements is due to the following proposition which deals with time-limited kernels.

Proposition 2 (Time-limited Case)**.** *Let s be the sparse signal defined in (2.10) and the time-limited sampling kernel $\psi(t)$ be defined in (2.77). Then, the filtered spikes simplify to*

$$y(t) = e^{-\jmath \mathsf{Q}(\mathsf{t})} \sum_{m\in\mathbb{Z}} \widehat{h}[m] \widehat{\psi}_{\mathbf{\Lambda}_\mathsf{S}}[m]\, \Phi_{\mathbf{\Lambda}_\mathsf{S}}(m\omega_0)\, e^{\jmath \frac{\omega_0 m}{b} t}, \tag{2.78}$$

where Q is defined in (2.63) and $\widehat{h}$ is defined in (2.65).

Proof. We will start by developing $\vec{s} * \vec{\psi}$ which appears in the definition of the convolution operator (2.26). Note that,

$$\begin{aligned}\vec{s}(t) &\stackrel{(2.66)}{=} e^{-\jmath \frac{p}{b} t} h(t), \quad \text{and} \\ \vec{\psi}(t) &\stackrel{(2.77)}{=} e^{-\jmath \frac{p}{b} t} \sum_{n\in\mathbb{Z}} \widehat{\psi}_{\mathbf{\Lambda}_\mathsf{S}}[n]\, \Phi_{\mathbf{\Lambda}_\mathsf{S}}(n\omega_0) e^{\jmath \frac{n\omega_0}{b} t}.\end{aligned}$$

By letting $\widehat{z}[n] \stackrel{\text{def}}{=} \widehat{\psi}_{\mathbf{\Lambda}_{\mathsf{S}}}[n]\,\Phi(n\omega_0)$, we may re-write $\vec{\psi}(t)$ in terms of Fourier series of $z(t)$,

$$\vec{\psi}(t) = e^{-\jmath\frac{p}{b}t}\sum_{n\in\mathbb{Z}}\widehat{z}[n]\,e^{\jmath\frac{n\omega_0}{b}t} \equiv e^{-\jmath\frac{p}{b}t}z(t).$$

Based, on this, we now develop,

$$\begin{aligned}(\vec{s} * \vec{\psi})(t) &= e^{-\jmath\frac{p}{b}t}h(t) * e^{-\jmath\frac{p}{b}t}z(t)\\ &\stackrel{(a)}{=} e^{-\jmath\frac{p}{b}t}(h * z)(t)\\ &\stackrel{(b)}{=} e^{-\jmath\frac{p}{b}t}T_h\sum_{m\in\mathbb{Z}}\widehat{h}[m]\,\widehat{z}[m]\,e^{\jmath\frac{m\omega_0}{b}t},\end{aligned}$$

where (a) is due to invariance of complex exponentials under convolution operation (eigen-function property) and (b) is due to convolution-product theorem for the Fourier series. For simplicity, let us assume that $T_hK_{\mathbf{\Lambda}_{\mathsf{S}}} = 1$. Then, we have,

$$\begin{aligned}y(t) &= K_{\mathbf{\Lambda}_{\mathsf{S}}}m^*_{\mathbf{\Lambda}_{\mathsf{S}}}(t)\,e^{-\jmath\frac{p}{b}t}T_h\sum_{m\in\mathbb{Z}}\widehat{h}[m]\,\widehat{z}[m]\,e^{\jmath\frac{m\omega_0}{b}t},\\ &= e^{-\jmath\mathsf{Q}(\mathsf{t})}\sum_{m\in\mathbb{Z}}\widehat{h}[m]\widehat{\psi}_{\mathbf{\Lambda}_{\mathsf{S}}}[m]\,\Phi(m\omega_0)\,e^{\jmath\frac{\omega_0 m}{b}t},\end{aligned} \tag{2.79}$$

which completes our proof. ■

In defining ψ in (2.77), time-limitedness was the only assumed property for developing the SAFS representation. In practice one would expect ψ to be a bounded, smooth function. From Fourier regularity conditions, we know that a function is bounded and N times continuously differentiable provided that [28],

$$\int |\widehat{\psi}_{\mathbf{\Lambda}_{\mathsf{FT}}}(\omega)|\left(1+|\omega|^N\right)d\omega < \infty.$$

In many cases, ψ is a smooth and compactly supported pulse/function [64, 66, 73]. The next proposition states a sufficient condition for smoothness (or differentiability) of a function ψ in the SAFT domain.

Proposition 3. *(Smoothness and Decay) A function f is bounded and N times continuously differentiable with bounded derivatives provided that (ignoring constant $K_{\mathbf{\Lambda}_{\mathsf{S}}}$)*

$$\int \left|[\mathsf{L}(\omega) + a\mathscr{D}]^N\widehat{f}_{\mathbf{\Lambda}_{\mathsf{S}}}(\omega)\right| d\omega < \infty,$$

where $\mathscr{D}$ is the usual derivative operator and L is some linear polynomial. The action of $[\mathsf{L}(\omega) + a\mathscr{D}]^N$ on $\widehat{f}_{\mathbf{\Lambda}_{\mathsf{S}}}$ should be understood in the operator sense.

Proof. In order to prove this result, we begin with the observation,

$$\left|f^{(k)}(t)\right| = \left|\int F_k(\omega)\,\kappa^*_{\mathbf{\Lambda}^{\mathsf{inv}}_{\mathsf{S}}}(\omega,t)\,d\omega\right| \leqslant \int |F_k(\omega)|\,d\omega < \infty, \tag{2.80}$$

where $F_k(\omega)$, expressed as a function of $\widehat{f}_{\mathbf{\Lambda}_\mathsf{S}}(\omega)$, is the SAFT of $f^{(k)}(t)$ which is yet to be determined. In analogy to the Fourier transform, $F_k(\omega) \propto (\jmath\omega)^k \widehat{f}_{\mathbf{\Lambda}_\mathsf{FT}}(\omega)$. To set up this proof, we will start with defining smooth functions. Let f be some function with norm defined as $\forall m, n \in \mathbb{Z}_+ \cup \{0\}$, $\|f\|_{m,n} = \sup_{t\in\mathbb{R}} \left|t^m f^{(n)}(t)\right|$. Then, we say f is smooth or $f \in \mathsf{S}$ provided that $\|f\|_{m,n} < \infty$. For functions u and v bounded in this norm, integration by parts results in,

$$\int u^{(1)}(t)\, v(t)\, dt = -\int u(t)\, v^{(1)}(t)\, dt. \tag{2.81}$$

Let $u(t) \stackrel{\text{def}}{=} f^{(k)}(t)$ and $v(\mathbf{r}) \stackrel{\text{def}}{=} \kappa^*_{\mathbf{\Lambda}_\mathsf{S}}(\mathbf{r})$ where $\mathbf{r} = [t\ \ \omega]^\top$. Also note two useful relations that will be used shortly,

$$\partial_t v(\mathbf{r}) = \beta(p - \omega + at)\, v(\mathbf{r}) \tag{2.82}$$

$$\partial_\omega v(\mathbf{r}) = \beta((d\omega - \mu) - t)\, v(\mathbf{r}), \quad \mu \stackrel{\text{def}}{=} dp - bq, \tag{2.83}$$

where $\beta = \jmath/b$. Next, with $Z_0(\omega) \stackrel{\text{def}}{=} \widehat{f}_{\mathbf{\Lambda}_\mathsf{S}}(\omega)$, let us define a sequence of functions $\{Z_k\}, k \in \mathbb{Z}_+ \cup \{0\}$,

$$Z_k(\omega) \stackrel{\text{def}}{=} \int f^{(k)}(t)\, v(t,\omega)\, dt \equiv \int f^{(k)}(t)\, \kappa^*_{\mathbf{\Lambda}_\mathsf{S}}(t,\omega)\, dt. \tag{2.84}$$

Similarly, we also define $\{X_k\}, k \in \mathbb{Z}_+ \cup \{0\}$,

$$X_k(\omega) \stackrel{\text{def}}{=} \int t f^{(k)}(t)\, v(t,\omega)\, dt.$$

Thanks to the sequences $\{Z_k, X_k\}$, (2.81) can be reduced to the following recursive form,

$$Z_{k+1}(\omega) \stackrel{(2.81)}{=} \beta(\omega - p)\, Z_k(\omega) - a\beta X_k(\omega). \tag{2.85}$$

Our result relies on Z_k and hence, we must eliminate X_k. We do so by observing that,

$$\begin{aligned} Z_k^{(1)}(\omega) &= \int f^{(k)}(t)\ \underbrace{\partial_\omega v(t,\omega)}_{\text{Replace by (2.83)}}\ dt \\ &= \int f^{(k)}(t)\, \beta((d\omega - \mu) - t)\, v(t,\omega)\, dt \\ &= \beta(d\omega - \mu)\, Z_k(\omega) - \beta X_k(\omega). \end{aligned} \tag{2.86}$$

We now solve for Z_k from the system of equations (2.85), (2.86),

$$\begin{bmatrix} Z_{k+1}(\omega) \\ Z_k(\omega) \end{bmatrix} = \beta \begin{bmatrix} \omega - p & -a \\ d\omega - \mu & 1 \end{bmatrix} \begin{bmatrix} Z_k(\omega) \\ X_k(\omega) \end{bmatrix}$$

which leads to a simple recursive equation,

$$\begin{aligned} Z_{k+1}(\omega) &= \mathsf{L}(\omega)\, Z_k(\omega) + a Z_k^{(1)}(\omega), \\ &= [\mathsf{L}(\omega) + a\mathscr{D}]\, Z_k(\omega) \end{aligned}$$

where $\mathsf{L}(\omega)$ is linear polynomial $\mathsf{L}(\omega) = \beta(\omega bc + a\mu - p)$ with $\mu = dp - bq$ and is completely characterized by $\mathbf{\Lambda}_{\mathsf{S}}$. Now since $Z_0(\omega) = \widehat{f}_{\mathbf{\Lambda}_{\mathsf{S}}}(\omega)$, we observe that,

$$Z_k(\omega) = [\mathsf{L}(\omega) + a\mathscr{D}]^k \widehat{f}_{\mathbf{\Lambda}_{\mathsf{S}}}(\omega), \quad Z_0(\omega) = \widehat{f}_{\mathbf{\Lambda}_{\mathsf{S}}}(\omega) \tag{2.87}$$

and by definition (2.84), $F_k = Z_k$. Back substituting Z_k in (2.80) proves to the result. ■

As an example, consider $N = 1$. In this case (by using (2.84) and (2.87)), $\mathscr{T}_{\mathsf{SAFT}} : f^{(1)}(t) \to \mathsf{L}(\omega)\widehat{f}_{\mathbf{\Lambda}_{\mathsf{S}}}(\omega) + a\mathscr{D}\widehat{f}_{\mathbf{\Lambda}_{\mathsf{S}}}(\omega)$. In view of this result,

$$\begin{aligned} |\mathscr{D}f(t)| &\leq \int \left| \mathsf{L}(\omega)\widehat{f}_{\mathbf{\Lambda}_{\mathsf{S}}}(\omega) + a\mathscr{D}\widehat{f}_{\mathbf{\Lambda}_{\mathsf{S}}}(\omega) \right| d\omega \\ &\leq ||\mathsf{L}\widehat{f}_{\mathbf{\Lambda}_{\mathsf{S}}}||_{L_1} + |a|\,||\mathscr{D}\widehat{f}_{\mathbf{\Lambda}_{\mathsf{S}}}||_{L_1} < \infty, \end{aligned}$$

where the last result is due to Minkowski's inequality. Note that for $N = 1$, both $\widehat{f}_{\mathbf{\Lambda}_{\mathsf{S}}}$ and $\mathscr{D}\widehat{f}_{\mathbf{\Lambda}_{\mathsf{S}}}$ should be in L_1. For the case of the Fourier transform, we have $a = 0$ (cf. Table 2.3) and the result collapses to $|\omega|^N |\widehat{f}_{\mathbf{\Lambda}_{\mathsf{FT}}}(\omega)|$.

The smoothness properties of kernels are of significant interest in the context of sampling and approximation theory [26]. While a detailed discussion is beyond the scope of this work, for sparse sampling, Proposition 3 is enough to establish that $\widehat{\psi}_{\mathbf{\Lambda}_{\mathsf{S}}}$ decays to zero whenever ψ is a smooth kernel. Consequently, for some $f_c = M > 0$, we have $\widehat{\psi}_{\mathbf{\Lambda}_{\mathsf{S}}}[m] = 0, |m| > M$ and therefore, M dictates the recovery bound for perfect reconstruction of s. Without loss of generality, by setting $T = 1$ and,

$$\widehat{\psi}'_{\mathbf{\Lambda}_{\mathsf{S}}}[m] \stackrel{\text{def}}{=} \widehat{\psi}_{\mathbf{\Lambda}_{\mathsf{S}}}[m]\,\Phi_{\mathbf{\Lambda}_{\mathsf{S}}}(m\omega_0),$$

the samples take the form of

$$g_n \stackrel{(2.78)}{=} \sum_{|m| \leq M} \widehat{h}[m]\widehat{\psi}'_{\mathbf{\Lambda}_{\mathsf{S}}}[m]\, e^{\jmath \frac{\omega_0 m}{b} n}, n = 0, \ldots, N-1.$$

This problem is similar to the one in Section 2.5.0.3 and in view of Theorem 7, perfect recovery is guaranteed provided that $N \geq 2M + 1$ with $M \geq K$.

2.5.0.6 Sparse Signals and the Gabor Transform Kernel

Several recent works consider recovery of sparse signals from Gabor transform measurements. Aubel *et al.* [117] study this problem in the context of super-resolution. Similarly, Matusiak *et al.* [123] studied the problem of sparse sampling using Gabor frames. Recently, Eldar *et al.* [118] developed algorithms for recovery of sparse signals in the context of the phase retrieval. Uniqueness guarantees with respect to phase retrieval problem for the Gabor transform were reported by Jaganathan *et al.* in [124]. In all of these cases, the results were developed for the Fourier domain ($\mathbf{\Lambda}_{\mathsf{S}} = \mathbf{\Lambda}_{\mathsf{FT}}$). Here, we generalize the sparse recovery problem to the SAFT domain. For this purpose, we introduce the Gabor transform associated with the SAFT domain together with some basic mathematical properties.

Definition 8 (Gabor Transform for the SAFT Domain)**.** *Let f be a function with well defined SAFT and*

$\psi \in L_2$ be some window. We define the SAFT Gabor transform (SAFT-GT) by,

$$\widehat{S}_{\mathbf{\Lambda}_{\mathsf{S}}}^{f,\psi}(\tau,\omega) = \int f(t)\,\psi(t-\tau)\,\kappa_{\mathbf{\Lambda}_{\mathsf{S}}}^{*}(t,\omega)\,dt. \tag{2.88}$$

Next, we derive the inversion formula linked with the SAFT domain. Without loss of generality, we assume that $K_{\mathbf{\Lambda}_{\mathsf{S}}} = 1$.

Proposition 4 (Inversion Formula for the SAFT-GT)**.** *Let f be some function with a well defined SAFT and $\psi_1, \psi_2 \in L_2$ be window functions. Furthermore, let $\widehat{S}_{\mathbf{\Lambda}_{\mathsf{S}}}^{f,\psi_1}(\tau,\omega)$ denote the SAFT-GT of f defined in (2.88). Provided that $b\langle\psi_1,\psi_2\rangle = 1$, the inverse SAFT-GT is defined by,*

$$f(t) = \iint_{\tau,\omega} \widehat{S}_{\mathbf{\Lambda}_{\mathsf{S}}}^{f,\psi_1}(\tau,\omega)\,\psi_2(t-\tau)\,\kappa_{\mathbf{\Lambda}_{\mathsf{S}}^{\mathsf{inv}}}^{*}(\omega,t)\,d\omega d\tau. \tag{2.89}$$

Proof. Let us assume (2.89) is true. Furthermore, we have,

$$\left\langle \kappa_{\mathbf{\Lambda}_{\mathsf{S}}}^{*}(x,\omega), \kappa_{\mathbf{\Lambda}_{\mathsf{S}}^{\mathsf{inv}}}(\omega,t)\right\rangle = e^{\jmath(\mathsf{Q}(x)-\mathsf{Q}(t))} \underbrace{\int e^{-\jmath\frac{\omega}{b}(x-t)}d\omega}_{b\delta(x-t)}. \tag{2.90}$$

Next, we substitute $\widehat{S}_{\mathbf{\Lambda}_{\mathsf{S}}}^{f,\psi}(\tau,\omega)$ in (2.89) to obtain,

$$\iint_{\tau,x} f(x)\,\psi_1(x-\tau)\,\psi_2(x-\tau)\left\langle \kappa_{\mathbf{\Lambda}_{\mathsf{S}}}^{*}(x,\omega), \kappa_{\mathbf{\Lambda}_{\mathsf{S}}^{\mathsf{inv}}}(\omega,t)\right\rangle dx d\tau.$$

Thanks to (2.90), by marginalizing ω and then x, the last equation yields $bf(t)\langle\psi_1,\psi_2\rangle = I_f$. Setting $I_f = f$ verifies the result. ■

In the context of the SAFT-GT, the sparse signal (2.10), or alternatively (2.64), can be represented as,

$$y(\tau,\omega) \overset{(2.88)}{=} \underbrace{\Phi_{\mathbf{\Lambda}_{\mathsf{S}}}^{*}(\omega)\sum_{k=0}^{K-1} c_k'\psi(t_k-\tau)\,e^{-\jmath\frac{\omega}{b}t_k}}_{\widehat{S}_{\mathbf{\Lambda}_{\mathsf{S}}}^{s,\psi}(\tau,\omega)}. \tag{2.91}$$

Let $y'(t,\omega) = y(t,\omega)\,\Phi(\omega)$ where $\Phi_{\mathbf{\Lambda}_{\mathsf{S}}}$ is a modulation operation with $\Phi_{\mathbf{\Lambda}_{\mathsf{S}}}\Phi_{\mathbf{\Lambda}_{\mathsf{S}}}^{*} = 1$.

$$y'(t,\omega) \overset{\text{def}}{=} \sum_{k=0}^{K-1} c_k'\psi(t_k-t)\,e^{-\jmath\frac{\omega}{b}t_k}. \tag{2.92}$$

Since ψ is a known, smooth window, a finite Fourier series approximation—time scaled by b—suffices to approximate ψ,

$$\widetilde{\psi}_M(t) \approx \sum_{|m|\leqslant M} \widehat{\psi}_{\mathbf{\Lambda}_{\mathsf{FT}}}[m]\,\kappa_{\mathbf{\Lambda}_{\mathsf{FT}}}^{*}(t,\omega_0 m/b), \quad \omega_0 = 2\pi b/T_h.$$

Let $M = f_c$ and assume sampled measurements of the form,

$$y(\tau, \omega)|_{\tau=nT}^{\omega=\ell\omega_0}, \quad (\tau, \omega) \in [0, N-1] \times [-f_c, f_c].$$

Next, we study the recovery of s in two separate cases:

- Case 1: Recovery with a fixed ω.

  By fixing $\omega = \omega_0$ and $\psi \to \psi_M$,

$$y(nT, \omega_0) = \underbrace{\Phi^*_{\mathbf{\Lambda}_\mathsf{S}}(\omega_0)}_{\text{Constant}} \sum_{k=0}^{K-1} \underbrace{c'_k e^{-\jmath \frac{\omega_0}{b} t_k}}_{\breve{c}_k} \psi_M(t_k - nT)$$

  where the weights reflect the effect of the SAFT, $\breve{c}_k \stackrel{\text{def}}{=} c'_k e^{-\jmath \frac{\omega_0}{b} t_k} = c_k e^{\jmath \mathsf{Q}(t_k)} e^{-\jmath \frac{\omega_0}{b} t_k}$. Finally, note that this is the classical sparse sampling problem (cf. compare (2.8)),

$$y'(nT, \omega_0) = \sum_{k=0}^{K-1} \breve{c}_k \overline{\psi}_M(nT - t_k)$$

  where $\overline{\psi}_M = \psi_M(-\cdot)$ and the result of Section 2.5.0.3 can be directly extended to the case at hand. Provided that $f_c = M \geq K$ and $N \geq 2M + 1$, perfect recovery is guaranteed.

- Case 2: Recovery using both (τ, ω).

  From (2.92) and $\psi_M \approx \psi$, we have,

$$\begin{aligned} y'(nT, \ell\omega_0) &= \sum_{k=0}^{K-1} c_k \sum_{|m| \leqslant M} \widehat{\psi}_{\mathbf{\Lambda}_\mathsf{FT}}[m] e^{\jmath \frac{t_k}{b}(m\omega_0 - \ell\omega_0)} e^{-\jmath \frac{m\omega_0}{b} nT} \\ &= \sum_{|m| \leqslant M} \breve{y}_{m,\ell} e^{-\jmath \frac{m\omega_0}{b} nT} \end{aligned} \tag{2.93}$$

  where,

$$\breve{y}_{m,\ell} \stackrel{\text{def}}{=} \sum_{k=0}^{K-1} \widehat{\psi}_{\mathbf{\Lambda}_\mathsf{FT}}[m] c_k e^{\jmath \frac{t_k}{b}(m\omega_0 - \ell\omega_0)}.$$

  This development is the standard form (with regards to the Fourier domain) and the results in [117] can be extended to solve for (2.93). For a Gaussian window function, the exact recovery principle based on minimum separation condition is discussed in [117] (cf. Theorem 11) and applies to (2.93).

अभिनक्षन्तो अभि ये तमानशुर्निधिं पणीनां परमंगुहा हितम ।
ते विद्वांसः परतिचक्ष्याऋता पुनर्यत उायन तदुदीयुराविशम ॥

रतावानः परतिचक्ष्याऋता पुनरात आ तस्थुः कवयो महस पथः ।
ते बाहुभ्यां धमितमग्निमश्मनि नकिः षो अस्त्यरणो जहुर्हि तम ॥

रतज्येन कषिप्रेण बरह्मणस पतिर्यत्र वष्टि पर तदश्नोति धन्वना ।
तस्य साध्वीरिषवो याभिरस्यति नर्चक्षसो दर्शये कर्णयोनयः ॥

"The truth-possessing poets, after observing the untruths again, from there mounted the great paths." [1]

— Rigveda (Mandala II, §24, ¶ 06–08)

3

The Unlimited Sensing Framework

3.1 Introduction and Overview

There is no doubt that Shannon's sampling theorem is one of the cornerstone results in signal processing, communications and approximation theory. An informal statement of this theorem is that any function with compactly supported Fourier domain representation can be uniquely represented from a set of equidistant points taken on the function. The spacing between the points—the sampling rate—is a function of the bandwidth. In the last few decades, the field has grown far and wide [125, 126, 27, 127] and a number of elegant extensions have been reported. These extensions relate to (but not limited to) shift-invariant subspaces [31, 26, 32, 35], union of subspaces [128, 129], sparse signals [69, 70, 130], phase space representations [38], spectrum blind sampling [131] and operator sampling [132, 133]. Broadly speaking and in most cases, the variation on the theme of sampling theory arises from the diversity along the *time-dimension*. For example, sparsity vs. smoothness and uniform vs. non-uniform grid are attributes based on the time dimension. A variation on the hypothesis linked with any of these attributes leads to a new sampling theorem. Here, we take a different approach and discuss a hypotheses based on the *amplitude-dimension*.

Almost all forms of data are captured using digital sensors or analog-to-digital converters (ADCs) which are inherently limited by dynamic range. Consequently, whenever a physical signal exceeds the maximum recordable voltage, the digital sensor saturates and results in clipped measurements. For example, a camera pointed towards the sun leads to an all-white photograph. Similarly, in scientific imaging systems such as ultrasound, terahertz, spectroscopic, radar and seismic imaging, strong reflections or pulse echoes blind the sensor. In communication systems, clipping results in performance degradation. In

context of music, clipped sound results in high frequency artifacts.

Motivated by a variety of applications, a natural question that arises is: Can we capture a signal with arbitrary dynamic range?

In this work, we introduce the **Unlimited Sensing** framework which is a novel, non-linear sensing architecture that allows for recovery of an arbitrarily high dynamic range, continuous-time signal from its low dynamic range, digital measurements or "samples". Our work is based on a radically different ADC design, which allows for the ADC to reset rather than to saturate, thus producing modulo or folded samples. In analogy to the Shannon-Nyquist sampling theorem, an open problem that remains is: Given such modulo samples of a bandlimited function, how can the original signal be recovered and what is the Nyquist rate for perfect recovery? In the first part of this work, we discuss a recovery guarantee which, remarkably, is independent of the maximum recordable ADC voltage. Our theory is complemented with a stable recovery algorithm. Moving further, we reinterpret the unlimited sensing framework as a generalized linear model and discuss the recovery of structured signals such as continuous-time sparse signals and sparse sinusoidal mixtures.

This new sensing paradigm that is based on a co-design of hardware and algorithms leads to several interesting future research directions. On the theoretical front, a fundamental interplay of sampling theory and inverse problems raises new standalone questions. On the practical front, the benefits of a new way to sense the world (without dynamic range limitations) are clearly visible. We conclude this chapter with a discussion on future directions and relevant applications.

3.1.1 Shannon's Sampling Theory and a Practical Bottleneck

From a practical standpoint, Shannon's sampling theorem (cf. Theorem 1) is implemented using so-called analog-to-digital converter (or the ADC) which is used to obtain point-wise samples of the function. This where the topic of *quantization* finds its way to the sampling theory. Quantization, in context of sampling theory of band-limited signals, is a mature topic which is fairly well understood. That said, one bottleneck that inhibits the functionality of an ADC is its *dynamic range*—the maximum recordable voltage range $[-\lambda, \lambda]$. Whenever a signal crosses this threshold, the ADC saturates and the resulting signal is clipped. This is shown in Fig. 3-1-(a).

The issue of clipping is a serious problem and manifests as non-linear artifacts in audio-visual data as well as applications that involve sampling of physiological or bio-medical data. Not surprisingly, a number of works have studied this problem in different contexts (cf. [134, 135, 136, 137]). When a bandlimited signal is clipped, the resulting function has discontinuities which amounts to creating high-frequency distortions to the signal. Hence, if a signal is not amplitude limited, it may be prone to aliasing artifacts [138]. Although important, this aspect is rarely discussed in context of Shannon's sampling theory [126, 27, 127, 31, 26, 32, 35]—something that is very relevant to our work. Clipped signals are typically handled by restoration algorithms [139, 138, 137] which seek to recover permanently lost data samples under certain assumptions.

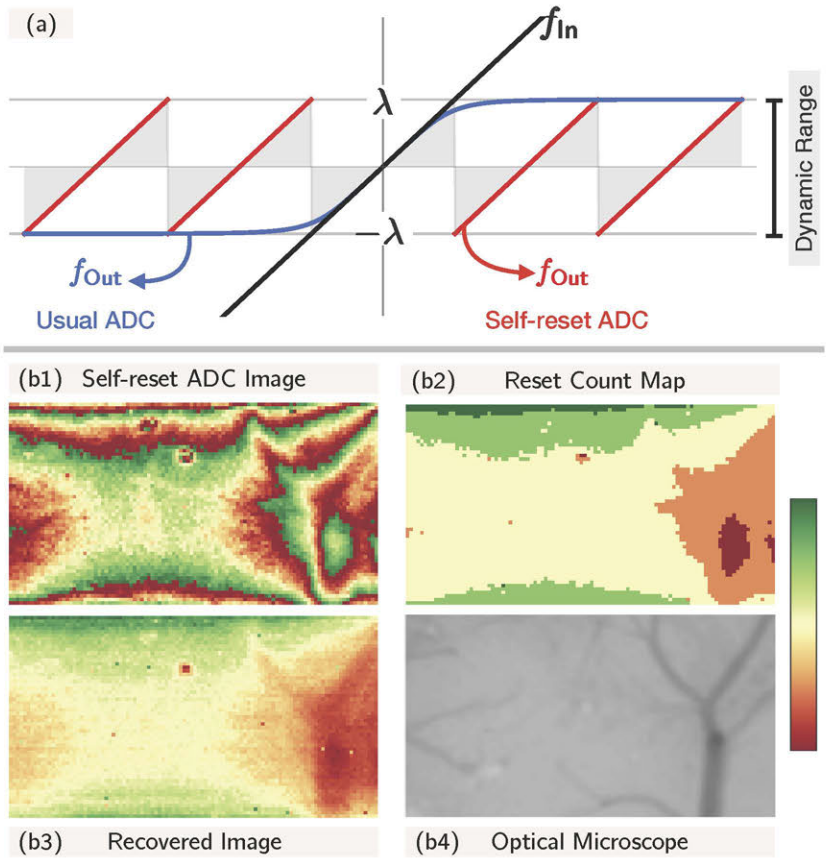

Figure 3-1: Usual ADC compared with self-reset ADC. (a) Whenever the input signal f_{In} voltage exceeds a certain threshold λ, the output signal f_{Out} in any conventional ADC saturates to λ and this results in clipping. In contrast, whenever $|f_{\mathsf{In}}| > \lambda$, the self-reset ADC folds f_{In} such that f_{Out} is always in the range $[-\lambda, \lambda]$. In this way, the self-reset configuration circumvents clipping but introduces discontinuities. (b) Images obtained with prototype self-reset ADC (b1) Image obtained with a self-reset ADC shows folded amplitudes. (b2) For each pixel, the "reset count map" shows the number of times the image amplitude has undergone folding. (b3) Unfolded image based on reset count map. (b4) Image obtained using an optical microscope.

3.1.2 A Solution via Modular Arithmetic

3.1.2.1 Practical Context: Analog-to-Digital Converters

Thanks to recent advancements in ADC design, a radically different approach is rapidly developing. Namely, when reaching the upper or lower saturation threshold, these ADCs would reset to the respective other threshold, in this way allowing to capture subsequent changes even beyond the saturation limit. Motivated by Tomlinson decoders as they appear in the context of communication theory [140], the theoretical concept of such ADCs already appeared in the literature as early as in the late 1970's under the name of a modulo limiter [141, 142], but only the nature of the resulting quantization noise, and neither their physical realization, nor their recovery properties were investigated.

Physical realizations only started to develop in the early 2000's. Depending on the community, the resulting ADC constructions are known as *folding*-ADC (cf. [143] and references therein) or the *self-reset*-ADC, recently proposed by Rhee and Joo [144] in context of CMOS imagers (see Fig. 3-1-(b1-b3))[1] for visualization of their approach). As noted in [146], the SR-ADCs allow for simultaneous enhancement of the dynamic range as well as the signal-to-noise ratio. The goal of developing SR-ADCs is motivated by the fact that the dynamic range of natural images typically surpasses what can be handled by the usual ADCs. This feature is not only critical to consumer photography [146] but also plays an important role in life sciences and bio-imaging. For instance, last year, Sasagawa [145] and Yamaguchi [147] developed SR-ADCs for functional brain imaging.

Common to all such architectures [144, 146, 142, 141] is a memoryless, non-linear mapping of the form,

$$\mathscr{M}_\lambda : t \mapsto 2\lambda \left(\left[\!\left[\frac{t}{2\lambda} + \frac{1}{2} \right]\!\right] - \frac{1}{2} \right), \tag{3.1}$$

where $[\![t]\!] \stackrel{\text{def}}{=} t - \lfloor t \rfloor$ defines the fractional part of t. The mapping in (3.1) is folding amplitudes, that is, the range of $\mathscr{M}_\lambda$ is $[-\lambda, \lambda]$. To visualize this operation, we plot $\mathscr{M}_\lambda(t)$ as a function of t in Fig. 3-1-(b). In effect, (3.1) can be interpreted as a centered modulo operation since $\mathscr{M}_\lambda(t) \equiv t \bmod 2\lambda$.

In comparison to the remarkable progress that has been made on the hardware front of the new ADCs, theoretical and algorithmic aspects related to the identifiability and recovery properties of the modulo samples remain largely unexplored. Namely, all previous approaches [144, 145, 147] would require additional information such as a detailed account of how often the amplitudes have been folded (cf. Fig. 3-1-(b2)), which leads to significantly more involved circuit architectures as well as additional power and storage requirements. No attempts have been made to take the viewpoint of an inverse problem, that is, to identify or recover the signal from modulo samples alone.

3.1.2.2 Theoretical Context: Generalized Linear Model for Inverse Problems

Linear Models and Classical Approaches

An effective approach towards modeling (exactly or approximately) physical phenomenon utilizes the *linear inverse model* described by,

$$\mathbf{b} = \mathbf{A}\mathbf{x} + \mathbf{e} \tag{3.2}$$

where,

- $\mathbf{b}$ is a vector of measurements.
- $\mathbf{A}$ is some linear transformation that models the physical world.
- $\mathbf{x}$ is the data to be recovered or reconstructed.
- $\mathbf{e}$ is the measurement uncertainty or noise.

This problem is frequently studied in high-dimension linear estimation. As shown in Fig. 3-2, in absence of uncertainty or $\mathbf{e}$, a classical approach towards recovery of $\mathbf{x}$ from measurements $\mathbf{b}$ is to consider least-squares constraint. In this way, the problem can be categorized into (a) over-determined case, (b)

[1]The data used in this image was provided by Sasagawa *et al.* cf. [145].

under-determined case and (c) constrained least-squares case. A more general approach towards this problem is to regularize the recovery of the unknown by promoting some prior information by introducing regularizer $\mathcal{R}$ so that one recovers $\mathbf{x}$ by minimizing cost:

$$\min_{\mathbf{x}} ||\mathbf{A}\mathbf{x} - \mathbf{b}||_2^2 + \lambda \mathcal{R}(\mathbf{x})$$

where $||x||_2 = \sqrt{|x_1|^2 + |x_2|^2 + \cdots + |x_N|^2}$ which is the Euclidean length of unknown vector $\mathbf{x}$. For example, in recent years, sparsity promoting priors have been exploited for recovery of $\mathbf{x}$. The sparsity prior is particularly interesting in context of under-determined systems where the number of measurements is smaller than the number of unknowns. However, this is only possible by assuming an additional structure on $\mathbf{x}$, that is, $\mathbf{x}$ is sparse or most of the entries in $\mathbf{x}$ are zeros. In order to activate the sparsity based prior, one my use $\mathcal{R}(\mathbf{x}) = ||\mathbf{x}||_1$ which is nothing but the sum of absolute values of $\mathbf{x}$. By letting $\mathbf{a}_m$ to be the mth column of matrix $\mathbf{A}$ and denoting the scalar product by $\langle \mathbf{a}_m, \mathbf{x} \rangle$, one of the most well known approaches towards recovery of K–sparse $\mathbf{x}$ from $\mathbf{b} \in \mathbb{R}^M$ by solving,

$$\min_{\mathbf{x} \in \mathbb{R}^N} \frac{1}{2M} \sum_{m=1}^{M} |b_m - \langle \mathbf{a}_m, \mathbf{x} \rangle|^2 \quad \text{such that} \quad \mathcal{R}(\mathbf{x}) = K, \quad M > N$$

is the *LASSO* (Least Absolute Shrinkage or Selection Operator) by Tibshirani [148]. Interestingly, it turns out that $K \log\left(\frac{2N}{K}\right)$ measurements are enough for recovery of the sparse vector $\mathbf{x}$. The logarithmic dependence on the ambient dimension is encouraging for since recovery is possible even in cases when $M \ll N$. Under-sampled systems have been studied as a part of the *compressed sensing* literature which traces its roots to the work of Donoho, Candes and Tao [149, 150, 151].

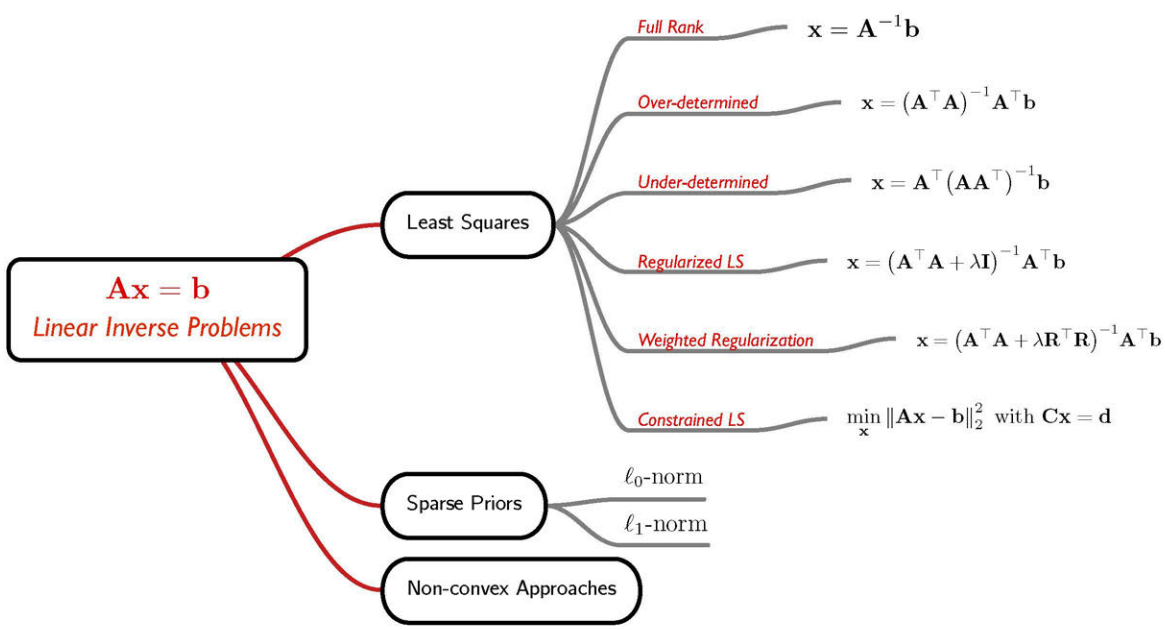

Figure 3-2: Standard approaches for regularizing linear inverse problems.

Table 3.1: Generalized Linear Model for Sparse Signal Recovery

Link Function	Sensing Operator $\mathbf{A}$	Prior/Structure on $\mathbf{x}$	Related Work	Problem Setup (Dimensionality)	Recovery Guarantees
Quantizer	Gaussian i.i.d	Sparsity	Quantized Compressive Sampling[152]	Finite	Yes [153]
$\text{sgn}(x)$	Gaussian i.i.d	Sparsity	One-bit Compressive Sampling[154, 155, 156]	Finite	Yes [155]
$\lvert x \rvert$	Fourier Matrix	Sparsity	Sparse Phase Retrieval [157]	Finite	Yes [158]
e^{jx}	Gaussian i.i.d	Sparsity	Random Sinusoidal Feature Maps [159]	Finite	Yes [159]
Arbitrary	Gaussian i.i.d	Sparsity	Generalized LASSO [160, 161]	Finite	Yes
$(\nabla \circ \log)(x)$	Sampling Matrix	Natural Images	Gradient Camera [162]	Finite	No

Generalized Linear Models

From a practical standpoint, linear model in (3.2) is a restrictive choice. It is well known that many electro-optical devices are non-linear. For example speakers demonstrate non-linearity in amplitude response and sensor saturation is common place phenomenon in all measurement systems. To incorporate non-linear behaviour in the model described in (3.2), we may generalize to the following measurement model,

$$\mathbf{b} = f(\mathbf{A}\mathbf{x}) + \mathbf{e} \tag{3.3}$$

where f, sometimes known as the *link function*, further maps the original linear measurements $\langle \mathbf{a}_m, \mathbf{x} \rangle$ to by a transformation (linear or non-linear) defined by f. In literature, such models have been dealt on case-by-case basis. While some directions are relatively new, some other cases have been extensively studied. Here we list a few well known examples that are also summarized in Table 3.1.

1. **Quantized Compressed Sensing**

   Zymnis and co-workers extend the topic of quantization to the case of sparse signals in [152]. As opposed to the conventional case of quantizing a bandlimited function acquired at Nyquist rate, in [152], f is defined to be a quantizer which maps reals to a a finite set of codewords, that is,

   $$f_k : \mathbb{R} \to \mathsf{C}_k, \quad \mathsf{C} : \text{finite set of codewords.}$$

   There on, the problem boils down to recovery of a sparse vector $\mathbf{x}$ from quantized measurements $\mathbf{b}$ observed using a Gaussian i.i.d sensing matrix $\mathbf{A}$.

2. **1–bit Compressive Sensing**

   This problem was introduced by Boufounos and Baraniuk in [154] and uses $f(x) = \text{sgn}(x)$ where,

   $$\text{sgn}(x) := \begin{cases} -1 & \text{if } x < 0, \\ 0 & \text{if } x = 0, \\ 1 & \text{if } x > 0. \end{cases}$$

   Therefore, in view of (3.2), the non-linear measurements $\text{sgn}(\langle \mathbf{a}_m, \mathbf{x} \rangle)$ simply amount to one bit representation of the underlying linear measurements $\langle \mathbf{a}_m, \mathbf{x} \rangle$. This setup is called compressive because $\mathbf{x}$ is assumed to be a sparse vector [154, 155, 156].

3. **Sparse Phase Retrieval**

   The problem of sparse phase retrieval seeks to recover a sparse vector from the magnitude of its

Fourier transform [157, 158]. We can adapt (3.3) for this case by using absolute operator or $f(x) = |x|$. In particular, the measurements (in noiseless setting) are described by,

$$\mathbf{b} = f(\mathbf{V}\mathbf{x}) = |\mathbf{V}\mathbf{x}|$$

where $\mathbf{V}$ is the discrete Fourier transform matrix. The presence of absolute operator maps the complex-valued Fourier transform given by $\mathbf{V}\mathbf{x}$ to real-valued measurements $\mathbf{b}$ by destroying the phase information.

4 Sinusoidal Feature Maps

In [159], the authors explore the problem of stable recovery of a sparse vector $\mathbf{x}$ from sinusoidal mapping of their random projections. In this case, $f(x) = \exp(\jmath x)$ and the sensing matrix $\mathbf{A}$ is considered to be Gaussian i.i.d.

5 LASSO with Non-linear Measurements

Plan and Vershynin [160] showed that vanilla Lasso could be repurposed for estimating a sparse or structured vector $\mathbf{x}$ through its linear projections via a Gaussian i.i.d sensing matrix $\mathbf{A}$ which are corrupted by some unknown, potentially non-linear mapping f. In particular, the measurements in their setup take form of:

$$b_m = f_m(\langle \mathbf{a}_m, \mathbf{x} \rangle).$$

This problem is further studied by Thrampoulidis and co-workers in [161] where they show that recovery procedure simply amounts to solving for the **Generalized Lasso** [160] problem,

$$\mathbf{x}^\star = \min_{\mathbf{x}} ||\mathbf{A}\mathbf{x} - \mathbf{b}||_2 + \lambda \mathcal{R}(x) \quad \text{(Root-LASSO)}$$

where $\mathcal{R}$ is a convex/non-convex regularizer that promotes sparsity. While f is assumed to be unknown, it is not the purpose of Generalized LASSO to recover f. This is because, whenever the sensing matrix $\mathbf{A}$ is Gaussian i.i.d, estimation of $\mathbf{x}$ is possible from $\mathbf{b}$ up to a multiplicative constant that purely depends on f_m. The roots of this result trace back to Brillinger's work in the 80's [163] and were first reported in the recent work of Plan and Vershynin [160]. A multi-channel extension of this work is considered by Genzel and Jung in [164, 165].

6 Gradient Imaging

Tumblin and co-workers introduce the "Gradient Camera" in [162] which measures static gradients of log-intensity of an image. In this case, the link function is chosen to be a composite function of a gradient after log, that is, $f = \nabla \circ \log$. The key purpose behind exploiting such a mapping is to obtain crisp images capable of capturing high contrast, high dynamic range images which can not be handled by conventional ADCs. Although the captured output may not be displayable (as is the case with conventional sensors), solving for the inverse problem of recovering image $\mathbf{x}$ from the "Gradient Camera" which produces image $\mathbf{y} = (\nabla \circ \log)(\mathbf{x})$ results in images with fine quantization and high contrast. The image recovery is based on Poisson equation [166]. The work of Agrawal and co-workers [166, 167] in this direction shows that an image, reinterpreted as a scalar field, can be reconstructed by integrating the gradient field and this task is accomplished via the solution of the Poisson equation.

In practice, the gradient field may be non-integrable in which case, a least-squares regularization

approach my be used to convert the ill-posed problem into a well-posed one.

From the above mentioned examples, it is clear that the flexibility offered by generalized linear models (3.3) can be either used to,

- handle uncertainties introduced by practical measurements systems, or,
- as a tool to device new acquisition systems which offer advantages that go beyond conventional systems.

Pitfalls and Bottlenecks in Existing Literature

Despite the utility of formulating such inverse problems with a link function f, existing approaches suffer from following disadvantages:

—• **Assumptions on Sensing Matrix** A common assumption on the sensing matrix is that its entries are Gaussian i.i.d. This is may not be well suited for modeling practical systems. For example, in many applications $\mathbf{A}$ is a Toeplitz matrix with a low-pass filter structure. This is true of all the standard super-resolution problems which has been covered in a large body of work [168, 69, 60, 57].

—• **Assumptions on the Unknown Signal** While sparse signals constitute an important class, existing methods can not handle a wider variety of functions which are covered in literature, for example, bandlimited functions [27], sum-of-sinusoids [67], polynomials/Splines [31] and union of subspace model [128].

—• **Assumptions on Dimensions** Existing work, as can be seen from Table 3.1 focuses on finite dimensional setting because the underlying model is a discrete time process. The physical world is defined on a continuum and hence, a better suited model should be able to handle continuous time processes.

While the above mentioned pitfalls are independent of the choice of link function f, there is no current theory which facilitates a unification of the above assumptions with a proper choice of link function. In the reminder of this work, our goal is to highlight the significance of the modulo operation as a link function and discuss new results in context of sampling theory.

3.1.3 Contributions

Within the context of the **Unlimited Sensing** framework, this chapter considers three classes:

1) Unlimited sampling of bandlimited functions is considered in Section 3.3.

   Our main contributions in this direction are two fold and set the stage for later contributions,

   i) We take a first step towards formalization of a sampling theorem which describes sufficient conditions for sampling and reconstruction of bandlimited functions in context of the SR-ADC and modulo samples.

   ii) Our sufficiency condition is complemented by a constructive algorithm which describes a recovery principle and that is stable with respect to noise.

2) Recovery of low-pass filtered spikes from modulo samples is considered in Section 3.4.

   In this case, we study the model described by (2.8) in Section 2.1.2 where we consider modulo samples. In this direction, our key contribution involves formalization of a sampling theorem for sparse signals which leads to a sufficient condition for prefect recovery of K–sparse signals from SR-ADC samples. Our sparse sampling theorem is complemented by a constructive algorithm which describes a linear and stable recovery procedure.

   The fundamental difference between recovery of sparse signal in (2.10) with respect to the bandlimited case discussed Section 3.3 is that we will working with finite number of samples. Of course, as opposed to the non-modulo samples considered in 2.1.2, we expect that N will be larger than $2K+1$ but the number of samples should still be finite. Consequently, in working with sparse signals, there is a trade-off between sampling rate T and number of modulo samples N. While T dictates the recovery conditions for unfolding modulo samples, N defines the critical number of samples required for estimation of the sparse signal from modulo samples. Furthermore, in case of excessive oversampling (when T is close to zero), we must note that matrices involved with estimation of unknowns $\{c_k, t_k\}_{k=0}^{K-1}$ will become ill-conditioned. In order to outline a numerically stable recovery method, one must seek an optimal balance between T and $N > 2K+1$.

3) Sparse sum of sinusoids is considered in Section 3.5.

   Here, we use the "local reconstruction" approach developed for the previous case and investigate the *parameter* or *spectral* estimation problem for sinusoids [67].

In this way, our work allows for *unlimited sampling*—the case when the amplitude range of a function far exceeds the dynamic range of the usual ADCs, that is, $\max|f_{\mathsf{In}}| \gg \lambda$. This is achieved by trading sampling rate for dynamic range.

3.2 Modulo Mapping

The modulo operation naturally arises in number theory and finds applications in a variety of problems that are linked with science and engineering. Qualitatively speaking, the modulo operation, sometimes also known as the modulus, amounts to recording the remainder after division of a number by another. A review of the modulo operation with key mathematical properties is presented in Box 1. In context of the model in (3.3), with the modulo operator, the measurements read,

$$\mathbf{b} \overset{(3.4)}{=} \operatorname{mod}(\mathbf{Ax}, \lambda) \equiv \operatorname{mod}_\lambda(\mathbf{Ax}), \quad \lambda \in \mathbb{R}^+.$$

In literature, one typically finds that $\mathbf{A} = \mathbf{I}$ (identity matrix) and hence, $\mathbf{b}$ amounts to some "wrapped" version of $\mathbf{x}$ where the amplitude of $\mathbf{x}$ is wrapped such that $\mathbf{b} \in [0, \lambda)$. Therefore, recovery of $\mathbf{x}$ requires some "unwrapping principle" and in literature, the art of recovery of $\mathbf{x}$ from $\mathbf{b}$ is often known as the "phase unwrapping problem" where $\lambda = 2\pi$. This is partly because phase in context of Fourier transform may only be estimated on a circle leading to a 2π–periodic representation. Also in several imaging modalities, phase information is critical for reconstruction of the image. Next, we review a landscape of known problems with respect to phase unwrapping problem.

Box:1 Modulo Operations

The modulo operation, sometimes also known as the modulus, amounts to recording the remainder after division of a number by another. Let m and n be given numbers and let us denote the quotient q and remainder r by quantities $q \in \mathbb{Z}$ and r, respectively. Then, we have,

$$q \in \mathbb{Z}, \qquad m = nq + r, \quad |r| < |n|$$

and,

$$\begin{aligned} \text{mod}\,(m, n) &\equiv \text{mod}_n\,(m) \\ &= m - |n| \left\lfloor \frac{m}{|n|} \right\rfloor = r. \end{aligned} \tag{3.4}$$

where $\lfloor \cdot \rfloor$ is the floor operation. We list a few important properties that are central to the modulo operation:

1. Identity
   - $\text{mod}\,(\text{mod}\,(m, n), n) = \text{mod}\,(m, n)$
   - $\forall p \in \mathbb{Z}^+, \text{mod}\,(n^p, n) = 0$
2. Inverse
   Let $m_{\text{inv}} = m^{-1}$ denote the modular multiplicative inverse then, we have,

   $$\text{mod}\,(\text{mod}\,(m_{\text{inv}}, n)\ \text{mod}\,(m, n), n) = 1.$$

   We also note that,

   $$\text{mod}\,(\text{mod}\,(-m, n) + \text{mod}\,(m, n), n) = 0.$$
3. Distributive Property:
   - $\text{mod}\,(m_1 + m_2, n) = \text{mod}\,(\text{mod}\,(m_1, n) + \text{mod}\,(m_2, n), n)$.
   - $\text{mod}\,(m_1 m_2, n) = \text{mod}\,(\text{mod}\,(m_1, n)\ \text{mod}\,(m_2, n), n)$.
4. Division
   The division is defined by,

   $$\text{mod}\left(\frac{m_1}{m_2}, n\right) = \text{mod}\left(\text{mod}\,(m_1, n)\ \text{mod}\left(m_2^{-1}, n\right), n\right),$$

   provided that m_2 and n are co-prime.
5. Inverse Multiplication $\text{mod}\left(\text{mod}\,(m_1 m_2, n)\ \text{mod}\left(m_2^{-1}, n\right), n\right) = \text{mod}\,(m_1, n)$.

3.2.1 Modulo Operator and Phase Unwrapping: The Case of One Dimensional Recovery

In order to develop an intuition behind phase unwrapping problem, we start with a simple mathematical observation that is depicted in Fig. 3-3. The key idea is that any function $s(t)$ (discrete or continuous) can be written as,

$$s(t) = \underbrace{\text{mod}_\lambda\,(s(t))}_{z(t)} + 2\lambda \sum_{k \in \mathbb{Z}} e_k \mathbb{1}_{\mathcal{D}_k}(t), \quad e_k \in \mathbb{Z}$$

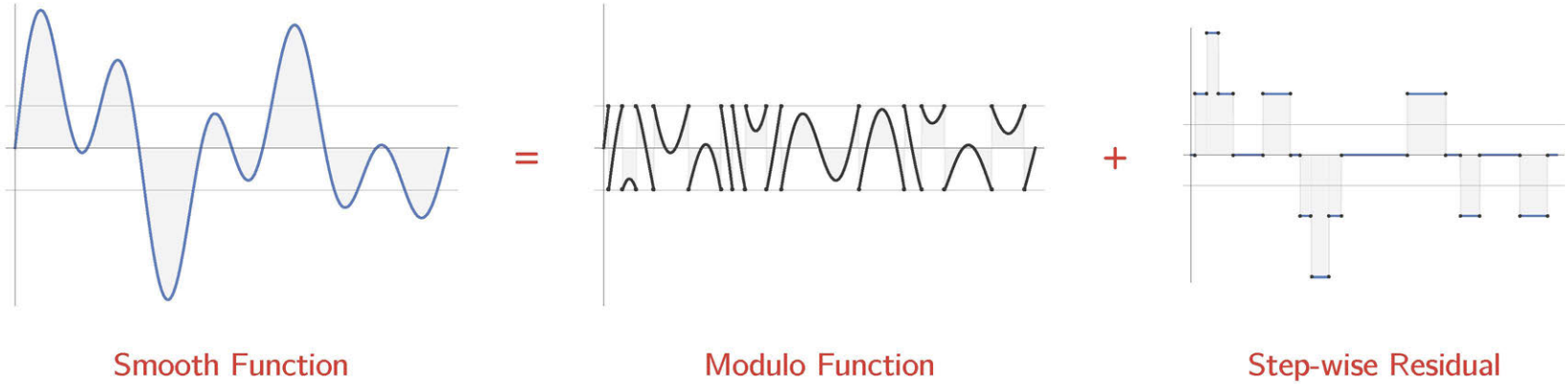

Figure 3-3: Decomposition of a smooth signal into a modulo part and a piecewise constant part.

where $\mathbb{1}_{\mathcal{D}}$ is the indicator function defined on set $\mathcal{D}$. Let us define the Nth derivative operation by $s^{(N)}(t) = \partial_t^N s(t)$. By differentiating the above expression, we observe that,

$$s^{(1)}(t) = z^{(1)}(t) + 2\lambda r(t)$$

where the residual r is a sum of spikes (to be understood in sense of distributions) and its amplitudes are such that $r(t) \in \mathbb{Z}$. We quickly note that, this property allows us to relate the derivatives of the signal s with the derivatives of the measurements z for since,

$$\text{mod}_\lambda s^{(1)}(t) = \text{mod}_\lambda z^{(1)}(t) + \underbrace{\text{mod}_\lambda 2\lambda r(t)}_{=0} \Rightarrow \text{mod}_\lambda s^{(1)}(t) = \text{mod}_\lambda z^{(1)}(t). \tag{3.5}$$

Provided that $s^{(1)}(t) < \lambda$, we have, a direct relation between the wrapped function z and the unknown s because,

$$s^{(1)}(t) < \lambda \Rightarrow s^{(1)}(t) = \text{mod}_\lambda z^{(1)}(t).$$

This critical link establishes a recovery condition as well as an algorithm:

Recovery Condition $s^{(1)}(t) < \lambda$.

Note that $s^{(1)}(t) < \lambda$ implies that the derivative of the signal is unaffected by the modulo operator and hence, $s^{(1)}(t) = \text{mod}_\lambda s^{(1)}(t)$. From this and (3.5) it follows that:

$$\underbrace{s^{(1)}(t)}_{\text{To be estimated}} = \text{mod}_\lambda \underbrace{z^{(1)}(t)}_{\text{Given}}.$$

Algorithm In view of the above, we can develop a naive algorithm. Starting with measurements $z(t) = \text{mod}_\lambda s(t)$, we compute $\text{mod}_\lambda z^{(1)}(t)$. Now since, $s^{(1)}(t) < \lambda$ (by assumption), we must have $s^{(1)}(t) = \text{mod}_\lambda z^{(1)}(t)$. Hence, the unknown on the left hand side can be estimated via integration (upto a constant).

A discrete version of this condition was first proposed by Itoh [169] and is a cornerstone result in phase unwrapping literature. That said, it is important to note that in many cases, higher order derivatives or finite-differences may be smaller in the max-norm compared to the first order finite-difference, that is to say,

$$s^{(1)}(t) > \lambda \quad \text{but} \quad 0 \leq s^{(N)}(t) < \lambda.$$

In such cases, an algorithm that can exploit higher order finite-differences should be used which is not the case in literature. Since polynomials are in the kernel of higher order derivatives or differences, this means that one either requires some boundary conditions or prior signal structure to deal with polynomial. Such cases are not covered by rather modest condition proposed in [169]. A compelling demonstration is shown in Fig. 3-4 where higher order difference allow for exact recovery of signals when the first order condition is insufficient. This also allows for shrinking λ which is particularly beneficial for conceptualizing novel acquisition systems where λ is an additional degree of freedom.

An overall review of the literature on this topic in Box. 2.

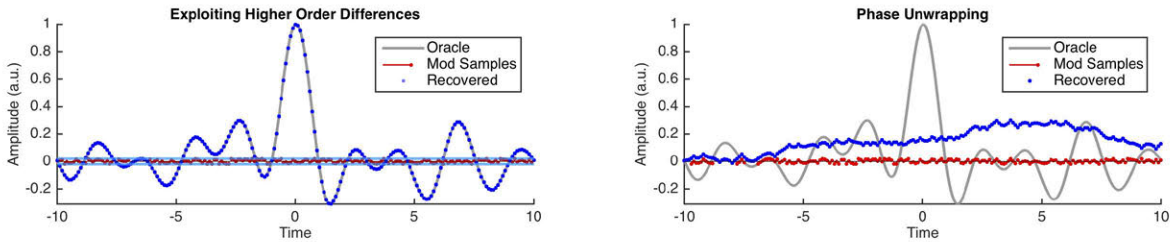

Figure 3-4: Recovery from modulo operator with $\lambda = 1/50$. (Left figure) Recovery procedure that exploits higher order finite-differences. (Right figure) Classical unwrapping algorithm which works with first order conditions fails in this case.

Box 2: Literature on Modulo Unwrapping

—• Assumptions

(A1) Finite dimensional signals.

(A2) First order finite difference is smaller than threshold λ (Itoh's condition [169]).

—• Limitations

The one-dimensional case is fundamentally limited by the assumptions under which this problem is solved. In particular,

(L1) Continuous-time signals or functions can not be handled by current literature.

(L2) The assumption that the first order derivative is bounded by λ is highly restrictive an in many cases, this is not satisfied by real world signals such as sparse and piecewise continuous signals.
Also it is important to note that in many cases, higher order finite-differences may be smaller in the max-norm compared to the first order finite-difference. In such cases, an algorithm that can exploit higher order finite-differences should be used which is not the case in literature.

(L3) The recovery strategy does not exploit any signal structure. For example, knowing that the function is bandlimited (which is a general assumption for most analog-to-digital converters) allows for recovery of signal from higher order finite-differences.

(L4) Robustness and recovery guarantees are largely unexplored.

—• Solved and Unsolved Problems

In view of (A1) and (A2), current solutions can only deal with discrete information that satisfies Itoh's condition [169]. The problems still remains unsolved for a broader class of signals and data models covered by (L1–L4).
Another important aspect is recovery in terms of the generalized linear model in (3.3). In many cases sensing matrix or operator $\mathbf{A}$ is defined by the physical system (e.g. point spread function or low-pass pulse shape). In such cases, one hopes to recover $\mathbf{x}$ directly from measurements $\mathbf{y} = \mathbf{b} = \mathrm{mod}_\lambda(\mathbf{Ax})$. This case not covered in literature as $\mathbf{A}$ is always considered to be identity.

—• Practical Issues

(P1) On the acquisition front, there is still scope for capitalizing on sophisticated measurement devices which can "sense" modulo information of the signal directly. This is analogous to the case of compressive or compressed sensing [150].

(P2) On the implementation front, current algorithms which rely on computing finite-difference of the measured data. This operation is highly unstable in presence of noise and also leads to biased estimates [170].

3.2.2 Modulo Operator and Imaging: The Case of Two Dimensional Recovery

Study of the modulo operation in two dimensional problems is largely linked with the topic of imaging. Earlier works date back to the 70s when the problem was introduced in context of radar interferometry [171, 172, 173, 174] and topographical measurements. This lead to a line of work where there was a need to undo the effect of modulo operation in order to recover terrain elevation from wrapped data. Unsurprisingly, the first step [174] towards recovery of two dimensional terrain—in spirit of Itoh's result [169]—consisted of differentiating the phase field followed by integration of the differences. This procedure seeks to recover the unknown function with smoothness constraints.

Over the course of past three decades, this philosophy has found a number of applications related to the field of imaging. Consequently, depending on the scale (macroscopic or microscopic), nature of object to be imaged (natural scenes or scientific specimen) and other imaging criteria, a number of algorithms have also been developed. These advances can be best understood in context of our initial model in (3.3). The sensing modality decides the operator $\mathbf{A}$ and the nature of image $\mathbf{x}$ to be recovered decides the choice of algorithm. As a result, key contributions over the course of decades can be broadly classified in terms of acquisition or capture process and algorithms involved with recovery of images. A summary of the main advances is presented in Fig. 3-5. In the remainder of this section, we will quickly overview the key results.

3.2.2.1 Acquisition Devices and Application Areas

Here we review scientific or consumer image capture techniques where the modulo operator finds applications.

—• **Interferometry via Synthetic Aperture Radar**

Earlier works of Graham [171], Zebker et al. [172] and Goldstein and co-workers [173, 174] investigated an approach for estimation of ground topography from space using interferometry principles. This technique allowed for recording surface deformations in context of geophysical exploration. To give the reader an idea about scale of imaging setup, the approach of Zebker et al. [172] was capable of imaging approximately 11 km by 10 km in size which was sampled on an 11 m pixel grid and with a relative error of 6 m (root mean square).

—• **Tomographic Phase Microscopy**

In [175], Choi and co-workers report a method which is capable of quantitative three-dimensional (3D) mapping of refractive index in live cells and tissues. Their setup uses a phase-shifting laser interferometric microscope with variable illumination angle. Their demonstrated approach shows

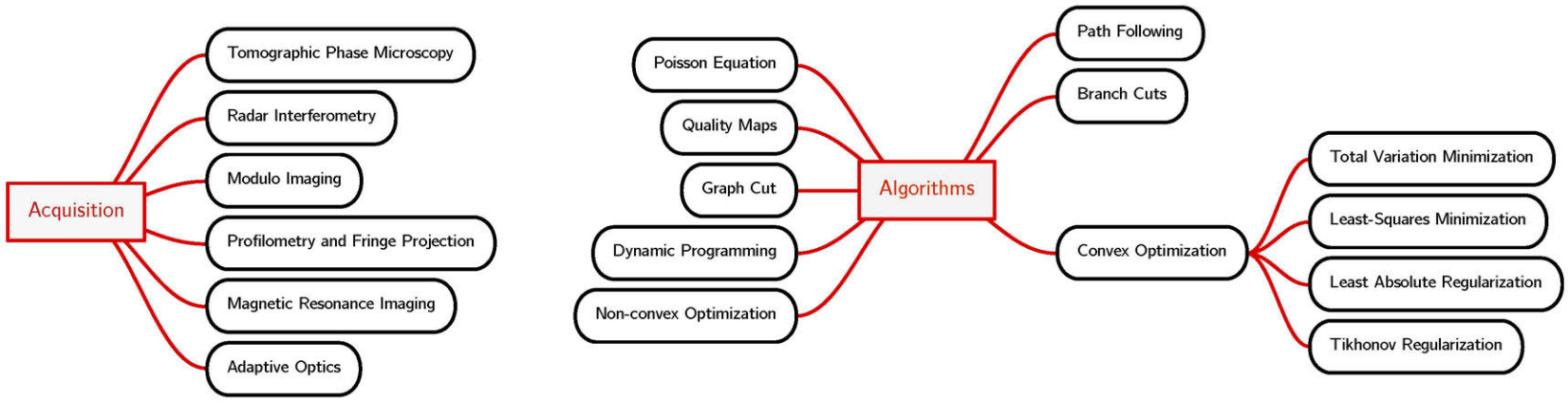

Figure 3-5: Classification of acquisition schemes and algorithms in context of two dimensional modulo operation.

tomographic imaging of cells and multicellular organisms, and is also capable of recording time-dependent changes in cell structure. In this line of work, the phase of transmitted wakefield undergoes modulo operation during acquisition process. This phase is equivalent to the line integral of the refractive index (along the direction of propagation) and hence, it must be unwrapped before estimating the refractive index.

—• **Optical and Digital Holographic interferometry**

Digital Holographic interferometry is a method for estimating three dimensional structure or displacement of an object and finds several applications due to full-field and sub-micron scale measurement capability. In this widely known technique, both the wrapped phase [176] as well as the phase derivatives [177] are of significance as the two quantities bear information regarding the scene.

—• **Magnetic Resonance Phase Imaging**

In context of magnetic resonance imaging, the phase information [178] can be designed to measure particular physical quantities. In this line of work, inverting the modulo operation finds applications in context of water and fat separation [179] as well as increasing dynamic range of phase contrast [180] in magnetic resonance velocity measurements.

—• **Adaptive Optics**

In context of adaptive optics [181], phase difference measurements can be used for estimation of wavefront distortions. The nature of measurements of being interferometric, recovering the correct phase from the wrapped phase is a problem of key interest.

—• **High Dynamic Range Imaging**

Rhee and Joo in [144] discuss the use of modified ADC architecture, mimicking modulo mapping, for increasing the dynamic range of native CMOS sensors. This work is later formally discussed in the context of SR-ADC in [182]. A quantitative study of CMOS imaging sensors in context of high dynamic range image sensor architectures is presented in [146]. More recently, Zhao *et al.* in [183] demonstrate the use of modulo sensors for high dynamic range imaging.

3.2.2.2 Recovery Algorithms

A broad classification of recovery algorithms is shows in Fig. 3-5. For an overview of the topic, we refer the reader to [184].

Classical approaches have aimed at extending the one dimensional philosophy. This involves recovery of wrapped phase information from the difference of phase field using integration. Recent and current approaches in the direction seek to reformulate phase recovery problem as an inverse problem. Such approaches seek to enforce smoothness or sparsity as a prior on the data and errors, respectively.

- **Least-squares** approaches have been formulated in the work of Hunt [185], Takajo [186] and Ghiglia [187]. Such approaches seek to minimize the squared error between the unwrapped and wrapped phases. Such approaches can be **further stabilized or improved by adding a regularizer**. For example, in [188], the authors use Tikhonov regularization. This has the advantage of

simultaneously dealing with both noise and missing data. Furthermore, the performance of such approaches can be improved by using total variation regularization [189] (instead of Tikhonov).

- Noting that quadratic regularizers end up smoothing singularities and edges, Ghiglia and Romero [190] proposed the use of ℓ_p**–norm regularization** with $p \in [0, 2)$ so that edges may be handled. However, such an approach comes with an added computational complexity since regularization with ℓ_p norms requires use of iterative algorithms (which is not the case with quadratic minization).

- **Non-convex approaches** have also been proposed in literature. For instance, the work of Rivera and Marroquin [191] studied half-quadratic loss function. Similarly, Gonzalez and Jacques [192] have used ℓ_1 penalty term for iteratively recovery the unwrapped phase by enforcing sparsity in wavelet domain.

- **Dynamic programming** based approach was used by Ying [193]. In their work, the phase is modeled using Markov random Field (MRF).

- **Graph-cut strategy** was employed by Bioucas-Dias and Valadao [194]. Their work seeks to minimize the generalized ℓ_p norm. The so-called PUMA algorithm is currently considered to be the state-of-the-art method.

- **Genetic algorithm** based approach has also been proposed in literature. For example, the work of Collaro and co-workers [195].

- Whenever the wrapped phase information follows a parametric form, for example, sum-of-complex exponentials, parameter estimation approaches may be used for phase recovery. In this context **matrix pencil method** has been proposed in literature [196, 197].

- **Poisson equation** based solutions have been proposed in medical imaging [178] and computer vision [167]. The key idea is to exploit the invariance of the gradient with respect to the modulo mapping. By considering images to be scalar fields, the solution to the recovery problem is based on the idea that the gradient field of the wrapped data can be integrated. In this context, Agrawal and co-workers [167] show that the range of solutions is linked with the degree of anisotropy in applying weights to the gradients in the recovery process. This is different from common approaches that use isotropic weights.

3.2.3 Modulo Operations in Higher Dimensions

The role of modulo operators in higher dimensions is largely unclear and hence, there is relatively lesser body of work in this direction. A conceptual extension from two to three dimensional unwrapping problem is studied by Huntley in [198]. In context of synthetic aperture radar imaging, simultaneous recovery of azimuth, range and time has been discussed in very recent papers. This requires a three dimensional recovery procedure. One such approach is due to Osmanoglu et al. [199].

3.2.4 Summary

We have reviewed the landscape of problems and solutions linked with modulo operators. In closing, we find three open areas with room for progress,

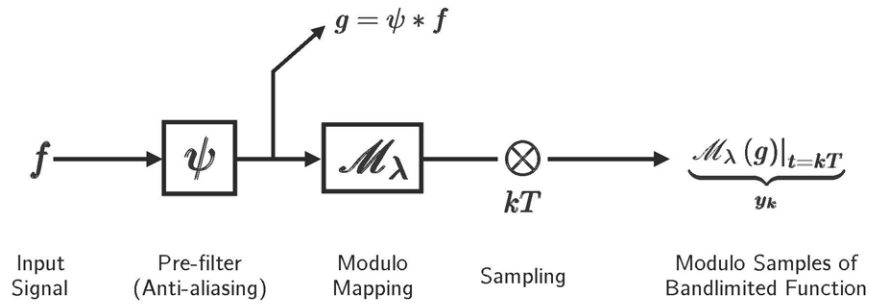

Figure 3-6: SR-ADC architecture for obtaining modulo samples.

- Recovery of structured signals with a known sensing matrix.
- Mathematical guarantees on the problem. Questions related to perfect reconstruction conditions are typically left out in the literature.
- All the cases discussed in literature deal with discrete time models. There is no theoretical framework that can handle continuous time models. For example, sparsity is an important instantiation of a continuous time model and grid-less approaches for recovery of signals is an important topic.

3.3 Unlimited Sampling of Bandlimited Signals

Motivated by the electronic architectures discussed in [144, 143], we will use the model in Fig. 3-6 for representing the SR-ADC using which we obtain modulo samples. Here $f \in L_2$ is the function to be sampled and ψ is the sampling kernel. Let $\widehat{\psi}(\omega) = \int \psi(t) e^{-\jmath\omega t} dt$ denote the Fourier Transform of ψ. We say ψ is Ω–bandlimited (cf. Definition 4 in Section 2.4.1) or,

$$\psi \in \mathcal{B}_\Omega^{\Lambda_{\mathsf{FT}}} \Leftrightarrow \quad \widehat{\psi}(\omega) = \mathbb{1}_{[-\Omega,\Omega]}(\omega)\, \widehat{\psi}(\omega) \text{ and } \psi \in L_2 \tag{3.6}$$

where $\mathbb{1}_{\mathcal{D}}(t)$ is the indicator function on domain $\mathcal{D}$. In working with Fourier domain, we will drop Λ_{FT} for notational convenience and simply write $\psi \in \mathcal{B}_\Omega$.

In practice, f may not be bandlimited, in which case, pre-filtering with $\psi \in \mathcal{B}_\Omega$ ensures that the signal to be sampled is bandlimited. In the remainder of this chapter, we will assume that we are given a low-pass filtered version of f, which we will refer to as $g \stackrel{\text{def}}{=} f * \psi$. Furthermore, we will normalize the bandwidth to π such that $g \in \mathcal{B}_\pi$. This function g then undergoes a non-linear, amplitude folding defined in (3.1) and results in,

$$z(t) = \mathscr{M}_\lambda(g(t)). \tag{3.7}$$

Finally, the output of (3.1), that is, $\mathscr{M}_\lambda(g(t))$ is sampled using impulse-modulation, $\otimes_{kT} \stackrel{\text{def}}{=} \sum_{n\in\mathbb{Z}} \delta(t - kT)$, where $T > 0$ is the sampling rate. This results in uniform samples,

$$y_k \stackrel{\text{def}}{=} z(kT) = \mathscr{M}_\lambda(g(kT)), \quad k \in \mathbb{Z} \tag{3.8}$$

as shown in Fig. 3-6. To develop a sense about the functionality of the SR-ADC, in Fig. 3-7-(a), we

plot $g(t)$, $z(t)$ and samples y_k. It is clear that the self-reset ADC converts a smooth function into a discontinuous one. This is an important aspect that is attributed to the presence of simple functions arising from (3.1).

Proposition 5 (Modular Decomposition)**.** *Let $g \in \mathcal{B}_\pi$ be a zero-mean function and $\mathscr{M}_\lambda(g(t))$ be defined in (3.1) with λ fixed, non-zero constants. Then, the bandlimited function g admits a decomposition*

$$g(t) = z(t) + \varepsilon_g(t), \tag{3.9}$$

where ε_g is a simple function, $\varepsilon_g(t) = 2\lambda \sum_{\ell \in \mathbb{Z}} e_\ell \mathbb{1}_{\mathcal{D}_\ell}(t), e_\ell \in \mathbb{Z}$.

Proof. Since $z(t) = \mathscr{M}_\lambda(g(t))$, by definition, we write,

$$\begin{aligned} \varepsilon_g(t) &\overset{(3.9)}{=} g(t) - \mathscr{M}_\lambda(g(t)) \\ &\overset{(a)}{=} 2\lambda\left(h(t) - [\![h(t)]\!]\right) \overset{(b)}{=} 2\lambda \lfloor h(t) \rfloor, \end{aligned} \tag{3.10}$$

where (a) is due to $(g/2\lambda) + 1/2 \mapsto h$ and in (b), we use $h = [\![h]\!] + \lfloor h \rfloor$. Since $\lfloor h \rfloor$, for an arbitrary function h, can be written as,

$$\lfloor h(t) \rfloor = \sum_{\ell \in \mathbb{Z}} e_\ell \mathbb{1}_{\mathcal{D}_\ell}(t), \quad e_\ell \in \mathbb{Z}, \tag{3.11}$$

we obtain the desired result. ■

3.3.1 A Sufficiency Condition and a Sampling Theorem

In this section, we concretely answer the following questions:

Consider the sampling architecture described in Fig. 3-6. Let $g \in \mathcal{B}_\pi$ and suppose that we are given modulo samples of g defined by y_k in (3.8),

Q1: *What are the conditions for recovery of g from y_k?*

Q2: *In the spirit of Shannon's sampling theorem, is there a constructive algorithm that maps samples $y_k \to g$?*

In what follows, we will answer the two questions affirmatively.

3.3.1.1 Main Result: The Unlimited Sampling Theorem

Given the sequence of modulo samples y_k, our basic strategy will be to apply a higher order finite difference operator Δ^N, where the first order finite difference Δ is given by

$$(\Delta y)_k = y_{k+1} - y_k$$

and similarly, higher order differences are directly obtained using,

$$y^{[N]} = \left(\Delta^N y\right)_k = \sum_{n=0}^{N} (-1)^n \mathrm{B}_n^N y_{k+(N-n)} \tag{3.12}$$

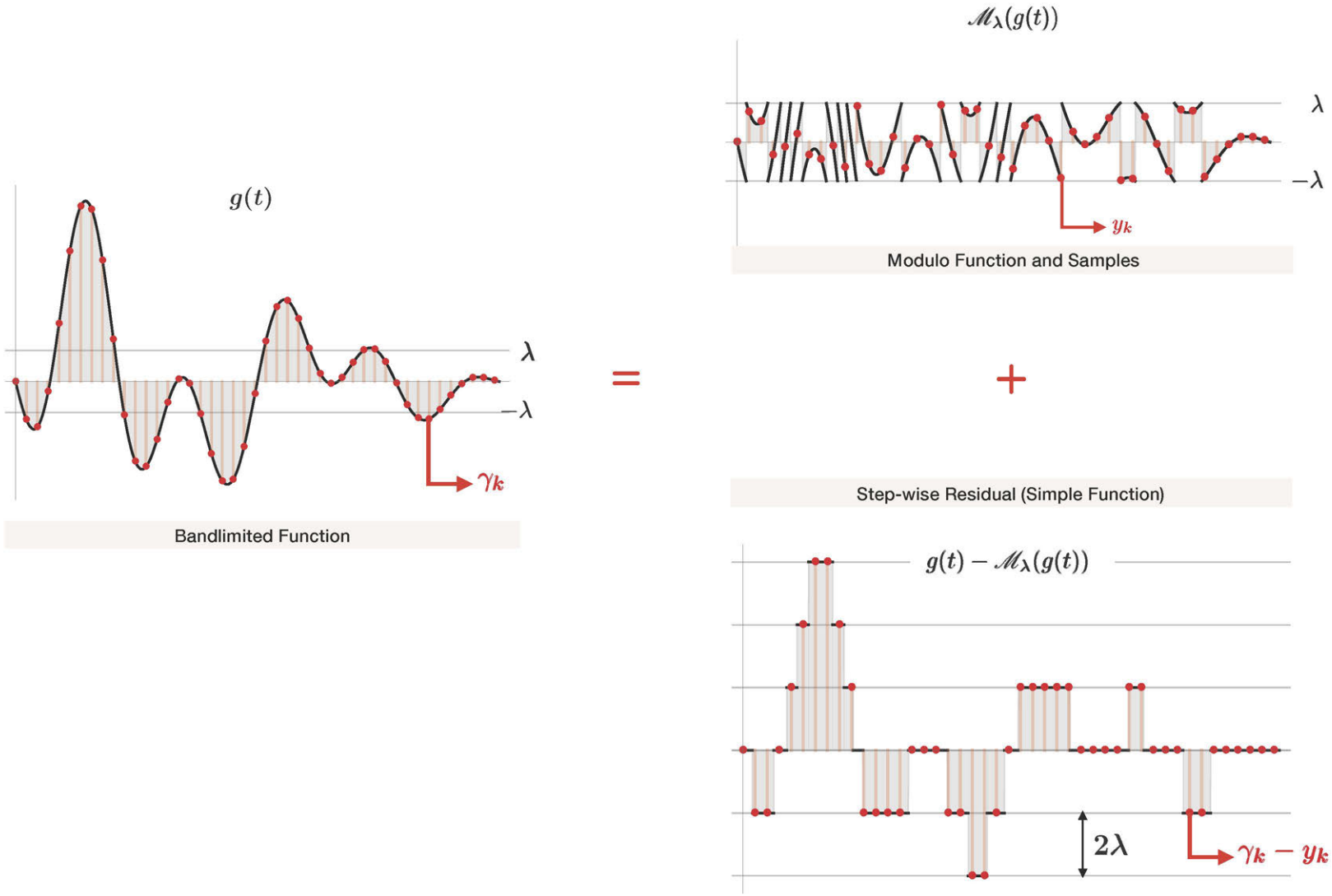

Figure 3-7: For a prototype low-pass filtered data $g = f * \psi$ (in ——) we plot the continuous version of the modulo-ADC $\mathscr{M}_\lambda(g(t))$ (in ——) together with uniform samples y_k (in —•). We plot the continuous time residual $\varepsilon_g(t) = g(t) - \mathscr{M}_\lambda(g(t))$ (in ——) and its sampled version $\{\varepsilon_\gamma = \gamma_k - y_k\}$ (in —•).

where B_n^N denotes binomial coefficient given by,

$$\mathrm{B}_n^N \stackrel{\text{def}}{=} \binom{N}{n} = \frac{N!}{n!\,(N-n)!} \tag{3.13}$$

and $n!$ is the factorial of n.

We will be exploiting that such operators commute with the modulo operation. So after applying the amplitude folding (3.1) to the resulting sequence, one obtains the same output as if one had started with g_k instead of y_k. That in turn will allow for recovery if the higher order finite differences of the g_k's are so small that the amplitude folding has no effect. This is conceptually illustrated in Fig. 3-8.

Consequently, our goal will be to investigate when higher order finite differences of samples of a bandlimited function are small enough. One way to ensure this is to sufficiently oversample. A first step towards this goal will be to relate the sample finite difference and the derivative of a bounded function. This well-known observation is summarized in the following lemma.

Lemma 2. *For any $g \in C^m(\mathbb{R}) \cap L_\infty(\mathbb{R})$, its samples $\gamma_k \stackrel{\text{def}}{=} g(kT)$ satisfy*

$$\|\Delta^N \gamma\|_\infty \leq T^N e^N \|g^{(N)}\|_\infty. \tag{3.14}$$

Proof. Using Taylor's theorem, we can express $g\,(t)$ locally around an anchor point τ as the sum of a polynomial of degree $N-1$ and a remainder term of the form $r_l = \frac{g^{(N)}(\xi_l)}{N!}(lT-\tau)^N$ for some intermediate value ξ_l between lT and τ. As $\gamma^{[N]}$ is a linear combination of $g\,(t_n)$'s with

$$t_n = (k+n)T \in [kT, (n+k)T], \;\; n = 0, \ldots, N,$$

we choose the anchor point $\tau = (k + \frac{N}{2})T$. As Δ^N annihilates any polynomial of degree $N-1$, only the remainder term takes effect and we have

$$(\Delta^N \gamma)_k = (\Delta^N r)_k = \left(\Delta^N r_{k|N}\right)_0,$$

where

$$r_{k|N} = \begin{bmatrix} r_k & r_{k+1} & \cdots & r_{k+N} \end{bmatrix}^\top.$$

Noting that for any vector $\mathbf{v}$ one has by definition $\|\Delta \mathbf{v}\|_\infty \leq 2\|\mathbf{v}\|_\infty$, it follows that

$$\begin{aligned} ||\Delta^N \gamma||_\infty &\leqslant 2^N ||r^{[k]}||_\infty \\ &\leqslant 2^N \frac{||g^{(N)}||_\infty}{N!} \left(\frac{NT}{2}\right)^N \\ &\leqslant T^N e^N ||g^{(N)}||_\infty, \end{aligned} \tag{3.15}$$

where in the last step, we used Stirling's approximation. ■

To bound the right hand side of (3.15), we invoke Bernstein's inequality (cf. pg. 116 in [200]),

$$||g^{(N)}||_\infty \leqslant \pi^N ||g||_\infty. \tag{3.16}$$

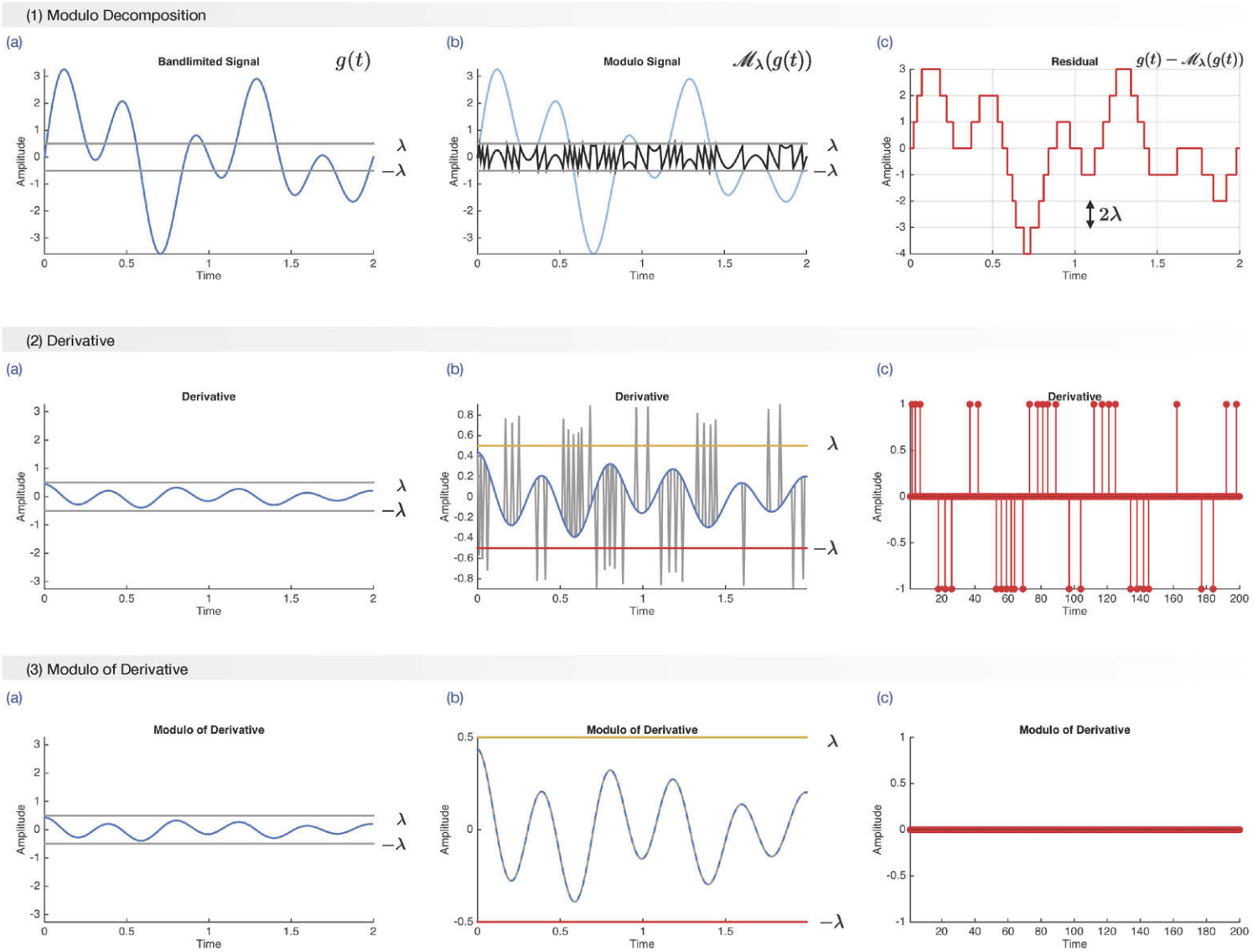

Figure 3-8: Higher order differences commute with the modulo operation. After applying the amplitude folding (via modulo operation) to the derivative (and difference of modulo samples, respectively), one obtains the same output as if one had started with g_k instead of y_k. That in turn will allow for recovery if the higher order finite differences of the samples or g_k's are so small that the amplitude folding has no effect.

Consequently, by combining (3.15) and (3.16), we obtain,

$$||\Delta^N \gamma||_\infty \leqslant (T\pi e)^N ||g||_\infty. \tag{3.17}$$

This inequality will be at the core of our proposed recovery methods. Namely, provided $T < \frac{1}{\pi e}$, choosing N logarithmically in $\|g\|_\infty$ ensures that the right hand side of (3.17) is less than λ. More precisely, assuming that some $\beta_g \in 2\lambda\mathbb{Z}$ is known with $||g||_\infty \leqslant \beta_g$, a suitable choice is

$$N = \left\lceil \frac{\log \lambda - \log \beta_g}{\log (T\pi e)} \right\rceil. \tag{3.18}$$

For the remainder of this chapter we will work with this choice of N and assume $T \leq \frac{1}{2\pi e}$, which yields the assumption in a stable way. We believe that a more precise analysis along the same lines will also yield corresponding bounds for $T \in [\frac{1}{2\pi e}, \frac{1}{\pi e})$.

The bound of λ for (3.17) in turn entails that the folding operation has no effect on $\Delta^N \gamma$, that is,

$$\gamma^{[N]} \stackrel{\text{def}}{=} \Delta^N \gamma \equiv \mathscr{M}_\lambda(\gamma^{[N]}) = \mathscr{M}_\lambda(\gamma^{[N]}), \tag{3.19}$$

which allows for recovery of $\gamma^{[N]}$, as the right hand side can be computed from the folded samples y. Here, the last equality in (3.19) follows by applying the following standard observation to $a = \gamma - \frac{1}{2}$.

Proposition 6. *For any sequence a it holds that*

$$\mathscr{M}_\lambda(\Delta^N a) = \mathscr{M}_\lambda(\Delta^N(\mathscr{M}_\lambda(a)). \tag{3.20}$$

Proof. As usual, let $a^{[N]} \stackrel{\text{def}}{=} \Delta^N a$. In view of Proposition 5 and (3.9), a admits a unique decomposition, $a = \mathscr{M}_\lambda(a) + \varepsilon_a$ where ε_a is a simple function. This allows us to write, $\Delta^N \mathscr{M}_\lambda(a) = a^{[N]} - \varepsilon_a^{[N]}$. Based on the distributive property of $[\![t]\!] \equiv t \bmod 1$, it is not difficult to show that,

$$\mathscr{M}_\lambda(a_1 + a_2) = \mathscr{M}_\lambda(\mathscr{M}_\lambda(a_1) + \mathscr{M}_\lambda(a_2)).$$

And hence,

$$\mathscr{M}_\lambda\left(\Delta^N \mathscr{M}_\lambda(a)\right) = \mathscr{M}_\lambda\left(a^{[N]} - \varepsilon_a^{[N]}\right) = \mathscr{M}_\lambda\left(\mathscr{M}_\lambda\left(a^{[N]}\right) - \mathscr{M}_\lambda\left(\varepsilon_a^{[N]}\right)\right).$$

Now since ε_a take values $2k\lambda$, $k \in \mathbb{Z}$, $\Delta^N \varepsilon_a = \varepsilon_a^{[N]}$ takes values of the form $\{(-1)^n 2\lambda \mathrm{B}_n^N\}_{n=0}^N \in \mathbb{Z}$ where B_n^N is the Binomial coefficient in (3.13). From this, we conclude that $\varepsilon_a^{[N]}$ is in the kernel of $\mathscr{M}_\lambda(\cdot)$ or $\mathscr{M}_\lambda\left(\varepsilon_a^{[N]}\right) = 0$ and it follows that,

$$\mathscr{M}_\lambda\left(\Delta^N \mathscr{M}_\lambda(a)\right) = \mathscr{M}_\lambda\left(\mathscr{M}_\lambda\left(a^{[N]}\right)\right) = \mathscr{M}_\lambda\left(a^{[N]}\right),$$

which proves the result in (3.20). ■

To choose N, we need some upper bound β_g such that $\|g\|_\infty \leq \beta_g$, which we assume to be available for the remainder of this chapter. As it simplifies the presentation, we assume w.l.o.g. that $\beta_g \in 2\lambda\mathbb{Z}$. Note that β_g is only needed for recovery; there are no limitations on β_g arising from the circuit architecture.

To recover the sequence γ, recall from Proposition 5 that $\varepsilon_\gamma \stackrel{\text{def}}{=} \gamma - y$, that is, the sampled version of ε_g takes as values only multiples of 2λ. As y is observed, finding ε_γ is equivalent to finding γ. Noting that $\varepsilon_\gamma^{[N]} \stackrel{\text{def}}{=} \Delta^N(\gamma - y)$ can be computed from the data (via (3.19)), it remains to investigate how ε_γ can be recovered from $\varepsilon_\gamma^{[N]} = \Delta^N \varepsilon_\gamma$. Due to the massive restriction on the range of all $\Delta^n \varepsilon_\gamma$, this problem is considerably less ill-posed than the problem of recovering γ from $\Delta^N \gamma$. In particular, repeatedly applying the summation operator $\mathsf{S} : (a_i)_{i=1}^\infty \mapsto (\sum_{i'=1}^i a_{i'})_{i=1}^\infty$, the inverse of the finite difference, is a stable procedure because in the implementation we can round to the nearest multiple of 2λ in every step.

There still is, however, an ambiguity that needs to be resolved. Namely, the constant sequence is in the kernel of the first order finite difference, so its inverse can only be calculated up to a constant. Thus when computing $\Delta^{n-1}\varepsilon_\gamma$ from $\Delta^n \varepsilon_\gamma, n = 1, \ldots, N$, the result can only be determined up to an integer multiple of the constant sequence ℓ with value 2λ, that is,

$$\Delta^{n-1}\varepsilon_\gamma = \mathsf{S}\Delta^n \varepsilon_\gamma + \kappa_{(n)}\ell,$$

for some $\kappa_{(n)} \in \mathbb{Z}$. For $n = 1$, this ambiguity cannot be resolved, as adding multiples of 2λ to a function results in the same modulo samples. To resolve this ambiguity for $n > 1$, we apply the summation operator a second time. Repeating the same argument, we obtain that

$$\Delta^{n-2}\varepsilon_\gamma = \mathsf{S}^2\Delta^n \varepsilon_\gamma + L\kappa_{(n)} + \kappa_{(n-1)}\ell, \tag{3.21}$$

where $L = \mathsf{S}\ell = (2\lambda i)_{i=1}^\infty$. This now implies that

$$\begin{aligned}
&\left(\mathsf{S}^2\Delta^n\varepsilon_\gamma\right)_1 - \left(\mathsf{S}^2\Delta^n\varepsilon_\gamma\right)_{J+1} \\
&\quad = \left(\Delta^{n-2}\varepsilon_\gamma\right)_1 - \left(\Delta^{n-2}\varepsilon_\gamma\right)_{J+1} + 2\lambda\kappa_{(n)}J \\
&\quad = \left(\Delta^{n-2}\gamma\right)_1 - \left(\Delta^{n-2}\gamma\right)_{J+1} - \left(\Delta^{n-2}y\right)_1 - \left(\Delta^{n-2}y\right)_{J+1} + 2\lambda\kappa_{(n)}J \\
&\quad \in 2\lambda\kappa_{(n)}J + \left(2(T\pi e)^{n-2}\beta_g + 2^{n-1}\lambda\right)[-1, 1] \qquad (3.22) \\
&\quad \subseteq 2\lambda J\left[\kappa_{(n)} - \tfrac{\beta_g}{\lambda J} - \tfrac{2^{n-2}}{J}, \kappa_{(n)} + \tfrac{\beta_g}{\lambda J} + \tfrac{2^{n-2}}{J}\right]
\end{aligned}$$

where (3.22) uses (3.17) together with the fact that $\|y\|_\infty \leq \lambda$. As $n \leq N$, (3.18) yields that

$$2^{n-1} \leq 2^{N-1} \leq \frac{\beta_g}{\lambda}^{-\frac{1}{\log_2(T\pi e)}} \leq \frac{\beta_g}{\lambda}, \tag{3.23}$$

where the last step uses that $T \leq \frac{1}{2\pi e}$. So one obtains

$$\left(\mathsf{S}^2\Delta^n\varepsilon_\gamma\right)_1 - \left(\mathsf{S}^2\Delta^n\varepsilon_\gamma\right)_{J+1} \in 2\lambda J\left[\kappa_{(n)} - \frac{3\beta_g}{2\lambda J}, \kappa_{(n)} + \frac{3\beta_g}{2\lambda J}\right]$$

and choosing $J = \frac{6\beta_g}{\lambda}$ directly yields that

$$\kappa_{(n)} = \left\lfloor \frac{(\mathsf{S}^2\Delta^n\varepsilon_\gamma)_1 - (\mathsf{S}^2\Delta^n\varepsilon_\gamma)_{J+1}}{8\beta_g} + \frac{1}{2} \right\rfloor. \tag{3.24}$$

With this last ingredient, we are now ready to formulate our recovery method, Algorithm 1. For this

Algorithm 1: Recovery from Modulo Folded Samples

Data: $y_k = \mathscr{M}_\lambda(g(kT))$, $N \in \mathbb{N}$, and $2\lambda\mathbb{Z} \ni \beta_g \geqslant \|g\|_\infty$.
Result: $\widetilde{g} \approx g$.
1) Compute $y^{[N]} = \Delta^N y$.
2) Compute $\varepsilon_\gamma^{[N]} = \mathscr{M}_\lambda\left(y^{[N]}\right) - y^{[N]}$. Set $s_{(1)} = \varepsilon_\gamma^{[N]}$.
3) for $n = 1 : N-1$
    Compute $\kappa_{(n)}$ in (3.24).
    $s_{(n+1)} = \mathsf{S}s_{(n)} + 2\lambda\kappa_{(n)}$.
    Round $s_{(n+1)}$ to the nearest integer multiple of 2λ. (Consistency Relation)
end
4) $\{\widetilde{\gamma}\}_k = \{\mathsf{S}s_{(N)}\}_k + y_k$.
5) Compute $\widetilde{g}$ from $\widetilde{\gamma}$ via low-pass filter.

algorithm, the discussion in the previous paragraph yields the following recovery result, the main result of this work.

Theorem 9 (Unlimited Sampling Theorem)**.** *Let $g(t) \in \mathcal{B}_\pi$ and $y_k = \mathscr{M}_\lambda\left(g(t)\right)|_{t=kT}$, $k \in \mathbb{Z}$ in (3.8) be the modulo samples of $g(t)$ with sampling rate T. Then a sufficient condition for recovery of $g(t)$ from the $\{y_k\}_k$ up to additive multiples of 2λ is that*

$$T \leq \frac{1}{2\pi e}. \tag{3.25}$$

Provided that this condition is met and assuming that $\beta_g \in 2\lambda\mathbb{Z}$ is known with $||g||_\infty \leqslant \beta_g$, then choosing

$$N = \left\lceil \frac{\log\lambda - \log\beta_g}{\log(T\pi e)} \right\rceil, \tag{3.26}$$

yields that $(T\pi e)^N \|g\|_\infty < \lambda$ and Algorithm 1 recovers g from y again up to the ambiguity of adding multiples of 2λ.

To put the theorem into perspective, note that in (3.25), there are two degrees of freedom that are of a very different nature. On the one hand, the time $T > 0$ between two samples is intrinsically related to the circuit design, on the other hand, the number N of finite difference applied is only relevant for the reconstruction. Hence only then, a bound for the supremum norm of the signal is required, the ADC itself is truly unlimited in that T does not depend on g and hence a fixed architecture allows to capture signals of arbitrary amplitude.

Recalling from the above discussion that one is in fact trying to satisfy the sufficient condition

$$(T\pi e)^N \|g\|_\infty < \lambda,$$

one sees that an alternative way to achieve this will be to consider a fixed N and increase the oversampling rate. While this may be preferred in certain scenarios for computational reasons, this approach will no longer be unlimited, as decreasing T would require to change the circuit architecture. That is why we decided to focus fixed T and variable N in our presentation.

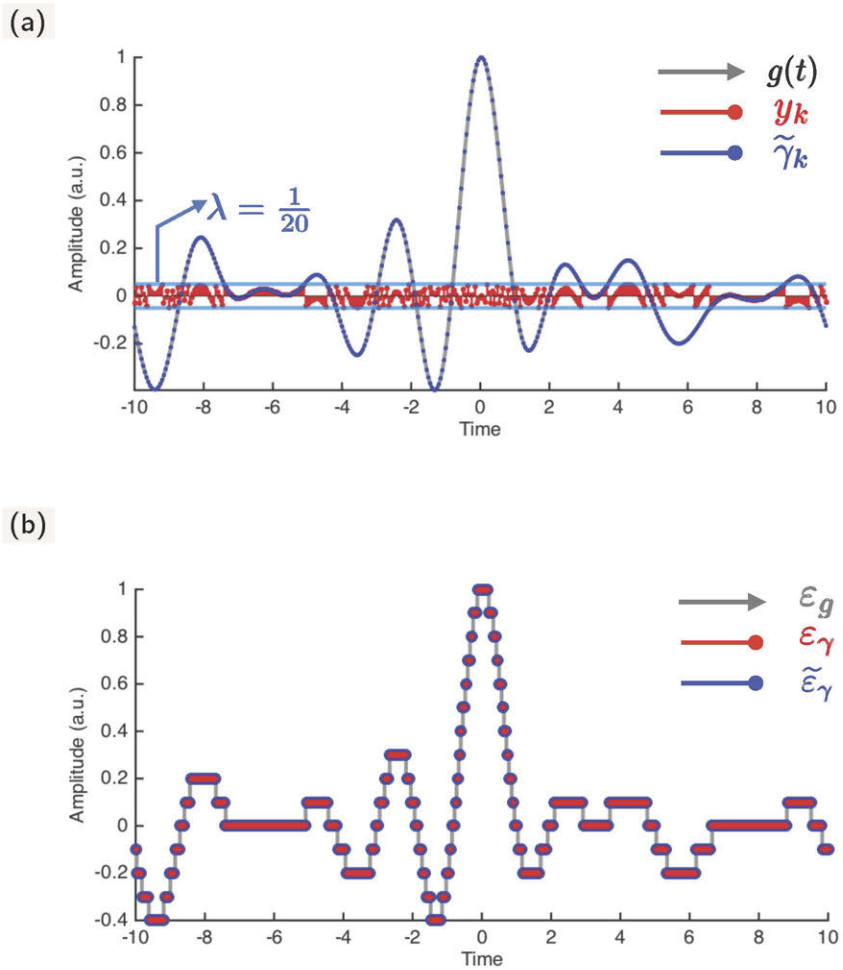

Figure 3-9: Modulo sampling of bandlimited functions. (a) Randomly generated bandlimited function $g \in \mathcal{B}_\pi$, its modulo samples y_k acquired with $\lambda = 1/20$ and $T \approx 1/2\pi e$, as well as reconstructed samples $\widetilde{\gamma}_k$ with $N = 5$. The mean squared error between $\gamma_k = g(kT)$ and reconstructed samples, $\widetilde{\gamma}_k$ was 1.6×10^{-33}. (b) We plot $\varepsilon_g(t) = g(t) - y(t)$ and compare the ground truth ε_γ with its reconstructed version $\widetilde{\varepsilon}_\gamma$. The mean squared error between ε_γ and $\widetilde{\varepsilon}_\gamma$ was of the order of machine precision, 1.5×10^{-33}.

3.3.2 Numerical Demonstration

We validate our approach via a numerical demonstration. We generate $g \in \mathcal{B}_\pi$ by multiplying the Fourier spectrum of the sinc–function with weights drawn from the standard uniform distribution and then rescale g so that $||g||_\infty = 1$. With $\lambda = 1/20$ and $T \approx 1/2\pi e$, we sample the signal and record y_k. This is shown in Fig. 3-9(a). By implementing Algorithm 1 described above with $N = 5$, rounding to the nearest multiple of 2λ for stability, we reconstruct samples $\widetilde{\gamma}_k$ as well as $\widetilde{\varepsilon}_g$ as shown in Fig. 3-9(a). The reconstruction error is of the order of Matlab's numerical precision. For comparison purposes, we plot ε_g and $\widetilde{\varepsilon}_g$ in Fig. 3-9(b).

3.4 Unlimited Sampling of Sparse Signals

As mentioned in Section 2.1.2, recovering spikes from low-pass filtered measurements is a problem that finds applications in several fields of science and engineering. Concretely speaking, consider the model:

$$g(t) = \sum_{k=0}^{K-1} c_k \psi(t - t_k) \equiv (s_K * \psi)(t) \tag{3.27}$$

where ψ is a bandlimited function and s_K is a continuous time, K–sparse, τ-periodic signal,

$$s_K(t) \overset{(2.11)}{=} \sum_{m \in \mathbb{Z}} \sum_{k=0}^{K-1} c_k \delta(t - t_k - m\tau), \quad t_{k+1} > t_k. \tag{3.28}$$

With ψ known and given sampled measurements

$$y_n = y(nT), n = 0, \ldots, N-1,$$

where $T > 0$ is the sampling rate, one is typically interested in recovering $s_K(t)$ from discrete set of N measurements $\{g_n\}_{n=0}^{N-1}$. In the recent years, this problem has been widely studied under the theme of

1. sparse deconvolution [57]
2. sparse or FRI sampling [69, 70]
3. super-resolution [60]

While this problem has a known history with roots tracing back to seismic imaging [201, 52], recent developments allow for recovery of sparse signals with support $\{t_k\}_{k=0}^{K-1} \in [0, \tau)$ at arbitrary points on the real line rather than restricted to a pre-described grid. Hence this leads to so-called "off-the-grid" recovery approaches [168].

Summarizing the contents of Section 2.1.2, the sparse signal recovery problem is closely tied to the topic of Shannon's sampling theory [28]. In analogy to the sampling of bandlimited signals where by the signal is pre-filtered with an anti-aliasing or low-pass filter, the measurements g_n can be written as,

$$g_n = \underbrace{\int s_K(t) \overline{\psi}(t - nT)\, dt}_{\text{Projection}} \equiv \underbrace{(s_K * \psi)(t)|_{t=nT}}_{\text{Pre-filtering and Sampling}}, \tag{3.29}$$

which is equivalent to low-pass projections of s_K onto subspace of bandlimited functions denoted by $\mathsf{V}_{\mathsf{BL}} = \text{span}\left\{\overline{\psi}(t - nT)\right\}_{n=0}^{N-1}$ and where $\overline{\psi}(t) = \psi(-t)$. A natural question then is: When is the mapping between the sparse signal $s_K(t)$ and samples $\{g_n\}_{n=0}^{N-1}$, one-to-one? It was shown by Li and Speed (cf. Thm 3.2,[57]) and Vetterli, Blu and co-workers (cf. Thm 1,[69],[70]) that $N \geq 2K + 1$ gurantees exact recovery of $s_K(t)$ from g_n provided that the support or the locations $t_k \in [0, \tau)$ are distinct. The recovery procedure [69] then relies on Fourier domain extrapolation which is outlined in Algorithm 2.

Algorithm 2: Sparse Sampling and Reconstruction [69, 70]

Data: K, $\{g_n\}_{n=0}^{N-1}$, $N \geq 2K+1$ and kernel $\psi_n = \psi(nT)$.

Result: Estimate of s_K in form of $\{\widetilde{c}_k, \widetilde{t}_k\}_{k=0}^{K-1}$.

1) Compute the (discrete) Fourier transform of g_n and $\psi(nT)$, that is, $\widehat{g}_m = \widehat{g}(m\omega_0)$ and $\widehat{\psi}_m = \widehat{\psi}(m\omega_0)$, respectively where $\omega_0 = 2\pi/\tau$.
2) Deconvolve to obtain $\widehat{s}_m = \widehat{g}_m/\widehat{\psi}_m, |m| \leqslant M$ where $M \geq K$ is the bandwidth of ψ.
3) Use spectral estimation to estimate $\{c_k, t_k\}_{k=0}^{K-1}$ from data $\widehat{s}_m$.

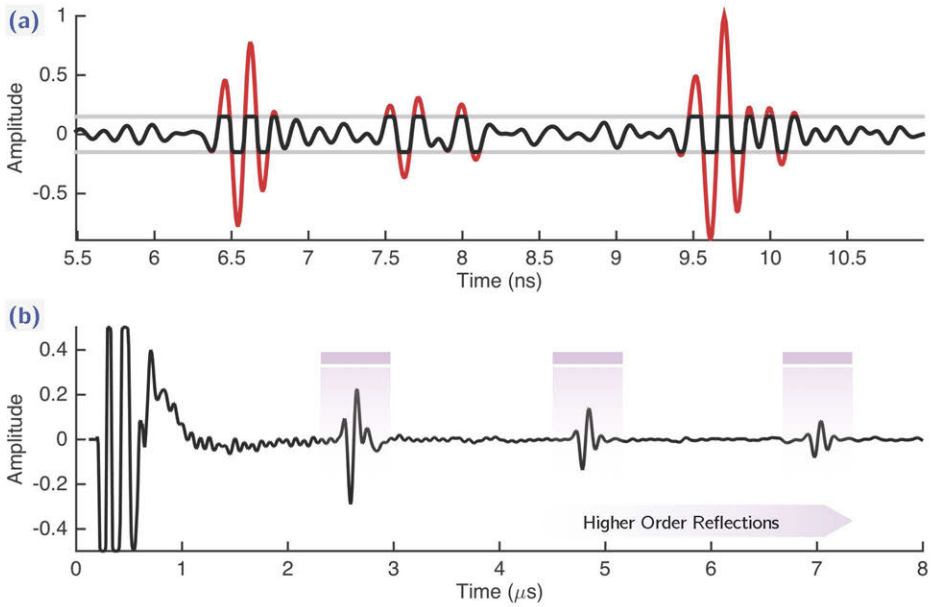

Figure 3-10: Two practical scenarios for amplitude limited sampling. (a) Ultra-wide band signal undergoes saturation. (b) Data from ultrasonic sensor reveals that the dominant reflection is clipped or saturated as it exceeds the maximum recordable voltage of the ADC. In this case, exact calibration of ψ is not possible.

3.4.0.1 Sampling and Recovery of Sparse Signals in Practice

In recovering sparse signals from low-pass projections, one fundamental assumption that is made in theory is that the dynamic range of the sensor or the analog to digital converter (ADC) is infinite. To the best of our knowledge, such assumptions appear in all previous works on the problem [57, 69, 60, 202, 72, 80, 78, 66, 73].

In practice, however, ADCs are finite dynamic range devices and whenever a signal crosses the threshold (or the maximum recordable voltage), the measurements are *saturated* or *clipped*. Clipping of a bandlimited signal results in discontinuities which manifest as aliasing due to high frequency distortion in the Fourier domain [138]. In view of this, a number of numerical methods have been proposed in the literature [134, 137, 136, 203], however, the exact link to sampling theory of bandlimited or sparse signals remains largely unclear.

This problem is of specific practical relevance in the context of calibration, namely, the knowledge of

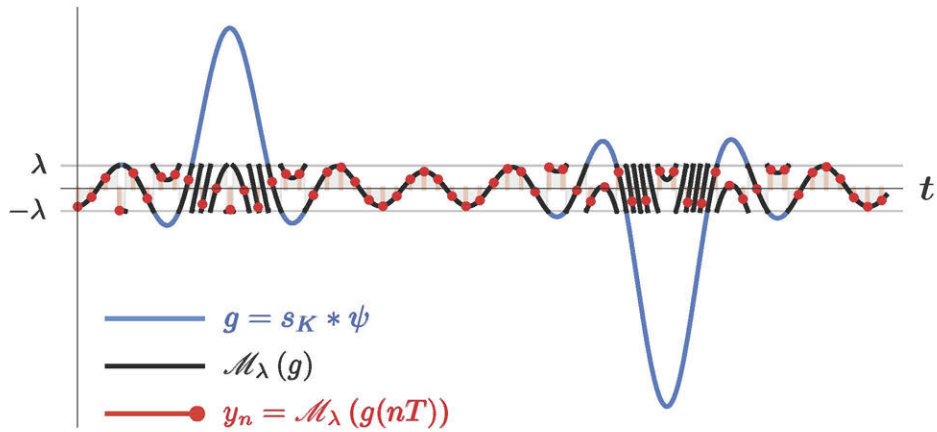

Figure 3-11: Unlimited sampling of sparse signals with $K = 2$. We plot low-pass filtered data g (cf. (3.27), the folded function $\mathscr{M}_\lambda(g)$ as well as modulo samples y_n in (3.8).

the unknown kernel ψ is critical for accurate recovery of s_K in sparse sampling models such as (3.27). In almost all of the applications, the kernel ψ is obtained in a calibration phase [73].

During this phase, the received amplitudes are typically larger than during the following sensing phase, as shown via experimental measurements in context of ultra-wide band sensing in Fig. 3-10(a) and ultra-sonic non-destructive testing in Fig. 3-10(b). Consequently, either saturation limits the exact calibration of ψ and the sparse sampling model (3.27) is invalid, or one has to work with a very high dynamic range, which will impact the measurement resolution as well as the penetration depth of ψ (cf. [73, 204, 205]. In view of model (3.27), some application areas where this problem frequently arises includes ground penetrating radar [204] (cf. pg. 149, Fig. 5.2), seismic imaging [205], ultra-wideband sensing [206] and ultrasound imaging [207]. Not surprisingly, most of these solutions rely on:

1) ADC level corrections [206, 207], or,

2) De-clipping followed by deconvolution [205, 135].

It is clear from literature that existing approaches decouple acquisition (hardware) from recovery algorithm (software). The downside being, hardware-only approaches [206, 207] are limited by computation that can be handled by hardware and algorithm-only approaches solve a sequential problem of de-clipping followed by spike recovery. For the latter, the quality of reconstruction depends on the effectivity of the de-clipping algorithm and is less attractive in practice because the ψ may still be unknown.

3.4.1 Problem Setup

Let $\psi \in \mathcal{B}_\pi$ be a given low-pass filter and s_K be defined in (3.28). Furthermore, let $\{y_n\}_{n=0}^{N-1}$ in (3.8) be the *modulo samples* of g defined in (3.27). We plot the low-pass filtered function $g(t)$ as well as modulo samples $\{y_n\}$ in Fig. 3-11. The purpose of this section is to study the perfect reconstruction condition which guarantees recovery of continuous-time sparse signal s_K from modulo samples y_n.

Our basic strategy for recovering s_K from y_n can be summarized as,

$$y_n \xrightarrow{\text{Unfolding}} g_n \xrightarrow{\text{Sparse Recovery}} s_K(t).$$

This approach relies on extracting unfolded, contiguous sample sequence g_n of size $2K+1$ from which $s_K(t)$ is estimated using high-resolution frequency estimation [69, 70, 57]. To see this, we split the problem into two parts which are discussed subsequently.

3.4.2 Localized Reconstruction from Unlimited Sampling

Given $g \in \mathcal{B}_\pi$ and $y_n, n \in \mathbb{Z}$ in (3.8), the problem of recovering $g_n, n \in \mathbb{Z}$ was discussed in . In this work, in contrast to Section 3.3, it suffices to recover a subset of g_n with size $N = 2K+1$ rather than the full sequence, but we only have finitely many modulo samples at our disposal. This fundamentally different setup requires a new approach which we will develop in this section. The first step towards that goal is the same as in Section 3.3. Namely the following lemma, which summarizes Lemma 2 and Proposition 6 of Section 3.3, shows that higher order differences Δ^L, that is., repeated applications of the first-order difference defined by $(\Delta y)_n = y_{n+1} - y_n$, of the modulo samples y_n allow for the reconstruction of the higher order differences of the original signal[2].

Lemma 3. *For $g \in \mathcal{B}_\pi$, set $g_n = g(nT), T \in \mathbb{R}^+$ and assume that some bound $\beta_g \geq \|g\|_\infty$ is available. Furthermore, assume that $T\pi e \leq \frac{1}{2}$ and choose*

$$L = \left\lceil \frac{\log \lambda - \log \beta_g}{\log(T\pi e)} \right\rceil.$$

Then the sequence $y_n = \mathscr{M}_\lambda(g_n)$ of modulo samples satisfies

$$\Delta^L g_n = \mathscr{M}_\lambda\left(\Delta^L g_n\right) = \mathscr{M}_\lambda\left(\Delta^L y_n\right). \tag{3.30}$$

Consequently, finding an L-th order finite differences of the sequence g_n just requires the corresponding L-th order finite differences of the sequence y_n of modulo samples, which in turn can be constructed from $L+1$ subsequent samples of y_n. Due to the overlap in the samples used, finding some number R of subsequent L-th order finite differences of the sequence g_n requires $L+R$ subsequent samples of y_n.

It remains to reconstruct the sequence g_n from its L-th order finite differences. As in Section 3.3, we invert each of the repeated finite difference operators sequentially, and the difficulty is that in each step, the inverse is only defined up to an additive constant. Given that the modulo samples are available, this ambiguity consists of even integer multiples of λ, and the right constants can be derived from boundedness properties of bandlimited functions (cf. Section 3.3).

More precisely, note that $g \in \mathcal{B}_\pi$ can be uniquely decomposed as $g = \mathscr{M}_\lambda(g) + \varepsilon_g$ where ε_g is a simple function, $\varepsilon_g(t) = 2\lambda \sum_{\ell \in \mathbb{Z}} e_\ell \mathbb{1}_{\mathcal{D}_\ell}(t), e_\ell \in \mathbb{Z}$. With $y_n = \mathscr{M}_\lambda(g(nT))$ given, knowing ε_g is equivalent to the knowledge of g_n. Due to highly structured form of ε_g, there is a strong restriction on the range of the same. Namely, we may enforce the amplitude restriction that $\Delta^{\ell-1}\varepsilon_g \in 2\lambda\mathbb{Z}$ when applying

[2]A similar observation has been made in the phase-unwrapping literature where the well known Itoh's condition [169] requires $||\Delta y||_\infty < \lambda$. However, this approach is highly restrictive for it works only with $L = 1$ and by inverting the discrete difference without exploiting any signal structure.

Algorithm 3: Sparse Recovery from Modulo Folded Samples

Data: Sparsity level K, $L \in \mathbb{N}$, modulo samples $\{y_n\}_{n=0}^{N-1}$ in (3.8), the low-pass filter ψ_n and $\beta_g \geq \|\psi\|_\infty \|s_K\|_{\mathrm{TV}}$.

Result: Estimate of s_K in form of $\left\{\widetilde{c}_k, \widetilde{t}_k\right\}_{k=0}^{K-1}$.

1) Compute $y^{[N]} = \Delta^N y$.
2) Compute $\varepsilon_\gamma^{[N]} = \mathscr{M}_\lambda\left(y^{[N]}\right) - y^{[N]}$. Set $s_{(1)} = \varepsilon_\gamma^{[N]}$.
3) for $\ell = 1 : L-1$ and $J = 6\beta_g/\lambda$,

   Compute $\kappa_{(n)} = \left\lfloor \frac{\nu_1^\ell - \nu_{J+1}^\ell}{8\beta_g} + \frac{1}{2} \right\rfloor$ with $\nu_n^\ell = \left(\mathsf{S}^2 \varepsilon_\gamma^{[N]}\right)_n$.

   $\mathsf{s}_{(\ell+1)} = \mathsf{S}\mathsf{s}_{(\ell)} - 2\lambda\kappa_{(n)}$.

   Round $s_{(\ell+1)}$ to the nearest integer multiple of 2λ. (Consistency Relation)

   end
4) $\widetilde{g}_n = \mathsf{S}\mathsf{s}_{(L)} + y_n$, $n = 0, \ldots, N-1$ and $N \geq 2K+1$.
5) Use $\widetilde{g}_n$ and ψ_n in Algorithm 2 to estimate $\left\{\widetilde{c}_k, \widetilde{t}_k\right\}_{k=0}^{K-1}$.

the anti-difference operation defined by, $\mathsf{S} : (a_i)_{i=1}^\infty \mapsto (\sum_{i'=1}^i a_{i'})_{i=1}^\infty$. We obtain that

$$(\Delta^{\ell-1}\varepsilon_g)_n = (\mathsf{S}\Delta^\ell \varepsilon_g)_n + \kappa_{(n)} a_n, \qquad a_n = 2\lambda \,.\, \kappa_{(n)} \in \mathbb{Z}. \tag{3.31}$$

Since constants are in the kernel of Δ, this cannot be resolved any further for $\ell = 1$, we can only estimate ε_g up to multiple of $2\lambda\mathbb{Z}$. For $\ell > 1$, however, we can apply S again and estimate the unknown $\kappa_{(n)}, \ell = 1, \ldots, L$. We obtain

$$(\Delta^{\ell-2}\varepsilon_g)_n = (\mathsf{S}^2\Delta^\ell \varepsilon_g)_n + \kappa_{(n)} \left(\mathsf{S}a\right)_n + \kappa_{(\ell-1)} a_n. \tag{3.32}$$

and, given that $\left(\mathsf{S}a\right)_n$ is growing linearly, all but one choice of $\kappa_{(n)}$ will yield a sequence that violates the supremum bound entailed by the prior knowledge of β_g. As shown in Section 3.3, a sufficient number of subsequent samples of $\Delta^\ell y$ to distinguish the feasible choice of $\kappa_{(n)}$ from the infeasible ones is $6\frac{\beta_g}{\lambda}$, and hence the required number of subsequent samples of g is bounded by $6\frac{\beta_g}{\lambda} + L + 1 \leq 7\frac{\beta_g}{\lambda} + 1$ to reconstruct one value of g and $7\frac{\beta_g}{\lambda} + N'$ to reconstruct N' subsequent values (cf. discussion after Lemma 3).

Theorem 10 (Local Reconstruction Theorem). *Let $g(t) \in \mathcal{B}_\pi$ with $\|g\|_\infty \leq \beta_g$ and*

$$y_n = \mathscr{M}_\lambda\left(g(t)\right)\big|_{t=nT}, \quad n = 0, \ldots, N-1$$

in (3.8) be the modulo samples of $y(t)$ with sampling rate T. Then a sufficient condition for recovery of N' contiguous samples of g from the y_n (up to additive multiples of 2λ) is that

$$T \leq \frac{1}{2\pi e} \;\; \textit{and} \;\; N \geq N' + 7\frac{\beta_g}{\lambda}. \tag{3.33}$$

3.4.3 A Sufficiency Condition for Recovering Sparse Signals

To apply this theorem to the case of sparse sampling, recall that the number of subsequent samples required for reconstruction is $2K+1$, which should hence also be our choice for N'. Also note that using Young's inequality, one can bound

$$\|g\|_\infty = \|s_K * \psi\|_\infty \leq \|\psi\|_\infty \|s_K\|_{\mathrm{TV}}, \tag{3.34}$$

where the $\|\cdot\|_{\mathrm{TV}}$ denotes the total variation of a measure, which, for spike trains, corresponds to the ℓ_1-norm of the coefficient sequence c_k in (3.28). Thus we obtain the following main result.

Theorem 11 (Unlimited sampling of sparse signals)**.** *Let $g = s_K * \psi$ for a known low-pass filter $\psi \in \mathcal{B}_\pi$ and s_K in* (3.28) *be the unknown K-sparse signal to be recovered, and assume one has access to an a priori bound $\beta_g \geq \|\psi\|_\infty \|s_K\|_{\mathrm{TV}}$. Let $y_n = \mathscr{M}_\lambda\left(g\left(t\right)\right)|_{t=nT}, n = 0, \ldots, N-1$ in (3.8) be the modulo samples of $y\left(t\right)$ with sampling rate T. Then a sufficient condition for recovery of s_K from the y_n (up to additive multiples of 2λ) is that*

$$T \leq \frac{1}{2\pi e} \;\; \textit{and} \;\; N \geq 2K + 1 + 7\frac{\beta_g}{\lambda}. \tag{3.35}$$

Provided that this sufficiency condition is satisfied, and assuming that β_g is known, by choosing L prescribed by Lemma 3, Algorithm 3 recovers the sparse signal $s_K\left(t\right)$ from modulo samples $\{y_n\}_{n=0}^{N-1}$.

In contrast to Section 3.3 and [208], where the sampling bound is independent of SR-ADC threshold λ, in case of sparse sampling note that $N \propto \lambda^{-1}$. Since we are dealing with finite number of samples, this result is intuitive and we do expect that the number of samples required for sparse recovery will depend on both the sparsity level K and the dynamic range β_g/λ of the signal $g = s_K * \psi$.

3.4.4 Numerical Demonstration

We set up a numerical example where we set $K = 3$ and $\tau = 10$ to define $s_K\left(t\right)$ using $\{c_k, t_k\}$ chosen arbitrarily. This immediately gives, $\beta_g = 3.2511$. We then acquire low-pass filtered measurements using $\psi\left(t\right) = \mathrm{sinc}\left(t\right)$ which is clearly π–bandlimited or $\psi \in \mathcal{B}_\pi$. With $\lambda = 1/4$ and modulo sampling rate $T = 1/\left(2\pi e\right) - 1/100$, we acquire modulo samples y_n using (3.8). By using result of Lemma 3, we obtain $L = 3$. Furthermore, in view of (3.35), we must have at least $N = 99$ modulo samples for recovery of $2K+1$ contiguous values of unfolded g_n. We plot the sparse signal, its low-pass filtered version and the resultant modulo samples in Fig. 3-12 (a). By using the localized recovery method developed in Algorithm 3, we estimate unfolded samples $\widetilde{g}_n$ which is exactly the same as g_n (up to machine precision) and this is shown in in Fig. 3-12 (b). In this computation, we assume the knowledge of constant offset since $\widetilde{g}_n$ may only be estimated upto a constant ambiguity of $2\lambda\mathbb{Z}$. The mean squared error between ground truth g_n and its estimate $\widetilde{g}_n$ is noted to be $5.0401e^{-34}$. By choosing any contiguous set of size $2K+1$ of the $N = 99$ samples of $\widetilde{g}_n$, we can use the approach developed in [69] to estimate s_K .

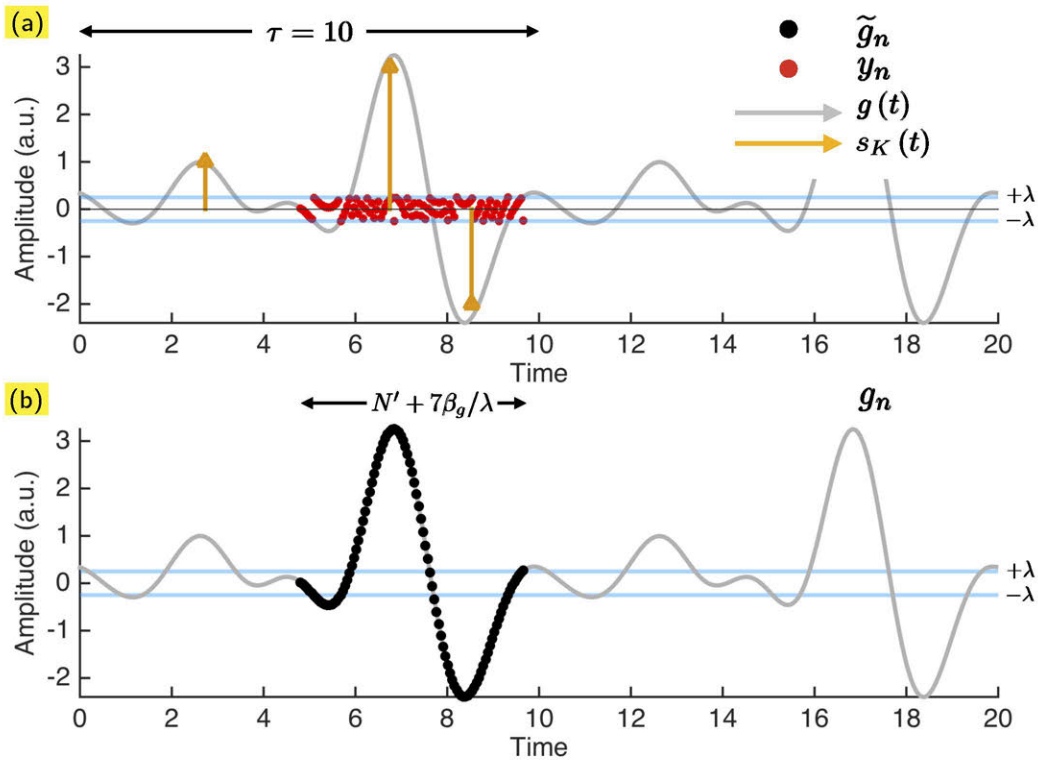

Figure 3-12: Sparse signal recovery via local reconstruction of modulo samples with $\beta_g = 3.2511$ and $\lambda = 0.25$. (a) We plot K–sparse signal $s_K(t)$ with $K = 3$ and $\tau = 10$, the low-pass filtered signal $g = s_K * \psi$ where $\psi(t) = \text{sinc}(t)$ as well as modulo samples $y_n = \mathscr{M}_\lambda(g_n)$ with $T = 0.0485$. Note that $\psi \in \mathcal{B}_\pi$. (b) Using Algorithm 1, we estimate unfolded samples $\widetilde{g}_n$ from $N = 99$ modulo samples of y_n. For this purpose $L = 3$. The reconstruction is observed to be exact (upto machine precision). Given $2K + 1$ of $\widetilde{g}_n$, the spikes are estimated using Algorithm 2.

3.5 Unlimited Sampling of Sparse Sinusoidal Mixture

3.5.1 Coding Theory, Spectral Estimation and Sinusoids

A basic model that finds applications in several areas of science and engineering is that of a continuous–time, sparse mixture of sinusoids,

$$g(t) = \sum_{k=0}^{K-1} c_k e^{\jmath \nu_k t}, \quad c_k \in \mathbb{C}, \;\; \nu_k \in \mathbb{R}. \tag{3.36}$$

Here $t \in \mathbb{R}$ denotes time and from here on, we will refer to (3.36) as a K–sparse model since it is completely characterized by K–complex exponentials. We will assume that,

$$k = 0, \ldots, K-1, \quad 0 < \nu_k < \nu_{k+1} < 2\pi.$$

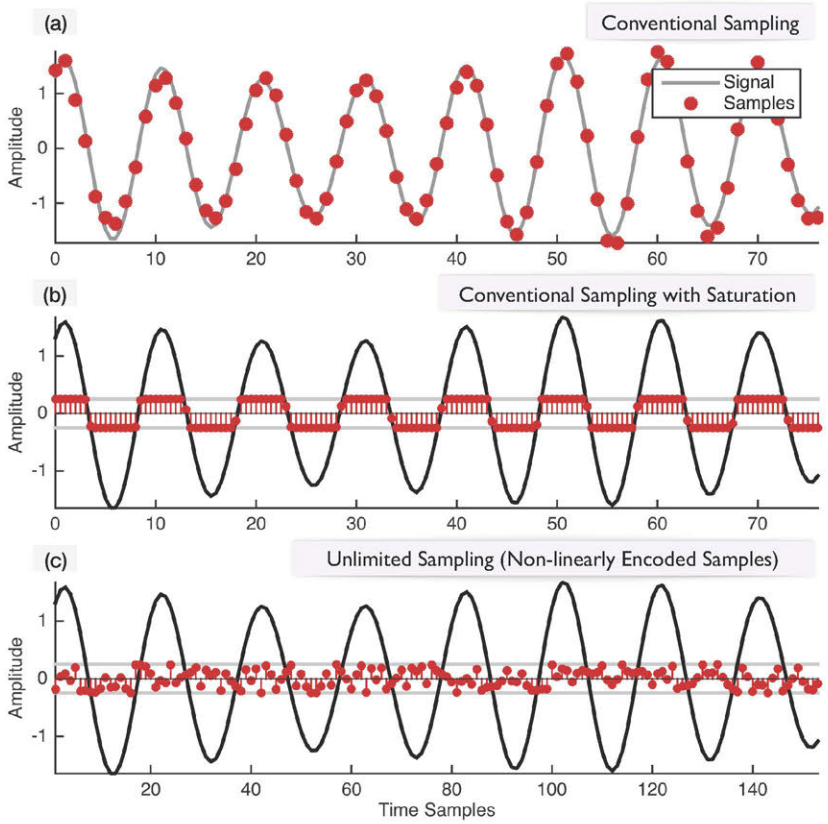

Figure 3-13: (a) Sampled version of a sinusoidal mixture with $K = 3$. These samples are obtained using time-resolved imaging sensor [209] where each sinusoidal frequency is related to an echo of light. (b) Conventional ADCs saturate or clip with the input signal exceeds the maximum recordable voltage of the ADC. (c) Sampling with *unlimited sensing framework* results in low dynamic range, scrambled samples. This is based on a new ADC design which non-linearly folds the amplitudes of the signal. In this way, entire dynamic range of the input signal is encoded in folded samples.

Given discrete measurements of the form $g_n = g(nT), n \in \mathbb{Z}$ and $T > 0$ (the sampling rate), the problem of estimating the unknowns $\{c_k, \nu_k\}_{k=0}^{K-1}$ arises in several areas. The field of *spectral estimation* [67, 122] is dedicated to this problem. In working with time-resolved imaging [66, 209] we have shown that (3.36) confirms to the measurements of reflected echoes of light. This allows for recovery of the same without having to sample at the speed of light. The data samples of a 3–sparse signal in Fig. 3-13 (a) are in fact obtained using a time-resolved sensor [66, 209]. The same problem is closely related to the field of *coding theory* where (3.36) is reinterpreted as the syndromes of the error word [210]. Estimation of sinusoidal frequencies then boils down to the problem of decoding Reed-Solomon codes [211]. Similarly, approximation with exponential sums of form (3.36) is a problem of interest in *approximation theory* where the topic has received widespread attention [212, 213]. Due to the pervasiveness of this problem, it is no surprise that over the course of decades, a number of estimation algorithms have been developed in the literature [67, 210, 122, 214, 212, 213, 202].

3.5.2 Sampling Sparse Mixtures of Sinusoids

Regardless of the application, in all cases, one starts with discrete-time samples $\{g_n\}_{n=0}^{N-1}$. Since (3.36) is a bandlimited function[3], Shannon's sampling theorem can be used, however, it requires infinitely many samples for representing $g(t)$. This sub-optimal behavior is expected as the sampling theorem is agnostic to the parametric nature of (3.36). This is not the case with non-linear approaches that aim to estimate the $2K$ parameters $\{c_k, \nu_k\}_{k=0}^{K-1}$. Examples date back to Prony's method [67] which requires as few as $N \geq 2K$ measurements.

There are two predominant problems related with the estimation of the unknown parameters. The first problem is that of measurement noise. In this case, as dictated by the Cramér-Rao bounds [215], over-sampling improves the performance of estimation. The second problem is associated with the practicalities of Shannon's sampling theorem. In practice, signals are sampled using analog-to-digital converters (ADCs) which are limited in dynamic range; there is a limit to the maximum voltage that can be recorded, say, λ. Let $\|g\|_\infty = \sup_{t\in\mathbb{R}} g(t)$ denote the max-norm. Whenever $\|g\|_\infty > \lambda$, the ADC clips or saturates (see Fig. 3-13 (b)). This leads to discontinuities resulting in aliasing [138]. To deal with this problem, several numerical and optimization based methods have been proposed in literature [216, 134, 136, 217]. That said, to the best of our knowledge, *none of the works*[4] *provide an information theoretic link between sparsity level K and the number of measurements N* that are required for recovery of $g(t)$ when $\|g\|_\infty > \lambda$.

In our work, we will exploit a co-design between hardware and recovery algorithms so that we can recover $g(t)$, even when $\|g\|_\infty$ is orders of magnitude higher than λ. By incorporating computation in the ADC, we develop an approach where samples of some high dynamic range (HDR) function g are scrambled in the low dynamic range measurements. This is shown in Fig. 3-13 (c). This is achieved this by injecting non-linearity in the measurement process. With the knowledge of non-linearity and the signal structure, we will study mathematical guarantees which answer the sampling theory question: *What sampling rate and how many measurements suffice for recover of $g(t)$ via $\{c_k, \nu_k\}_{k=0}^{K-1}$ when $\|g\|_\infty > \lambda$?*

3.5.3 Sufficiency Condition for Recovery of Sparse Mixtures of Sinusoids

Our approach builds upon the results developed in Section 3.4, in which we studied the case of recovering K Dirac measures from low-pass filtered measurements. In Section 3.4, we showed that $N \propto 2K + 1 + \mathcal{S}(\lambda, \|\psi\|_\infty, \sum_k |c_k|)$ where $\mathcal{S}$ is some linear function and ψ is some low-pass filter.

With regard to (3.36), when $\|g\|_\infty > \lambda$, the approach that will study in this work relies on two steps:

1) Descrambling folded measurements, that is, mapping $\{y_n\}_{n=0}^{N-1} \to \{g_n\}_{n=0}^{2K-1}$.
2) Parameter estimation; mapping usual samples to parameters, that is, $\{g_n\}_{n=0}^{2K-1} \to \{c_k, \nu_k\}_{k=0}^{K-1}$. This is done by using any of the known methods [67].

We use the result of Theorem 10 to derive sufficient conditions for recovery of continuous-time $g(t)$ in (3.36) from folded samples $\{y_n\}_{n=0}^{N-1}$. Let $\mathbf{c} = \begin{bmatrix} c_0 & \cdots & c_{K-1} \end{bmatrix}^\top$. We note that,

$$\|g\|_\infty \leqslant \|\mathbf{c}\|_{\ell_1} = \sum_k |c_k|.$$

[3]Functions that have a compactly supported Fourier transform. A formal definition is used in Definition 4 in Section 2.4.1.
[4]For instance, recovering mixture of sinusoids from clipped measurements is discussed in [217] and references therein.

This allows us to set $\beta_g \geq \|\mathbf{c}\|_{\ell_1}$ which we will assume to be known. Furthermore, estimation of unknown parameters $\{c_k, \nu_k\}_{k=0}^{K-1}$ requires $N' = 2K$ contiguous samples of g_n. By combining the two facts, we have the sampling theorem for sparse mixture of sinusoids in (3.36).

Theorem 12 (Unlimited Sampling of Sparse Sinusoidal Mixture)**.** *Let $g \in \mathcal{B}_\pi$ defined in* (3.36) *be the K-sparse sinusoidal mixture to be recovered, and assume that $\beta_g \geq \|\mathbf{c}\|_{\ell_1}$ is known. Let $y_n = \mathscr{M}_\lambda\left(g\left(t\right)\right)|_{t=nT}, n = 0, \ldots, N-1$ in* (3.8) *be the modulo samples of $y\left(t\right)$ with sampling rate T. Then a sufficient condition for recovery of $g\left(t\right)$ from the y_n (up to additive multiples of 2λ) is that*

$$T \leq \frac{1}{2\pi e} \text{ and } N \geq 2K + 7\frac{\beta_g}{\lambda}. \tag{3.37}$$

Provided that the conditions of Theorem 12 are satisfied, we can use the appropriate value of L prescribed by Lemma 3. There on, a version of Algorithm 3 recovers the continuous-time signal $g\left(t\right)$ from modulo samples $\{y_n\}_{n=0}^{N-1}$.

Remark In similar spirit to the unlimited sampling theorem discussed in Section 3.3, the sampling rate T is independent of the SR-ADC threshold λ. However, the number of samples $N \propto \lambda^{-1}$. This is mainly because we are working with finite number of samples. Consequently, N is a function of both the sparsity level, K and the dynamic range, β_g/λ. This is similar to the behavior in case of Dirac measures discussed in Section 3.4.

3.5.4 Numerical Demonstration

In order to validate our theoretical approach, we set up a numerical demonstration with $K = 3$ and parameters,

$$\mathbf{c} = \left[\begin{array}{ccc} 4 & -2 & 1 \end{array}\right]^\top \text{ and } \boldsymbol{\nu} = \left[\begin{array}{ccc} \pi/6 & \pi/3 & 2\pi - \frac{2}{10} \end{array}\right]^\top.$$

With this choice, we construct $g\left(t\right)$ which is shown in Fig. 3-14 (a). In order to restrict ourselves to real-valued, us use $g \mapsto \Re\left(g\right)$ which in turn implies that $y_n \in \mathbb{R}$ and we must estimate twice the number of sinusoids[5] or $K_{\mathsf{eff}} = 2K = 6$. From this setup, we numerically estimate $\beta_g = 6.9918$, $\beta_g \approx \|\mathbf{c}\|_{\ell_1}$. Furthermore, we set $\lambda = 1/2$ and $T = 1/2\pi e - 1/100$ (where λ is typically fixed by design). This leads to modulo samples y_n in Fig. 3-14 (a). By using Lemma 3, we estimate $L = 3$. In order to guarantee exact recovery of $2K_{\mathsf{eff}}$ samples of g_n, from Theorem 12 we have $N \geq 2K_{\mathsf{eff}} + 7\frac{\beta_g}{\lambda}$ and we set[6] $N = 112$. We then use Algorithm 1 to recover unfolded samples denoted by $\widetilde{g}_n$. As mentioned earlier, we can only estimate $\widetilde{g}_n$ up to an additive constant of $2\lambda\mathbb{Z}$. In our simulation, we use the knowledge of this offset to account for ambiguity. The estimated samples $\widetilde{g}_n$ are shown in Fig. 3-14 (b) and match the original samples g_n with machine precision (mean squared error $\propto 10^{-32}$). Next we use exponential fitting using spectral estimation method [67]. This leads to the estimates $\widetilde{\boldsymbol{c}}$ and $\widetilde{\boldsymbol{\nu}}$. These estimates are exact (up to numerical precision). The parameters are then used to resynthesize $\widetilde{g}$ which we plot in Fig. 3-14 (c). The mean squared error between full length sequences g and $\widetilde{g}$ is noted to be 1.3191×10^{-15}.

[5]This is because each real-valued complex-exponential can be written as $\Re\left(e^{\jmath\nu_k t}\right) = \left(e^{\jmath\nu_k t} + e^{-\jmath\nu_k t}\right)/2$, which is twice as many sinusoids.

[6]Due to over-sampling involved with the unfolding operation, we have empirically observed that one may still use $2K + \lceil 7\beta_g/\lambda \rceil \geq N \geq 2K$.

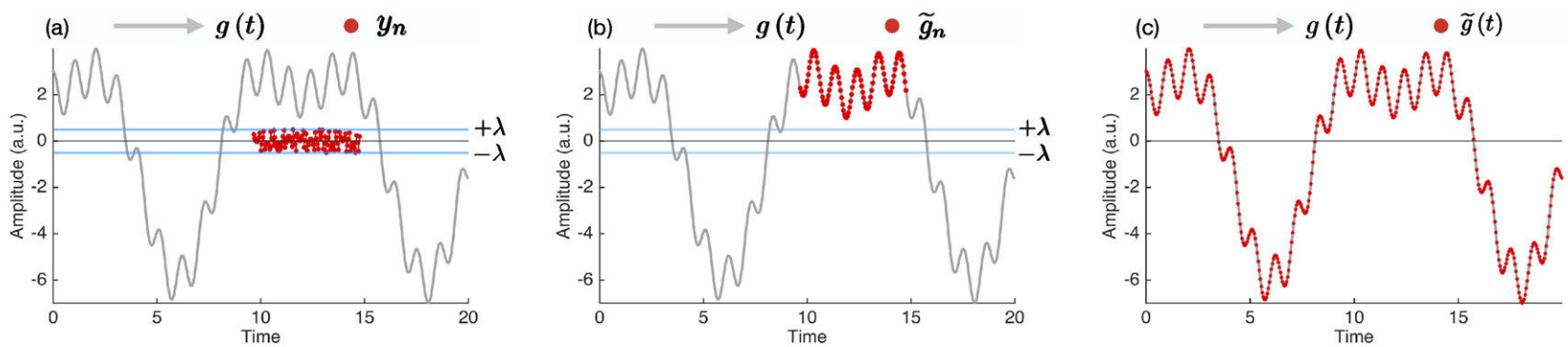

Figure 3-14: Unlimited sampling and recovery of sinusoidal mixtures (a) Sinusoidal mixture with $K = 3$. We plot g together with unlimited samples $\{y_n\}_{n=0}^{N-1}$ where N is chosen in accordance with Theorem 12. (b) Using modulo samples y_n, we estimate unfolded samples $\widetilde{g}_n$. The estimated samples match the oracle valued samples, g_n up to machine precision. (c) We use spectral estimation [67] to estimate unknowns $\widetilde{c}_k$ and $\widetilde{\nu}_k$ which are used to synthesize $\widetilde{g}(t)$ using (3.36). The estimated signal matches the original. The mean squared error between g and $\widetilde{g}$ is noted to be 1.3191×10^{-15}.

रतस्य हि शुरुधः सन्ति पूर्वीर रतस्य धीतिर वर्जिनानि हन्ति ।
रतस्य शलोको बधिरा ततर्द कर्णा बुधानः शुचमान आयोः

रतस्य द्ळ्हा धरुणानि सन्ति पुरूणि चन्द्रा वपुषे वपूंषि ।
रतेन दीर्घम इषणन्त पर्क्षं रतेन गाव रतम आ विवेशुः

रतं येमान रतम इद् वनोत्य रतस्य शुष्मस तुरया उ गव्युः ।
रताय पर्त्वी बहुले गभीरे रताय धेनू परमे दुहाते

"Of truth there exist many riches. The vision of truth smashes the crooked, and the signal call of truth bored open deaf ears—(the signal call) of Āyu [=Agni], awakening and blazing." [1]

— Rigveda (Mandala IV, §23, ¶ 08–10)

4

Sampling Parametric Functions of the Rational Family

4.1 Introduction to the Sampling Problem

Preceding sections have considered two important classes of parametric signal representation—sparse signals (cf. (3.28)) and sum of complex exponentials (cf. (3.36)). This chapter considers a somewhat unconventional class of parametric functions that arises in applications such as lifetime imaging. A more concrete link is discussed in the context of fluorescence lifetime estimation in Chapter 6. Here we will focus on the sampling theoretic formulation and the associated recovery algorithm. In particular, we will focus on time-domain transfer function which is specified by,

$$\begin{aligned} g(t) &= \delta(t-t_0) * \left(\Gamma\delta(t) + \mu \exp\left(-\frac{t}{\tau}\right)\Pi(t)\right) \\ &= \underbrace{\Gamma\delta(t-t_0)}_{\text{Pulse Echo}} + \underbrace{\mu \exp\left(-\frac{t-t_0}{\tau}\right)\Pi(t-t_0)}_{\text{Decaying Echo}} \end{aligned} \tag{4.1}$$

where $\Pi(t) = \mathbb{1}_{[0,\infty)}(t)$ is the Heaviside function.

The contribution due to the constituent term[1] $\Gamma\delta(t-t_0)$ arises in several problems such as time-

[1]We say *constituent term* because typically, one observes a mixture or super-position of such terms, for instance, see (3.28).

delay estimation [53], sparse sampling [69] and time-of-flight imaging [66]. A lesser familiar contribution due to $\exp\left(-\frac{t-t_0}{\tau}\right)\Pi\left(t-t_0\right)$ arises in applications related to channel modeling in wireless optical communications (cf. (8) in [218] and [219]), time-resolved imaging [220, 15] and bio-imaging [21]. In practice, it is more convenient to measure the Fourier transform of $g\left(t\right)$ in (4.1) which is given by,

$$\widehat{g}\left(\omega\right)=\left(\Gamma+\frac{\mu\tau}{1+\jmath\omega\tau}\right)e^{-\jmath\omega t_0}. \tag{4.2}$$

In fact, we will show how to acquire such measurements using consumer grade depth sensors in Chapter 6. In practice, Γ depends on the wavelength of light and hence can be filtered out or, $\Gamma=0$. A further generalization of the transfer function in (4.1) is due to the presence of multiple decaying exponentials and takes form of,

$$g_K\left(t\right)=\delta\left(t-t_0\right)*\left(\Gamma\delta\left(t\right)+\Pi\left(t\right)\sum_{k=0}^{K-1}\mu_k\exp\left(-\frac{t}{\tau_k}\right)\right). \tag{4.3}$$

In this case, the Fourier transform takes form of a rational transfer function given by,

$$\widehat{g}_K\left(\omega\right)=\left(\Gamma+\sum_{k=0}^{K-1}\frac{\mu_k}{\frac{1}{\tau_k}+\jmath\omega}\right)e^{-\jmath\omega t_0}. \tag{4.4}$$

The sampling problem in this case is set-up as follows: Suppose we are given measurements,

$$y_n=\widehat{g}_K\left(\omega_n\right),\quad \omega_n=n\omega_0\quad \omega_0>0,\quad n=0,\ldots,N-1 \tag{4.5}$$

what is the minimum number of samples required for recovery of $2K+1$ unknowns, $\left\{t_0,\left\{\mu_k,\tau_k\right\}_{k=0}^{K-1}\right\}$?

4.1.1 Special Case: Single Exponential

We will start with the simpler case of $K=1$ based on which we will develop our strategy for the general case in (4.3).

In this case, we start by setting $\nu=1/\tau$ and $\theta=t_0$ for notational convenience. Then, in view of (4.2) with $\Gamma=0$, the Fourier domain samples read:

$$y_n\overset{(4.5)}{=}\frac{\mu e^{-\jmath\omega_n\theta}}{\nu+\jmath\omega_n}=\frac{\mu e^{-\jmath n\omega_0\theta}}{\nu+\jmath n\omega_0}. \tag{4.6}$$

Similarly, we have,

$$y_{n+1}=\frac{\mu e^{-\jmath\omega_{n+1}\theta}}{\nu+\jmath\omega_{n+1}}=\frac{\mu\,\overbrace{e^{-\jmath\omega_n\theta}e^{-\jmath\omega_0\theta}}^{e^{-\jmath\omega_{n+1}\theta}}}{\nu+\jmath\omega_{n+1}}. \tag{4.7}$$

By factoring the common term, that is, $\mu e^{-\jmath\omega_n\theta}$, in the above two equations, we conclude that,

$$y_{n+1}\left(\nu+\jmath\omega_{n+1}\right)e^{\jmath\omega_0\theta}=y_n\left(\nu+\jmath\omega_n\right). \tag{4.8}$$

This can now be formulated as a linear system of equations. Let $u_\theta = e^{\jmath\omega_0\theta}$, then, $u_{-\theta} = \frac{1}{u_\theta}$. Therefore, we have,

$$\begin{aligned}
&y_{n+1}\left(\nu + \jmath\omega_{n+1}\right)u_\theta = y_n\left(\nu + \jmath\omega_n\right)\\
&\Rightarrow y_{n+1}\nu + \jmath y_{n+1}\omega_{n+1} = y_n\nu u_{-\theta} + \jmath y_n\omega_n u_{-\theta}\\
&\Rightarrow y_{n+1}\nu - y_n\nu u_{-\theta} - \jmath y_n\omega_n u_{-\theta} = -\jmath y_{n+1}\omega_{n+1}
\end{aligned}$$

which is a linear system of equations which in vector–matrix notation reads,

$$\underbrace{\begin{bmatrix} y_1 & -y_0 & -\jmath y_0\omega_0 \\ y_2 & -y_1 & -\jmath y_1\omega_1 \\ \vdots & \vdots & \vdots \\ y_N & -y_{N-1} & -\jmath y_{N-1}\omega_{N-1} \end{bmatrix}}_{\mathbf{Y}} \underbrace{\begin{bmatrix} \nu \\ \nu u_{-\theta} \\ u_{-\theta} \end{bmatrix}}_{\mathbf{x}} = -\jmath \underbrace{\begin{bmatrix} y_1\omega_1 \\ y_2\omega_2 \\ \vdots \\ y_N\omega_N \end{bmatrix}}_{\mathbf{z}}$$

The unknown vector $\mathbf{x}$ can be recovered by solving for

$$\mathbf{Y}\mathbf{x} = \mathbf{z} \Rightarrow \widetilde{\mathbf{x}} = \mathbf{Y}^{+}\mathbf{x}$$

where $\mathbf{Y}^{+}$ is the pseudo-inverse of matrix $\mathbf{Y}$. Furthermore, the matrix $\mathbf{Y}$ has full rank when,

$$\begin{bmatrix} y_1 & -y_0 & -\jmath y_0\omega_0 \\ y_2 & -y_1 & -\jmath y_1\omega_1 \\ y_3 & -y_2 & -\jmath y_2\omega_2 \end{bmatrix} \begin{bmatrix} \nu \\ \nu u_{-\theta} \\ u_{-\theta} \end{bmatrix} = -\jmath \begin{bmatrix} y_1\omega_1 \\ y_2\omega_2 \\ y_3\omega_3 \end{bmatrix}$$

in which case $N = 4$ measurements $\{y_0, y_1, y_2, y_3\}$ suffice for recovery of the unknowns $\{t_0, \mu_0, \tau_0\}$.

4.1.2 General Case: K Exponential Functions

As in the previous case, let us set $u_\theta = e^{\jmath\omega\theta}$ and $\nu_k = \frac{1}{\tau_k}$ and also let $y(\omega) = \widehat{g}_K(\omega)$. Again, since Γ can be filtered out using optical wavelengths, we set $\Gamma = 0$. This results in,

$$y(\omega) \overset{(4.4)}{=} \underbrace{e^{-\jmath\omega\theta}}_{u_{-\theta}} \sum_{k=0}^{K-1} \frac{\mu_k}{\nu_k + \jmath\omega} = u_{-\theta}\frac{\sum_{k=0}^{K-1} p_k\omega^k}{\sum_{k=0}^{K} q_k\omega^k}.$$

In this case, apart from u_θ, we have $2K+1$ unknowns in form of the polynomial coefficients $\{p_k\}_{k=0}^{K-1}$ and $\{q_k\}_{k=0}^{K}$ which are of degree K and $K+1$, respectively. As in the previous case, so that we may factor[2] of $u_{-\theta} = u_\theta^*$, we evaluate the polynomial $y(\omega + \omega_0)$,

[2]This is due to the fact that the space of polynomials is shift-invariant and hence $y(\omega + \omega_0)$ spans the same space as $y(\omega)$. Shifting the polynomial leads to the common factor u_θ and this is a property that we will exploit.

Note that polynomial coefficients

$$y(\omega+\omega_0) = e^{-\jmath(\omega+\omega_0)\theta}\frac{\sum\limits_{k=0}^{K-1} p_k(\omega+\omega_0)^k}{\sum\limits_{k=0}^{K} q_k(\omega+\omega_0)^k}$$
$$= u_{-\theta}e^{-\jmath\omega_0\theta}\frac{\sum\limits_{k=0}^{K-1} p_k(\omega+\omega_0)^k}{\sum\limits_{k=0}^{K} q_k(\omega+\omega_0)^k} = u_{-\theta}e^{-\jmath\omega_0\theta}\frac{\sum\limits_{k=0}^{K-1} \breve{p}_k(\omega)^k}{\sum\limits_{k=0}^{K} \breve{q}_k(\omega_0)^k}.$$

Since ω_0 shift of $y(\omega)$ spans the same space as $y(\omega)$, the coefficient sequences p_k and $\breve{p}_k$ as well as well q_k and $\breve{q}_k$, respectively, are related by the convolution operation. In particular,

$$\sum_{k=0}^{K} q_k(\omega+\omega_0)^k = \sum_{k=0}^{K} \breve{q}_k\omega^k$$

where,

$$\breve{q}_k = \frac{1}{k!}\left(a * \bar{b}\right)_k, \quad a_k = k!q_k, \quad b_k = \frac{\omega_0^k}{k!}, \quad \bar{b}_k = b_{K-k}.$$

By defining the polynomials $\{\mathsf{P}, \mathsf{Q}, \mathsf{N}, \mathsf{D}\}$,

$$\begin{cases} \mathsf{P}_{K-1}(\omega) \\ \mathsf{Q}_K(\omega) \\ \mathsf{N}_{2K-1}(\omega) \\ \mathsf{D}_{2K-1}(\omega) \end{cases} \quad \text{where} \quad \mathsf{R}_K(\omega) = \sum_{k=0}^{K} r_k\omega^k, \tag{4.9}$$

we have,

$$y(\omega+\omega_0) = e^{-\jmath(\omega+\omega_0)\theta}\frac{\mathsf{P}(\omega+\omega_0)}{\mathsf{Q}(\omega+\omega_0)}.$$

Observe that the ratio of measurements $y(\omega+\omega_0)$ and $y(\omega)$ leads to another rational polynomial of higher degree,

$$\frac{y(\omega+\omega_0)}{y(\omega)} = e^{-\jmath\omega_0\theta}\frac{\mathsf{P}(\omega+\omega_0)\,\mathsf{Q}(\omega)}{\mathsf{Q}(\omega+\omega_0)\,\mathsf{P}(\omega)} \equiv \frac{\mathsf{N}(\omega)}{\mathsf{D}(\omega)}. \tag{4.10}$$

Let $v_\theta = e^{-\jmath\omega_0\theta}$. The above equation allows us to eliminate v_θ using the first annihilation equation,

First Annihilation Relation

$$\mathsf{D}(\omega)\,y(\omega+\omega_0) - \mathsf{N}(\omega)\,y(\omega) = 0, \;\; \omega = n\omega_0. \tag{4.11}$$

Here, polynomials D and N are parameterized by $2K$ coefficients $\{d_k\}_{k=0}^{2K-1}$ and $\{n_k\}_{k=0}^{2K-1}$, respectively. With measurements defined in (4.5), we have $4K$ unknowns in (4.11). Provided that $N \geq 4K$, we can estimate $\{d_k, n_k\}_{k=0}^{2K-1}$ using the linear system of equations (4.11).

Noting that $\left\{\nu_k = \frac{1}{\tau_k}\right\}_{k=0}^{K-1}$ are the roots of the polynomial,

$$\mathsf{Q}(\omega) = \prod_{k=0}^{K-1} (\nu_k + \jmath\omega) = \sum_{k=0}^{K} q_k \omega^k,$$

we eliminate P in (4.10) to obtain the second annihilation equation,

Second Annihilation Relation

$$\mathsf{N}(\omega - \omega_0)\,\mathsf{Q}(\omega + \omega_0) - v_\theta \mathsf{D}(\omega)\,\mathsf{Q}(\omega - \omega_0) = 0, \quad v_\theta = e^{-\jmath\omega_0\theta} \tag{4.12}$$

where v_θ and Q remain unknown. However, $\{d_k, n_k\}_{k=0}^{2K-1}$ are known using (4.11). Let us define a Vandermonde matrix with elements,

$$\mathbf{V}_n^{K,N} = \left[(n\omega_0)^k\right]_{n,k} \text{ with } \begin{array}{c} n = 0, \ldots, N-1 \\ k = 0, \ldots, K \end{array}$$

and diagonal matrices with matrix elements, $\mathbf{\Delta}_\mathsf{N} = [\mathsf{N}((n-1)\omega_0)]_{n,n}$ and $\mathbf{\Delta}_\mathsf{D} = [\mathsf{D}(n\omega_0)]_{n,n}$, each of size $N \times N$, respectively. We may then re-write (4.12) as the *generalized eigen-value problem*,

$$\underbrace{\mathbf{\Delta}_\mathsf{N}\mathbf{V}_{n+1}^{K,N}}_{\mathbf{A}}\,\mathbf{q} \overset{(4.12)}{=} v_\theta \underbrace{\mathbf{\Delta}_\mathsf{D}\mathbf{V}_{n-1}^{K,N}}_{\mathbf{B}}\,\mathbf{q} \quad \Rightarrow \mathbf{A}\mathbf{q} = \lambda\mathbf{B}\mathbf{q}. \tag{4.13}$$

Construction of matrices $\mathbf{A}$ and $\mathbf{B}$ is given as follows,

$$\mathbf{A} = \underset{(N\times N)}{\boxed{\mathbf{\Delta}_\mathsf{N}}}\ \underset{(N\times K+1)}{\boxed{\mathbf{V}_{n+1}}} \quad \text{and} \quad \mathbf{B} = \underset{(N\times N)}{\boxed{\mathbf{\Delta}_\mathsf{D}}}\ \underset{(N\times K+1)}{\boxed{\mathbf{V}_{n-1}}}$$

The advantage of (4.12) is that we have access to v_θ as well as the coefficient vector $\mathbf{q}$. We estimate

$$\widetilde{\theta} = -\angle v_\theta / \omega_0$$

and $\{\widetilde{\tau}_k\}_{k=0}^{K-1}$ are the roots of the polynomial Q which is completely characterized by $\mathbf{q}$. Thus estimation of parameters of interest is accomplished without having to estimate $\mathbf{p}$. Alternatively, $\mathbf{p}$ or $\{\mu_k\}_{k=0}^{K-1}$ may be solved for by using

$$\mathsf{D}(\omega) = \mathsf{P}(\omega)\,\mathsf{Q}(\omega + \omega_0).$$

One may even use the annihilation equation $y(\omega)\,\mathsf{Q}(\omega) - \lambda\mathsf{P}(\omega) = 0$. In context of lifetime imaging discussed in Chapter 6, this provides a general approach to solving for multiple lifetimes with unknown distance. We summarize our result in form of the following theorem.

Theorem 13 (Sampling Theorem for Rational Functions)**.** *Suppose we are given N samples $\{y_n\}_{n=0}^{N-1}$ defined by* (4.5) *of the rational function $\widehat{g}_K(\omega)$ in* (4.4)*. Then, $N \geq 4K$ is a sufficient condition for recovery of $2K+1$ unknown parameters $\left\{t_0, \{\mu_k, \tau_k\}_{k=0}^{K-1}\right\}$.*

Applications and Experimental Demonstration

रतस्य पथि वेधा अपायि शश्रिये मनांसि देवासो अक्रन ।
दधानो नाम महो वचोभिर्वपुर्दृशये वेन्यो वयावः

दयुमत्तमं दक्षं धेह्यस्मे सेधा जनानां पूर्वीररातीः ।
वर्षीयो वयः कर्णुहि शचीभिर्धनस्य सातावस्मानविड्ढि

इन्द्र तुभ्यमिन मघवन्नभूम वयं दात्रे हरिवो मा विवेनः ।
नकिरापिर्दद्रुशे मर्त्यत्रा किमङग रध्रचोदनन्त्वाहुः

"On the path of truth, the ritual adept has been drunk. The gods have set their minds for glory. Acquiring the name of "great" by (ritual) speeches, the one worthy of the quest has disclosed his wondrous form to be seen." [1]

— Rigveda (Mandala VI, §44, ¶ 08–10)

5 Super-resolved Multi-bounce Imaging

5.1 Introduction

In recent years, there has been a surge of research interest in studying time–of–flight or ToF imaging sensors. ToF sensors are active sensors that capture three dimensional information of a scene [221, 23, 222]. Unlike conventional digital sensors, a ToF sensor captures two images per acquisition: an amplitude image and a phase/range image. The amplitude image is the usual two dimensional photograph. The unconventional phase image at each pixel provides the depth information of the scene. The range image is computed using the ToF principle—the amount of time it takes for light to reflect back from an object. The amplitude/phase image combination provides a 3D point cloud of the scene.

Several optical ToF systems have been designed [221, 23, 222] using either pulsed or continuous wave technology. All these sensors function on the premise that there is a one–to–one mapping between the scene and the sensor. Each sensor pixel is associated with one depth value. In this chapter we consider single pixel measurements only, as shown in Fig. 5-1(a).

In practice, the scene of interest is often complex and results in multi-echo backscattered signal [64, 223]. This leads to multiple reflections observed at a given pixel where each reflection (or the corresponding time delay) must be computed to estimate the correct depth value. We discuss this case in Fig. 5-1(b) and the corresponding LiDAR or *light detection and ranging* based ToF data is plotted in Fig. 5-1(d). The problem of resolving constituent components of the superimposed echoes has been addressed in a number of papers (cf. [64, 224, 223] and references therein).

In this chapter, we demonstrate *super–resolution* capability using data from a photon counting, ToF

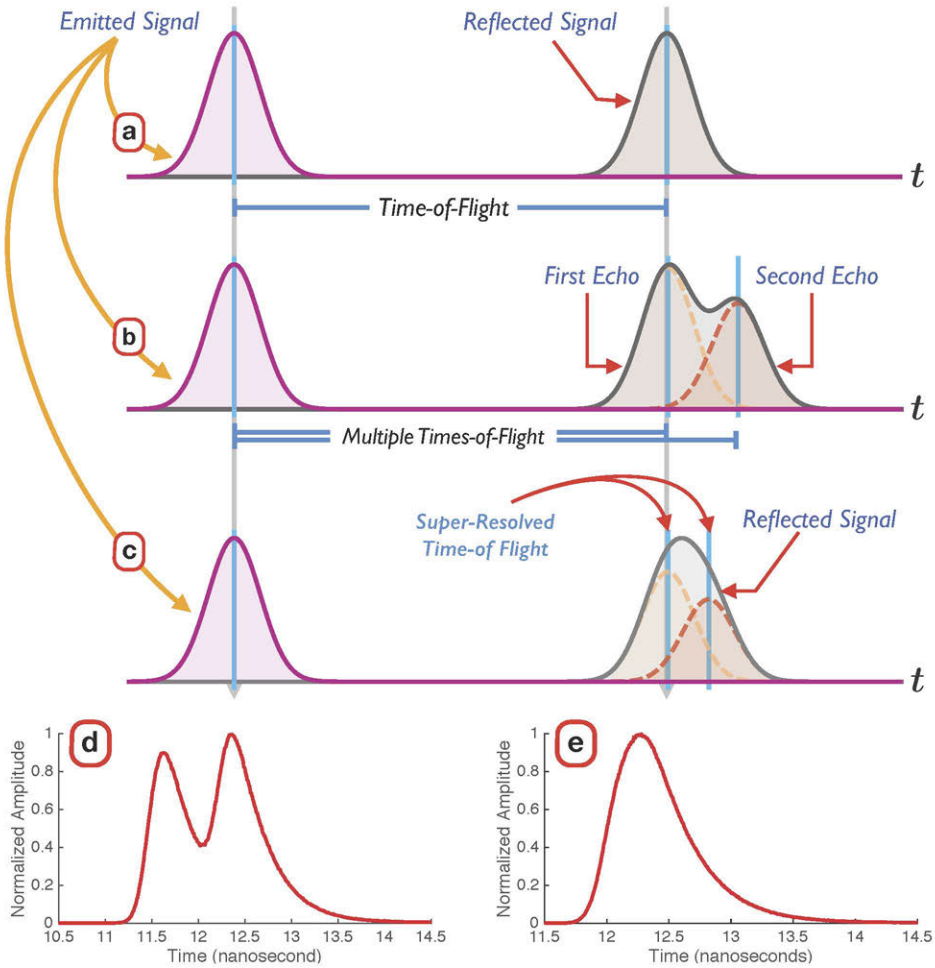

Figure 5-1: Illustration of the time–of–flight (ToF) principle. (a) The sensor emits a signal and the reflected signal is time delayed version of the emitted signal. The time delay is proportional to the distance of the object form the sensor. (b) ToF principle in complex environment which suffers from multiple reflected echoes. (c) Challenging case of super-resolution of multiple overlapping echoes. (d) Lidar ToF data corresponding to (b). (e) Lidar ToF data corresponding to the super-resolution problem in (c).

imaging sensor. This is a challenging setting in that the backscattered signal contains echoes that defy the *Rayleigh criterion*[225], that is to say, the echoes overlap such that no clear peaks are evident in the return signal. In general, a simple peak finding or correlation algorithm is unable to resolve the two returns. We describe this setting in Fig. 5-1(c). In 5-1(e), we plot experimentally acquired LiDAR ToF data.

In previous work [64] et al. have shown how Bayesian analysis of (TCSPC) ToF data can both detect very low signal levels, sometimes less than the background, and also resolve surfaces in depth at the order of 1 cm at a distance of 330 m. In this work we present a new, non-iterative method to process the ToF data with comparable resolution, thereby allowing deterministic and fixed time processing of lower complexity. We show the comparable performance on the same data set as used previously [64, 224].

The remainder of this chapter is organized as follows: Starting with a generalized image formation

model common to most ToF sensors, we establish a link between ToF sensors and sampling theory [27]. There on, we model multiple echoes of light as a sparse signal:

$$h(t) \overset{(2.10)}{=} \sum_{k=0}^{K-1} \Gamma_k \delta(t - t_k), \tag{5.1}$$

where δ denotes Dirac distribution, $\{\Gamma_k\}_{k=0}^{K-1}$ denotes the strength of kth echo and $\{t_k\}_{k=0}^{K-1}$, the corresponding time delay. In summary, we re-formulate the ToF super-resolution problem as recovery of stream of Dirac impulses in (5.1) from the knowledge of its low-pass filtered samples. Our reinterpretation allows us to invoke the *finite–rate–of–innovation* sampling theory [69, 70]. We demonstrate our results on experiments conducted with LiDAR ToF systems [64, 223]. Compared to previously studied solutions [64, 223], our method enjoys the advantage being non-iterative, of fixed time complexity and faster by capitalizing on spectrum estimation methods [67].

5.2 ToF Image Formation Model

5.2.1 A General Model for ToF Sensors

We begin with a general description of the image formation model for ToF sensors. A ToF system emits a probing function $p(t), t \in \mathbb{R}$ which may be a time-localized pulse or a continuous wave signal. The probing function interacts with the scene or the environment that is characterized by *scene response function* (SRF), $h(t, \tau)$. This results in the reflected signal $r(t)$ modeled by the Fredholm integral operator,

$$p \rightarrow \boxed{h} \rightarrow \underbrace{r(t) = \int_{\Omega_1} p(\tau)\, h(t, \tau)\, d\tau}_{\text{Reflected Signal}}. \tag{5.2}$$

The reflected signal is observed at the sensor characterized by *instrument response function* (IRF) or the *sensor response function*, $\varphi(t, \tau)$. For example, in context of optical imaging, this may be thought of as the point spread function. The resulting measurements $m(t)$ then read,

$$r \rightarrow \boxed{\varphi} \rightarrow \underbrace{m(t) = \int_{\Omega_2} r(\tau)\, \varphi(t, \tau)\, d\tau}_{\text{Measured Signal}}. \tag{5.3}$$

Finally, the ToF sensor samples the measured signal with the sampling rate Δ and stores a digital sequence, $m[n] = m(t)|_{t=n\Delta}, n \in \mathbb{Z}$.

Based on the choice of probing function, p and the IRF $\varphi(t, \tau)$, ToF imaging modalities may be categorized taxonomically. For example, continuous wave based optical ToF imaging systems [65, 226] such as the Microsoft Kinect use a sinusoidal probing function $p(t) = 1 + \cos(\omega_0 t)$ and the IRF is designed to be $\varphi(t, \tau) = p(\tau - t)$.

In most applications, the SRF is modeled as,

$$h(t, \tau) = \Gamma_0 \delta\left(t - \tau - \frac{2d_0}{c}\right) \tag{5.4}$$

Table 5.1: Different Modalities for Optical Time-of-Flight Sensor Based Depth Imaging

Modality	CW–ToF[(1)]	AMCW-ToF[(2)]	SPAD/Lidar[(3)]
Probing Function	$p(t) = 1 + p_0 \cos(\omega_0 t)$	$p(t) =$ PN–Seq.[(4)]	$p(t) = \delta(t)$
Reflected Function	$\Gamma_0 p\left(t - \frac{2d_0}{c}\right)$		
IRF	$\varphi(t,\tau) = p(\tau - t)$	$\varphi(t,\tau) = p(\tau - t)$	$\varphi(t,\tau) \overset{(5.10)}{=} \varphi_{\Theta}(t - \tau)$
Measurements	$\Gamma_0\left(1 + \frac{p_0^2}{2}\cos\left(\omega\left(t + \frac{2d_0}{c}\right)\right)\right)$	$\Gamma_0 (p * \overline{p})\left(t - \frac{2d_0}{c}\right)$	$\Gamma_0 \varphi_{\Theta}(t - 2d_0/c)$

[(1)] Continuous Wave ToF [(2)] Amplitude Modulated CW ToF [(3)] Laser Detection and Ranging
[(4)] Pseudo–random Sequence.

which leads to a shift–invariant SRF representing a scene at a distance d_0 from the sensor and where $c = 3 \times 10^8$ is the speed of light.

5.2.2 ToF Sensors and Sampling Theory

In many practical cases of interest, the SRF and the IRF are shift–invariant functions such that,

$$h_{\mathsf{SI}}(t,\tau) = h(t - \tau) \quad \text{and} \quad \varphi_{\mathsf{SI}}(t,\tau) = \varphi(t - \tau), \tag{5.5}$$

respectively. We list the most prevalent examples in Table 5.1. Whenever (5.5) holds, we can rewrite (5.2) and (5.3) as convolution integrals and hence,

$$m(t) \overset{(5.5)}{=} (p * h * \varphi)(t) \equiv (\phi * h)(t), \quad \phi(t) = (p * \varphi)(t). \tag{5.6}$$

In analogy to shift–invariant *sampling theory* [27], we re-interpret (5.6), as sampling of an unknown, shift–invariant SRF with sampling kernel ϕ. Finally, the ToF sensor measurements are uniform samples,

$$m[k] = (\phi * h)(t) \sum_{k \in \mathbb{Z}} \delta(t - k\Delta). \tag{5.7}$$

where $\phi(t)$ is the identified sampling kernel in (5.6). At this point, we make no assumptions on the unknown SRF or the nature of probing function as well as the IRF.

5.2.3 Lidar Based ToF Imaging

Lidar based imaging sensors probe the scene with a time-localized pulse with resolution of the order of few picoseconds [227] which one may approximate as $p_{\mathsf{LiDAR}}(t) \approx \delta(t)$.

$$p_{\mathsf{Lidar}}(t) \approx \delta(t). \tag{5.8}$$

Reflection from an opaque surface leads to the SRF in (5.4) resulting in the reflected signal, $r_{\mathsf{LiDAR}}(t) = \Gamma_0 \delta(t - t_0)$.

$$r_{\mathsf{Lidar}}(t) = \Gamma_0 \delta(t - t_0), \quad t_0 = 2d_0/c. \tag{5.9}$$

As shown in [224, 64], the IRF due to SPAD detectors may be modeled as a parametric, shift–invariant kernel of form,

$$\varphi_{\boldsymbol{\Theta}}(t) = \alpha \begin{cases} \theta\left(-\frac{(T_1-T_0)^2}{2\sigma^2}\right)\theta\left(\frac{t-T_1}{\lambda_1}\right) & t < T_1 \\ \theta\left(-\frac{(t-T_0)^2}{2\sigma^2}\right) & t \in [T_1, T_2) \\ \theta\left(-\frac{(T_2-T_0)^2}{2\sigma^2}\right)\theta\left(-\frac{t-T_2}{\lambda_2}\right) & t \in [T_2, T_3) \\ \theta\left(-\frac{(T_2-T_0)^2}{2\sigma^2}\right)\theta\left(-\frac{T_3-T_2}{\lambda_2}\right)\theta\left(-\frac{t-T_3}{\lambda_3}\right) & t \geqslant T_3 \end{cases}, \tag{5.10}$$

where, $\theta(t) = e^{-t}$ and $\boldsymbol{\Theta}$ is an unknown parameter vector,

$$\boldsymbol{\Theta} = \begin{bmatrix} \alpha & \sigma & T_0 & T_1 & T_2 & T_3 & \lambda_1 & \lambda_2 & \lambda_3 \end{bmatrix}^\top. \tag{5.11}$$

As a result of this IRF, the measurements read $m(t) = \Gamma_0 \varphi_{\boldsymbol{\Theta}}(t - t_0)$. As shown in [227, 64], the parameter vector $\boldsymbol{\Theta}$ may be calibrated and the depth/delay t_0 is estimated using a linear relation [227].

5.3 Super–Resolved ToF Imaging

In this section, we formulate the ToF super-resolution problem. In case when the ToF sensor receives a multi-echo backscattered signal (cf. Fig. 5-1(b),(c)), the SRF can be modeled as [65, 226, 16],

$$h_{\mathsf{SI}}(t, \tau) = \sum_{k=0}^{K-1} \Gamma_k \delta\left(t - \tau - 2\frac{d_k}{c}\right), \quad c = 3 \times 10^8 \text{ m/s}. \tag{5.12}$$

In view of (5.6), the continuous time measurements amount to,

$$m(t) = \sum_{k=0}^{K-1} \Gamma_k \phi(t - t_k), \qquad t_k = 2\frac{d_k}{c}. \tag{5.13}$$

This brings us to our problem statement: *Given N discrete measurements, $\{m[n]\}_{n=0}^{N-1}$ defined in (5.7), estimate the SRF in (5.12) parameterized by $\{\Gamma_k, t_k\}_{k=0}^{K-1}$.*

5.3.1 Bandlimited Approximation of Sampling Kernel

The super-resolution problem is ill–posed if ϕ is unknown. In context of FRI sampling theory, the so–called "sampling kernel" [69, 70] ϕ is assumed to be known. Similarly, in ToF context, ϕ is either designed or calibrated. We discuss two examples based on Table 5.1.

1. In case of AMCW–ToF [65, 226, 65], $p(t)$ is pre-defined and the IRF is the time reversed version

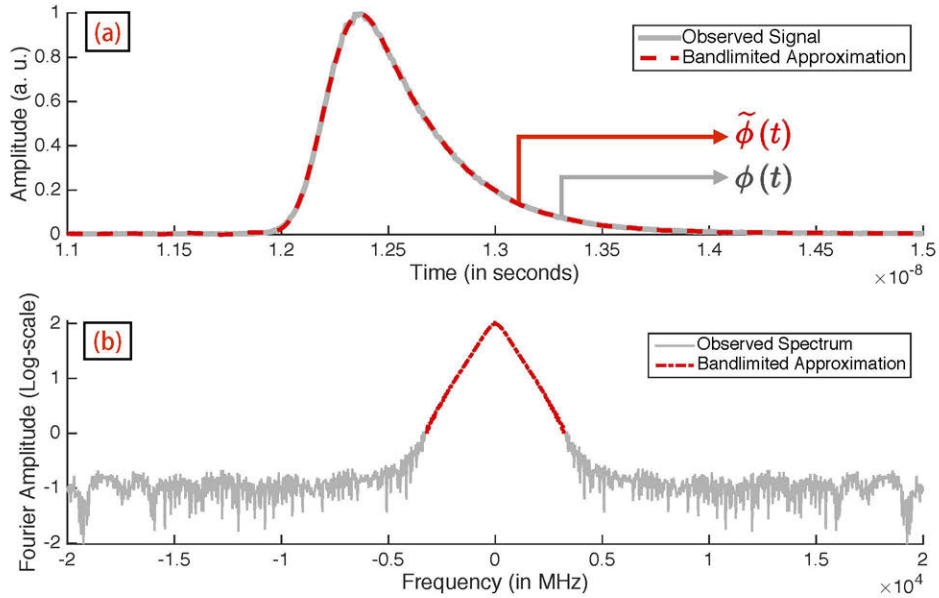

Figure 5-2: Instrument response function for LiDAR ToF system. (a) Observed time profile and its Fourier Series approximation (5.15) with $L = 25$ ns and $M_0 = 80$. (b) Fourier spectrum together with Fourier Series coefficients $\{\widehat{\phi}_m\}_{|m|\leqslant M_0=80}$ (5.15). With $f_0 = \omega_0/2\pi = 40.0195$ MHz, the maximum frequency used for approximation of $\phi(t)$ is $M_0 f_0$.

---

of the probing function. Hence,

$$\phi_{\mathsf{AMCW}}(t) = \lim_{T\to\infty} \frac{1}{T} \int_{-T/2}^{+T/2} p(\tau)\, p(t+\tau)\, d\tau \equiv (p * \overline{p})(t), \tag{5.14}$$

where $\overline{p}(t) = p(-t)$ denotes the time reversal operation.

2. In case of LiDAR based ToF systems, we have $\phi(t) = \varphi_{\boldsymbol{\Theta}}(t)$ (cf. (5.10)). The parameter vector $\boldsymbol{\Theta}$ is estimated via calibration[64].

In this work, we take an alternate approach towards modeling of ϕ. To this end, we use *bandlimited approximation*, that is, we approximate $\phi(t)$ over an interval of size L with its first M_0 frequency components. This is accomplished by truncating the Fourier series so that,

$$\widetilde{\phi}(t) = \sum_{|m|\leqslant M_0} \widehat{\phi}_m e^{\jmath m\omega_0 t} \text{ with } \widehat{\phi}_m = \frac{1}{L}\int_0^L \phi(t)\, e^{-\jmath m\omega_0 t} dt, \tag{5.15}$$

where $\widetilde{\phi}(t)$ is the M_0–coefficient approximation of $\phi(t)$, $\widehat{\phi}_m, m = -M_0, \ldots, M_0$ are the Fourier Series coefficients of $\phi(t)$ and $\omega_0 = 2\pi/L$ is the fundamental frequency depending on L which is chosen to be the maximum operating range of the ToF system. For example, L may be chosen to be the length of

duration of the IRF obtained via calibration. Alternatively,

$$L = \left|\max\left(\mathbb{T}_K\right) - \min\left(\mathbb{T}_K\right)\right|, \quad \mathbb{T}_K = \{t_k\}_{k=0}^{K-1}.$$

The bandlimited approximation approach is a natural choice for modeling the sampling kernel ϕ. This is because:

1. Almost all optical systems are approximately bandlimited due to physical limitations. In previous work [65, 21], we have shown that the AMCW ToF (cf. Table 5.1) based sampling kernel (5.14) admits a bandlimited approximation. Here, we show the same for LiDAR based systems. Note that $\phi(t) = \varphi_{\boldsymbol{\Theta}}(t)$ (cf. (5.10)) implying that the sampling kernel is the same as the IRF. In Fig. 5-2(a), we plot the observed $\phi(t)$ acquired experimentally together with its bandlimited approximation $\widetilde{\phi}$ using $M_0 = 80$.
2. Bandlimited approximation also circumvents the need to estimate the unknown parameter vector $\boldsymbol{\Theta}$ (5.11) associated with ϕ.

5.3.2 Super-Resolution via FRI Principles

Bandlimited approximation of ϕ allows us to rewrite (5.13) as

$$\begin{aligned} m(t) &\overset{(5.13)}{=} \sum_{k=0}^{K-1} \Gamma_k \phi(t - t_k) \\ &\overset{(5.15)}{\approx} \sum_{k=0}^{K-1} \Gamma_k \sum_{|m| \leqslant M_0} \hat{\phi}_m e^{\jmath m \omega_0 (t - t_k)} \\ &= \sum_{|m| \leqslant M_0} \hat{\phi}_m \underbrace{\sum_{k=0}^{K-1} \Gamma_k e^{-\jmath m \omega_0 t_k}}_{y_m} e^{\jmath m \omega_0 t} \\ &= \sum_{|m| \leqslant M_0} \hat{\phi}_m y_m e^{\jmath m \omega_0 t}. \end{aligned} \tag{5.16}$$

In vector–matrix notation we write the sampled measurements (5.7) as $\mathbf{m} = \mathbf{V}\mathbf{D}_\Phi \mathbf{y}$ or,

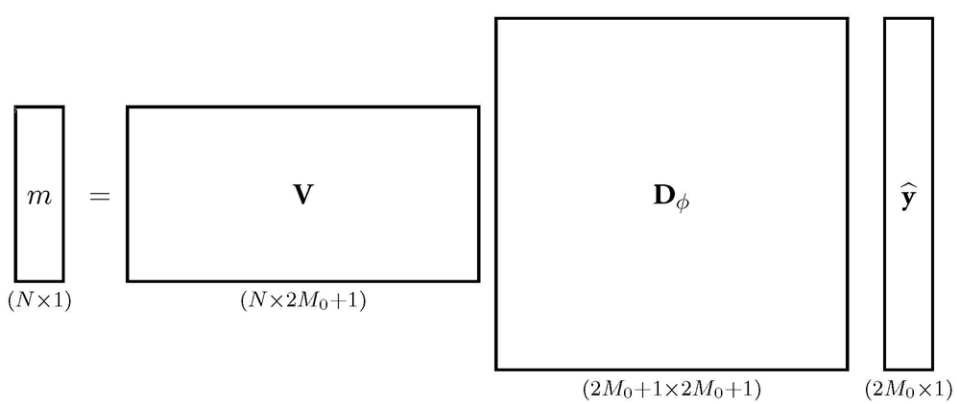

where,

1. $\mathbf{m} \in \mathbb{R}^N$ is a vector of N, low–pass filtered measurements, $\mathbf{m}$.
2. $\mathbf{V} \in \mathbb{C}^{N\times(2M_0+1)}$ is a Vandermonde/DFT matrix with matrix element $\left[e^{\jmath m\omega_0 n\Delta}\right]_{n,m}$.
3. $\mathbf{D}_\Phi \in \mathbb{C}^{(2M_0+1)\times(2M_0+1)}$ is a diagonal matrix with matrix element $[\hat{\phi}_m]_{m,m}$ which are the Fourier Series coefficients of ϕ (5.15).
4. $\mathbf{y} \in \mathbb{C}^{(2M_0+1)}$ is a vector of a sum of complex exponentials,

$$y_m = \sum_{k=0}^{K-1} \Gamma_k e^{-\jmath n\omega_0 t_k}. \tag{5.17}$$

Hence, given $\mathbf{m} = \mathbf{V}\mathbf{D}_\Phi\mathbf{y}$, we estimate $\{\Gamma_k, t_k\}_{k=0}^{K-1}$ in two steps:

1. First we obtain the vector $\mathbf{y}$. Provided that $N \geq 2M_0+1$, we have $\mathbf{y} = \mathbf{D}_\Phi^{-1}\mathbf{V}^+\mathbf{m}$ where $\mathbf{D}_\Phi^{-1}$ is the inverted diagonal matrix with elements $[\hat{\phi}_n^{-1}]_{n,n}$ and $(\cdot)^+$ denotes the pseudo–inverse operation.
2. Having obtained $\mathbf{y}$, we are left with task of estimating parameters $\{\Gamma_k, t_k\}_{k=0}^{K-1}$. In the noiseless setting, this can be accomplished by using Prony's method which relies on the observation that there exists a sequence $\{h_m\}_{m=0}^{K}$ which *annihilates* y_m [67],

$$y_m + \sum_{l=1}^{K} h_l y_{m-l} = 0, \quad m \geqslant K+1. \tag{5.18}$$

It turns out that the roots of the polynomial $\mathsf{H}(z)$ constructed with coefficients as $\{h_m\}_{m=0}^{K}$, that is,

$$\mathsf{H}(z) = \prod_{k=0}^{K-1} \left(1 - e^{-\jmath\omega_0 t_k} z^{-1}\right) = \sum_{m=0}^{K-1} h_m z^{-1},$$

encode the information of time delays $\{t_k\}_{k=0}^{K-1}$. This is because $\mathsf{H}\left(e^{-\jmath\omega_0 t_k}\right) = 0$. With $\{t_k\}_{k=0}^{K-1}$, estimating $\{\Gamma_k\}_{k=0}^{K-1}$ boils down to a linear least squares problem,

$$\min_{\{\Gamma_k\}_{k=0}^{K-1}} \sum_{|m|\leqslant M_0} \left| y_m - \sum_{k=0}^{K-1} \Gamma_k e^{-\jmath n\omega_0 t_k} \right|^2.$$

In view of (5.18), we have $M_0 > K$. With $y_m = y_m^*$, provided that $N \geq K+1$, we can estimate $\{\Gamma_k, t_k\}_{k=0}^{K-1}$ given $\mathbf{m}$. This method can be extended to the *noisy case* [70]. In fact, a number of methods discuss estimation of $\{\Gamma_k, t_k\}_{k=0}^{K-1}$ given $\mathbf{y}$ in presence on noise. We refer the reader to [67] for a comprehensive overview of techniques. In this work, we will use the *Matrix Pencil Method* due to Hua and Sarkar [228].

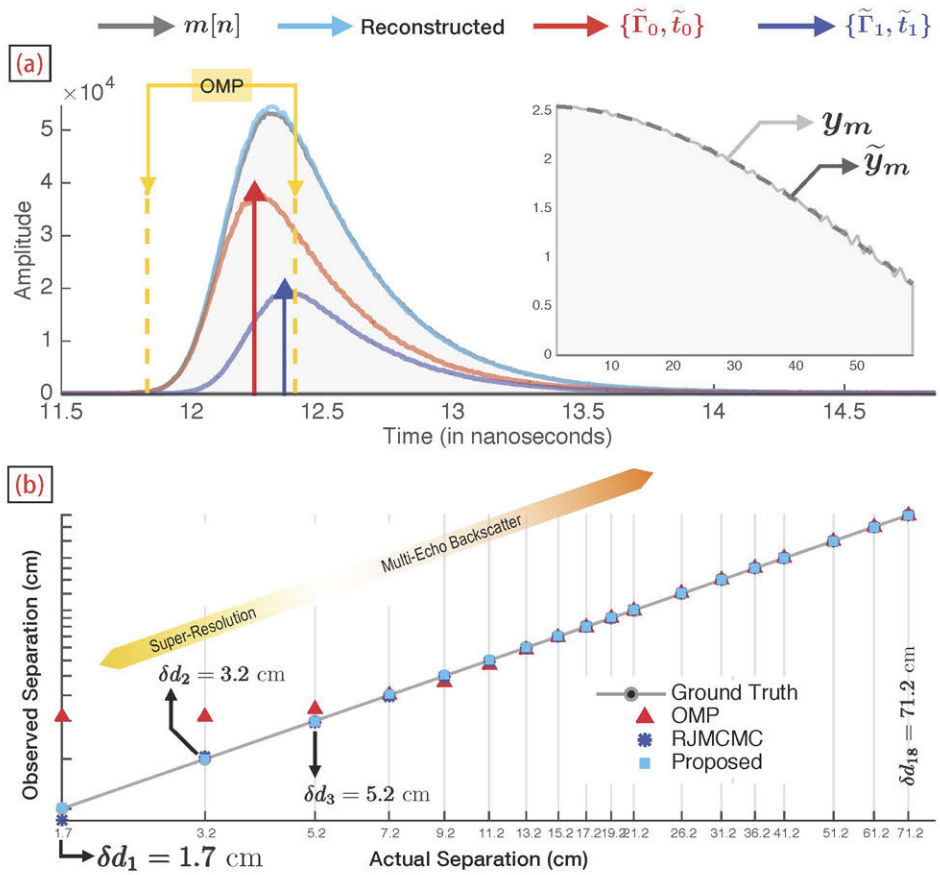

Figure 5-3: LiDAR based Super-resolution ToF Imaging. (a) The experiment consists of two retro-reflecting cubes at distance of 330 m from the sensor. We show the recovery of reflectors with inter-reflector separation $\delta d_{\ell_1} = 1.7$ cm. We also plot the result due to Orthogonal Matching Pursuit [229]. (b) We conduct experiments with various separations and plot the results on log–log scale. Our method outperforms previously reported results on the same data in [64].

5.3.3 Experimental Results and Performance Evaluation

To measure the depth resolution of the TCSPC-TOF system, two retro-reflecting corner cubes were placed at a distance of 330m from the LiDAR transmitter-receiver and the distance between these surfaces was varied from $\delta d_\ell = 1.7$ cm to 71.2 cm. For a corner cube, all beams, independent of incident angle, are reflected back in the original direction so the behavior is that of a perfect reflecting surface. In these experiments, the timing resolution of the receiver was $\Delta = 6.1$ ps, and the collection time for each histogram was 30s. We calibrated the sampling kernel $\phi(t) = \varphi_\Theta(t)$ in (5.10) which is shown in Fig. 5-2(a). This is done by recording the response of the LiDAR system to Lambertian reflector.

In this subsection, we discuss the effectiveness of our approach on LiDAR based ToF systems. First, we calibrate the sampling kernel $\phi(t) = \varphi_\Theta(t)$ in (5.10) which is shown in Fig. 5-2(a). This is done by recording the response of the LiDAR system to Lambertian reflector. Our experimental set-up consists of two retro-reflecting corner cubes at a distance of 330 m from the sensor. With the position of first cube

constant, the distance/separation between the two cubes is varied for the ℓth experiment according to the rule $s_\ell = 2\ell + 1.2$ cm, $\ell = 1, \ldots, 10$. The measurements are acquired according to (5.7) with $N = 4095$ and $\Delta = 6.10$ ps.

We plot measurements for $\delta d_1 = 1.7$ cm in Fig. 5-3(a). Setting $M_0 = 60$ and discarding the boundary values, we use $\mathbf{y} = \mathbf{D}_\Phi^{-1}\mathbf{V}^+\mathbf{m}$, to estimate $\{y_m\}_{m=2}^{m=59}$. We then use *Matrix Pencil* method [228] with pencil parameter $1/2$ to estimate $\{\widetilde{\Gamma}_k, \widetilde{t}_k\}_{k=0}^{K-1}$. Based on these estimates, we re-synthesize $\{\widetilde{y}_m\}_{m=2}^{m=59}$ using (5.17) which is plotted in the inset of Fig. 5-3(a). For the ℓth experiment with separation δd_ℓ, we estimate the separation using $\delta\widetilde{d}_\ell = 50(\widetilde{t}_2^{(\ell)} - \widetilde{t}_1^{(\ell)})c$ (in cm) with performance metric MSE or the *mean squared error*, $\mathsf{MSE}(\delta\widetilde{d}_\ell, \delta d_\ell) = |50(\widetilde{t}_2^{(\ell)} - \widetilde{t}_1^{(\ell)})c - \delta d_\ell|^2$ as our evaluation metric. The ToF estimates for super-resolution case with $\ell = 1$ results in $[\,\widetilde{t}_1^{(1)}, \widetilde{t}_2^{(1)}\,] = [\,12.2398, 12.3542\,]$ ns. Similarly, for $\ell = 2$, we report, $[\,\widetilde{t}_1^{(2)}, \widetilde{t}_2^{(2)}\,] = [\,12.1338, 12.3474\,]$ ns. The resulting MSE is,

$$\mathsf{MSE}(\delta\widetilde{d}_1, \delta d_1) = 2.6 \times 10^{-4} \text{ and } \mathsf{MSE}(\delta\widetilde{d}_2, \delta d_2) = 2.5 \times 10^{-5}.$$

respectively. We compare our method to sparse recovery methods such as the OMP or the *Orthogonal Matching Pursuit* [229]. For the super-resolution problem corresponding to $\ell = 1$, the estimates are erroneous, $[\,\widetilde{t}_1^{(1)}, \widetilde{t}_2^{(1)}\,]_{\mathsf{OMP}} = [\,12.2803, 12.6465\,]$ with $\mathsf{MSE} = 14.3884$ which is orders of magnitude higher. For higher values of ℓ, the performance of OMP is comparable. We note this behavior for $\ell \geq 3$. RJMCMC based approach of Marin et al. [64] provides better estimates compared to the OMP but is computationally intensive. Our proposed approach provides better estimates compared to OMP and RJMCMC method. For $\{\delta d_\ell\}_{\ell=1}^{18}$ we compare the estimates in Fig. 5-3(b) and note that our proposed approach is reasonably accurate and outperforms previously reported results on the same data in [64].

The matrix pencil method is near optimal in performance (in sense of achieving the Cramér–Rao bounds) [228]. In Fig. 5-4(a) we plot the MSE as a function of signal–to–noise ratio or the SNR for separations 1.74 cm (super-resolution case), 3.204 cm (super-resolution case) and 18.3105 cm. The performance of our method is consistent with our experiments. We omit discussion on Cramér-Rao bounds in this work due to space limitations but results from [65] may be adapted to our setting. We estimate the system SNR using the IRF which is approximately 43.18 dB (cf. Fig. 5-4(b)). Furthermore, our method is computationally efficient compared to common-place sparse solver, OMP. As shown in Fig. 5-4(c), it is about 5 times more efficient. A detailed discussion on computational complexity can be found in [65].

5.4 Summary

In this chapter, we report a method for super-resolution for ToF signals that is applicable to a wide variety of ToF sensors. We present a unifying image formation model for ToF systems which consolidates two major classes of ToF sensors: AMCW and LiDAR. Based on our image formation model, we draw a parallelism between ToF imaging and sampling theory. In particular, we show that the super-resolution problem in context of ToF imaging can be re-formulated as a finite–rate–of–innovation sampling problem. We discuss the effectivity our approach by performing experiments with LiDAR ToF sensors. Our preliminary experiments show promising results towards super-resolving multi-echo, backscattered, ToF signals. Compared to existing solutions (cf. [64, 224, 223] and references therein), our method is computationally attractive and more accurate in performance.

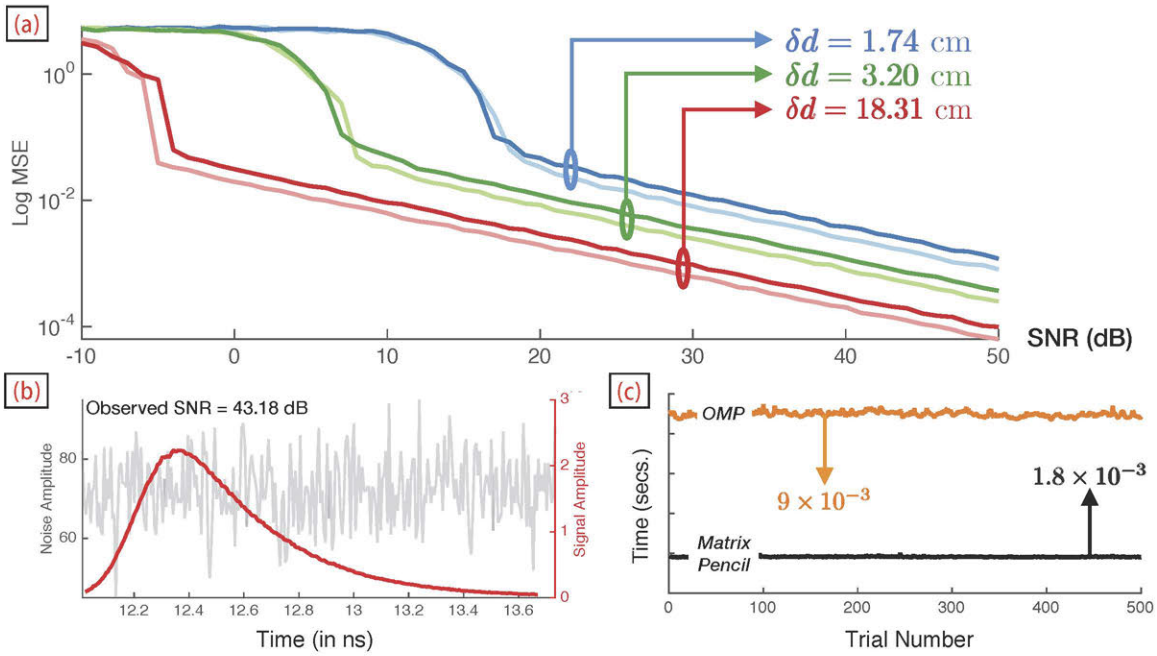

Figure 5-4: (a) We setup experiments with separation distances $\delta d = 1.74$, 3.20 and 18.21 cm, respectively and plot the log-MSE as a function of signal–to–noise ratio or the SNR (in dB). (b) We use the IRF to estimate the SNR. The observed SNR for the system is 43.18 dB. (c) We compare computational times for OMP and matrix pencil method. The average of all trials is marked in the figure. In contrast, the RJMCMC method due to [64] requires about a second per pixel.

इछन्ति देवाः सुन्वन्तं न सवप्राय सप्रहयन्ति ।
यन्ति परमादमतन्द्राः

ओ षु पर याहि वाजेभिर्मा हर्णीथा अभ्यस्मान ।
महानिव युवजानिः ॥

मो षवद्य दुर्हणावान सायं करदारे अस्मत ।
अश्रीर इव जामाता ॥

विद्मा हयस्य वीरस्य भूरिदावरीं सुमतिम ।
तरिषु जातस्य मनांसि ॥

"The gods seek a presser. They are not eager for sleep. Tireless, they go to exhilaration." [1]

— Rigveda (Mandala VIII, §02, ¶ 18–21)

6

Fluorescence Lifetime Imaging A Blind and Calibration-free Approach

6.1 Introduction

Fluorescence lifetime imaging (FLI) is a significant research area spanning many engineering applications. Knowledge of a sample's fluorescence lifetime allows, for example, DNA sequencing [230], tumor detection [231, 232], fluorescence tomography [233, 234], in vivo imaging [235] and high resolution microscopy [236]. Typically, FLI is categorized into to two complementary modes [237, 233]. In time-domain FLI [236, 238] (TD-FLI), an impulse-like excitation pulse probes the fluorescent sample, and the time-resolved reflection is used to calculate lifetimes. In frequency-domain FLI [239, 240, 241] (FD-FLI), the sample is excited with (sinusoidal) intensity modulated light, and the measured phase shift of the reflected signal at the same modulation frequency encodes the lifetime. The FD-FLI is theoretically appealing in that phase measurements at one given modulation frequency suffice to resolve the sample lifetime. From a practical standpoint, model mismatch [239] and sample contamination due to multiple lifetimes [242] often limits the accuracy of single frequency based systems. Frequency diversity [242, 243] may be used for imaging multiple lifetimes. Since this approach requires sweeping of frequencies over a given bandwidth, frequency diversity method is not suitable for wide field imaging of dynamic samples. In either case (TD–FLI or FD–FLI), because of the costly equipment, system constraints are often strict, so that precise knowledge of the illumination signal and calibration measurements (to compensate for path length delays) are required [244].

Alternatively, time-of-flight (ToF) sensors, which are far more cost-effective and operate in real time,

offer a great deal of flexibility in design. ToF sensors (such as the Microsoft Kinect) are essentially depth/range imaging devices and are at the heart of entertainment industry. Recently, ToF sensing has found prodigious use in computer graphics, computer vision [226], and computational imaging [17, 226, 19], with applications in multi-path imaging [245, 209, 65, 16], ultrafast imaging [15, 16] and imaging through scattering media [18, 17].

Here, we demonstrate the extension of ToF sensing to FLI which is both blind and calibration-free. To do so, we generalize (from the distinct time or frequency domains) the active illumination signal, which is common to both modalities, to show that neither calibration measurements nor knowledge of the signal are necessary for estimation of fluorescent lifetimes. This blind, reference-free method is implemented in a consumer-grade ToF sensor to estimate simultaneously the range and lifetime of a CdSe-CdS quantum dot sample. This method suggests a cost-effective alternative to the usual FLI methods.

6.1.1 Roadmap for this Chapter

This chapter is organized as follows:

- starting from first principles, we propose a ToF sensor-based image formation model and discuss its role in depth/range estimation in Section 6.2.
- We then discuss the two complimentary modes of operation of ToF sensors—time and frequency domain. Section 6.2.1 deals with time-domain ToF sensor based depth imaging while Section 6.2.2 is devoted to frequency-domain depth imaging.
- In Section 6.3, we provide a mathematical model for fluorescence lifetime imaging with ToF sensors. We show that consumer ToF sensors such as the Microsoft Kinect can be used to estimate the lifetime of a fluorescent sample. We develop theoretical models for both time- and frequency-domain modes. Our theory is corroborated with experiments for both time- and frequency-domain mode of operation.
- The two complimentary approaches that we will now discuss in detail are covered in Section 6.3.
- Finally, we conclude this work with possible future directions in Section 6.5.

6.2 ToF Image Formation Model

ToF sensors operate using the lock-in principle [23]: active illumination probes a sample, and the reflected light is cross-correlated electronically to calculate range and amplitude information. In this way, each ToF sensor exposure results in two images–the usual intensity image and a range image where each pixel relates to the depth of the scene. Usually, the signal is sinusoidal, essentially classifying a ToF sensor as a homodyne detection system, but the illumination signal can be far more general. Both ToF sensors and current FLI technologies acquire scene information in either the time or frequency domains, so the present analysis for ToF sensing is compatible with both.

Regardless of the operating domain or physical implementation, the ToF imaging process can be understood as follows. A scene is illuminated with a time-dependent, Δ-periodic, probing intensity signal $p(t)$ such that $p(t+\Delta) = p(t), \Delta > 0$. Similar to FLI, time-domain [16, 65] ToF (TD-ToF) systems

use a time-localized pulse $p(t)$ (not necessarily an impulse); the frequency-domain ToF (FD-ToF) counterpart uses a modulated probing function $p(t) = 1 + \cos(\omega_0 t)$, where ω_0 (usually in the MHz range) is the modulation frequency. Below, however, we do not use a specific form for $p(t)$.

This signal interacts with the scene, whose response is characterized by a time-dependent scene response function (SRF) $h(t, t')$, where t' is a time-domain variable which models the time-variant scene response function. This interaction results in the reflected signal $r(t)$,

$$r(t) = \int p(t')\, h(t, t')\, dt' \tag{6.1}$$

ToF sensor detects $r(t)$ and electronically cross-correlates it with $p(t)$:

$$m(t) = \int \overline{p}(t') r(t - t')\, dt', \tag{6.2}$$

where $\overline{p}(t) = p(-t)$. The K stored measurements are digital samples of this cross-correlation, $m_k = m(kT_s), k = 0, \ldots, K-1$ ($T_s > 0$ is the sampling rate).

In many cases of interest, the SRF is shift-invariant, that is (cf. 2.2.4, pg. 50 [246]),

$$h(t, t') = h_{\mathsf{SI}}(t - t'),$$

so that (6.1) represents the convolution operation defined by

$$r(t) = (p * h_{\mathsf{SI}})(t) = \int p(t') \underbrace{h_{\mathsf{SI}}(t - t')}_{h(t,t')} dt'. \tag{6.3}$$

We remind the reader that t' is a a time-domain dummy variable in the superposition integral. In case of shift-invariant SRFs, the measurements simplify to

$$m(t) = (p * \overline{p} * h_{\mathsf{SI}})(t) \equiv (\phi * h_{\mathsf{SI}})(t), \tag{6.4}$$

implying linear filtering of cross-correlated function $\phi(t)$ with the scene response filter h_{SI}.

Conventional ToF sensors [226] are designed for range imaging and depth estimation. For simple reflections from an object (with reflection coefficient ρ) that is at a depth d from the sensor, the SRF becomes

$$h(t, t') = \rho\delta(t - t' - 2d/c) \tag{6.5}$$

where c is the speed of light, and δ denotes the Dirac distribution. The reflected signal in this case is simply a delayed version of the probing function and the delay is proportional to the depth parameter d. More precisely, in view of the ToF sensor operation, the reflected signal in (6.1) reads, $r(t) = \rho p(t - t_0)$ where the delay $t_0 = 2d/c$. In this case, the measurements amount to,

$$m(t) = \rho\phi(t)(t - t_0) \equiv \rho(p * \overline{p})(t - t_0).$$

Estimation of the scene parameters $\{\rho, d\}$ by the ToF sensor results in range and intensity images. The estimation process depends on the choice of probing function p which may be a time-localized pulse or an amplitude modulated continuous wave (AMCW) function leading to time-domain (Fig. 6-1 (a)) and

Table 6.1: Time and Frequency Domain Time-of-Flight Depth Imaging

	Time-domain ToF	Frequency-domain ToF
Probing Function	$p(t) = \frac{1}{\Delta}\sum_{\lvert m\rvert\leqslant M_0} \hat{p}_m e^{\jmath\omega_0 m t}$	$p(t) = 1 + p_0 \cos(\omega t)$
Scene Response Function	$h_{\mathsf{SI}}(t) \overset{(6.5)}{=} \rho\delta(t - 2d/c)$	
Reflected Function	$r(t) \overset{(6.3)}{=} \rho p\left(t - \frac{2d}{c}\right)$	
Measurements	$\frac{\rho}{\Delta}\sum_{\lvert m\rvert\leqslant M_0} \lvert\hat{p}_m\rvert^2 e^{\jmath\omega_0 m\left(t-\frac{2d}{c}\right)}$	$\rho\left(1 + \frac{p_0^2}{2}\cos\left(\omega\left(t + \frac{2d}{c}\right)\right)\right)$

frequency-domain (Fig. 6-1 (b)) mode of operation, respectively.

6.2.1 Time-Domain ToF Imaging (TD-ToF)

For TD-ToF imaging, the probing function is ideally well localized in time, that is, a Dirac delta distribution. In this case, $p(t) \sim \delta(t)$, and the measurements in (6.4) simplify to $m(t) = h_{\mathsf{SI}}(t)$. In practice, maximum length sequences (MLS) [247] provide an optimal time-localized probing function. Such sequences are a function of the signal length or period Δ.

In view of the depth estimation problem where $h(t, t') = \rho\delta(t - t' - 2d/c)$, the depth is estimated by the operation,

$$\widetilde{t_0} = \max_t m(t) = \max_t \phi(t - t_0), \quad t_0 = \frac{2d}{c}.$$

More sophisticated methods have been developed for the case of multiple reflections or multi-path interference [16, 65].

The exact characterization of the true TD-ToF probing function $p(t)$ is challenging due to the electronics of the sensor and the physical process involved. Using a Fourier series expansion [65] to represent the probing function,

$$p(t) = \frac{1}{\Delta}\sum_{n=-\infty}^{\infty} \widehat{p}_n e^{\jmath n\omega_0 t}, \quad \omega_0 = 2\pi/\Delta, \tag{6.6}$$

where

$$\widehat{p}_n = \int_0^{\Delta} p(t)\, e^{-\jmath n\omega_0 t} dt,$$

we define the cross-correlation of the probing function p by

$$\phi(t) = (p * \overline{p})(t) = \sum_{n=-\infty}^{\infty} \widehat{\phi}_n e^{\jmath\omega_0 n t}. \tag{6.7}$$

The Fourier series coefficients of the cross-correlated signal and the probing signal are related by

$$\widehat{\phi}_n = \widehat{p}_n \widehat{p}_n^* = \lvert\widehat{p}_n\rvert^2. \tag{6.8}$$

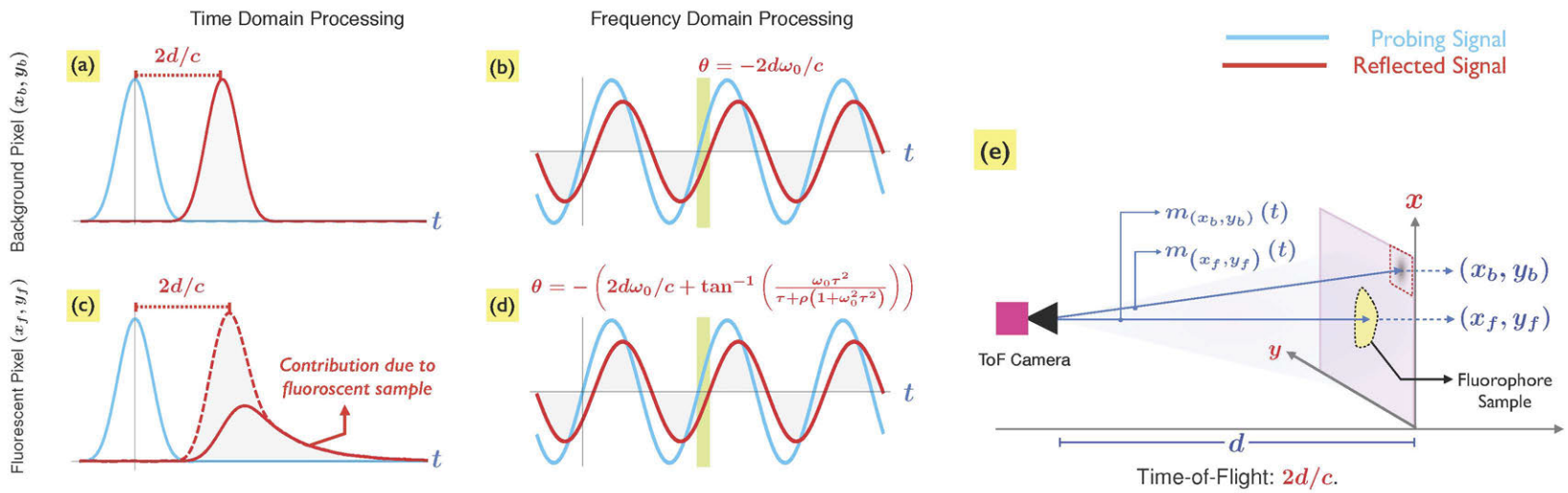

Figure 6-1: Depth or range imaging based on time-of-flight (ToF) principles and its link with fluorescence lifetime imaging. For the choice of scene response function (SRF) $h(t,x) = \rho\delta(t - x - 2d/c)$ (a) and (b) compare time and frequency based methods for depth imaging based on ToF principles. (a) Probing and reflected signal for time-domain time-of-flight (TD–ToF) setup. The time delay is proportional to distance d. (b) Probing and reflected signal for frequency-domain time-of-flight (FD–ToF) setup. The phase is proportional to distance d and modulation frequency ω_0. For the SRF $h(t,x) = h_{\text{Depth}}(t,x) + h_{\text{Sample}}(t,x)$ in (6.13), (c) and (d) compare time and frequency based methods for fluorescence lifetime imaging based on ToF principles. (c) Probing and reflected signal for time-domain time-of-flight (TD–ToF) setup. The time delay is proportional to distance d and the waveform shape is linked with lifetime τ. (b) Probing and reflected signal for frequency-domain time-of-flight (FD–ToF) setup. The phase is proportional to distance d, modulation frequency ω_0 and lifetime τ. (e) Experimental setup for fluorescence lifetime estimation using ToF sensors.

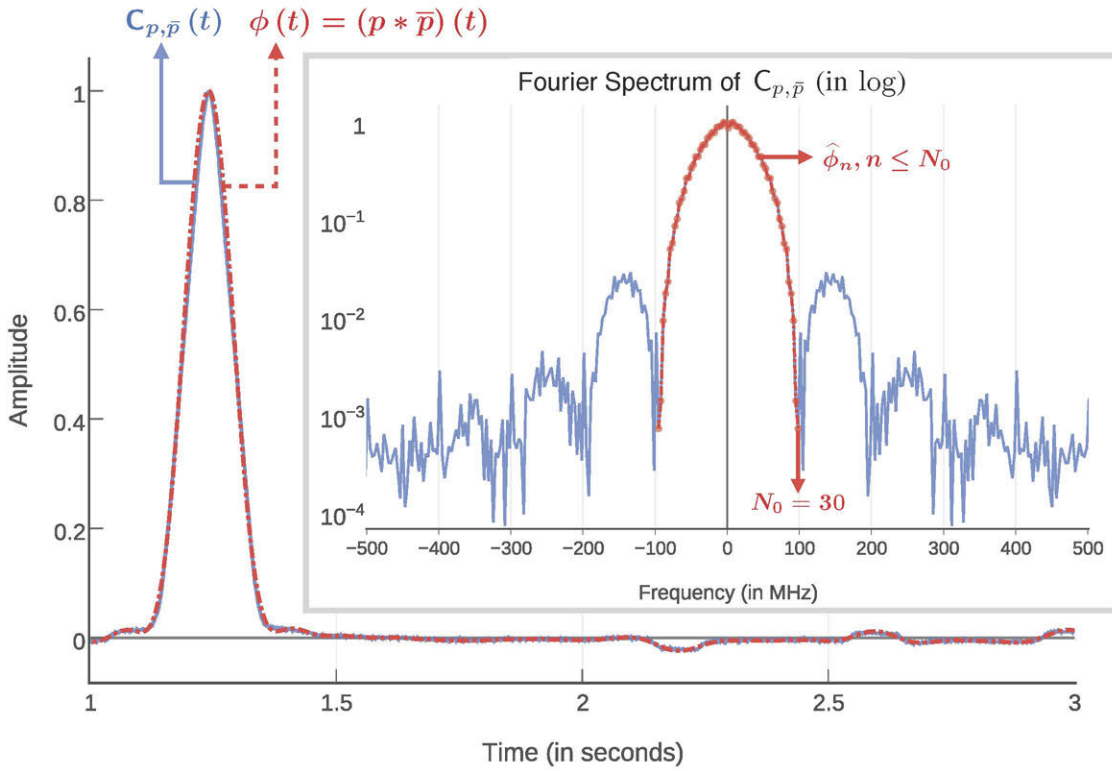

Figure 6-2: Experimental cross-correlated probing function Eq. (6.8) (– –) and its Fourier series approximation (–•–), Eq. (6.9), with $N_0 = 30$. Since the time-domain signal $\mathsf{C}_{p,\overline{p}}$ lasts for $\Delta = 309.902$ ns, the corresponding fundamental Fourier harmonic is $\omega_0/2\pi = 3.2268$ MHz. Consequently, Fourier coefficient $N_0 = 30$ corresponds to ~ 96.80 MHz. Inset: Fourier series coefficients $\widehat{\phi}_n, n = -N_0, \ldots, N_0$.

Practically, a bandlimited approximation, $\mathsf{C}_{p,\bar{p}}(t)$, suffices to represent $\phi(t)$:

$$\mathsf{C}_{p,\overline{p}}(t) \approx \frac{1}{\Delta} \sum_{|n| \leqslant N_0} \widehat{\phi}_n e^{jn\omega_0 t}, \tag{6.9}$$

where we have retained the first N_0 Fourier coefficients of $\phi(t)$. Fig. 6-2 shows an experimentally obtained $\phi(t)$ and its Fourier approximation $\mathsf{C}_{p,\overline{p}}$, with their Fourier spectra with $N_0 = 30$, for an impulsive probe function.

6.2.2 Frequency-Domain ToF Imaging (FD-ToF)

In FD-ToF imaging, the scene is probed with a continuous wave, sinusoidal probing function with a modulation frequency ω:

$$p(t) = 1 + p_0 \cos(\omega t),$$

where p_0 is the modulation amplitude. For pure depth estimation, with the SRF specified in (6.5), the reflected signal becomes

$$\begin{aligned} r(t) &= \rho p(t - t_0) \\ &= \rho \left(1 + p_0 \cos\left(\omega \left(t - t_0\right)\right)\right). \end{aligned}$$

The ToF lock-in sensor acts as a homodyne detector array: each pixel cross-correlates the reflected signal with the probing signal to produce measurements

$$m(t) = \lim_{B \to \infty} \frac{1}{2B} \int_{-B}^{+B} \overline{p}\left(t'\right) r\left(t - t'\right) dt' \tag{6.10}$$

$$= \rho \left(1 + \frac{p_0^2}{2} \cos\left(\omega \left(t + t_0\right)\right)\right), \tag{6.11}$$

where in (6.10), we generalize the cross-correlation in (6.2) for sinusoids.

The two quantities of interest, ρ and d, are estimated with the four digital measurements of the measured signal in (6.11), that is, $m_k = m\left(\pi k / 2\omega T_s\right),\ k = 0, \ldots, 3$. Based on these discrete measurements, we define a complex number $z \in \mathbb{C}$:

$$z = (m_0 - m_2) + \jmath(m_3 - m_1). \tag{6.12}$$

The scene parameters are thus estimated by

$$\widetilde{\rho} = \frac{|z|}{p_0^2} \quad \text{and} \quad \widetilde{d} = \frac{c}{2\omega} \angle z.$$

Note that this technique for extracting phase is identical to conventional phase-shifting holography [248].

To summarize, object range is estimated via time delays in TD-ToF (cf. Fig. 6-1 (a)), whereas FD-ToF (cf. Fig. 6-1 (b)) encodes range into the signal phase. A quantitative summary of ToF sensor based depth estimation problem for time-domain and frequency-domain approach is presented in Table 6.1.

In most consumer ToF sensors, $m(t)$ (6.2) is a set of measurements that is used to estimate the scene parameters $\{\rho, d\}$ [16, 23]. The goal of this chapter is to show that by using exactly the same set of measurements but with a different SRF, one can recover fluorescent lifetimes in context of the FLI.

6.3 Fluorescence Lifetime Imaging with Time-of-Flight Sensors

The experimental setup for FLI using a ToF sensor is depicted in Fig. 6-1 (e). A fluorescent sample is located in an xy plane a distance $z = d$ from the ToF sensor. Pixels corresponding to a non-fluorescent background object (x_b, y_b) produce only a time delay proportional to $2d/c$, precisely the case of conventional ToF imaging with the SRF specified in (6.5).

The probing function that interacts with the pixels corresponding to a fluorescent sample at location (x_f, y_f) undergoes two transformations. The first transformation is attributed to the same depth contribution, d. The second transformation results from flourescence: a fraction of the excitation light excites

Table 6.2: Time and Frequency Domain Time-of-Flight Fluorescence Lifetime Imaging

	Time-domain ToF	Frequency-domain ToF
Probing Function	$p(t) = \frac{1}{\Delta}\sum_{\lvert m\rvert \leqslant M_0} \hat{p}_m e^{j\omega_0 m t}$	$p(t) = 1 + p_0 \cos(\omega t)$
Scene Response Function	$h_{\mathsf{SI}}(t) \overset{(6.13)}{=} \rho\delta(t - 2d/c) + \mu e^{-\left(\frac{t-2d/c}{\tau}\right)}\Pi(t - 2d/c)$	
Reflected Function	$r(t) \overset{(6.3)}{=} (p * h_{\mathsf{SI}})(t)$	
Measurements	(6.17)	(6.31)

the sample, which fluoresces with a characteristic decay time τ. The total SRF at (x_f, y_f) is then

$$h(t, t') = h_{\mathsf{Depth}}(t, t') + h_{\mathsf{Sample}}(t, t') \tag{6.13}$$

where the contributions due to respective components are

$$h_{\mathsf{Depth}}(t, t') = \rho\delta(t - t' - 2d/c), \tag{6.14}$$

$$h_{\mathsf{Sample}}(t, t') = \mu e^{-\left(\frac{t-t'-2d/c}{\tau}\right)}\Pi(t - t' - 2d/c). \tag{6.15}$$

μ is the emission strength of the fluorescent sample, and $\Pi(t)$ is the unit step function. (Note that h_{Depth} and h_{Sample} represent signals at the excitation and emission optical wavelengths, respectively. The former can be eliminated experimentally via, e.g., a dielectric interference filter.) Because (6.13) is linear and shift-invariant system, the resulting measurements are

$$\begin{aligned} m(t) &\overset{(6.4)}{=} (p * \overline{p} * h_{\mathsf{SI}})(t) \\ &\overset{(6.9)}{\approx} (\mathsf{C}_{p,\bar{p}} * h_{\mathsf{SI}})(t) \\ &= \mathsf{C}_{p,\bar{p}} * \left(\delta(t - 2d/c) * \left(\rho\delta(t) + \mu e^{-\frac{t}{\tau}}\Pi(t)\right)\right), \end{aligned} \tag{6.16}$$

where $\mathsf{C}_{p,\overline{p}}(t)$ is the cross-correlated probing function.

We emphasize that our ToF system is completely compatible with FLI. In TD-FLI, $p(t) = \delta(t)$, whereas in FD-FLI, $p(t) = 1 + \cos(\omega_0 t)$. Conventionally, separate calibration steps provide explicit knowledge of d, which is used for subsequent measurements. However, we make no such assumption. Instead, we simultaneously compute d and τ from our measurements (6.16). We need not perform a separate measurement to obtain d explicitly.

6.3.1 Time-Domain ToF FLI: Theory and Experiments

6.3.1.1 Theoretical Modeling

As in TD-ToF, we utilize the same truncated cross correlation function, (6.9), for FLI. Importantly, note that explicit knowledge of $p(t)$ is not required. To show this, note that the eigenfunctions of (6.16) are

precisely the complex exponentials of (6.9). Using the convolution theorem,

$$m(t) \approx \frac{1}{\Delta} \sum_{|n| \leqslant N_0} \left(\widehat{\phi}_n \widehat{h}_n \right) e^{\jmath \omega_0 n t}, \tag{6.17}$$

where $\widehat{h}_n = \widehat{h}(\omega_0 n)$ and $\widehat{h}(\omega)$ is the Fourier transform of $h_{\mathsf{SI}}(t)$:

$$\begin{aligned} \widehat{h}(\omega) &= \int h(t) e^{-\jmath \omega t} dt \qquad \text{(Fourier Transform)} \\ &= \rho e^{-\jmath \omega \left(\frac{2d}{c}\right)} + \frac{\mu \tau}{1 + \jmath \omega \tau} e^{-\jmath \omega \left(\frac{2d}{c}\right)}. \end{aligned} \tag{6.18}$$

From here onwards and for all practical purposes, we assume that (6.17) is an equality instead of an approximation. Expressing $\widehat{h}(\omega)$ in polar form, we have $\widehat{h}(\omega) = |\widehat{h}(\omega)| e^{\jmath \angle \widehat{h}(\omega)}$ where,

$$\begin{aligned} |\widehat{h}(\omega)| &= \sqrt{\frac{(\rho + \mu\tau)^2 + (\omega \rho \tau)^2}{1 + (\omega \tau)^2}} \\ \angle \widehat{h}(\omega) &= -\tan^{-1} \left(\frac{\omega \mu \tau^2}{\rho + \mu \tau + \rho (\omega \tau)^2} \right) - \frac{2d}{c} \omega. \end{aligned}$$

Note that the phase of the spectrum encodes both the depth and the lifetime parameters. We may write

$$\angle \widehat{h}(\omega) = -\theta_\tau(\omega) - \theta_d(\omega), \tag{6.19}$$

where

$$\theta_\tau(\omega) = \tan^{-1} \left(\frac{\omega \tau^2}{\tau + \rho \left(1 + (\omega \tau)^2\right)} \right) \text{ and } \theta_d(\omega) = 2d\omega/c. \tag{6.20}$$

(Because we consider a single lifetime, we set $\mu = 1$.)

In vector-matrix notation, the discretized system of equations in (6.17) can be written as

$$\mathbf{m} = \mathbf{V} \mathbf{D}_{\widehat{\phi}} \widehat{\mathbf{h}}, \tag{6.21}$$

where

- $\mathbf{m}$ is $K \times 1$ vector of discretized ToF sensor measurements $m_k = m(kT_s), k \in [0, K-1]$;
- $\mathbf{V}$ is a Vandermonde matrix of size $K \times (2N_0 + 1)$ with matrix element $[V]_{k,n} = e^{\jmath (2\pi/\Delta) T_s n k}$, $n \in [-N_0, +N_0]$;
- $\mathbf{D}_{\widehat{\phi}}$ is a $(2N_0 + 1) \times (2N_0 + 1)$ diagonal matrix with diagonal entries $[D]_{n,n} = \widehat{\phi}_n$; and
- $\widehat{\mathbf{h}}$ is $(2N_0 + 1) \times 1$ vector of discretized spectrum (6.18) with entries $\widehat{h}(2\pi n/\Delta), n = -N_0, \ldots, N_0$.

Equivalently, we write the measurement vector as,

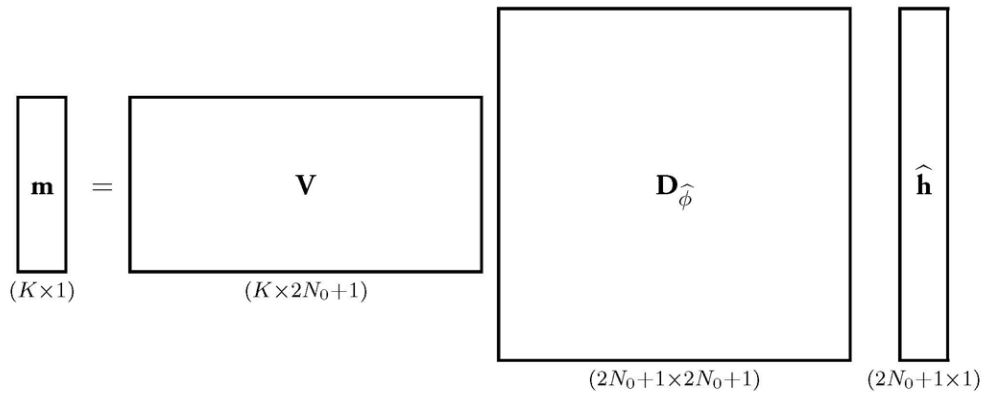

The estimation problem is thus: given K measurements $\mathbf{m}$, estimate parameters d and τ.

Because $\phi(t)$ is a real, time symmetric function by construction, the matrix $\mathbf{D}_{\widehat{\phi}}$ does not contribute to the phase of vector $\widehat{\mathbf{h}}$ in (6.21). Hence, we rely on only the measurements $\mathbf{m}$. Thus, p (or ϕ) need not be known, so that we eliminate the calibration requirements that are central to both FLI and ToF imaging [16].

To see this, note that TD-FLI uses [237] $p = \delta(t) = \phi$, so the corresponding measurements are

$$m_{\mathsf{TD\text{-}FLI}}(t) = \mu e^{-\left(\frac{t-t_0}{\tau}\right)} \Pi(t - t_0). \tag{6.22}$$

Now because $\log(m_{\mathsf{TD\text{-}FLI}}(t))$ is linear, a direct fit [237] can be used to estimate τ, and hence calibration is implicitly avoided by the choice of $p = \delta$.

On the other hand, for our proposed TD-ToF method for FLI, the illumination/probing function is composed of N_0 multiplexed frequencies, which yield measurements

$$m_{\mathsf{TD\text{-}ToF\text{-}FLI}}(t) \overset{(6.17)}{=} \frac{1}{\Delta} \sum_{|n|\leqslant N_0} \left(\widehat{\phi}_n \widehat{h}_n\right) e^{\jmath\omega_0 n t}, \tag{6.23}$$

and because $\mathsf{C}_{p,\overline{p}}$ is a bandlimited approximation of ϕ (cf. (6.9)), a linear fit no longer suffices. However, because of the properties of (the generalized) $p(t)$, we solve this more complex inverse problem to estimate $\{d, \tau\}$ without knowing ϕ. We summarize the results in Table 6.2.

6.3.1.2 Experimental Verification of TD-ToF-FLI

The setup for the TD-ToF-FLI method is shown in Fig. 6-1 (e). A 405 nm laser diode illuminates the scene. We use a precomputed, quantized p (cf. (6.6)) based on 31-bit maximum length sequence described by code,

$$\mathsf{MLS} = 0101110110001111100110100100001, \tag{6.24}$$

with $\Delta = 309.9$ ns and $T_s = 7.8120$ ps. The sample consists of a CdSe-CdS quantum dot sample prepared by dissolving it in hexane and PMMA onto a glass slide. This sample has a lifetime of $\tau = 32$ ns, and it is located at 1.05 m from the sensor.

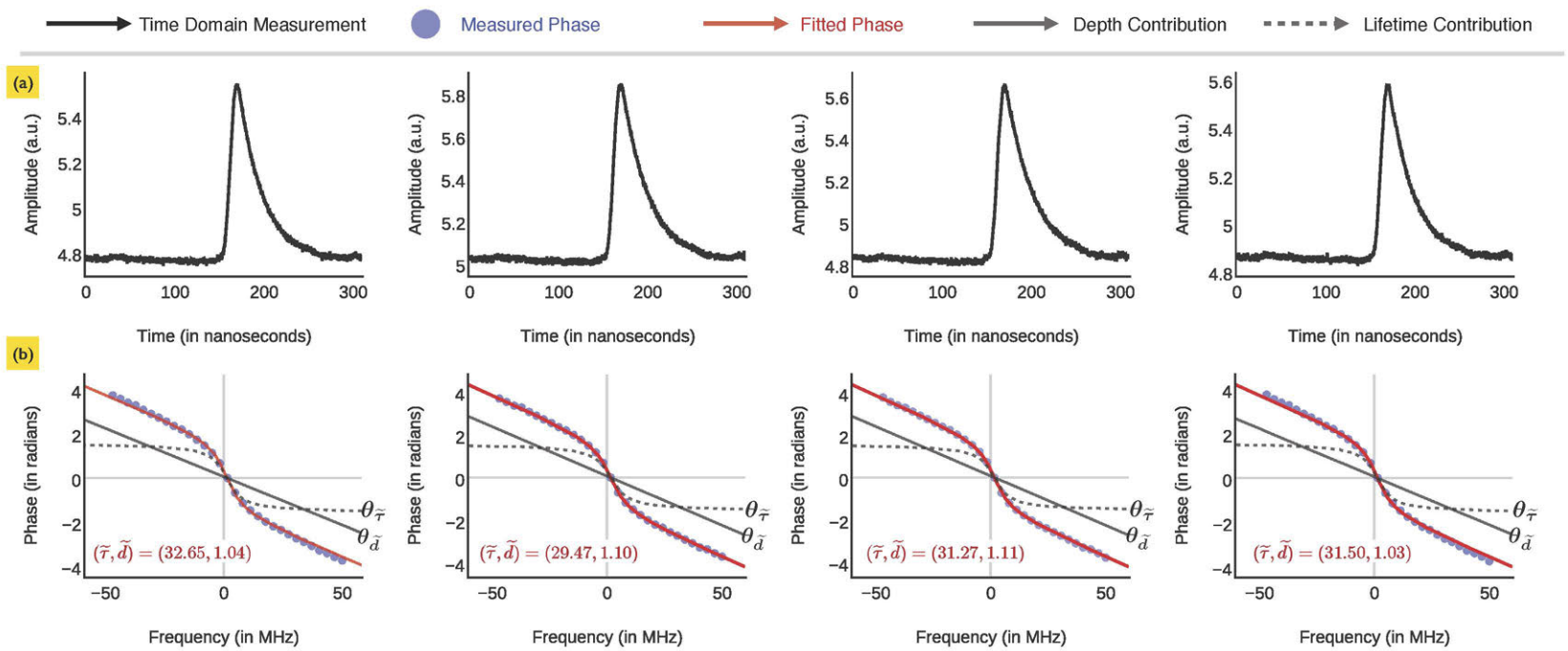

Figure 6-3: TD-ToF-FLI measurements. (a) Time profile of measurements $m_k = m(kT_s), T_s = 7.8120$ ps based on $K = 3968$ samples. These measurements result from convolving cross-correlation of the probing function with the SRF, Eq. (6.17). (b) Phase measurements computed using $\angle\widehat{\mathbf{h}} = \angle\mathbf{V}^{+}\mathbf{m}$ with $N_0 = 15, \Delta = 309.9$ ns. We estimate the distance $\widetilde{d}$ and lifetime $\widetilde{\tau}$ parameter using nonlinear least squares fitting, which results in the fitted curve. The fitted result is marked in —. The estimated phase contribution Eq. (6.19) due to distance $\theta_{\widetilde{d}}$ and lifetime $\theta_{\widetilde{\tau}}$ is also plotted.

Table 6.3: Time Domain ToF FLI ($\tau = 32$ ns and $d = 1.05$ m).

$\widetilde{\tau}$ (ns)	$\widetilde{d}$ (m)	$\sqrt{\mathsf{MSE}}_\tau$ (log-scale)	$\sqrt{\mathsf{MSE}}_d$ (log-scale)	$\sqrt{\mathsf{MSE}}_{\angle h}$ (log-scale)	SNR (dB)
35.24	1.09	−8.49	−1.40	−1.5	38.14
31.29	1.12	−9.15	−1.15	−1.96	47.42
33.20	1.05	−8.92	—	−1.11	30.31
36.12	1.03	−8.39	−1.70	−1.08	29.60
31.17	1.07	−9.08	−1.70	−1.39	35.76
33.46	1.04	−8.84	−2.00	−1.13	30.61
35.65	1.11	−8.44	−1.22	−1.71	42.46
32.50	1.08	−9.30	−1.52	−1.47	37.47
30.25	1.12	−8.76	−1.15	−1.76	43.49
28.61	1.12	−8.47	−1.15	−1.72	42.55
32.66	1.04	−9.18	−2.00	−1.07	29.31
29.48	1.10	−8.60	−1.30	−1.78	43.70
31.27	1.11	−9.14	−1.22	−1.70	42.21
31.50	1.03	−9.30	−1.70	−1.07	29.31

The reflected light is passed through a dielectric interference filter with cut-off wavelength of 450 nm leading to $\rho = 0$ (6.20). A 160×120 pixel PMD 19k-S3 lock-in sensor with custom FPGA programming cross-correlates the reflected signal to produce measurements $\mathbf{m}$. The sensor has a 80 MHz modulation bandwidth operating within 90 frames per second [249]. The total cost of our system is \$ 1200.

With $N_0 = 15$, we compute

$$\angle\widehat{\mathbf{h}}_{\mathsf{obs}} = \angle\mathbf{V}^{+}\mathbf{m} = -\left(\theta_\tau\left(\frac{2\pi n}{\Delta}\right) + \theta_d\left(\frac{2\pi n}{\Delta}\right)\right), \tag{6.25}$$

where $\mathbf{V}^{+}$ denotes the pseudo-inverse of the matrix $\mathbf{V}$ and $\angle\widehat{\mathbf{h}}_{\mathsf{obs}}$ is the experimentally observed phase. Since we know that the observed phase is related to theoretical phase in (6.19), we estimate the parameters of interest by solving the nonlinear least squares problem

$$\underset{d,\tau}{\arg\min} \sum_{n=-N_0}^{n=+N_0} \left|\angle\widehat{h}\left(n\omega_0\right) - \angle\widehat{h}_{\mathsf{obs}}\left(n\omega_0 + \beta\right) + \alpha\right|^2, \tag{6.26}$$

where α and β are offset parameters to ensure a solution that is centered at origin. We use the trust-region [250] based algorithm with least absolute residual criterion. The nonlinear parameter estimation problem is solved using bounded constraints that are accommodated within the trust-region optimization framework. We require that the minimum and maximum lifetimes and distances are in range of 0 to 100 ns and 0 to 10 m, respectively.

Per-pixel fluorescent sample measurements are shown in Fig. 6-3, which shows both the time-domain measurement (cf. Fig. 6-3 (a)) and the raw phase measurement (cf. Fig. 6-3 (b)). We also show the fitted phase measurement in Fig. 6-3 (b). We assign a confidence level to each pixel to estimate the signal-

to-noise ratio (SNR). We use ToF measurements from 14 different pixels imaging the same scene (cf. Fig. 6-1 (e)). The results from our computation are tabulated in Table 6.3. In addition to the estimated lifetimes and distances, we tabulate two relevant metrics.

1. First, the *mean squared error* or MSE, a measure of distortion, is defined as follows: let ν be the oracle estimate and $\{\widetilde{\nu}_n\}_{n=0}^{N-1}$ be N estimated values of ν. The MSE is

$$\mathsf{MSE}_\nu = \frac{1}{N}\sum_{n=0}^{N-1} |\widetilde{\nu}_n - \nu|^2. \tag{6.27}$$

   We compute $\log\left(\sqrt{\mathsf{MSE}}\right)$ for $\widetilde{\tau}$, $\widetilde{d}$ and $\angle\widetilde{\widehat{h}}$ in Table 6.3, where the last term is due to fitted measurements,

$$\angle\widetilde{\widehat{h}}\left(n\omega_0\right) \overset{(6.19)}{=} -\tan^{-1}\left(n\omega_0\widetilde{\tau}\right) - 2\frac{n\omega_0\widetilde{d}}{c} \tag{6.28}$$

   which are synthesized after estimating $\{\widetilde{\tau}, \widetilde{d}\}$.

2. We use the observed SNR to estimate measurement fidelity. Including additive Gaussian noise ε_n, we have

$$\angle\widehat{h}_{\mathsf{obs}}\left(n\omega_0\right) = \angle\widehat{h}\left(n\omega_0\right) + \varepsilon_n. \tag{6.29}$$

   We define

$$\mathsf{SNR} = 20\left(\log||\angle\widehat{h}|| - \log||\angle\widehat{h}_{\text{obs}} - \angle\widehat{h}||\right),$$

   measured in decibel, and $||\angle\widehat{h}||^2 = \sum_{n=0}^{N-1}|\angle\widehat{h}\left(n\omega_0\right)|^2$. In Table 6.3, we use $\angle\widehat{h} = \angle\widetilde{\widehat{h}}$—the fitted phase function computed using estimates $\{\widetilde{\tau}, \widetilde{d}\}$.

Based on the estimates in Table 6.3, the expected lifetime is $\widetilde{\tau} = 31.3142$ ns, and the estimated expected distance is $\widetilde{d} = 1.0799$ meters, both consistent with the ground truth.

6.3.2 Frequency-Domain ToF FLI: Theory and Experiments

As described in Section 6.2.2, in the FD-ToF mode of operation, the ToF sensor probes the scene with an amplitude modulated continuous wave of form $p\left(t\right) = 1 + p_0\cos\left(\omega t\right)$. Following (6.3), the reflected signal is

$$r\left(t\right) \overset{(6.3)}{=} \left(p * h_{\mathsf{SI}}\right) = |\widehat{h}\left(0\right)| + |\widehat{h}\left(\omega\right)|p_0\cos\left(\omega t + \angle\widehat{h}\left(\omega\right)\right). \tag{6.30}$$

The reflected signal is cross-correlated (6.10) at the ToF sensor to produce measurements

$$m\left(t\right) \overset{(6.10)}{=} |\widehat{h}\left(0\right)| + |\widehat{h}\left(\omega\right)|\frac{p_0^2}{2}\cos\left(\omega t - \angle\widehat{h}\left(\omega\right)\right). \tag{6.31}$$

To estimate the phase and amplitude, we utilize the method from Section 6.2.2. Noting, however, that the scene transfer function is not constant, we express z explicitly as a function of the modulation frequency

ω_0: $z = z(\omega_0)$. The amplitude and phase estimates are

$$\underbrace{|\widehat{h}(\omega_0)| \approx |z(\omega_0)|/p_0^2}_{\text{Amplitude Estimate}} \qquad \text{and} \qquad \underbrace{\angle\widehat{h}(\omega_0) \overset{(6.19)}{\approx} \angle z(\omega_0)}_{\text{Phase Estimate}} \tag{6.32}$$

respectively. Note that the estimation of amplitude $|\widehat{h}(\omega_0)|$ requires the knowledge of p_0. However, this is not the case for estimation of phase which is prescribed by $\angle\widehat{h}(\omega_0)$ and is devoid of p_0. Again our method is blind in that we can directly estimate $\angle\widehat{h}(\omega_0)$ from $z(\omega_0)$ even if we do not know anything about p_0.

Note in passing that multiple frequency measurements can be used to estimate multiple depths [251, 226, 209, 65], for which

$$h(t) = \sum_{k=0}^{K-1} \rho_k \delta(t - 2d_k/c) \overset{\text{Fourier}}{\longleftrightarrow} \widehat{h}(\omega) = \sum_{k=0}^{K-1} \rho_k e^{\jmath\omega\left(\frac{2d_k}{c}\right)}.$$

Based on the image formation model for the SRF in (6.13), we will next show how multiple frequency measurements of the form $\{z(k\omega_0)\}_{k=1}^{K}$ can be used alternately to estimate the parameters of interest, that is, $\{d, \tau\}$ in context of FLI. We summarize the results in Table 6.2.

6.3.2.1 Experimental Verification of FD-ToF-FLI

Using the same physical setup as that in Section 6.3.1.2, we move the sample to $d = 2.5$ m, and we set $\omega_0/2\pi \equiv f_0 = 1$ MHz and acquire equi-spaced ToF measurements,

$$\{z(kf_0)\}_{k=1}^{K}, \quad k = 1, 2, \ldots, 40. \tag{6.33}$$

The amplitudes and phases of z for $k = 20,\ 30$ and 40 are shown in Fig. 6-4 (a). The effects of fluorescence are clearly visible in both amplitude and phase. The 450 nm dielectric filter prevents any reflected light leading low signal strength in the amplitude image. The fluorescing quantum dot causes an increase in the measured phase. The increased phase measurement at the sample location is due to the presence of θ_τ term in (6.19). In context of the experimental setup described in Fig. 6-1 (e), we mark the background pixel (x_b, y_b) as well as the fluorescent pixel (x_f, y_f) in Fig. 6-4 (a). The average phase of the background pixel is noted to be $\angle z_{(x_b,y_b)}(40f_0) = 4.1625$ radians. This amounts to a depth of 2.4843 m which is consistent with the experimental setup where $d = 2.5$ m. On the other hand, the average phase at the location of the quantum dot is observed to be $\angle z_{(x_f,y_f)}(40f_0) = 5.5822$ radians. This relates to an erroneous depth of 3.3316 m which is a result of multipath interference [209].

By using ToF phase measurements (6.33) for 10 different pixel locations corresponding to (x_f, y_f), we solve for the nonlinear least squares problem,

$$\arg\min_{d,\tau} \sum_{k=1}^{K=40} |\angle z(k\omega_0) + \theta_\tau(k\omega_0) + \theta_d(k\omega_0)|^2. \tag{6.34}$$

As before in Section 6.3.1.2, we use the trust–region based algorithm with least absolute residual criterion. As a result of fitting, we estimate $\widetilde{d}$ and $\widetilde{\tau}$ for each pixel. The estimated distance and lifetime values together

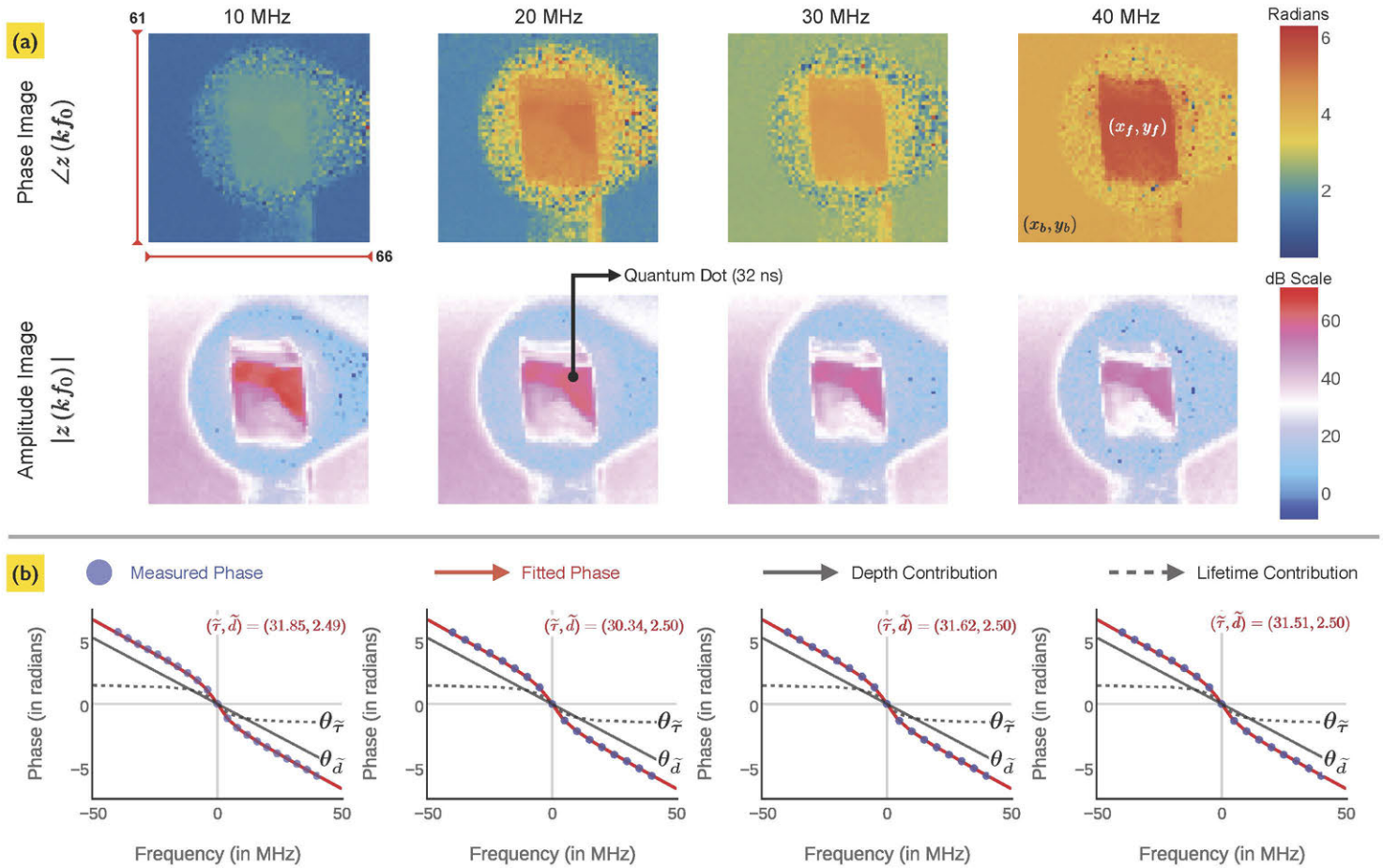

Figure 6-4: FD-ToF-FLI measurements of a 61×66 pixel patch of 120×160 pixel sensor image. The size of the scene is approximately 2.3 in^2. (a) Multi-frequency measurements of $\tau = 32$ ns quantum dot based fluorescent sample. We show phase and amplitude images, that is, $\{\angle z(10f_0), \angle z(20f_0), \angle z(30f_0), \angle z(40f_0)\}$ (in radians, $[0, 2\pi]$) and $\{|z(10f_0)|, |z(20f_0)|, |z(30f_0)|, |z(40f_0)|\}$ (in decibels), respectively. The base modulation frequency for the experiment is $f_0 = \omega_0/2\pi = 1$ MHz. The phase at the background pixel is recorded to be $\angle z_{(x_b,y_b)}(40f_0) = 4.1625$ radians which amounts to a depth of 2.48 m which is consistent with the experimental setup. At the location of the fluorescent sample, we recored a higher phase value $\angle z_{(x_f,y_f)}(40f_0) = 5.5822$ which is attributed to the fluorescence phenomenon. (b) Multi–frequency, raw phase measurements $\{\angle z_{(x,y)}(kf_0)\}_{k=1}^{K=40}$ for four pixels. The measurements confirm with the theoretical hypothesis of Eq. (6.19) as well as the fitted phase obtained by Eq. (6.34). The estimated phase contribution Eq. (6.19) due distance $\theta_{\tilde{d}}$ and lifetime $\theta_{\tilde{\tau}}$ is also plotted.

Table 6.4: Frequency Domain ToF FLI ($\tau = 32$ns and $d = 2.5$ m).

$\widetilde{\tau}$ (ns)	$\widetilde{d}$ (m)	$\sqrt{\mathsf{MSE}}_{\tau}$ (log-scale)	$\sqrt{\mathsf{MSE}}_{d}$ (log-scale)	$\sqrt{\mathsf{MSE}}_{\angle h}$ (log-scale)	SNR (dB)
29.79	2.49	-8.66	-2.00	-1.71	45.55
30.34	2.49	-8.78	-2.00	-1.69	45.04
30.72	2.50	-8.89	—	-1.69	45.07
30.72	2.50	-8.89	—	-1.73	45.80
30.79	2.50	-8.92	—	-1.71	45.51
31.28	2.50	-9.14	—	-1.73	46.00
31.51	2.50	-9.31	—	-1.72	45.80
31.62	2.50	-9.42	—	-1.59	43.10
31.62	2.50	-9.42	—	-1.71	45.58
31.86	2.50	-9.85	—	-1.63	43.88

with $\log\left(\sqrt{\mathsf{MSE}}\right)$ for $\widetilde{\tau}$, $\widetilde{d}$ and $\angle\widetilde{\widehat{h}}$ for all the pixels is tabulated in in Table 6.4. The average lifetime and distance is estimated to be,

$$\left\{\widetilde{d}, \widetilde{\tau}\right\} = \{2.4961 \text{ m} \,,\, 31.024 \text{ ns}\}\,.$$

Both the measured phase $\{\angle z(kf_0)\}_{k=1}^{K=40}$ and the fit obtained by (6.34) for four pixels are plotted in Fig. 6-4 (b).

6.4 Discussion

6.4.1 ToF Sensors for Microscopy

The method generalizes to microscopy modes. A salient feature about the technique is that it is a local, per-pixel calculation, so that the lateral scale of the problem does not influence the technique. Thus, our proof-of-principle demonstration can be extended to integration with microscopy, both wide-field and point-scanning techniques, provided there is no pixel crosstalk. In fact, our current system is not aberration-corrected, and the resulting model mismatch makes reconstruction more challenging. A well-calibrated microscopy setup should alleviate this mismatch and improve results.

6.4.2 Nanosecond Range Lifetime Sensing

For biological imaging, lifetimes are on the order of nanoseconds. Recent work suggests that current ToF sensors (with bandwidths of tens of MHz) are optimal for recovering lifetimes under 5 ns [252]. For example, a 3 ns, lifetime is optimally estimated by a 30 MHz signal (cf. pg. 378, [252]). Further, a similar ToF setup estimated lifetimes on the order of 4 ns [241] (though it did not simultaneously estimate distance).

The important difference here is that the present approach simultaneously estimates lifetime and distance based on the same measurement. Numerical simulations in Fig. 6-5 indicate that our method is

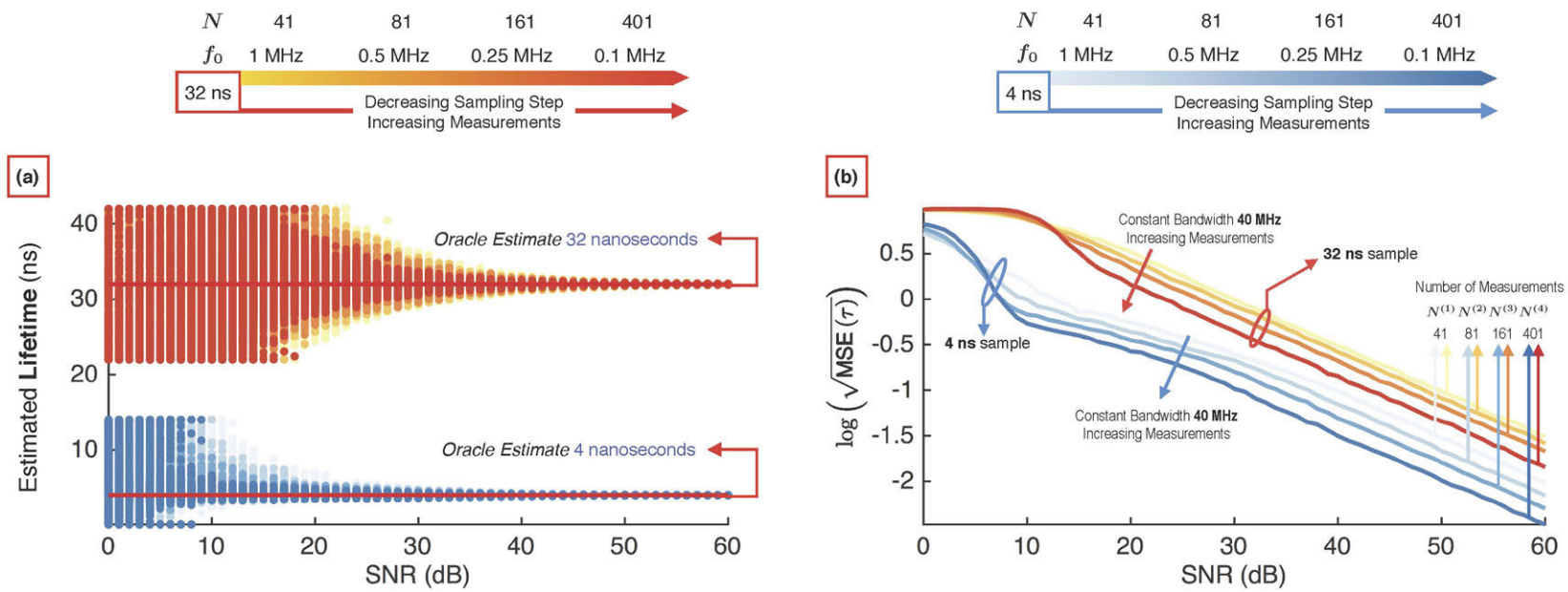

Figure 6-5: Estimation accuracy of $\tau_1 = 4$ ns and $\tau_2 = 32$ ns. (a) We plot 2000 estimated values of lifetime as a function of SNR ranging from 0–60 dB. As the SNR increases, the estimates cluster around the oracle estimate of $\tau = 4$ ns and $\tau = 32$ ns, respectively. (b) We plot the $\sqrt{\mathsf{MSE}_\tau}$ on log scale as a function of SNR. After 15 dB, we note a consistent linear relationship Eq. (6.35) between SNR and the $\log\left(\sqrt{\mathsf{MSE}_\tau}\right)$.

suitable for recovering a 4 ns lifetime. We simulate a system bandwidth of 40 MHz. (Note that this is half the true PMD sensor bandwidth [249]). Numerically, we compare the estimation accuracy of $\tau_1 = 4$ ns and $\tau_2 = 32$ ns with $d = 2.5$ m. We do so by studying the upper bounds on the $\sqrt{\mathsf{MSE}}$ linked with estimation of set of parameters of interest, $\{\tau_1, d\}$ and $\{\tau_2, d\}$. For a fixed ToF sensor bandwidth, we vary the number of measurements (6.32) by sampling with equi-spaced frequencies from 0 to 40 MHz. We use four different step sizes, $f_0^{(k)}$ (corresponding to $N^{(k)}$ samples), specified by

$$\begin{aligned} f_0^{(1)} &= 0.10 \;\Rightarrow\; N^{(1)} = 401 \quad & f_0^{(2)} &= 0.25 \;\Rightarrow\; N^{(2)} = 161 \\ f_0^{(3)} &= 0.50 \;\Rightarrow\; N^{(3)} = 81 \quad & f_0^{(4)} &= 1.00 \;\Rightarrow\; N^{(4)} = 41. \end{aligned}$$

$f_0^{(k)}$ is measured in MHz. For example, the step size in experiments in Sec. 6.3.2.1 was $f_0 = 1$ MHz. For each $f_0^{(k)}$, we generate a the vector of measurements,

$$\angle \hat{h}_{\mathsf{obs}}^{(k)}(n\omega_0) \overset{(6.29)}{=} \angle \hat{h}(n\omega_0) + \varepsilon_n, \quad n = 0, \ldots, N^{(k)} - 1,$$

where ε_n represents additive white Gaussian noise for a SNR ranging from 0 dB to 60 dB. Each SNR value is averaged over 2000 realizations.

In Fig. 6-5 (a) we plot the 2000 estimated values of the lifetime parameters for each value of SNR. Intuitively, as the SNR increases, the estimates cluster around the oracle estimate of $\tau_1 = 4$ ns and $\tau_2 = 32$ ns, respectively.

In Fig. 6-5 (b), we plot the $\sqrt{\mathsf{MSE}}_\tau$ on log scale as a function of SNR. Note that the MSE_τ (6.27) is the average over all 2000 trials. After 15 dB, we note a consistent linear relationship of form,

$$\log\left(\sqrt{\mathsf{MSE}}_\tau\right) \propto \log K_0 - \lambda \log(\text{SNR}). \tag{6.35}$$

As the number of measurements N increase, the $\log\left(\sqrt{\mathsf{MSE}}_\tau\right)$ drops consistently. This observation is consistent throughout all of our experiments. In fact, we note that $\sqrt{\mathsf{MSE}}_{\tau_1} < \sqrt{\mathsf{MSE}}_{\tau_2}$ implying that the 4 ns sample may be estimated with higher accuracy when compared to 32 ns sample. As noted in Table 6.4, the operational SNR of our system is around 45 dB implying that the lifetime parameter can be estimated with sufficient accuracy as plotted in Fig. 6-5 (b).

Thus, although our demonstration here operates at a lower time scale (cf. Fig. 6-2) than what is typical in practice, this is not a fundamental limitation of the method. The reason is that we compensate for lower time resolution by utilizing a computationally different method of inversion. Indeed, appropriate modeling and prior information lend themselves naturally to ToF sensing and offer a path toward super-resolution [253, 65].

Of course, calculation of the theoretical lower bounds (on lifetimes and distances) requires calculation of the Cramér-Rao Bound. Though beyond the scope of the present work, this limit is ultimately dictated by noise. For instance, the Cramér-Rao Lower Bound for distance estimation is derived in [65] and obeys a version of the law in (6.35). For typical systems, we expect from Fig. 6-5 that the method is suitable for current application needs.

6.4.3 Experimental and Computational Precision

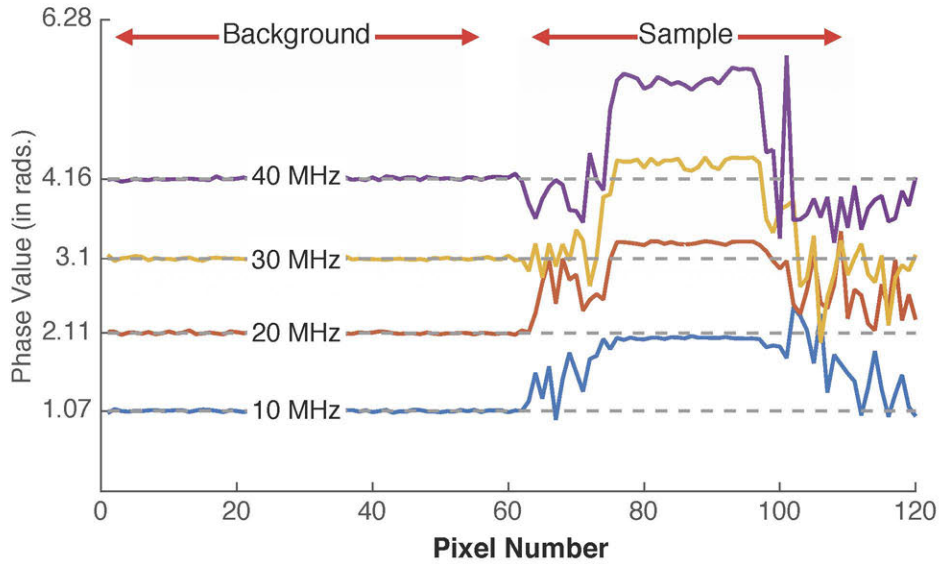

Figure 6-6: Measured phase as a function of the modulation frequency. We plot the measured phase corresponding to a 120 pixel cross-section of the 160×120 ToF sensor image for modulation frequencies $f = \{10,\ 20,\ 30,\ 40\}$ MHz. The first 50 phase measurements are due to the background pixel which is at a depth $d = 2.5$ m. The dashed line marks the average phase value over first 50 pixels. The average phase value for each modulation frequency leads to a distance estimate: $d = \{2.56,\ 2.52,\ 2.47,\ 2.48\}$ in meters.

The current optical ToF technology allows for range estimation in millimeter precision. The variation in estimated lifetime is due to sample inhomogeneity, nonuniform lighting [254], and potential model mismatch from lens aberration.

The measurement precision here is indicated in Fig. 6-6, which shows cross sections of the four phase plots in Fig. 6-4 (a). The phase contribution along first 50 pixels is due to the background. We mark the average phase value on the y-axis. Using $\theta_d(f) = 4\pi f d/c$, we estimate the distance d given $\theta_d(f)$ and $f = \{10,\ 20,\ 30,\ 40\}$ MHz. At each modulation frequency, the estimated distance is $d = \{2.56,\ 2.52,\ 2.47,\ 2.48\}$ m, whereas the actual distance is 2.5 m. The variability in the distance estimates is mainly due to the fact that across modulation frequencies, the phase-frequency relation, $\theta_d(f) = 4\pi f d/c$ which is linear, may not be strictly linear due to distortions.

6.5 Summary of Results

In conclusion, we have demonstrated a FLI alternative that is based on cost-effective ToF sensors. We simultaneously estimate the lifetime and the distance of the sample from the sensor. Unlike existing methods [241, 237], our approach is calibration-free and requires no prior information on the experimental path length and thus allows for faster acquisition time. Furthermore, our technique is blind in that we do not assume the knowledge of illumination waveform. Overall, our system shows promise for two-dimensional imaging, and can be generalized to volumes [255]. Because the technique is modular, it can be implemented with other computational imaging techniques to create a new platform for wide-field

FLI.

The method offers new possibilities for open questions. The case of multiple lifetime imaging [239, 242] is interesting and is yet to be explored in the context of ToF sensors, both theoretically as well as experimentally. Comparison with other FLI techniques [256] and fundamental resolution limits for simultaneous estimation of lifetime and depth information will allow for better understanding of applicability of ToF sensors for bio-imaging tasks such as tumor detection [231, 232] and fluorescence tomography [233, 234].

तवं ह्यग्ने अग्निना विप्रो विप्रेण सन सता ।
सखा सख्या समिध्यसे ॥

स तवं विप्राय दाशुषे रयिं देहि सहस्त्रिणम ।
अग्ने वीरवतीमिषम ॥

अग्ने भरातः सहस्त्रत रोहिदश्व शुचिव्रत ।
इमं सतोमंजुषस्व मे ॥

"For you—o Fire by fire, a poet by a poet, the real (thing) by a real (man), a comrade by a comrade—are kindled. " [1]

— Rigveda (Mandala VIII, §43, ¶ 14–16)

7

Sampling without Time Information: Phase-retrieval in Time-resolved Imaging

7.1 Introduction

Imaging modalities work on the premise that there is one–to–one mapping between the scene and the pixels. If this were not the case, it would be almost impossible to make sense of the photographs that we capture on a daily basis. Meanwhile, the illustration in Fig. 7-1 is a characteristic counter–example.

To elaborate, consider the *Gedankenexperiment* version of Fig. 7-1 described in Fig. 7-2 (a). Let us assume that a light source is co-located with the imaging sensor (such as a digital camera). The reflection from the semi-reflective sheet (such as a window pane) arrives at the sensor at time $t_1 = 2d_1/c$ while the mannequin is only observable on or after $t_2 = 2d_2/c$. Here, c is the speed of light. While we typically interpret images as a two dimensional, spatial representation of the scene, let us for now, consider the photograph in Fig. 7-1 along the time-dimension. For the pixel (x_0, y_0), this time-aware image is shown in Fig. 7-2 (b). Mathematically, our time-aware image can be written as a 2–sparse signal (and as a K–sparse signal in general),

$$m(\mathbf{r}, t) = (\lambda_1\Gamma_1)(\mathbf{r})\,\delta(t - t_1(\mathbf{r})) + (\lambda_2\Gamma_2)(\mathbf{r})\,\delta(t - t_2(\mathbf{r})) \tag{7.1}$$

where $\{\Gamma_k(\mathbf{r})\}$ are the constituent image intensities, $\{\lambda_k(\mathbf{r})\}$ are the reflection coefficients, $\mathbf{r} = (x, y)^\top$ is the 2D spatial coordinate, and $\delta(\cdot)$ is the Dirac distribution.

A conventional imaging sensor produces images by marginalizing time information, resulting in the

Figure 7-1: Reflection from semi-reflective surfaces. The Memorial Church can be seen imprinted on the glass facade of the Harvard University Science Center.

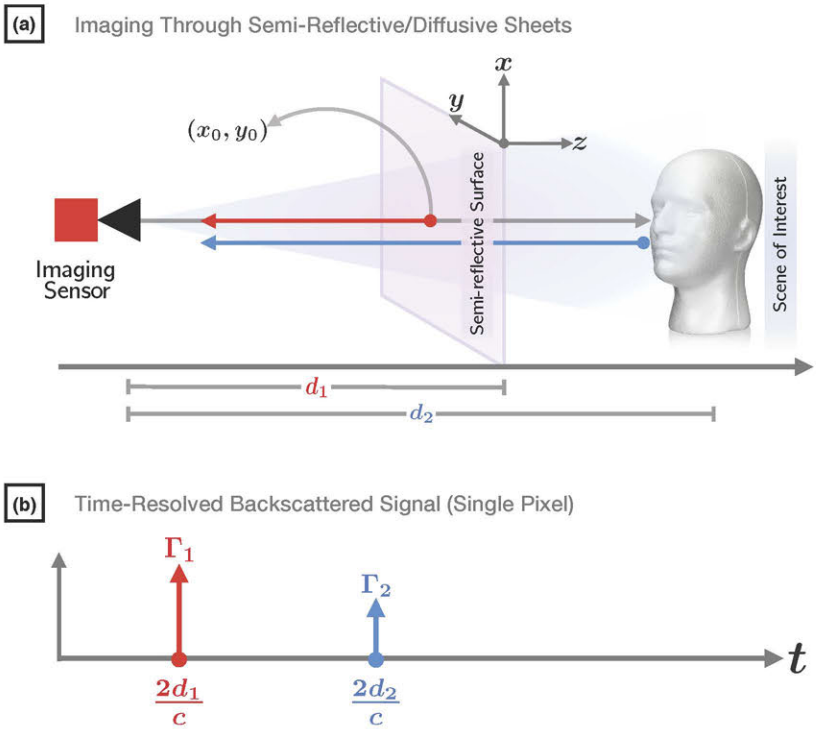

Figure 7-2: Time-aware imaging. (a) Exemplary setting for imaging through semi-reflective media. (b) Corresponding time-aware image at pixel $\mathbf{r}_0 = (x_0, y_0)^\top$.

2D photograph,

$$\int_0^{\Delta \gg t_2} m(\mathbf{r}, t)\, dt = (\lambda_1 \Gamma_1)(\mathbf{r}) + (\lambda_2 \Gamma_2)(\mathbf{r}) \equiv I(\mathbf{r}). \tag{7.2}$$

Recovering $\{\Gamma_k\}, k = 1, 2$ given I, more generally, K echoes of light,

$$m(\mathbf{r}, t) = \sum_{k=0}^{K-1} (\lambda_k \Gamma_k)(\mathbf{r})\, \delta(t - t_k(\mathbf{r})) \tag{7.3}$$

is an ill-posed problem. Each year, a number of papers [257, 258, 259, 260, 261, 262] attempt to address this issue by using regularization and/or measurement-acquisition diversity based on image statistics, polarization, shift, motion, color, or scene features. Unlike previous works, here, we ask the question: Can we directly estimate $\{\Gamma_k\}_{k=0}^{K-1}$ in (7.1)? In practice, sampling (7.3) would require exorbitant sampling rates and this is certainly not an option. Also, we are interested in $\{\Gamma_k\}_{k=0}^{K-1}$ only, as opposed to $\{\Gamma_k, t_k\}_{k=0}^{K-1}$ [263] where t_k is a non-linear argument in (7.3). As a result, our goal is to recover the intensities of a sparse signal. For this purpose, we explore the idea of *sampling without time*—a method for sampling a sparse signal which does not assume the knowledge of sampling instants or the sampling rate.

7.1.1 Contributions

In this work, our contributions are twofold:

1) For the general case of K-echoes of light, our work relies on estimating the constituent images $\{\Gamma_k\}_{k=0}^{K-1}$ from the filtered, auto-correlated, time-resolved measurements. This is the distinguishing feature of our approach and is fundamentally different from methods proposed in literature which are solely based on spatio-angular information (cf. [257, 258, 259, 260, 261, 262] and references therein).

2) As will be apparent shortly, our work is intimately linked with the problem of (sparse) phase retrieval (cf. [264, 265, 266, 267, 268] and references therein). Our "sampling without time" architecture leads to an interesting measurement system which is based on time-of-flight imaging sensors [66] and suggests that $K^2 - K + 1$ measurements suffice for estimation of K echoes of light. To the best of our knowledge, neither such a measurement device nor bounds have been studied in the context of image source separation [257, 258, 259, 260, 261].

3) In Section 7.6, we extend our approach to frequency domain architecture and validate the effectivity of our approach.

For the sake of simplicity, we will drop the dependence of m and Γ on spatial coordinates $\mathbf{r}$. This is particularly well suited for our case because we do not rely on any cross-spatial information or priors. Also, scaling factors λ_k are assumed to be absorbed in Γ_k.

7.1.2 Role of Temporal Phase Retrieval

Significance of Phase-free or Amplitude-only measurements: It is worth emphasizing that resolving spikes from a superposition of low-pass filtered echoes, is a problem that frequently occurs in many other disciplines. This is a prototype model used in the study of multi-layered or multi-path models. Some examples include seismic imaging [201], time-delay estimation [56], channel estimation [72], optical

tomography [80], ultrasound imaging [269], computational imaging [66, 270, 271, 209, 16] and source localization [48]. Almost all of these variations rely on amplitude and phase information or amplitude and time-delay information. However, recording amplitude-only data can be advantageous due to several reasons. Consider a common-place example based on pulse-echo ranging. Let $p(t) = \sin(\omega t)$ be the emitted pulse. Then, the backscattered signal reads $r(t) = \Gamma_0 \sin(\omega t - \theta_0)$. In this setting, on-chip estimation of phase (θ_0) or time delay (t_0)[209],

- can either be computationally expensive or challenging since t_k is a non-linear parameter in (7.3), and hence, in $r(t)$.
- requires more measurements. For instance, 2 measurements suffice for amplitude-only estimation (Γ_0) while amplitude-phase pair requires 4 measurements [66]. This aspect of phase estimation is an important bottleneck as the the frame rate of an imaging device is inversely proportional to number time-domain measurements.
- is prone to errors. In many applications, multiple-frequency measurements, $\omega = k\omega_0$, are acquired [209, 21, 66] assuming that phase and frequency, $\theta_0 = \omega t_0$ are linearly proportional. However, this is not the case in practice. The usual practice is to oversample [272, 273].

In all such cases, one may adopt our methodology of working with intensity-only measurements.

7.2 Problem Formulation

Optical ToF sensors are active devices that capture 3D scene information. We adopt the generic image–formation model used in [66] which is common to all ToF modalities such as lidar/radar/sonar, optical coherence tomography, terahertz, ultrasound, and seismic imaging. In its full generality, and dropping dependency on the spatial coordinate for convenience, one can first formalize this ToF acquisition model as:

$$p \rightarrow \boxed{h} \rightarrow r \rightarrow \boxed{\phi} \rightarrow y \xrightarrow{\text{Sampling}} \mathbf{y} \mapsto \underbrace{m = \mathcal{C}[\mathbf{y}]}_{\text{Intensity}} \tag{7.4}$$

where,

- ▷ $p(t) > 0$ is a T-periodic probing function which is used to illuminate the scene. This may be a sinusoidal waveform, or even a periodized spline, Gaussian, or Gabor pulse, for instance.
- ▷ $h(t, \tau)$ is the scene response function (SRF). This may be a filter, a shift-invariant function $h_{\mathsf{SI}}(t, \tau) = h(t - \tau)$, or a partial differential equation modeling some physical phenomenon [21].
- ▷ $r(t) = \int p(\tau)\, h(t, \tau)\, d\tau$ is the reflected signal resulting from the interaction between the probing function and the SRF.
- ▷ $y(t) = \int r(\tau)\, \phi(t, \tau)\, d\tau$ is the continuous-time signal resulting from the interaction between the reflected function and the instrument response function (IRF), or ϕ, which characterizes the electro-optical transfer function of the sensor.
- ▷ $\mathbf{y}$ is a set of discrete measurements of the form $y(t)|_{t=n\Delta}$.
- ▷ $\mathcal{C}[\mathbf{y}] = \mathbf{y} * \overline{\mathbf{y}}$ is the cyclic auto-correlation of $\mathbf{y}$, where $*$ and $\overline{(\cdot)}$ denote the convolution and time reversal operators, respectively.

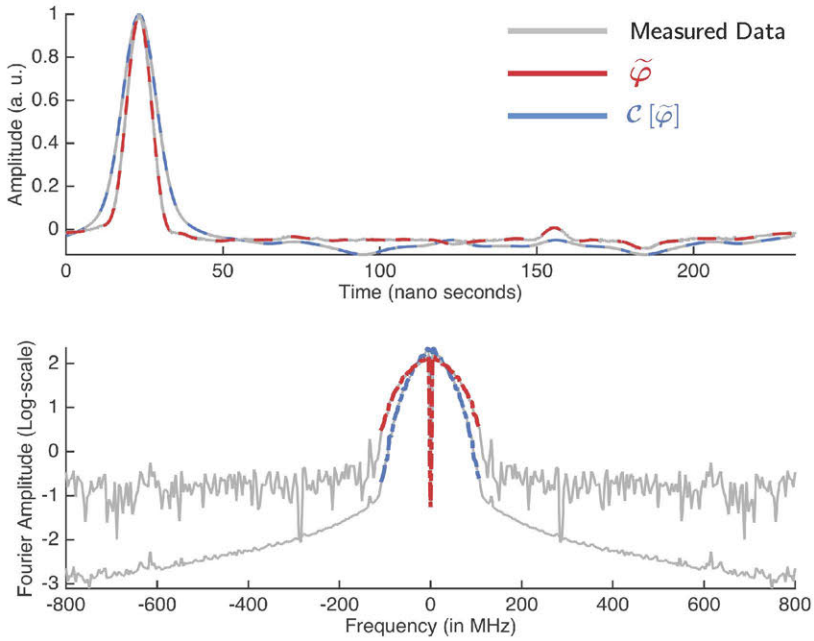

Figure 7-3: Bandlimited approximation $\widetilde{\varphi} \approx \mathcal{C}[p]$ with $L = 25$ (red curves) and its cyclic auto-correlation $\mathcal{C}[\widetilde{\varphi}]$ (blue curve). Shown are the spatial-domain signals (top) and the corresponding Fourier-domain magnitudes in log scale (bottom).

The interplay between p, h, and ϕ results in variations on the theme of ToF imaging [66]. In this work, we will focus on an optical ToF setting. Accordingly:

1) The probing function corresponds to a time-localized pulse.
2) The SRF, accounting for the echoes of light, is a K-sparse filter (2.10),

$$h_{\mathsf{SI}}(t,\tau) \equiv h_K(t-\tau) = \sum_{k=0}^{K-1} \Gamma_k \delta(t-\tau-t_k). \tag{7.5}$$

3) The IRF is fixed by design as $\phi_{\mathsf{SI}}(t,\tau) = p(t+\tau)$. This implements the so-called homodyne, lock-in sensor [66].

Due to this specific shift-invariant structure of the SRF and IRF, we have,

$$\begin{aligned} y(t) &= \left(p * \bar{p} * \bar{h}_K\right)(t) \\ &= \left(\mathcal{C}[p] * h_K\right)(t). \end{aligned} \tag{7.6}$$

Finally, the measurements read,

$$m(t) = \mathcal{C}[y] = \left(\mathcal{C}[\varphi] * \mathcal{C}[h_K]\right), \quad \varphi = \mathcal{C}[p](t). \tag{7.7}$$

7.3 Sampling Echoes of Light

7.3.1 Bandlimited Approximation of Probing Function

Due to physical constraints inherent to all electro-optical systems, it is reasonable to approximate the probing signal as a bandlimited function [21, 66]. We use L–term Fourier series with basis functions $u_n(\omega_0 t) \stackrel{\text{def}}{=} e^{\jmath\omega_0 n t}$, $\omega_0 T = 2\pi$, to approximate p with,

$$p(t) \approx \widetilde{p}(t) = \sum_{|\ell|\leqslant L} \widehat{p}_\ell u_\ell(\omega_0 t), \tag{7.8}$$

where the $\widehat{p}_\ell$ are the Fourier coefficients. Note that there is no need to compute $p(t)$ explicitly as we only require the knowledge of $\mathcal{C}[p]$ (cf. (7.7)). In Fig. 7-3, we plot the calibrated $\mathcal{C}[p]$ and its Fourier coefficients. In this case, $T = 232.40$ ns. We also plot its approximation, $\widetilde{\varphi} = \mathcal{C}[\widetilde{p}]$ with $L = 25$ together with the measured $\mathcal{C}[p]$ and φ.

7.3.2 Sampling Theory Context

The shift-invariant characterization of the ToF image–formation model allows to re-interpret the sampled version of (7.7) as the filtering of a sparse signal $\mathcal{C}[h_K]$ with a low-pass kernel $\psi = \mathcal{C}[\varphi]$ (cf. [202, 263]).

$$\begin{aligned} m(t) &\stackrel{(7.7)}{=} \mathcal{C}[h_K] * \mathcal{C}[\varphi] \equiv \mathcal{C}[h_K] * \psi \\ &= \sum_{k=0}^{K-1} |\Gamma_k|^2 \psi(t) + 2\sum_{k=0}^{K-1}\sum_{m=k+1}^{K-1} |\Gamma_k|\,|\Gamma_m| \psi(t - t_{k,m}) \end{aligned} \tag{7.9}$$

where $t_{k,l} = t_k - t_l$ and,

$$m(n\Delta) = \int \mathcal{C}[h_K](\tau)\,\overline{\mathcal{C}[\varphi]}(\tau - n\Delta)\,d\tau.$$

Note that the properties of the auto-correlation operation imply that the sparsity of $\mathcal{C}[h_K]$ is $K^2 - K + 1$, unlike h_K that is K-sparse and is completely specified by $(K^2 - K)/2 + 1$ due to symmetry. Based on the approximation (7.8) and the properties of convolution and complex exponentials, and defining $\widehat{\psi}_\ell = |\widehat{p}_\ell|^4$, we rewrite $m(t)$ as,

$$m(t) = \sum_{|\ell|\leq L} \widehat{\psi}_\ell u_\ell(\omega_0 t) \underbrace{\int \mathcal{C}[h_K](\tau)\, u_\ell^*(\omega_0\tau) d\tau}_{\text{Fourier Integral}}, \tag{7.10}$$

Finally, the properties of the Fourier transform imply that sampling the above signal $m(t)$ at time instants $t = n\Delta$, results in discrete measurements of the form $\mathbf{m} = \mathbf{U}\mathbf{D}_{\widehat{\psi}}\widehat{\mathbf{s}}$, which corresponds to the available acquired data in our acquisition setting. Combining all the above definitions, it follows that:

- $\mathbf{m} \in \mathbb{R}^N$ is a vector of filtered measurements (cf. (7.9)).
- $\mathbf{U} \in \mathbb{C}^{N\times(2L+1)}$ is a DFT matrix with elements $[u_n(\omega_0 \ell\Delta)]_{n,\ell}$.

—• $\mathbf{D}_{\widehat{\psi}} \in \mathbb{C}^{(2L+1)\times(2L+1)}$ is a diagonal matrix with diagonal elements $\widehat{\psi}_\ell$. These are the Fourier-series coefficients of $\mathcal{C}[\varphi]$.

—• $\widehat{\mathbf{s}} \in \mathbb{R}^{2L+1}$ is a phase-less vector containing the Fourier coefficients of $\mathcal{C}[h_K]$, which is obtained by sampling the Fourier transform $\widehat{s}(\omega)$ of $\mathcal{C}[h_K]$ at instants $\omega = \ell\omega_0$. The signal $\widehat{s}(\omega)$ directly depends on the quantities $|\Gamma_k|$ of interest to be retrieved and is expressed as

$$\begin{aligned}\widehat{s}(\omega) &= \left|\sum_{k=0}^{K-1} \Gamma_k u_{t_k}(\omega)\right|^2 \equiv |\widehat{h}_K(\omega)|^2 \\ &= \underbrace{\sum_{k=0}^{K-1} |\Gamma_k|^2}_{a_0} + 2\sum_{k=0}^{K-1}\sum_{m=k+1}^{K-1} \underbrace{|\Gamma_k||\Gamma_m|}_{a_{k,m}} \cos(\omega t_{k,m} + \angle\Gamma_{k,m})\end{aligned} \tag{7.11}$$

where $t_{k,m} = t_k - t_m$ and $\angle\Gamma_{k,m} = \angle\Gamma_k - \angle\Gamma_m$.

It is instructive to note that the relevant unknowns $\{\Gamma_k\}_{k=0}^{K-1}$ can be estimated from $\widehat{\mathbf{s}} \in \mathbb{R}^{2L+1}$ in (7.11) which in turn depend only on L as opposed to sampling rate and sampling instants. This aptly justifies our philosophy of *sampling without time*.

7.4 Reconstruction via Phase Retrieval

Given data model $\mathbf{m} = \mathbf{U}\mathbf{D}_{\widehat{\psi}}\widehat{\mathbf{s}}$ (7.10), we aim to recover the image parameters $|\Gamma_k|$ at each sensor pixel. For this purpose, we first estimate samples of $\widehat{s}(\omega)$ as $\widehat{\mathbf{s}} = \mathbf{D}_{\psi}^{-1}\mathbf{U}^{+}\mathbf{m}$, where $\mathbf{U}^{+}$ is the matrix pseudo-inverse of $\mathbf{U}$. This is akin to performing a weighted deconvolution, knowing that $\mathbf{U}$ is a DFT matrix. Next, we solve the problem of estimating $|\Gamma_k|$ in two steps (1) First we estimate $a_{k,m}$, and then, (2) based on the estimated values, we resolve ambiguities due to $|\cdot|$.

Parameter Identification via Spectral Estimation: Based on the coefficients $\widehat{\mathbf{s}}$, one can then retrieve the amplitude and frequency parameters that are associated with the oscillatory terms as well as the constant value in (7.11). The oscillatory-term and constant-term parameters correspond to $\{a_{k,m}, t_{k,m}\}$ and a_0, respectively. All parameter values are retrievable from $\widehat{\mathbf{s}}$ through spectral estimation [67]; details are provided in [66] for the interested reader.

Note that, given the form of (7.11) and our acquisition model, the sparsity level of the sequence $\widehat{\mathbf{s}}$—corresponding to the total amount of oscillatory and constant terms—is $(K^2-K)/2+1$. The magnitude values $a_{k,m}$ and a_0 can thus be retrieved if at least $L \geq (K^2-K)+1$ autocorrelation measurements are performed [274, 66], which is the case in the experiments described in Section 7.5.

Resolving Ambiguities: Based on the aforementioned retrieved parameters, one wishes to then deduce $\{|\Gamma_k|\}_{k=0}^{K-1}$. The estimated cross terms $\{a_{k,m}, t_{k,m}\}$ allow to retrieve the values of $|\Gamma_k|$ through simple pointwise operations. Here we will focus on the case, $K = 2$. Due to space limitations, we refer the interested readers to our companion paper [66] for details on the general case ($K > 2$). The case when

$K = 2$,

$$\widehat{s}(\omega) \overset{(7.11)}{=} \left|\Gamma_0 u^*_{t_0}(\omega) + \Gamma_1 u^*_{t_1}(\omega)\right|^2 + \underbrace{\varepsilon_\omega(\Gamma_k, t_k)_{k>2}}_{\approx 0}$$
$$= \underbrace{|\Gamma_0|^2 + |\Gamma_1|^2}_{a_0} + \underbrace{2|\Gamma_0||\Gamma_1|}_{a_{01}} \cos(\omega t_{0,1} + \angle\Gamma_{0,1}),$$

may be a result of two distinct echoes (Fig. 7-2) or due to approximation of higher order echoes by two dominant echoes (due to inverse-square law). In this case, we effectively estimate two terms: a_0 and a_{01} (7.11). The set of retrieved magnitude values then amount to solving[66]:

$$||\Gamma_0| \pm |\Gamma_1|| = \sqrt{a_0 \pm a_{01}}, \qquad a_0, a_{01} > 0. \tag{7.12}$$

Thanks to the *isoperimetric property* for rectangles: $a_0 \geq a_{01}$, the r.h.s above is always positive unless there is an estimation error in which case, an exchange of variables leads to the unique estimates,

$$\left\{|\widetilde{\Gamma}_k|\right\}_{k=1,2} = \frac{\sqrt{\widetilde{a}_0 + \widetilde{a}_{01}} \pm \sqrt{\widetilde{a}_0 - \widetilde{a}_{01}}}{2}. \tag{7.13}$$

7.5 Experimental Validation

7.5.1 Simulation

Noting that measurements $\mathbf{m} = \mathbf{UD}_{\widehat{\psi}}\widehat{\mathbf{s}}$ and $\widehat{\mathbf{s}}$ are linked by an invertible, linear system of equations, knowing $\mathbf{m}$ amounts to knowing $\widehat{\mathbf{s}}$. We have presented detailed comparison of simulation results in [66] for the case where one directly measures $\widehat{\mathbf{s}}$. In this chapter, we will focus on practical setting where the starting point of our algorithm is (7.10).

7.5.2 Practical Validation

Our experimental setup mimics the setting of Fig. 7-2. A placard that reads "Time–of–Flight" is covered by a semi-transparent sheet, hence $K = 2$. The sampling rate is $\Delta \approx 70 \times 10^{-12}$ seconds using a our custom designed ToF imaging sensor [73]. Overall, the goal of this experiment is to recover the magnitudes $\{|\Gamma_k|\}_{k=0}^{k=1}$ given auto-correlated measurements $m(n\Delta) \overset{(7.7)}{=} \mathcal{C}[y](n\Delta), \mathbf{m} \in \mathbb{R}^{2795}$. To be able to compare with a "ground truth", we acquire time-domain measurements $y(n\Delta)$ before autocorrelation, whose Fourier-domain phases are intact. In Fig. 7-4(a), we plot the non-autocorrelated measurements $\mathbf{y}$ while phase-less measurements $\mathbf{m}$ are shown in Fig. 7-4(c) from which we note that the samples are symmetric in time domain due to $m = \mathcal{C}[y]$ (cf. 7.7). In the first case (cf. Fig. 7-4(a)) where $y = \mathcal{C}[p] * \overline{h}_K$, we have [73],

$$\widehat{y}(\omega) = |\widehat{p}(\omega)|^2 h^*_K(\omega), \quad h_K(\omega) = \sum_{k=0}^{K-1} \Gamma_k u_{t_k}(\omega).$$

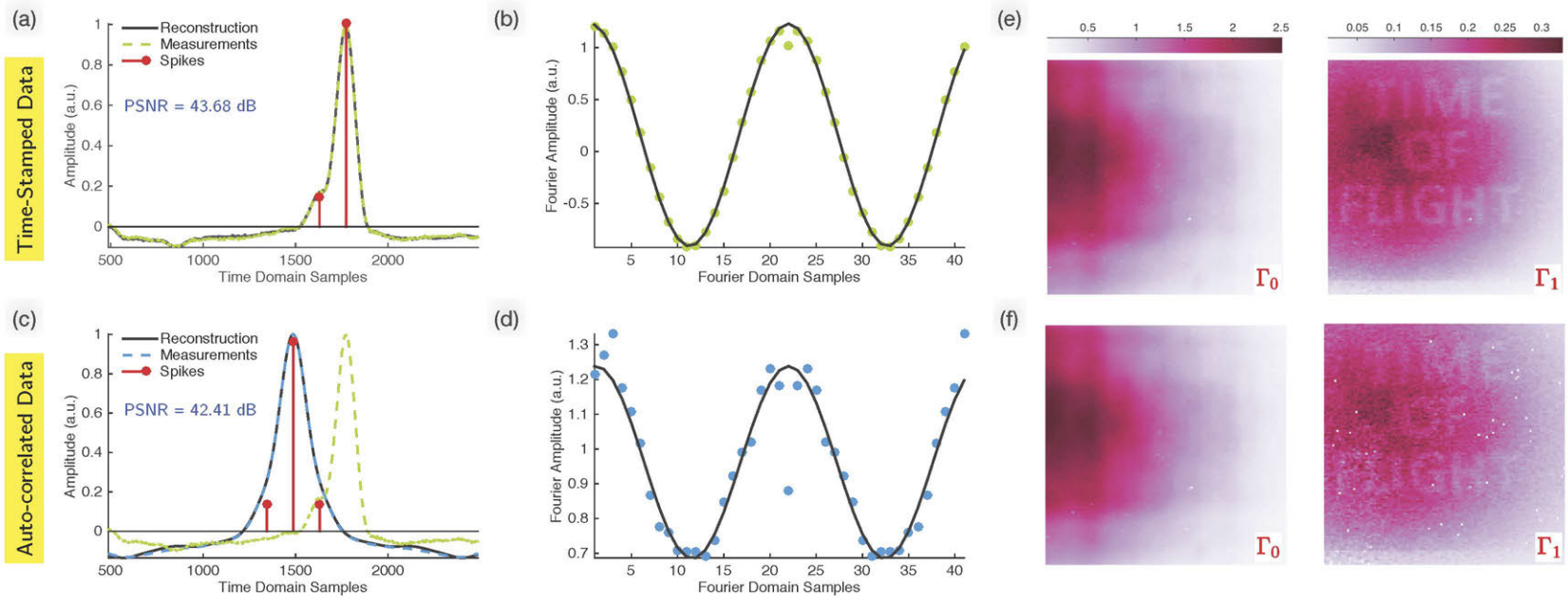

Figure 7-4: Experimental results on acquisition and reconstruction of echoes of light in a scene. (a) Single pixel, time-stamped samples $y = \mathcal{C}[p] * \overline{h}_2$ serve as our ground truth because the phase information is known. We also plot the estimated, 2-sparse SRF (7.5) in red ink. (b) Fourier domain frequency samples of the SRF, $\widehat{h}_2(\ell\omega_0)$ with $L = [-20, 20]$ and $\omega_0 = 2\pi/\Delta$, $\Delta = 70$ ps. We plot the measured data in green and the fitted data in black. The frequencies are estimated using Cadzow's method. (c) Same pixel, time-stampless, low-pass filtered, auto-correlated samples (7.9) together with the estimated, auto-correlated SRF $\mathcal{C}[h_2]$ in red ink. (d) Fourier domain samples $\widehat{s}(\ell\omega_0)$ (7.11) and its fitted version (black ink). (e) Ground truth images for the experiment. (f) Estimated images using temporal phase retrieval.

Similar to $\mathbf{m}$ in (7.10), in this case, the measurements read $\mathbf{y} = \mathbf{U}\mathbf{D}_{\widehat{\varphi}}\widehat{\mathbf{h}}$ and we can estimate the complex-valued vector $\widehat{\mathbf{h}}$. The phase information in $\widehat{\mathbf{h}}$ allows for the precise computation of $\{\Gamma_k, t_k\}_{k=0}^{K-1}$ [73, 263]. These "intermediate" measurements serve as our ground truth. The spikes corresponding to the SRF (7.5) are also marked in Fig. 7-4(a). Fourier-domain measurements $\widehat{h}_2^*$ linked with $y(n\Delta)$ are shown in Fig. 7-4(b). Accordingly, $\widehat{h}_2^*(\omega)$, $\omega = \ell\omega_0, l = \{-L, \ldots, L\}$ where $\omega_0 = 2\pi/\Delta$ and $L = 20$. We estimate the frequency parameters $\{\Gamma_k, t_k\}_{k=0}^{K-1}$ using Cadzow's method [275]. The resulting fit is plotted in Fig. 7-4(b).

In parallel to Figs. 7-4(a),(b), normalized, autocorrelated data $\mathbf{m} = \mathcal{C}[\mathbf{y}]$ are marked in Fig. 7-4(c). The signal $\mathbf{y}$ is also shown as reference in green dashed line. We also plot the estimated $\mathcal{C}[h_2]$ (auto-correlated SRF). In Fig. 7-4(d), we plot measured and deconvolved vector $\widehat{\mathbf{s}} = \mathbf{D}_{\psi}^{-1}\mathbf{U}^{+}\mathbf{m}$ from which we estimate $a_0, a_{k,m}$ (7.11). The result of fitting using Cadzow's method with 41 samples is shown in Fig. 7-4(d).

The reconstructed images, $|\Gamma_0|$ and $|\Gamma_1|$, due to amplitude-phase measurements (our ground truth, Fig. 7-4(a)) are shown in Fig. 7-4(e). Alternatively, the reconstructed images with auto-correlated/intensity-only information are shown in 7-4(f). One can observe the great similarity between the images obtained in both cases, where only a few outliers appear in the phase-less setting. The PSNR values between the maps reconstructed with and without the phase information are of 30.25 dB for $|\Gamma_1|$ and 48.88 dB for $|\Gamma_0|$. These numerical results indicate that, overall, the phase loss that occurs in our autocorrelated measurements still allows for accurate reconstruction of the field of view of the scene.

Finally, in order to determine the consistency of our reconstruction approach, the PSNR between the original available measurements and their re-synthesized versions—as obtained when reintroducing our reconstructed profiles $|\Gamma_k|$ into our forward model—are also provided. As shown in Figs. 7-4(a) and (c), the PSNR values in the oracle and phase-less settings correspond to 43.68 dB and 42.41 dB, respectively, which confirms that our reconstruction approach accurately takes the parameters and structure of the acquisition model into account.

7.6 Extension to Frequency Domain Time-resolved Imaging

The time-domain measurements in (7.7) can be acquired directly in Fourier domain. For the choice of sinusoidal illumination,

$$p(t) = 1 + p_0 \cos(\omega_0 t) \quad \omega_0 = \frac{2\pi}{T_p},$$

the reflected signal from an object at depth d_0 meters, undergoes a delay proportional d_0 and reads,

$$\begin{aligned} r(t) &= \Gamma_0 p\left(t - \frac{2d_0}{c}\right) \\ &= \Gamma_0 \cos\left(\omega_0\left(t - \frac{2z_0}{c}\right)\right) = \Gamma_0 \cos(\omega_0(t - t_0)). \end{aligned}$$

7.6.1 Estimating Fourier Transform from Measurements

Here, we show that the ToF sensor measurements can directly measure the Fourier transform of the scene response function (7.5) using lock-in principle. The ToF lock–in sensor then measures the cross–

correlation between the probing function p and its reflected version r at four equidistant locations,

$$y_k \stackrel{\text{def}}{=} \mathsf{C}_{\omega_0}(k\Delta), \quad \Delta = \frac{\pi}{2\omega_0}, \quad k = 0, \ldots, 3 \tag{7.14}$$

where,

$$\begin{aligned}
\mathsf{C}_{\omega_0}(t) &= (\overline{p} * r)(t), \quad \bar{p}(t) = p(-t) \\
&= \lim_{T_p \to \infty} \frac{1}{2T_p} \int \overline{p}(x)\, r(t-x)\, dx \\
&= \lim_{T_p \to \infty} \frac{1}{2T_p} \int_{-T_p}^{+T_p} \underbrace{(1 + p_0 \cos(-\omega_0 x))}_{\overline{p}(x)} \underbrace{\Gamma_0 \cos(\omega_0 (t - x - t_0))}_{r(t-x)}\, dx \\
&= \lim_{T_p \to \infty} \frac{I_{\omega_0}(t)}{2T_p},
\end{aligned}$$

with,

$$\begin{aligned}
I_{\omega_0}(t) = 2\Gamma_0 T_p + {p_0}^2 \Gamma_0 T_p \cos(\omega_0 (t+d)) + 2p_0\Gamma_0 \frac{\sin(\omega_0 T_p)}{\omega_0} \\
+ 2p_0\Gamma_0 \cos(\omega_0 (t+t_0)) \frac{\sin(\omega_0 T_p)}{\omega_0} - p_0^2 \Gamma_0 \frac{\sin(\omega_0 (t + t_0 - 2T))}{4\omega_0} \\
+ p_0^2 \Gamma_0 \frac{\sin(\omega_0 (t + t_0 + 2T))}{4\omega_0}.
\end{aligned} \tag{7.15}$$

Now since,

$$\lim_{T_p \to \infty} \frac{\sin(\omega_0 T_p)}{\omega_0 T_p} = 0,$$

we conclude,

$$\mathsf{C}_{\omega_0}(t) = \lim_{T_p \to \infty} \frac{I_{\omega_0}(t)}{2T_p} = \Gamma_0 + \Gamma_0 \frac{{p_0}^2}{2} \cos(\omega_0 (t + t_0)).$$

Next, the phase-shift method [248] involving four measurements of the cross-correlated function (7.14) leads to the estimates of $\{\Gamma_0, t_0\}$. To see this in effect, we start with the stacking the four sampled measurements (7.14) in the following matrix,

$$\mathbf{Y} = \begin{bmatrix} y_0 & y_1 \\ y_2 & y_3 \end{bmatrix} = \frac{\Gamma_0}{2} \begin{bmatrix} 2 + p_0^2 \cos(\omega_0 t_0) & 2 - p_0^2 \sin(\omega_0 t_0) \\ 2 - p_0^2 \cos(\omega_0 t_0) & 2 + p_0^2 \sin(\omega_0 t_0) \end{bmatrix}. \tag{7.16}$$

Based on the measurements, we see that the estimates are given by,

$$\begin{cases} \Gamma_0 = \frac{1}{p_0^2} \left((y_3 - y_1)^2 + (y_0 - y_2)^2 \right)^{\frac{1}{2}} \\ t_0 = \frac{1}{\omega_0} \tan^{-1} \left(\frac{y_3 - y_1}{y_0 - y_2} \right) \end{cases}.$$

A more concise representation involves defining a complex number $Y_{\omega_0} \in \mathbb{C}$,

$$Y_{\omega_0} = (y_0 - y_2) + \jmath\,(y_3 - y_1)$$

whereby,

$$\begin{cases} \Gamma_0 = \frac{|Y_{\omega_0}|}{p_0^2} \\ t_0 = \frac{\angle Y_{\omega_0}}{\omega_0} \end{cases}. \tag{7.17}$$

In contrast to prior work linked with ToF imaging [209, 15] and references therein, our assumption in this section is that only the *amplitude information* of the measurements can be accessed.

7.6.2 Direct Measurement of Fourier Magnitude Information

The above definitions imply that phase information encodes the parameters t_k. Now, the quantities that are of interest to us consist in the time-resolved-image intensities. In the case $K = 1$, we have

$$|\widehat{y}(\omega)|^2 = |\Gamma_0|^2, \text{ (measurement)} \tag{7.18}$$

which is the intensity corresponding to the time–resolved image $\Gamma_0\delta\,(t - t_0)$. Such measurements are computed using the auto–correlation function,

$$\begin{aligned} m\,(t) &\overset{(7.7)}{=} \mathcal{C}\,[y]\,(t) \\ &= \left(\mathsf{C}_{\omega_0} * \overline{\mathsf{C}}_{\omega_0}\right)(t) \\ &= \frac{\Gamma_0^2}{8}\left(8 + p_0^4 \cos\left(\omega_0 t\right)\right). \end{aligned} \tag{7.19}$$

By letting,

$$m_k = m\left(\frac{\pi k}{2\omega_0}\right)$$

we see that 4 measurements lead to,

$$\mathbf{M} = \begin{bmatrix} m_0 & m_1 \\ m_2 & m_3 \end{bmatrix} = \Gamma_0^2 \begin{bmatrix} 1 + \frac{p_0^4}{8} & 1 \\ 1 - \frac{p_0^4}{8} & 1 \end{bmatrix}.$$

However, once can estimate $|\Gamma_0|^2$ using *two measurements*

$$|\widehat{s}\,(\omega_0)\,|^2 = |\widetilde{\Gamma}_0|^2 = \frac{4}{p_0^4}\,(m_0 - m_2)\,. \tag{7.20}$$

As opposed to measurement of both Fourier phase and amplitude discussed in Section 7.6.1, this procedure bypasses phase computations producing a single real-valued measurement per ToF exposure unlike the usual two-value case. In this way, when K light paths meet at the sensor, at each frequency $n\omega_0, n \in \mathbb{Z}$, one can directly measure $|\widehat{s}\,(n\omega_0)|^2$ in (7.11). This is done by computing (7.20) at each frequency $\{n\omega_0\}_{n=0}^{N-1}$,

$$\frac{4}{p_0^4}\left\{m\,(0) - m\left(\frac{\pi}{n\omega_0}\right)\right\}_{n=0}^{N-1} \Rightarrow \left\{|\widehat{s}\,(n\omega_0)|^2\right\}_{n=0}^{N-1}. \tag{7.21}$$

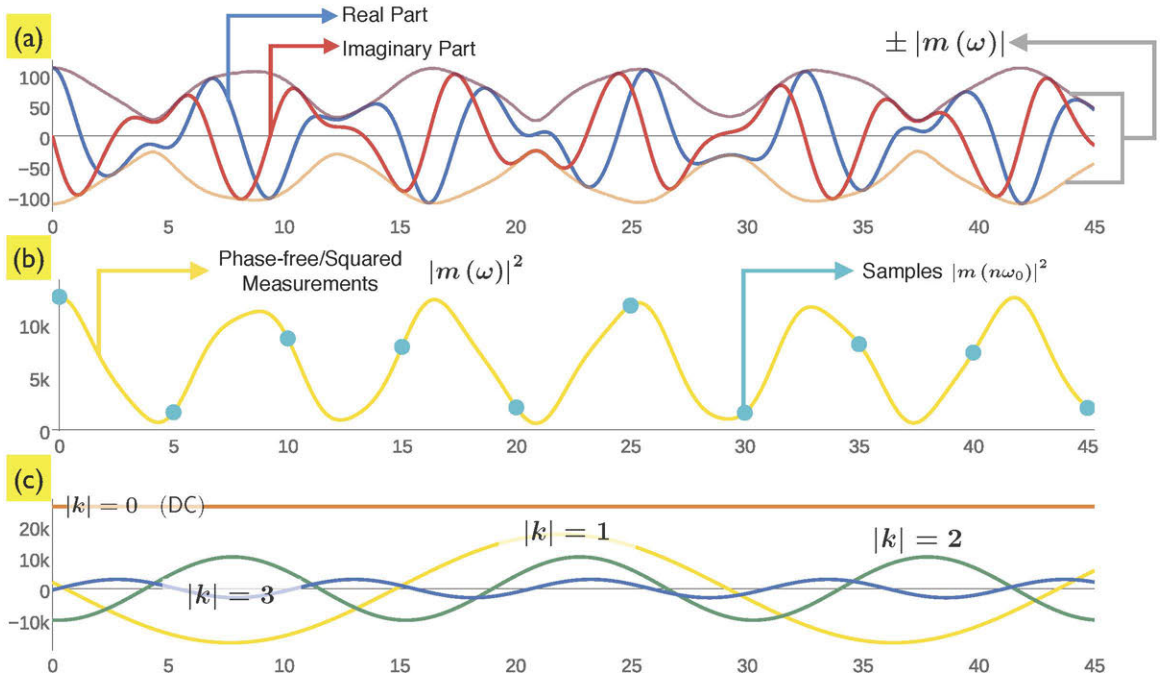

Figure 7-5: Phase Retrieval in Setting $K = 3$. This measurement corresponds to pixel $(20, 20)$ of the synthetic experiment in Section 7.6.6. (a) Complex–valued $\widehat{s}(\omega)$ with the real and imaginary parts together with the envelope $\pm|\widehat{s}(\omega)|$. (b) Phase–less $|\widehat{s}(\omega)|^2$ with $s_n = |\widehat{s}(n\omega_0)|^2, \omega_0 = 5$. (c) Decomposition of s_n into terms of $\{\gamma_k, \nu_k\}_{|k|\leqslant K_0}$ as in (7.22).

7.6.3 Reconstruction via Frequency Estimation

Let us re-arrange (7.11) based on Euler's identity to obtain a variant of the *Line Spectrum Estimation* or the LSE problem [67]:

$$s_n = |\widehat{s}(n\omega_0)|^2 \overset{(7.11)}{=} \sum_{k=-K_0}^{k=+K_0} \gamma_k e^{\jmath n\omega_0\nu_k}, \quad K_0 = \left(K^2 - K\right)/2 \tag{7.22}$$

where $\gamma_k \propto \Gamma_{kl}$ and $\nu_k \propto t_{kl}$. When $K = 2$, $\gamma_1 = \gamma_{-1}^* = \Gamma_0\Gamma_1$ and $\nu_1 = -\nu_{-1} = t_{01}$. In practice, $\{\Gamma_k\}_{k=0}^{K-1}$ are real-valued, but, even if this is not the case, we always have conjugate symmetry, *i.e.*, $\gamma_k = \gamma_{-k}^*$ and $\nu_k = -\nu_{-k}$. We recover $\{\gamma_k\}_{k=0}^{K-1}$ in two steps:

1. We first estimate ν_k given $s_n = |\widehat{s}(n\omega_0)|^2, n = 0, \ldots, N-1$.

   Using the idea of Prony [67], we define the polynomial,

$$\mathsf{H}(z) = \prod_{|m|\leqslant K_0} \left(1 - e^{-\jmath\omega_0 v_k} z^{-1}\right) = \sum_{m=0}^{2K_0+1} h_m z^{-m} \tag{7.23}$$

which is yet to be computed. However, note that, $(h * s)_n = 0$,

$$\begin{aligned}(h * s)_n &= \sum_{m=0}^{2K_0+1} h_m s_{n-m} \overset{(7.22)}{=} \sum_{m=0}^{2K_0+1} h_m \sum_{k=-K_0}^{k=+K_0} \gamma_k e^{\jmath(n-m)\omega_0\nu_k} \\ &= \sum_{k=-K_0}^{k=+K_0} \gamma_k \underbrace{\left(\sum_{m=0}^{2K_0+1} h_m e^{-\jmath m\omega_0\nu_k}\right)}_{\Leftrightarrow \mathsf{H}\left(e^{-\jmath\omega_0\nu_k}\right)=0} e^{\jmath n\omega_0\nu_k} = 0. \end{aligned} \tag{7.24}$$

Hence, the key idea is to find a filter sequence h which, when filtered with s_n, produces zeros. This problem is at the heart of *spectrum estimation* [67]. In this work, we use the composite mapping property algorithm (CMPA) devised by Cadzow [275].

2 With ν_k known, estimating γ_k in (7.22) is a linear problem.

We solve the linear least–squares problem to estimate $\widetilde{\gamma}_k$,

$$\widetilde{\gamma}_k = \min_{\gamma_k} \sum_{n=0}^{N-1} \left| s_n - \sum_{k=-K_0}^{k=+K_0} \gamma_k e^{\jmath n\omega_0\widetilde{\nu}_k} \right|^2. \tag{7.25}$$

Now, since $s_n = s_{-n}$, we need $N \geq K_0 + 1$ measurements in (7.21) to solve for $\{h_m\}_{m=0}^{K}$ (cf. (7.24)) [276]. We show a step–by–step decomposition of s_n in terms of $\{\gamma_k, \nu_k\}_{|k|\leqslant K_0}$ (7.22) in Fig. 7-5. Next, we discuss how to estimate $\{\Gamma_k\}$ from $\{\gamma_k\}$ in (7.25).

7.6.4 Revisiting the case of $K = 2$: Estimating $\{\Gamma_k\}$ from $\{\gamma_k\}$

The case has two interesting interpretations. The first one is simply the setting being described in Fig. 7-2. An alternate interpretation arises from approximation of scattering where one sets $K = 2$, assuming negligible contribution of higher-order terms $K \geq 3$, *i.e.*,

$$|\widehat{s}(\omega)|^2 \overset{(7.11)}{=} \left|\Gamma_0 e^{-\jmath\omega t_0} + \Gamma_1 e^{-\jmath\omega t_1}\right|^2 + \varepsilon_\omega(\Gamma_k, t_k)_{k\geqslant 3},$$

where $\varepsilon_\omega(\Gamma_k, t_k)_{k\geqslant 3} = \left|\sum_{k=0}^{K-1} \Gamma_k e^{-\jmath\omega t_k}\right|^2 \approx 0$. In either case,

$$|\widehat{s}(\omega)|^2 = \underbrace{|\Gamma_0|^2 + |\Gamma_1|^2}_{a_0} + \underbrace{2|\Gamma_0||\Gamma_1|}_{a_{12}} \cos(\omega t_{01} + \angle\Gamma_{01}). \tag{7.26}$$

The first step towards retrieving $|\Gamma_{0,1}|$ involves the estimation of a_0, a_{12} based on the available samples s_n (7.22). Given the equivalence between (7.26) and (7.22), the set of parameters a_0, a_{12}, t_{01}, and $\angle\Gamma_{01}$ are retrieved using $K_0 = 1$.

The parameters a_0 and a_{12} allow to estimate the values of the transmitted and reflected magnitudes $|\Gamma_0|$, $|\Gamma_1|$ based on algebraic relations. Specifically, the non-negativity of a_0, a_{12} implies that $||\Gamma_0| \pm |\Gamma_1|| = \sqrt{a_0 \pm a_{12}}$. Thus, based on $\widetilde{a}_0, \widetilde{a}_{12}$, we compute (7.13).

$$\left\{|\widetilde{\Gamma}_0|, |\widetilde{\Gamma}_1|\right\} \overset{(7.13)}{=} \frac{1}{2}\left(\sqrt{\widetilde{a}_0 + \widetilde{a}_{12}} \pm \sqrt{\widetilde{a}_0 - \widetilde{a}_{12}}\right) \tag{7.27}$$

where a_{01} in (7.13) is replaced a_{12} in the above equation.

The definition of a_0 and a_{12} implies the non-negativity of the above square-root argument, except if estimation errors occur. In such cases, our algorithm replaces $\widetilde{a}_{12}$ by $\widetilde{a}_0$, thus yielding the double solution $\sqrt{\widetilde{a}_0/2}$ for both magnitude values.

Following the above estimation operations, the retrieved values must be correctly assigned to the corresponding magnitudes. The phase-less setting precludes direct identification because the absolute distance parameters cannot be retrieved as such. Now, according to the inverse-square law, one can still assume that the magnitudes of $|\Gamma_1|$—given the relative proximity of this map—are *in average* larger than those of $|\Gamma_0|$. However, this assumption does not hold for every pixel in general. This implies that the assignments may suffer from some ambiguities that cannot be solved pointwise. We thus propose to address this issue by leveraging inter-pixel scene dependencies. In particular, we exploit the fact that maps stemming from real-world scenes display a certain degree of spatial regularity. Qualitatively, the disambiguation approach that we follow consists in (a) first detecting value-crossing locations $\mathbf{k}_i$ where both map magnitudes are (nearly) equal, and (b) then determining suitable assignments by decomposing the field of view into associated adjacent areas satisfying either $|\Gamma_1[\mathbf{k}]| \geq |\Gamma_0[\mathbf{k}]|$ or $|\Gamma_1[\mathbf{k}]| < |\Gamma_0[\mathbf{k}]|$.

7.6.5 Higher-Order Settings

The magnitudes $|\Gamma_i|$ can also be retrieved when $K \geq 3$. As in (7.27), a set of real numbers a_0 and a_{ij} can be identified in association with the constant and oscillatory terms. Disambiguation even becomes more straightforward in such settings because the presence of intermediate sheets allows to assign all magnitude values of interest pointwise based on the relative-distance t_{kl}. The latter quantities are also obtained (as byproducts) from the LSE method.

Let us consider the 3-bounce setting where the constant term is $a_0 = |\Gamma_0|^2 + |\Gamma_1|^2 + |\Gamma_2|^2$, the oscillatory terms being $a_{12} = 2|\Gamma_0||\Gamma_1|$, $a_{23} = 2|\Gamma_1||\Gamma_2|$, and $a_{13} = 2|\Gamma_0||\Gamma_2|$. Based on the estimates of the a_0 and a_{ij} provided by the LSE method, the set of values v_i corresponding to the unknown magnitudes $|\Gamma_{0,1,2}|$ is retrieved as $\{\widetilde{a}_{12}\widetilde{a}_{13}\mu, \widetilde{a}_{12}\widetilde{a}_{23}\mu, \widetilde{a}_{13}\widetilde{a}_{23}\mu\}$, where

$$\mu = \frac{\sqrt{\widetilde{a}_0}}{\sqrt{\left((\widetilde{a}_{12}\widetilde{a}_{13})^2 + (\widetilde{a}_{23}\widetilde{a}_{13})^2 + (\widetilde{a}_{23}\widetilde{a}_{12})^2\right)}}$$

In this setting, 7th–order estimation is performed with the LSE method, the order number ($N = 2K_0+1$) being here related to the constant and to the 6 complex exponentials associated with the $K = 3$ cosine terms (7.22). An estimation example is illustrated in Figure 7-5.

7.6.6 Experimental Results

Synthetic Data: In this first experiment, we consider scene with $K = 3$ with constituent images shown in Fig. 7-6(a). Each of the images $\{\Gamma_k\}_{k=0}^{K-1}$ are of size 160×160 and $\{t_k\}_{k=0}^{K-1} = [0.31\ \ 0.55\ \ 0.93]\pi$. We use $N = 4 = (K^2-K)/2+1$, multi-frequency, magnitude measurements $|\widehat{s}(nf_0)|, n = 0, \ldots, 3, f_0 =$ 1 MHz. The corresponding results are shown in Fig. 7-6 (a). In this synthetic scenario, the reconstructions that are obtained are virtually identical to the oracle, *i.e.*, the SNR reaches machine precision. This first set of results thus already validates our approach in the synthetic, noiseless case.

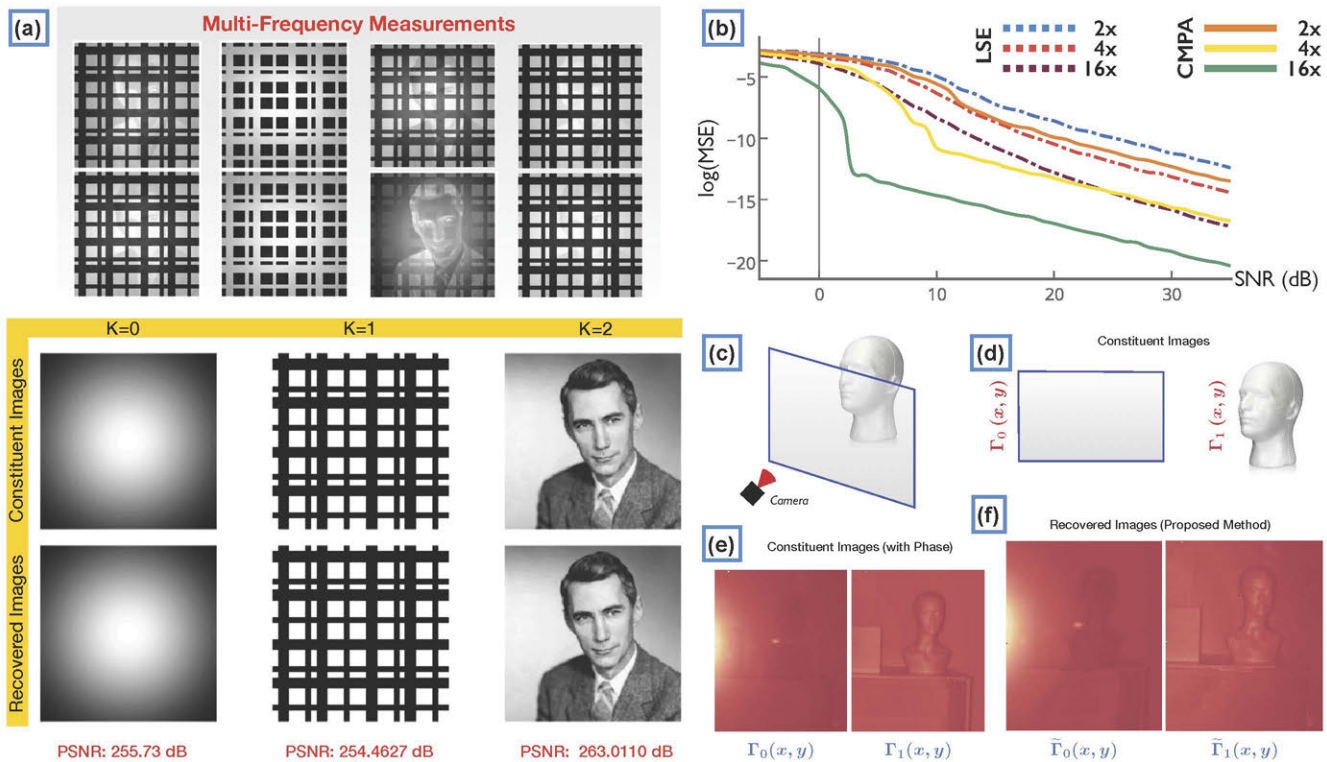

Figure 7-6: (a) Experimental results for simulated data with $K = 3$. The images on the top are spatial maps of the available magnitude multi-frequency measurements $|\hat{s}(2n\omega_0 + 1)|^2, n = 1, \ldots, 8$. For $K = 3$ we show the ground truth which consists of distinct layers constituting the scene as well as the reconstruction from the phase-less data with $N = 1 + (K^2 - K)/2 = 4$ measurements. We list the PNSR value indicating reconstruction up to machine precision. (b) Performance analysis of the Cadzow's CMPA algorithm [275] for $K = 2$ for the noisy case. We show the effect of over–sampling, that is $N = \kappa(K + 1)$ samples, on mean squared error (MSE) as a function of signal–to–noise ratio (SNR). As can be seen, when $\kappa = 2$ or we have $2N$ samples of s_n, the CMPA algorithm has a stabilizing effect on MSE. For the case of $16x$ oversampling, the MSE decreases linearly with increase in SNR. This effect happens as early as SNR $= 3$ (dB) for the CMPA algorithm. We also compare the LSE method with the CMPA method for different over–sampling factors. (c) Scene setup for experiment for $K = 2$ with Microsoft Kinect. (d) Schematic representation of the constituent images. (e) We reconstruct the assuming that we measure $\widehat{s}(nf_0), n = 50, \ldots, 100$ with $f_0 = 1$ MHz. (f) Reconstruction via phase retrieval using $|\widehat{s}(nf_0)|^2, n = 50, \ldots, 100$ with $f_0 = 1$ MHz.

The effect of noise is studied in Fig. 7-6(b) where we plot the observed *mean squared error* as a function of signal-to-noise-ratio (SNR) with consideration to the over-sampling factor using Cadzow's method [275]. With SNR =20 and $K = 2$, 4 times over-sampling achieves reasonable bound on the MSE.

ToF Sensor Based Data: We use the Microsoft Kinect One ToF camera. This camera is equipped with a modified firmware facilitating customized frequencies at $f_0 = 1$ MHz steps in range 50 to 100 MHz. The setup is described in 7-6 (c) and a schematic of the ground truth is shown in 7-6 (d). The back scene consists of a mannequin head at approximately 1.5m from the sensor. In addition, a semi-transparent sheet at a distance of 15 cm covers the sensor's field-of-view. This transparency sheet reflects a fraction of the emitted infrared light directly back to the sensor, thus $K = 2$. The available measurements consist of 145×119 multi-frequency profiles captured at $N = 51$ distinct frequencies.

Our algorithm is used for the phase-less setting where we measure $s_n = |\widehat{s}\,(n\omega_0)\,|^2$ (7.21). We also retain complex-valued measurements $\widehat{s}(n\omega_0)$ computed in (7.17). The ground truth is hard to obtain for our experiment. Consequently, we use the method described in [209, 226] to estimate $\{\widetilde{\Gamma}_0^{\mathsf{GT}}, \widetilde{\Gamma}_1^{\mathsf{GT}}\}$ using (7.17) which serves as a proxy of our oracle estimate (cf. Fig. 7-6 (e)). Cadzow's method is employed as a standalone tool for this purpose. We then estimate $\{|\widetilde{\Gamma}_0|, |\widetilde{\Gamma}_1|\}$ from the knowledge of $s_n = |\widehat{s}(n\omega_0)|^2$ (7.22), using our proposed approach, for example, (7.27). As in the first experiment, the goal of these experiments is to reconstruct and identify the distinct magnitude maps $|\Gamma_k|$ associated with $k = 0$ and $k = 1$. We show the estimates obtained by our approach in Fig. 7-6 (f). Our results show the effectivity of our model as well as the applicability of our algorithm. We use the SSIM index [277] as our performance metric to compare image reconstruction with and without phase measurements in Fig. 7-6 (e) and Fig. 7-6 (f), respectively. The SSIM measures for the first and the second sheets correspond to 0.750 and 0.408. Even though there is model mismatch in the data due to non-idealities of the system as well as noise, Cadzow's method [275] works reasonably well and warrants future work.

7.7 Summary of Results

In this chapter, we have introduced a method to satisfactorily recover the intensities of superimposed echoes of light, using a customized ToF imaging sensor for acquisition and temporal phase retrieval for reconstruction. Up to our knowledge, this is the first method that performs time-stampless sampling of a sparse ToF signal, in the sense that we only measure the amplitudes sampled at uniform instants without caring about the particular sampling times or sampling rates. This innovation can potentially lead to alternative hardware designs and mathematical simplicity as phases need not be estimated in hardware.

यो विश्वाभि विपश्यति भुवना सं च पश्यति ।
स नः पूषाविता भुवत ॥

तत सवितुर्वरेण्यं भर्गो देवस्य धीमहि ।
धियो यो नः परचोदयात ॥

देवस्य सवितुर्वयं वाजयन्तः पुरन्ध्या ।
भगस्य रातिमीमहे ॥

Gāyatrī mantra

— Rigveda (Mandala III, §62, ¶ 09–11)

8

Photo-acoustic Time-resolved Tomography

8.1 Introduction

Mathematical imaging in life sciences is the key to understanding biological features ranging from molecular to anatomical scales. While ultrasound imaging, MRI and computed tomography are well established imaging methods at the anatomical level, a number of challenges still remain at the microscopic level. Some attributes include penetration depth, spatial-temporal resolution as well as imaging contrast.

To this end, photoacoustic or PA imaging proves to be advantageous in many ways [278]. As the name suggests, the photoacoustic effect is the conversion or transformation of electromagnetic energy into acoustic energy—a phenomenon that was first observed by Alexander Graham Bell in 1880 [279]. Qualitatively speaking, the interaction of an optical excitation pulse with a material results in a rise in temperature. Although infinitesimal ($\sim$ milli kelvin [280]), the rise in temperature is enough to catalyze thermoelastic expansion resulting in stress waves that manifest as acoustic energy. Due to the fact that photoacoustic imaging utilizes a combination of light and sound in the process of imaging, disadvantages in one regime (for example, sound) can be compensated by the other. A concrete example is that of biological tissues. Tissues are known to scatter light but this is orders of magnitude lesser in the case of sound. Therefore, photoacoustic imaging offers greater penetration depth [278].

Due to the numerous advantages centric to the PA imaging technology [281, 280], within the the last decade, there has been a surge of research interest in this area. This includes development of efficient instrumentation as well as mathematical algorithms for solving inverse problems. For a detailed overview of the topic, we refer to [282].

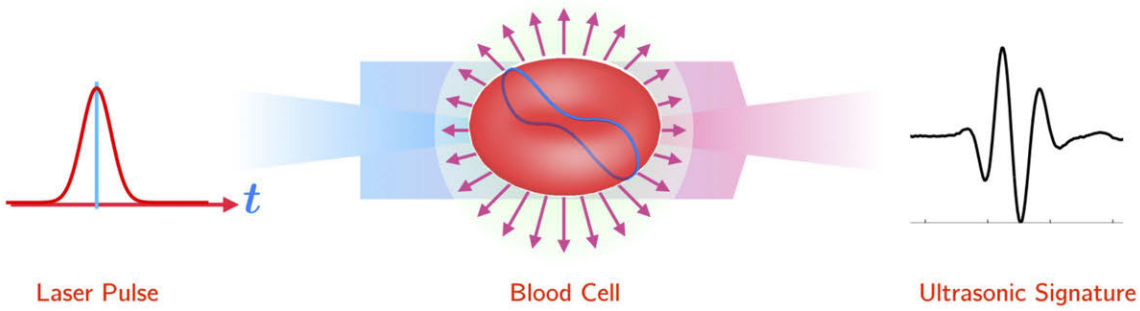

Figure 8-1: Conceptual explanation of the *photoacoustic effect* which is the conversion or transformation of electromagnetic energy into acoustic energy. This phenomenon that was first observed by Alexander Graham Bell in 1880 [279]. In this example, a pulse of light excited a cell which in turn releases acoustic energy. The *ultrasonic* acoustic signature was acquired experimentally.

As pointed out in [283], the shape of the PA wave encodes important information linked with physical parameters such as dimensions, sound speed and density. By capitalizing on this aspect of PA imaging, recently, Strohm and Kolios [284] developed a label–free technique for classification of cell types: red blood cells (RBC), white blood cells (WBC) and circulating melanoma cells (CMC). This one of a kind imaging modality was the first demonstration of a setup capable of,

- identification of cells,
- estimation of the cell size

Thus leading to a classification algorithm that can distinguish cancer cells from their healthy counterparts, besides understanding cell morphology [285].

The approach discussed in [284] is based on the *spectral periodicity* of the measured data. By computing the power spectrum of the measurements, the authors argue that cell parameters are related to spectral features such as the inter-spacing between two consecutive minima. This heuristic approach works whenever the spectral features are distinctly visible. However, this may not always hold.

Let us begin with a discussion on the mathematical intuition behind the visibility of spectral features. Consider the case of RBCs which have a biconcave shape. This is shown in Fig. 8-2 (also check Fig. 8-5 for clarity) where we overlay the biconcave cross-section in blue ink and the approximate time spread (similar to full width at half maximum) in red ink. When a pulse or a wave propagates in the horizontal configuration (cf. Fig. 8-5, $\theta = 0$), it is reflected by the cell walls. The resulting PA pulse echo measurement has minimal spread in time-domain as the pulse propagates through the center of the RBC—the point of minimum thickness[1]. On the other hand, in the vertical configuration, the PA pulse echo measurement has a larger spread in time-domain as the pulse propagates through the diameter[2] of the cell.

As an example, assume that two dominant reflections of equal intensity occur in any possible configuration. Much in the same way as time-of-flight or ToF imaging [66], we may model the reflectors or

[1]This corresponds to a physical distance of 0.8–1.0 μm.
[2]This corresponds to a physical distance of 6.2–8.2 μm.

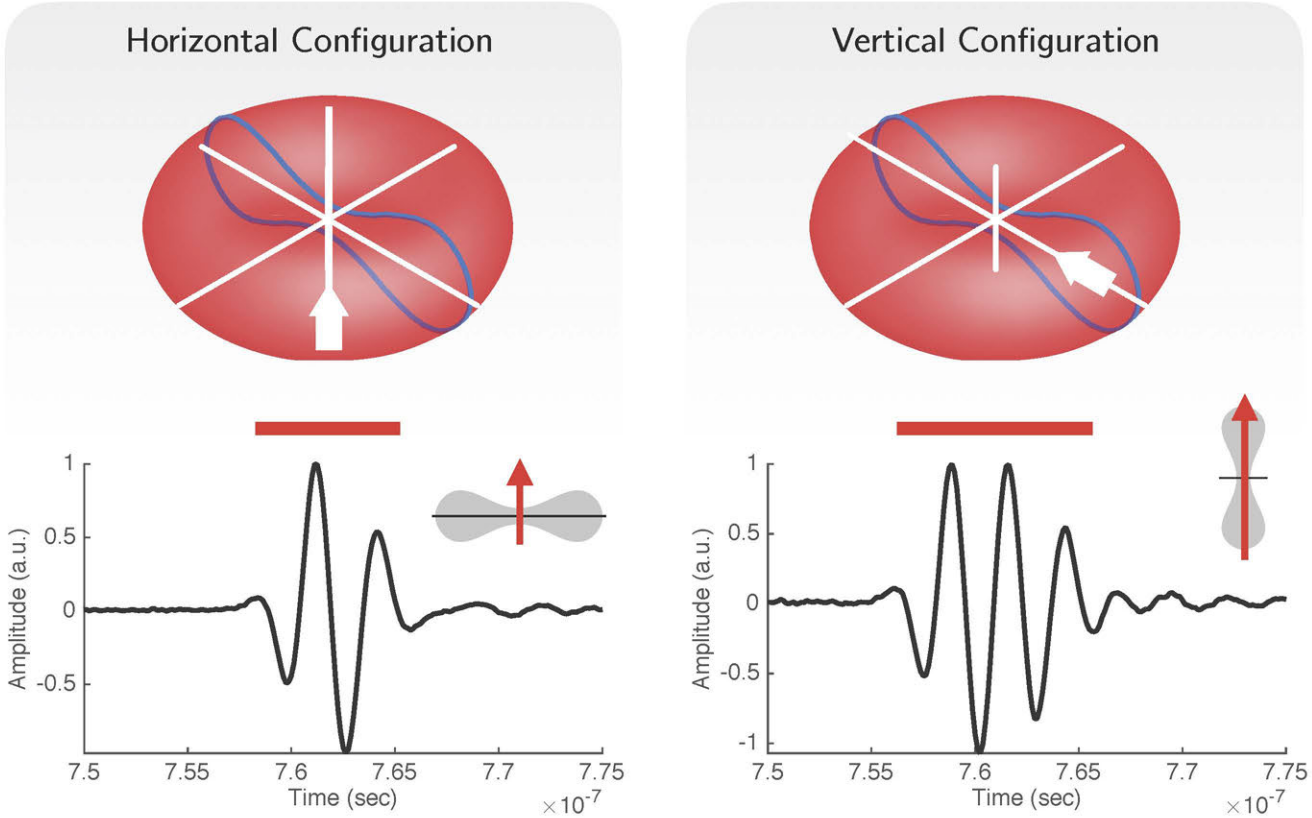

Figure 8-2: Photoacoustic measurements of single RBC. The cross-section of the biconcave RBC is shown in blue ink. The arrow shows the direction of wave/pulse propagation. (a) Horizontal configuration with minimal spread in time-domain. (b) Vertical configuration with a larger spread in time-domain. The red bars mark the approximate time-spread of the pulses. Also see Fig. 8-5.

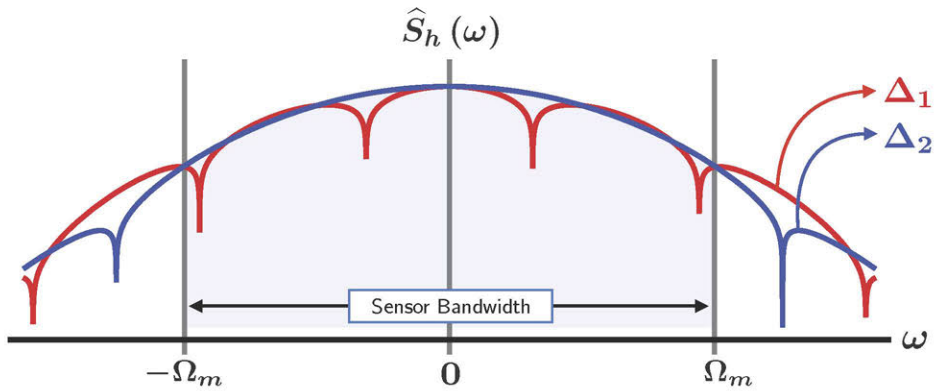

Figure 8-3: Power spectrum of low-pass measurements: $\widehat{B}_h(\omega) = \widehat{S}_h(\omega)\, b(\omega)$ where $b(\omega)$ is the frequency response of the low-pass measurement device. With $\Delta_2 < \Delta_1$, no spectral minima occur in the bandwidth $\omega \in [-\Omega_m, \Omega_m]$.

---

sources as,

$$h(t) = \delta\left(t - \frac{d_1}{\nu}\right) + \delta\left(t - \frac{d_2}{\nu}\right)$$

where $d_k, k = 1, 2$ are the relative locations of the reflectors from the sensor, ν is the propagation speed and δ denotes the Dirac distribution. Let $\Delta = |d_2 - d_1|$ be the separation between the cell walls and $\widehat{h}(\omega) = \int h(t)\, e^{-\jmath\omega t} dt$ denote the Fourier transform of h. Then, the power spectrum of h denoted by $\widehat{S}_h$ is given by,

$$\widehat{S}_h(\omega) \stackrel{\text{def}}{=} |\widehat{h}(\omega)|^2 = 4\cos^2\left(\frac{\omega\Delta}{2\nu}\right).$$

Since most physical devices have a finite bandwidth, observations are written as $\widehat{B}_h(\omega) = \widehat{S}_h(\omega)\, b(\omega)$ with $b(\omega) = 0, |\omega| > \Omega_m$. As the inter-spacing Δ between the cell walls decreases, it is very likely that none of the spectral minima are visible within the bandwidth. This is shown in Fig. 8-3 where $\Delta_2 < \Delta_1$ and $b(\omega)$ is chosen to be a Gaussian window. This approach is similar to cepstral analysis used in acoustic microscopy (cf. pg. 157, [286]). Clinical and pre-clinical systems typically have a bandwidth $\Omega_m < 60$ MHz and lack the sensitivity to detect signals from single cells. UHF transducers used for single cell imaging have 200–500 MHz bandwidth [287, 284]. However, observing all cellular features ranging 5–30 μm requires bandwidths in the GHz range [287]. Our simple mathematical reasoning justifies the bottleneck quoted in [284] (cf. pg. 744):

> It was not possible to calculate the RBC size, as the spectral fitting method is highly sensitive to the orientation of the RBC relative to the transducer, and the orientation could not be determined in these measurements.

Can we do better than this? Overcoming this computational drawback has important consequences in,

1. cell counting and classification [284] specially in the context of circulating tumor cells and cancer related diagnosis, and

2. understanding cell morphology [285].

The main goal of this chapter is to formalize the inverse problem of accurate estimation of cell parameters from the PA measurements which allows us to recover cell parameters (not limited to RBCs) from PA measurements. Starting with the wave equations of PA imaging, we reformulate the inverse problem as a time-of-flight or ToF estimation problem [66, 21] whereby estimating cell parameters amounts to temporal super-resolution given a finite set of trigonometric moments.

In Section 8.2, we develop the PA wave equation solution for cellular ToF imaging problem. We discuss the solution to the inverse problem of ToF estimation in Section 8.3. In Section 8.4, we validate our approach with PA measurements based on RBCs and CMCs. Finally we conclude in Section 8.5.

8.2 Problem Setup: Photoacoustic ToF Imaging

8.2.1 ToF Imaging Pipeline

The main components of any ToF imaging [66] modality are the probing function, $p(t)$, the scene response function (SRF), $h(t,\tau)$ and the instrument response function (IRF), $\varphi(\tau,t)$.

Said simply, the probing function "probes" the scene. This may be a pulse or a continuous wave function, such as a sinusoid [65]. The interaction between the probing function and the SRF results in the reflected signal (equivalent to PA wave generated signal in PA imaging),

$$r(t) = \int p(\tau)\, h(t,\tau)\, d\tau. \tag{8.1}$$

For example, in ranging or time-delay estimation problems, $h(t,\tau) = \Gamma_0 \delta(t-\tau-t_0)$ where Γ_0 is the intensity of an object at a distance d_0 which results in delay $t_0 = 2d_0/\nu$. In this case, $r(t) = \Gamma_0 p(t-t_0)$. Alternatively, the SRF may arise from a Green's function linked with a physical system, for example, fluorescence lifetime [21].

The reflected signal $r(t)$ then interacts with the sensor equipped with some instrument response function (IRF) and the measurements are recorded in the form,

$$m(t) = \int r(\tau)\, \underbrace{\varphi(t,\tau)}_{\text{IRF}}\, d\tau \tag{8.2}$$

where φ may be the point spread function of a lens (spatial context) or the temporal response of a transducer, for example, the ultrasound detector in the case of PA imaging. Typically, m is sampled $m_k = m(kT), k \in \mathbb{Z}$ where $T > 0$ is the sampling rate. Furthermore, whenever h and φ are shift-invariant, that is, $h(t,\tau) = h(t-\tau)$, the measurements simplify to a convolution/filtering equation,

$$m(t) = (p * h * \varphi)(t). \tag{8.3}$$

Next, we will discuss the probing function, the SRF and the IRF that stem from the PA imaging problem.

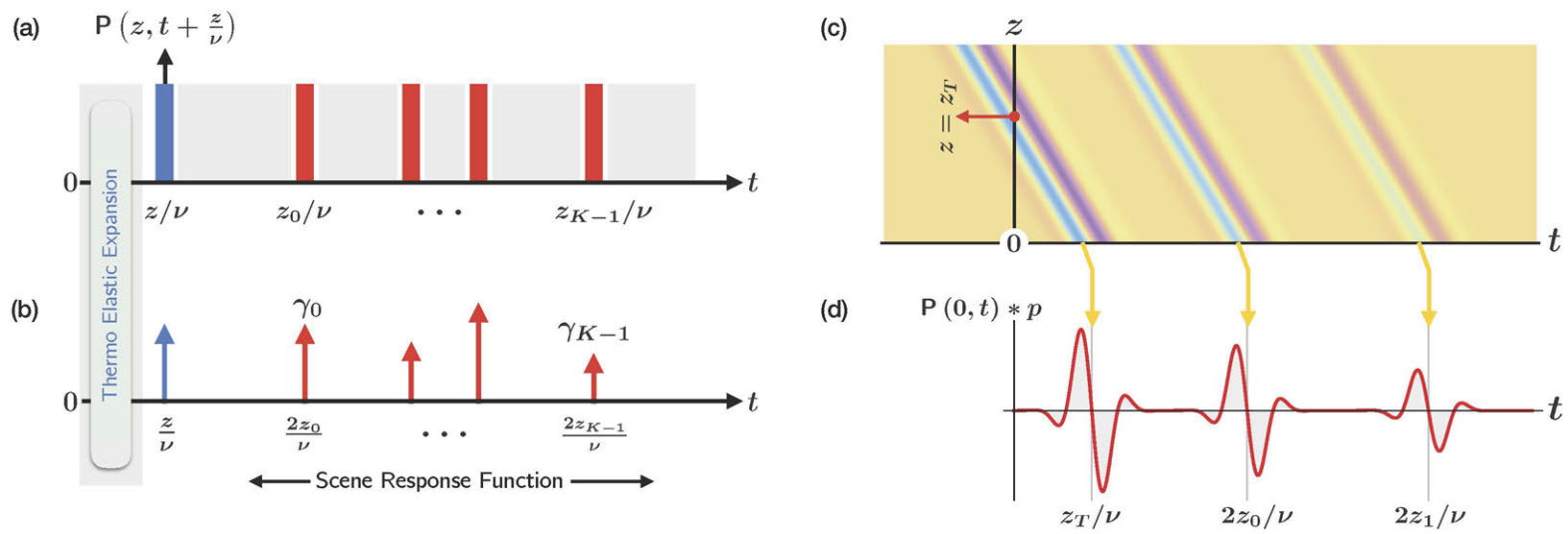

Figure 8-4: Photoacoustic waves in layered media. All figures should be understood in sense of negative time. (a) Geometrical setup with K reflecting boundaries or layers. The first reflective surface marked in blue is virtual. Optical excitation causes thermo elastic expansion resulting in sound waves and $t = z/\nu$ is the instant at which sound waves travel to the source. There on, sound waves are reflected from each layer at $t = z_k/\nu$. (b) Corresponding scene respond function. Here, each reflecting boundary results in a round trip travel time of $t_k = 2z_k/\nu$. (c) We plot the propagating wave, $\mathsf{P}(z, t)$ in the case of optical excitation $\mathsf{H}(z, t) = \delta(z - z_T)\, p(t)$, where the probing function $p(t)$ is chosen to be a Gabor pulse. (d) Time-domain waves reflected towards the source at $z = 0$.

8.2.2 From PA Wave Equations to Time-of-Flight

We use capitalized symbols $\mathsf{P}, \mathsf{T}, \mathsf{H}$ to denote the spatio-temporal functions with arguments $\vec{r} = (x, y, z)^\top$ (spatial co-ordinates) and t (time), that is, $\mathsf{P}(\vec{r}, t)$, and so on. The PA effect is explained by coupled differential equations based on temperature T and pressure P [288],

$$\begin{cases} \frac{\partial}{\partial t}(\mathsf{T} - \kappa_1 \mathsf{P}) = \kappa_2 \nabla^2 \mathsf{T} + \kappa_3 \mathsf{H} \\ \Box_\nu \mathsf{P} = \kappa_4 \partial_t^2 \mathsf{T} \end{cases}$$

where

— $\nabla^2(\cdot)$ is the Laplace operator and,

$$\Box_\nu = \nabla^2 - \nu^{-2}\partial_t^2$$

is the d'Alembert operator and ν is the speed of sound in given medium.

— $\{\kappa_m\}_{m=1}^4$ are some physical constants (for details, we refer to [282]).

— $\mathsf{H}(\vec{r}, t)$ is the heat or thermal energy attributed to the electromagnetc or EM radiation of the optical excitation pulse.

— $\mathsf{P}(\vec{r}, t)$ is the resultant acoustic pressure wave.

In practice, it is justifiable that the thermal conductivity is zero and the P–T coupled differential equations reduce to (cf. pg. 4 in [282]),

$$\Box \mathsf{P} \equiv \left(\nabla^2 - \frac{1}{\nu^2}\partial_t^2\right)\mathsf{P} = -\kappa \partial_t \mathsf{H}. \tag{8.4}$$

In the case of one-dimensional propagation, $\vec{r} = (0, 0, z)^\top$, the above admits a simple solution based on the integral equation,

$$\mathsf{P}(z, t) = \frac{\kappa\nu}{2}\int \mathsf{H}\left(r, t - \frac{z - r}{\nu}\right) dr.$$

Consider an instantaneous source $\mathsf{H}(z, t) = \delta(t)\,\delta(z)$ and a reflective surface at $z = z_0 > 0$. In that case [289],

$$\mathsf{P}(z, t) = \underbrace{\delta\left(t - \frac{z}{\nu}\right)}_{\text{(a)}} + \underbrace{\delta\left(t - \frac{z + 2z_0}{\nu}\right)}_{\text{(b)}}, \tag{8.5}$$

where,

(a) arises from the direct excitation of energy which is delayed by the travel time of sound, and,

(b) (b) is the travel time between the source and the reflective surface (cf. Fig. 8-4(a)).

Furthermore, if we consider $\mathsf{H}(z, t) = p(t)\,\delta(z)$ where p is temporal probing function, we obtain a convolution between $\mathsf{P}(z, t)$ and p, ignoring a constant dilation $\propto \nu$. This is consistent with the experiments in layered media (cf. Fig. 4, [290]) as well as the convolution equations in acoustic microscopy (cf. pg. 152,[286]). In general, for the case of K reflecting boundaries at $z = z_k$ with reflection coefficient

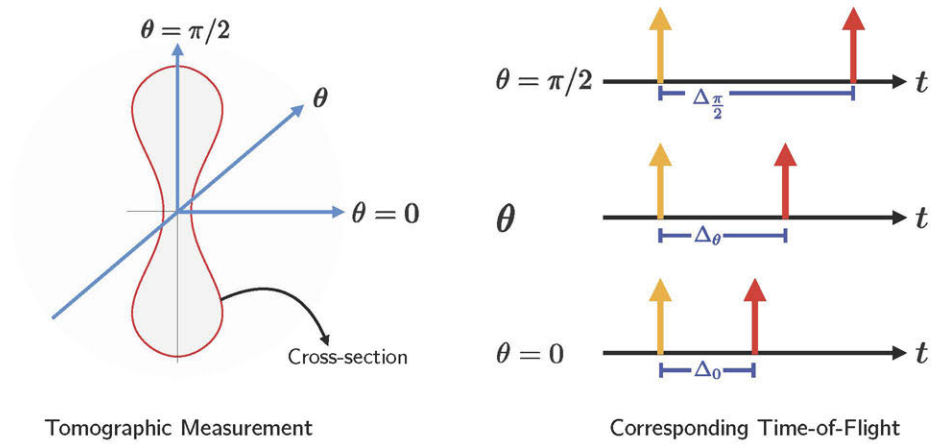

Figure 8-5: Tomography of RBCs. At each θ, reflections from the cell walls (layered media) result in a distinct time-of-flight, $\Delta_\theta = |z_1 - z_0|$. Note that Δ_θ encodes the geometric properties of the enclosure which may be RBC, WBC or CMC.

γ_k, we have,

$$h(t,\tau) \equiv \mathsf{P}(z, t-\tau) = \sum_{k=0}^{K-1} \gamma_k \delta\left(t - \tau - \tfrac{z+2z_k}{\nu}\right), \tag{8.6}$$

which also serves as our SRF for the PA imaging context. In Fig. 8-4(b) we plot the SRF corresponding to the general case of K reflective surfaces. With $K = 2$ and optical excitation of the form,

$$\mathsf{H}(z,t) = \delta(z - z_0)\, p(t)$$

we plot the pressure wave $\mathsf{P}(z,t)$ in Fig. 8-4(c) and the corresponding time-domain waveform at $z = 0$ in Fig. 8-4(d).

Typically, the incoming pressure wave is sensed through an ultrasound transducer with some IRF, φ. Furthermore, by ignoring the constant offset of z_T/ν due to virtual source (or the delayed sound wave), we model the measurements as,

$$m(t) = \left(p * \mathsf{P}\left(0, t + \tfrac{z}{\nu}\right) * \varphi\right)(t) = \sum_{k=0}^{K-1} \gamma_k \left(p * \varphi\right)\left(t - 2\tfrac{z_k}{\nu}\right). \tag{8.7}$$

8.2.3 Tomographic Measurements for Geometric Estimation

Blood cells have distinct geometrical features based on their shape, size and morphology. Here, we will focus on the RBCs. As shown in Fig. 8-5, tomographic measurements of the RBCs leads to a functional relationship between ToF and the orientation of the RBC. In Fig. 8-5, measurements at $\theta = 0$ are associated with the smallest possible ToF. This corresponds to the horizontal configuration in Fig. 8-2 where the experimentally obtained time-domain measurements are relatively concentrated when compared to

the vertical configuration, $\theta = \pi/2$. We may therefore write,

$$m_\theta(t) \overset{(8.7)}{=} \sum_{k=0}^{K-1} \gamma_k^{(\theta)} (p * \varphi) \left(t - t_k^{(\theta)}\right), \quad t_k^{(\theta)} \triangleq 2\frac{z_{k,\theta}}{\nu}. \tag{8.8}$$

Ideally, for the case of cell imaging, $K = 2$. Since RBCs are bi-concave, $\Delta_\theta = |t_1^{(\theta)} - t_0^{(\theta)}|$ is a proxy of its relative orientation with respect to the source. On the other hand WBCs are spherical and

$$\Delta_\theta = |t_1^{(\theta)} - t_0^{(\theta)}| \propto 2\rho$$

where ρ is the radius. As a result, $\{\theta, \Delta_\theta\}$ may be used to characterize the geometry of cells (in our case) and a layered enclosure, in general. In practice, one acquires measurements of the form,

$$m_{\theta_\ell}(nT), n = 0, \ldots, N-1, \ \left\{\theta_\ell = \tfrac{2\pi}{L}\ell\right\}_{\ell=0}^{L} \tag{8.9}$$

and the inverse problem is to recover $\{\gamma_k^{(\theta)}, t_k^{(\theta)}\}_{k=0}^{K-1}$ from which Δ_θ may be estimated. In this work, we will restrict ourselves to $K = 2$.

8.3 Inverse Problem: Estimating Time-of-Flight

In order to recover unknowns $\{\gamma_k^{(\theta)}, t_k^{(\theta)}\}_{k=0}^{K-1}$ from (8.9), we will begin with writing $p * \varphi = \phi$ in (8.8). Furthermore, we will *approximate* ϕ with trigonometric moments [291, 292, 66], $u_m(\omega_0 t) \triangleq e^{\jmath m \omega_0 t}$,

$$\phi(t) \approx \widetilde{\phi}(t) = \sum_{|m| \leqslant M} b_m u_m(\omega_0 t), \tag{8.10}$$

where b_m's are Fourier series coefficients and $\omega_0 = 2\pi/NT$, assuming that $T_0 = NT$ is large enough that all the K reflections are observed. This is typically the case in almost all pulse-echo ToF systems [66, 21]. Here, $\omega_0 M \approx \Omega_m$ and M is a function of the transducer bandwidth. By substituting the approximation of ϕ in (8.8), we obtain,

$$m_\theta(t) = \sum_{|m| \leqslant M} b_m \sum_{k=0}^{K-1} \gamma_k^{(\theta)} u_m(\omega_0 t - \omega_0 t_k^{(\theta)}),$$

and since u_m is separable, $u_m(f+g) = u_m(f)\, u_m(g)$, we have,

$$\begin{aligned} m_\theta(t) &= \sum_{|m| \leqslant M} b_m u_m(\omega_0 t) \underbrace{\sum_{k=0}^{K-1} \gamma_k^{(\theta)} u_m^*\left(\omega_0 t_k^{(\theta)}\right)}_{s_m^{(\theta)}} \\ &= \sum_{|m| \leqslant M} b_m \widehat{h}_m^{(\theta)} u_m(\omega_0 t) \end{aligned}$$

where,

$$\widehat{h}_m^{(\theta)} = \sum_{k=0}^{K-1} \gamma_k^{(\theta)} u_m^* \left(\omega_0 t_k^{(\theta)}\right), \quad m = -M, \ldots, M \tag{8.11}$$

are the Fourier series coefficients of the sparse SRF denoted by $h_\theta(t) = \sum_{k=0}^{K-1} \gamma_k^{(\theta)} \delta(t - t_k^{(\theta)})$. The above, (8.11), is the standard form of equation that shows up in context of spike deconvolution [291], time-delay estimation[55] and sampling theory[69]. Given sampled measurements in (8.9), we stack them in vector–matrix form,

$$\mathbf{m}_{\boldsymbol{\theta}} = \mathbf{U}\mathbf{D}_b \widehat{\mathbf{h}}^{(\boldsymbol{\theta})} \tag{8.12}$$

where,

- $\mathbf{m}_{\boldsymbol{\theta}} \in \mathbb{R}^N$ is a vector of measured data (cf. Fig. 8-2).
- $\mathbf{U} \in \mathbb{C}^{N \times (2M+1)}$ is a DFT matrix with elements $\left[e^{jm\omega_0 nT}\right]_{n,m}$.
- $\mathbf{D}_b \in \mathbb{C}^{(2M+1 \times 2M+1)}$ is a diagonal matrix with diagonal elements $b_{m,m} = \widehat{\phi}(m\omega_0)$.
- $\widehat{\mathbf{h}}^{(\boldsymbol{\theta})} \in \mathbb{C}^{2M+1}$ is a vector whose elements are the Fourier transform of the SRF (cf. (8.11)).

Since (8.12) is a linear system of equations, we can estimate $\widehat{\mathbf{h}}^{(\boldsymbol{\theta})}$ directly provided that $\{b_m\}_m$ are known. With $\widehat{\mathbf{h}}^{(\boldsymbol{\theta})}$ known, we will use trigonometric interpolation [67, 291, 69] to estimate the unknowns $\{\gamma_0^{(\theta)}, \gamma_1^{(\theta)}, t_0^{(\theta)}, t_1^{(\theta)}\}$. While trigonometric interpolation works for finite K, for the specific case hand, $K = 2$, we outline a closed form solution (assuming noiseless setting). For this purpose, let us define, $\mu_k^m \stackrel{\text{def}}{=} u_1^*(\omega_0 t_k^{(\theta)})$ and hence, we have, $\widehat{h}_m^{(\theta)} = \mu_0^m + \mu_1^m$, resulting in,

$$\begin{cases} \hat{h}_0^{(\theta)} = \gamma_0^{(\theta)} + \gamma_1^{(\theta)} \\ \hat{h}_1^{(\theta)} = \gamma_0^{(\theta)}\mu_0 + \gamma_1^{(\theta)}\mu_1 \\ \hat{h}_2^{(\theta)} = \gamma_0^{(\theta)}\mu_0^2 + \gamma_1^{(\theta)}\mu_1^2 \\ \hat{h}_3^{(\theta)} = \gamma_0^{(\theta)}\mu_0^3 + \gamma_1^{(\theta)}\mu_1^3 \end{cases}.$$

Let $\mathcal{Q}(x) = (x - \mu_0)(x - \mu_1) = x^2 + \lambda_1 x + \lambda_0$ be some quadratic polynomial. It follows that, $\mathcal{Q}(\mu_k) = 0 = \mu_k^2 + \lambda_1\mu_k + \lambda_0$, $k = 0, 1$. Based on this, we can write,

$$\underbrace{\mathcal{Q}(\mu_0) = \mathcal{Q}(\mu_1)}_{=0} \Leftrightarrow \begin{cases} \gamma_0^{(\theta)}\mathcal{Q}(\mu_0) + \gamma_1^{(\theta)}\mathcal{Q}(\mu_1) = 0 \\ \gamma_0^{(\theta)}\mu_0\mathcal{Q}(\mu_0) + \gamma_1^{(\theta)}\mu_1\mathcal{Q}(\mu_1) = 0 \end{cases}$$

which is equivalent to solving the linear system of equations,

$$\begin{bmatrix} \widehat{h}_0^{(\theta)} & \widehat{h}_1^{(\theta)} \\ \widehat{h}_1^{(\theta)} & \widehat{h}_2^{(\theta)} \end{bmatrix} \begin{bmatrix} \lambda_0 \\ \lambda_1 \end{bmatrix} = - \begin{bmatrix} \widehat{h}_2^{(\theta)} \\ \widehat{h}_3^{(\theta)} \end{bmatrix}. \tag{8.13}$$

Hence, at a fixed θ and noiseless conditions, four values of $\widehat{h}_m^{(\theta)}$ suffice to compute the four unknowns. This is accomplished by implementing the algorithm outlined in Algorithm 4. Next, we experimentally validate our approach and discuss practical aspects of our implementation.

Algorithm 4: Photoacoustic Time-of-Flight Estimation

Data: Measurements $m_\theta(nT)$ in (8.9) with $N \geq 2M+1$ with $M \geq 2$.

Result: Cell Parameters: $\{\gamma_0^{(\theta)}, \gamma_1^{(\theta)}, t_0^{(\theta)}, t_1^{(\theta)}\}$ and $\Delta_\theta = |t_1^{(\theta)} - t_0^{(\theta)}|$.

1) Estimate $\widehat{\mathbf{h}}^{(\boldsymbol{\theta})} = \mathbf{U}^+\mathbf{D}_b^+\mathbf{m}_{\boldsymbol{\theta}}$ (8.12) where $^+$ is the matrix psuedo inverse.
2) Given $\widehat{\mathbf{h}}^{(\boldsymbol{\theta})}$, estimate $\{\widetilde{\lambda}_0, \widetilde{\lambda}_1\}$ using (8.13).
3) With $\{\widetilde{\lambda}_0, \widetilde{\lambda}_1\}$ known, solve for $\mathcal{Q}(x) = 0 \rightarrow \{\widetilde{\mu}_0, \widetilde{\mu}_1\}$ and hence, the time-of-flight $\widetilde{t}_k^{(\theta)} = -\angle\widetilde{\mu}_k/\omega_0$.
4) The estimates $\{\widetilde{\gamma}_0^{(\theta)}, \widetilde{\gamma}_1^{(\theta)}\}$ are obtained using least-squares solution,

$$\underset{\{\gamma_0^{(\theta)},\gamma_1^{(\theta)}\}}{\arg\min} \sum\nolimits_n \left| m(nT) - \gamma_0^{(\theta)}\widetilde{\phi}(nT - \widetilde{t}_0^{(\theta)}) - \gamma_1^{(\theta)}\widetilde{\phi}(nT - \widetilde{t}_1^{(\theta)}) \right|^2.$$

8.4 Photoacoustic ToF Imaging: Experimental Verification

Our proposed approach is validated via experiments using PA imaging setup and the data is acquired using the procedure described in [284].

8.4.1 ToF Estimation of RBCs

In the first case, we consider RBCs at four different orientations. For this purpose, PA measurements m_θ are acquired using the experiments in [284]. Conceptually, this is similar to tomography as shown in Fig. 8-6. As the RBC rotates from horizontal to vertical state, one should expect the ToF to increase (cf. Fig. 8-5). As highlighted in the literature [284], previously, this was not possible. Here we model ϕ as a Gabor pulse. While this choice is heuristic, in our experience, and as will be shown shortly, this achieves near exact performance (in context of the maximum likelihood estimation or the MLE). As an approximation to the transducer response, the bandpass pulse is chosen such that its maximum response is between 200 to 500 MHz [287, 285]. With ϕ in place, we use a finite Fourier series approximation which specifies $\{b_m\}$ in (8.10) and hence $\mathbf{D}_b$ [66, 21] with $M = 18$ and $f_0 = \omega_0/2\pi = 25.80$ MHz. To deal with model mismatch and noise in experimental data, we replace steps 1) and 2) in Algorithm 4 with Cadzow's method [275].

In Fig. 8-7(a), we plot $\{m_{\theta_\ell}(nT)\}_{\ell,n}$ (cf. (8.9)) with $T = 0.125$ ns, $N = 311$ and $\theta = 0$ to $\pi/2$ (approximately) in 108 steps, which we call, time-resolved *pixel*. For each of the four orientations, the PA signal or the time-resolved pixel is plotted in Fig. 8-7 (a_1) to (a_4). The estimated locations of layers or cell walls, that is $\{\gamma_k^{(\theta)}, t_k^{(\theta)}\}_{k=0,1}$ are also marked. Since this is the case of $K = 2$, it is possible to compare our results with exhaustive search or MLE. Hence we also compute the MLE estimates, $\{\gamma_k^{(\theta)}, t_k^{(\theta)}\}_{k=0,1}$. We use peak signal-to-noise ratio or PSNR denoted by η as our performance metric. The results are summarized in Table 8.1.

where η_{PSR} is the PSNR due to PA–ToF super-resolution and η_{MLE} is due to the MLE and we use $\nu = 1570$ m/s. Since we rely on optical microscopy (cf. Fig. 8-6) for estimating orientation angle θ, the registration between θ and $m_\theta(t)$ is challenging. However, near exact performance in context of MLE

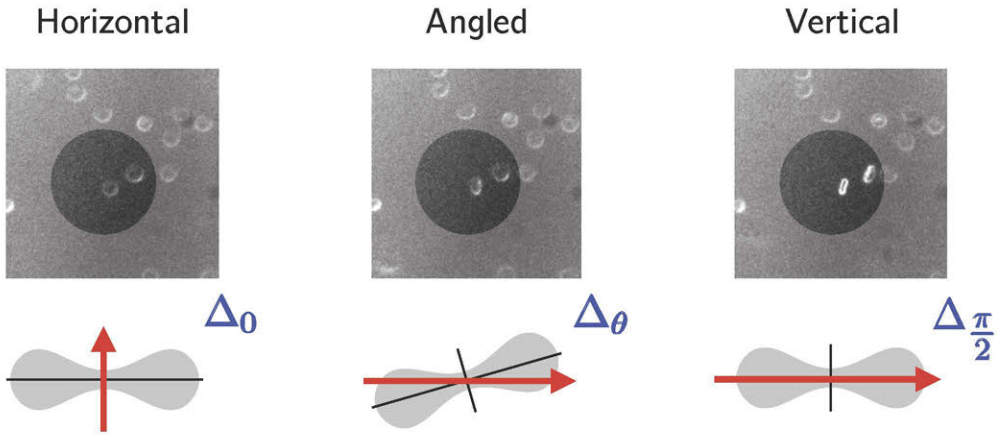

Figure 8-6: Optical images of RBCs at various orientations ranging from horizontal to vertical. Optical images are used to register with corresponding PA measurements.

Table 8.1: Estimates of Cell Size

	θ_1	θ_1	θ_1	θ_1	units
η_{MLE}	32.97	31.05	35.88	35.89	dB
η_{PSR}	32.97	31.05	34.61	35.88	db
Size/ToF	5.780	5.300	3.820	1.960	μm

suggests that the PA–ToF can recover a proxy of the orientation which can be used to discern features. To exemplify this point, we move to the next case.

8.4.2 ToF Estimation of Melanoma Cells

In Fig. 8-7(b), we plot PA measurements for CMCs. With $K = 4$, we super-resolve measurements and plot $\{\gamma_k^{(\theta)}, t_k^{(\theta)}\}_{k=0,3}$. The reconstruction accuracy is $\eta_{\mathsf{PSR}} = 33.07$ db. We note that $|\gamma_0^{(\theta)}|$ and $|\gamma_2^{(\theta)}|$ correspond to the dominant reflections. Based on this, we compute the ToF which is $\Delta = 10.75$ ns. The corresponding cell size is $\Delta\nu = 16.87$ μm. This is consistent with the results in [287]. Clearly, the estimated cell size is the distinct feature which distinguishes CMCs from RBCs.

8.5 Summary

Starting with a forward model for the photoacoustic phenomenon, we compare the measurements of blood cells to a sum of overlapping echoes. Instead of using the exact physical model, we approximate the measurements with an empirical pulse that confirms with physical characteristics of our measurement device. We represent such pulses with a finite number of trigonometric moments. Based on this approximate representation, we use trigonometric interpolation for time-of-flight super-resolution. Experimentally acquired tomographic measurements validate our model. While this study is in a preliminary stage, it offers a compelling solution to a bottleneck in photoacoustic imaging. Our work raises several questions in the direction of classification of cellular features and this will be addressed in our future studies.

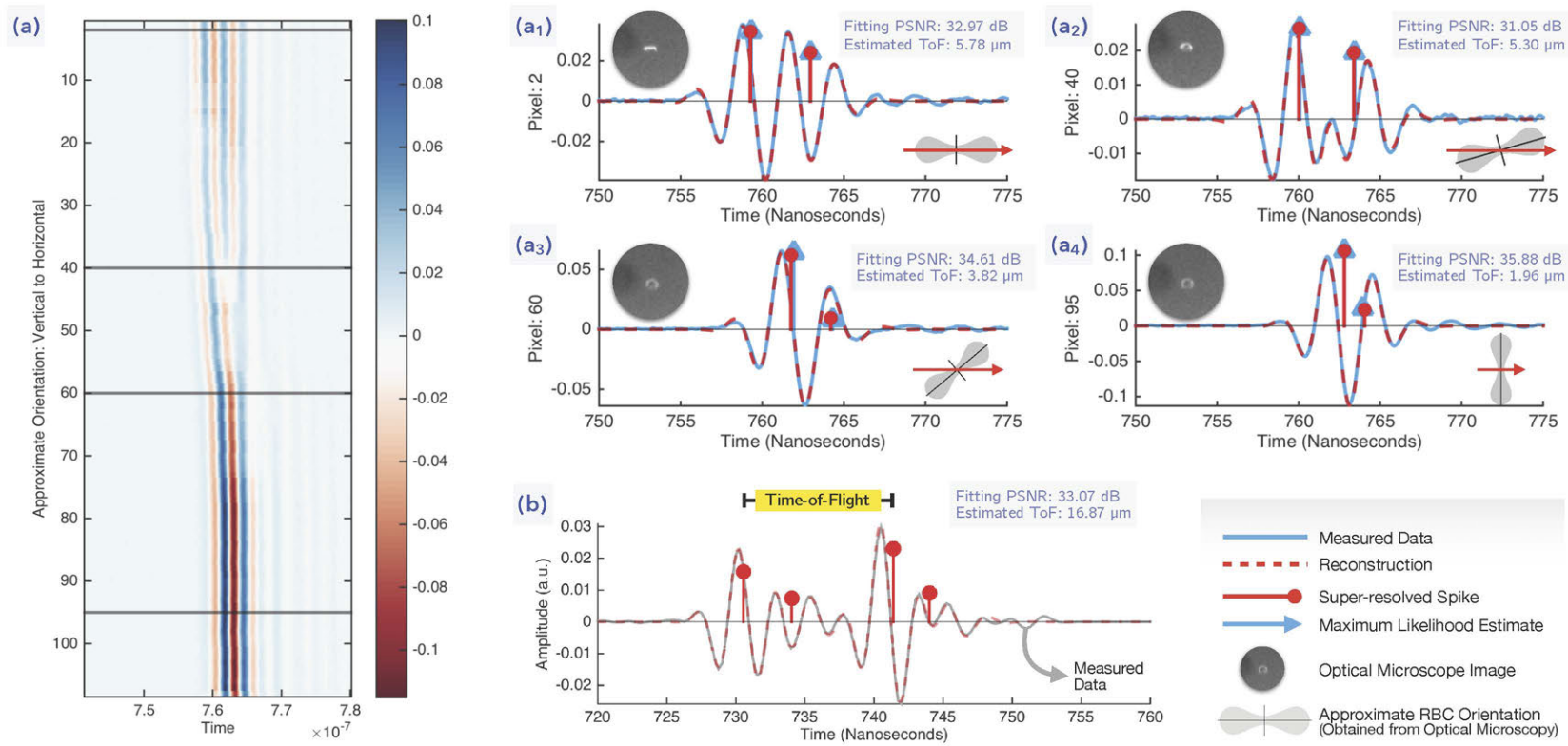

Figure 8-7: (a) Photoacoustic measurements $\{m_{\theta_\ell}(nT)\}_{\ell,n}$ with $T = 0.125$ ns, $N = 311$ and θ_ℓ ranging from vertical to horizontal orientation in 108 steps. (a_1) to (a_4) We plot PA measurements for four orientations. In the inset, we plot the optical image of the single cell RBC together with an approximate orientation angle. The measured data in blue ink (——). Super–resolved SRF specified by $\{|\gamma_k^{(\theta)}|, t_k^{(\theta)}\}_{k=0,1}$ in (8.6) and (8.8) is marked in red ink (—•). Based on the estimates $\{|\widetilde{\gamma}_k^{(\theta)}|, \widetilde{t}_k^{(\theta)}\}_{k=0,1}$, the reconstructed data $\widetilde{m}_\theta$ (8.8) is plotted in red ink (- - -). Reconstruction quality metric, the PSNR and the ToF are also annotated in the inset. Finally, we show the result of maximum likelihood estimation (exhaustive search) with blue spikes (—▶). (b) PA measurements of melanoma cells (CTC). We show the data in gray ink (——). Super–resolved SRF, $\{|\gamma_k^{(\theta)}|, t_k^{(\theta)}\}_{k=0,3}$ is marked in red ink (—•) and the reconstructed data is plotted in red ink (- - -).

Conclusions and Future Directions

नासदासीन नो सदासीत तदानीं नासीद् रजो नो वयोमापरो यत ।
किमावरीवः कुह कस्य शर्मन्नम्भः किमासीद् गहनं गभीरम ॥

न मर्त्युरासीदम्रतं न तर्हि न रात्र्या अह्न आसीत्प्रकेतः ।
आनीदवातं सवधया तदेकं तस्माद्धान्यन न परः किं चनास ॥

तम आसीत तमसा गूळमग्रे.अप्रकेतं सलिलं सर्वमिादम ।
तुछ्येनाभ्वपिहितं यदासीत तपसस्तन्महिनाजायतैकम ॥

कामस्तदग्रे समवर्तताधि मनसो रेतः परथमं यदासीत ।
सतो बन्धुमसति निरविन्दन हृदि परतीष्याकवयो मनीषा ॥

Nāsadīyasūkta
"The nonexistent did not exist, nor did the existent exist at that time. Death did not exist nor deathlessness then. There existed no sign of night nor of day.
Darkness existed, hidden by darkness, in the beginning. All this was a signless ocean... " [1]

— Rigveda (Mandala X, §29, ¶ 01–04)

9 Conclusion

This thesis is a confluence of harmonic analysis and time-resolved imaging which is based on the time-of-flight principle.

On the theory front, there are several theoretical directions for future research. We list a few key ideas:

- How can modulo operations be combined with sampling theory linked with special affine Fourier transforms?
- Within the unlimited sensing framework, how does noise and quantization affect the reconstruction quality? We anticipate some interesting results in the context of rate-distortion theory.
- Empirically, we have observed that the sampling bounds for unlimited sensing are quite aggressive and this warrants interesting future work.
- In context of linear inverse problems, how can the unlimited sensing framework be extended to a general class of inverse problems? For example, sparse recovery or compressed sensing and phase retrieval.

In context of time-resolved sensing and imaging, several directions remain unexplored.

ToF Imaging Pipeline We started with an image formation model that allows for studying different ToF modalities under one common framework. Almost all ToF systems can be characterized by the model parameters $\{p, h, \varphi\}$. Depending on the problem at hand, the role of $\{p, h, \varphi\}$ and the associated algorithms needs to be adapted. For example, the SRF discussed in context of MPI appears naturally in other problems such as ultrasound tomography and light detection and ranging

(LiDAR). However, the probing function and the IRF are very different for each case. In particular, consider the case of LiDAR. The probing function is modeled as $p = \delta$ and the IRF is a parametric function of form $\varphi(t) = \alpha e^{(a_k - T_0)t + b_k}$ where $\{a_k, b_k\}_{k=1}^4$ take 4 different values with continuous transitions, depending whether $t \in \{I_k\}_{k=1}^4$, where I_k is an instrument or sensor dependent quantity. This gives rise to a new form of sampling kernel $\phi = \varphi$, as opposed to $\phi = p * \overline{p}$ (TD–ToF case). Hence, we believe that by systematically studying the role of $\{p, h, \varphi\}$ across various ToF problems—optical and non–optical—better insights may developed.

Another interesting direction may be to consider the case when the SRF is modeled by a differential equation. For example, in case of fluorescence lifetime imaging, the associated differential equation is $\mathcal{L}_\lambda = \partial_t + (1/\lambda)$ and the resulting reflected signal is the solution to $\Gamma \mathcal{L}_\lambda [r(t)] = p(t), t \geqslant 0$. The SRF in this case is the Green's function. Similar ideas may be used to develop algorithms for imaging through scattering/diffusive media where $\mathcal{L}$ is some differential equation that models diffusion. The parameters of $\mathcal{L}$ encode physical properties such as lifetime or scattering coefficient.

Probing Function Since the probing function is the only available degree-of-freedom in ToF imaging pipeline, it is important to understand what mathematical principles should be used for designing probing functions. Waveform design is a known art in radar and wireless communications. However, such options are rarely considered in optical ToF systems. Maximum length sequences for TD–ToF and sinusoids for the FD–ToF are the de facto examples. On the hand, it may not always be feasible to calibrate the probing function. In that case, it may be worthwhile to use blind deconvolution algorithms for image reconstruction.

Algorithms and Fundamental Limits In case of inverse problems related with time-resolved imaging (for example, multi-bounce imaging, non-line-of-sight imaging and even fluorescence lifetime imaging) fundamental limits remain to be explored.

Modeling Non-ideal Reflections In our experience, the SRF of form $\Gamma_k \delta(t - t_k)$ only approximately models a reflection. In a practical setting, $\Gamma_k \psi_k (t - t_k)$ may serve as a good starting point for modeling reflections. Here, ψ_k is a filter that models the interaction of the probing function with the material property or accounts for distortion, system non-linearities and dispersive media. In seismic engineering, terahertz spectroscopy and ultrasound systems, this behavior is much more pronounced as material properties play an important role when the probing function undergoes a reflection.

FD-ToF This is specifically interesting mode of operation since most consumer ToF systems are based on FD-ToF which uses phase estimation. In that case, if $\theta_\omega > 2\pi$, the depth estimates suffer with ambiguity or phase-wrapping problem. Previous solutions use co-prime frequencies, however, there is room for improvement. For example, in theory, phase is a linear function of frequency, $\theta_\omega = 2\omega d/c$. This is not the case in practice and leads to erroneous depth estimates with multiple frequency measurements. Hence, a desirable phase estimation algorithm should jointly correct for any distortions and phase-wrapping.

Calling

$$m(t, \omega) = \Gamma_0 \left(1 + \frac{p_0^2}{2} \cos(\omega t + \theta_\omega)\right),$$

θ_ω is estimated by sampling in time-domain, that is, $m_k = m(kT, \omega_0)$ given a fixed modulation frequency ω_0. Alternatively, one may use multi-frequency sampling using $m_k = m(t_0, k\omega_0)$ for estimation of θ_ω. This gives rise to a broader question of when can time-frequency sampling be

used, that, $m_{\ell,k} = m(\ell t_0, k\omega_0)$ in context of solving inverse-problems linked with ToF imaging. Specifically, when $\omega = t$ for depth imaging, the problem boils down to parameter estimation of chirp signals.

Sensor Design for Higher Modulation Frequencies Most consumer-grade ToF sensors are based on continuous wave probing functions. Currently, such sensors work with high fidelity up till modulation frequency of about 80 MHz. We believe that a lot of the interesting physical phenomenon may only be observed as higher frequencies. For example, higher modulation frequencies will certainly enhance depth resolution and MPI correction capabilities. In context of fluorescence lifetime imaging, shorter lifetimes may be resolved with higher modulation frequencies. Similarly, sub-surface scattering properties can be studies with streak tubes [10]. This hints that indeed higher modulation frequencies are the pathway to scattered imaging. Such examples motivate the necessity of hardware or computational imaging solutions that can over come the current technological limits.

Bibliography

[1] S. W. Jamison and J. P. B. (translators), *The Rigveda: The Earliest Religious Poetry Of India*. Oxford University Press (OUP), 2014, translated from Vedic Sanskrit.

[2] O. Cossairt, M. Gupta, and S. K. Nayar, "When does computational imaging improve performance?" *IEEE Transactions on Image Processing*, vol. 22, no. 2, pp. 447–458, 2013.

[3] R. Raskar, A. Agrawal, and J. Tumblin, "Coded exposure photography: motion deblurring using fluttered shutter," *ACM Transactions on Graphics (TOG)*, vol. 25, no. 3, pp. 795–804, 2006.

[4] S. S. Gorthi, D. Schaak, and E. Schonbrun, "Fluorescence imaging of flowing cells using a temporally coded excitation," *Optics express*, vol. 21, no. 4, pp. 5164–5170, 2013.

[5] P. E. Debevec and J. Malik, "Recovering high dynamic range radiance maps from photographs," in *ACM SIGGRAPH 2008*. ACM, 2008, p. 31.

[6] R. Ng, "Fourier slice photography," in *ACM Transactions on Graphics*, vol. 24, no. 3. ACM, 2005, pp. 735–744.

[7] A. Veeraraghavan, R. Raskar, A. Agrawal, A. Mohan, and J. Tumblin, "Dappled photography: Mask enhanced cameras for heterodyned light fields and coded aperture refocusing," *ACM Transactions on Graphics*, vol. 26, no. 3, p. 69, 2007.

[8] M. F. Duarte, M. A. Davenport, D. Takhar, J. N. Laska, T. Sun, K. E. Kelly, and R. G. Baraniuk, "Single-pixel imaging via compressive sampling," *IEEE Signal Processing Magazine*, vol. 25, no. 2, p. 83, 2008.

[9] G. Zheng, R. Horstmeyer, and C. Yang, "Wide-field, high-resolution fourier ptychographic microscopy," *Nature photonics*, vol. 7, no. 9, pp. 739–745, 2013.

[10] A. Velten, T. Willwacher, O. Gupta, A. Veeraraghavan, M. Bawendi, and R. Raskar, "Recovering three-dimensional shape around a corner using ultrafast time-of-flight imaging," *Nature Comm.*, vol. 3, p. 745, 2012.

[11] O. Katz, P. Heidmann, M. Fink, and S. Gigan, "Non-invasive single-shot imaging through scattering layers and around corners via speckle correlations," *Nature Photonics*, vol. 8, no. 10, pp. 784–790, 2014.

[12] M. Laurenzis, J. Klein, E. Bacher, and N. Metzger, "Multiple-return single-photon counting of light in flight and sensing of non-line-of-sight objects at shortwave infrared wavelengths," *Optics letters*, vol. 40, no. 20, pp. 4815–4818, 2015.

[13] G. Gariepy, N. Krstajić, R. Henderson, C. Li, R. R. Thomson, G. S. Buller, B. Heshmat, R. Raskar, J. Leach, and D. Faccio, "Single-photon sensitive light-in-flight imaging," *Nature Communications*, vol. 6, 2015.

[14] A. Kirmani, D. Venkatraman, D. Shin, A. Colaço, F. N. Wong, J. H. Shapiro, and V. K. Goyal, "First-photon imaging," *Science*, vol. 343, no. 6166, pp. 58–61, 2014.

[15] F. Heide, M. B. Hullin, J. Gregson, and W. Heidrich, "Low-budget transient imaging using photonic mixer devices," *ACM Transactions on Graphics*, vol. 32, no. 4, pp. 45:1–45:10, Jul. 2013.

[16] A. Kadambi, R. Whyte, A. Bhandari, L. Streeter, C. Barsi, A. Dorrington, and R. Raskar, "Coded time of flight cameras," *ACM Transactions on Graphics*, vol. 32, no. 6, pp. 1–10, nov 2013.

[17] F. Heide, L. Xiao, W. Heidrich, and M. B. Hullin, "Diffuse mirrors: 3D reconstruction from diffuse indirect illumination using inexpensive time-of-flight sensors," in *Proc. IEEE Conf. Computer Vision and Pattern Recognition*, Jun. 2014, pp. 3222–3229.

[18] F. Heide, L. Xiao, A. Kolb, M. B. Hullin, and W. Heidrich, "Imaging in scattering media using correlation image sensors and sparse convolutional coding," *Optics Express*, vol. 22, no. 21, pp. 26 338–26 350, Oct. 2014.

[19] A. Kadambi, A. Bhandari, R. Whyte, A. Dorrington, and R. Raskar, "Demultiplexing illumination via low cost sensing and nanosecond coding," in *Proc. IEEE Int. Conf. Computational Photography (ICCP)*, May 2014, pp. 1–10.

[20] N. Kitsunezaki, E. Adachi, T. Masuda, and J.-i. Mizusawa, "KINECT applications for the physical rehabilitation," in *Proc. of IEEE MeMea*, 2013, pp. 294–299.

[21] A. Bhandari, C. Barsi, and R. Raskar, "Blind and reference-free fluorescence lifetime estimation via consumer time-of-flight sensors," *Optica*, vol. 2, no. 11, p. 965, Nov. 2015.

[22] E. H. Adelson and J. R. Bergen, *The Plenoptic Function and the Elements of Early Vision*. MIT Press, 1991, pp. 3–20.

[23] S. Foix, G. Alenya, and C. Torras, "Lock-in time-of-flight (tof) cameras: A survey," *IEEE Sensors Journal*, vol. 11, no. 9, pp. 1917–1926, Sep. 2011.

[24] C. E. Shannon, "Communication in the presence of noise," *Proc. Institute of Radio Engineers*, vol. 37, no. 1, pp. 10–21, Jan. 1949.

[25] G. H. Hardy, "Notes on special systems of orthogonal functions (IV): the orthogonal functions of Whittaker's cardinal series," *Math. Proc. Camb. Phil. Soc.*, vol. 37, no. 04, p. 331, Oct. 1941.

[26] T. Blu and M. Unser, "Quantitative Fourier analysis of approximation techniques: Part I—Interpolators and projectors," *IEEE Trans. Sig. Proc.*, vol. 47, no. 10, pp. 2783–2795, Oct. 1999.

[27] M. Unser, "Sampling–50 years after Shannon," *Proc. IEEE*, vol. 88, no. 4, pp. 569–587, Apr. 2000.

[28] Y. C. Eldar, *Sampling Theory: Beyond Bandlimited Systems*. Cambridge University Press, 2015.

[29] M. I. Kadec, "The exact value of the Paley–Wiener constant," *Doklady Akademii Nauk SSSR*, vol. 5, no. 02, pp. 559–561, 1964.

[30] C. de Boor and A. Ron, "Fourier analysis of the approximation power of principal shift-invariant spaces," *Constr. Approx*, vol. 8, no. 4, pp. 427–462, Dec. 1992.

[31] C. de Boor, R. A. DeVore, and A. Ron, "Approximation from shift-invariant subspaces of $L_2(\mathbf{R}^d)$," *Transactions of the American Mathematical Society*, vol. 341, no. 2, pp. 787–806, 1994.

[32] A. Aldroubi and K. Gröchenig, "Nonuniform sampling and reconstruction in shift-invariant spaces," *SIAM Review*, vol. 43, no. 4, pp. 585–620, Jan. 2001.

[33] S. Mallat, "A theory for multiresolution signal decomposition: the wavelet representation," *IEEE Trans. Pattern Anal. Mach. Intell.*, vol. 11, no. 7, pp. 674–693, Jul. 1989.

[34] G. Walter, "A sampling theorem for wavelet subspaces," *IEEE Trans. Inf. Theory*, vol. 38, no. 2, pp. 881–884, Mar. 1992.

[35] Y. C. Eldar and T. Michaeli, "Beyond bandlimited sampling," *IEEE Signal Process. Mag.*, vol. 26, no. 3, pp. 48–68, May 2009.

[36] A. J. E. M. Janssen, "The zak transform and sampling theorems for wavelet subspaces," *IEEE Trans. Sig. Proc.*, vol. 41, no. 12, pp. 3360–3364, Dec. 1993.

[37] G. G. Walter and A. I. Zayed, "Multiresolutional analysis with sampling subspaces," *Fractional Calculus & Applied Analysis*, vol. 1, no. 2, pp. 109–124, 1998.

[38] A. Bhandari and A. I. Zayed, "Shift-invariant and sampling spaces associated with the fractional Fourier transform domain," *IEEE Trans. Sig. Proc.*, vol. 60, no. 4, pp. 1627–1637, Apr. 2012.

[39] P. Thevenaz, T. Blu, and M. Unser, "Interpolation revisited," *IEEE Trans. Med. Imag.*, vol. 19, no. 7, pp. 739–758, Jul. 2000.

[40] M. Unser and T. Blu, "Wavelet theory demystified," *IEEE Trans. Sig. Proc.*, vol. 51, no. 2, pp. 470–483, Feb. 2003.

[41] M. Unser and I. Daubechies, "On the approximation power of convolution-based least squares versus interpolation," *IEEE Trans. Sig. Proc.*, vol. 45, no. 7, pp. 1697–1711, Jul. 1997.

[42] G. Strang and G. Fix, "A Fourier analysis of the finite element variational method," in *Constructive Aspects of Functional Analysis*. Edizioni Cremonese, Rome, 1973, pp. 793–840.

[43] M. Unser, "Approximation power of biorthogonal wavelet expansions," *IEEE Transactions on Signal Processing*, vol. 44, no. 3, pp. 519–527, Mar. 1996.

[44] S. Azizi, D. Cochran, and J. McDonald, "Reproducing kernel structure and sampling on time-warped spaces with application to warped wavelets," *IEEE Trans. Inf. Theory*, vol. 48, no. 3, pp. 789–790, Mar. 2002.

[45] A. Hirabayashi and M. Unser, "Consistent sampling and signal recovery," *IEEE Trans. Sig. Proc.*, vol. 55, no. 8, pp. 4104–4115, Aug. 2007.

[46] T. G. Dvorkind, Y. C. Eldar, and E. Matusiak, "Nonlinear and nonideal sampling: Theory and methods," *IEEE Trans. Sig. Proc.*, vol. 56, no. 12, pp. 5874–5890, Dec. 2008.

[47] B. D. Rao, "Signal processing with the sparseness constraint," in *IEEE Intl. Conf. on Acoustics, Speech and Signal Processing (ICASSP)*, vol. 3, May 1998, pp. 1861–1864.

[48] J. J. Fuchs and H. Chuberre, "A deconvolution approach to source localization," *IEEE Trans. Sig. Proc.*, vol. 42, no. 6, pp. 1462–1470, Jun. 1994.

[49] A. Bruckstein, T.-J. Shan, and T. Kailath, "The resolution of overlapping echos," *IEEE Trans. Acoust., Speech, Signal Process.*, vol. 33, no. 6, pp. 1357–1367, Dec. 1985.

[50] Y. Bresler and A. H. Delaney, "Resolution of overlapping echoes of unknown shape," in *IEEE Intl. Conf. on Acoustics, Speech and Signal Processing (ICASSP)*, May 1989, pp. 2657–2660.

[51] J. J. Fuchs, "Detection and estimation of superimposed signals," in *IEEE Intl. Conf. on Acoustics, Speech and Signal Processing (ICASSP)*, vol. 3, May 1998, pp. 1649–1652 vol.3.

[52] F. Santosa and W. W. Symes, "Linear inversion of band-limited reflection seismograms," *SIAM Jour. on Sci. and Stat. Computing*, vol. 7, no. 4, pp. 1307–1330, Oct. 1986.

[53] H. Zi-qiang and W. Zhen-dong, "A new method for high resolution estimation of time delay," in *IEEE Intl. Conf. on Acoustics, Speech and Signal Processing (ICASSP)*, vol. 7, May 1982, pp. 420–423.

[54] M. A. Pallas and G. Jourdain, "Active high resolution time delay estimation for large BT signals," *IEEE Trans. Sig. Proc.*, vol. 39, no. 4, pp. 781–788, Apr. 1991.

[55] J. Li and R. Wu, "An efficient algorithm for time delay estimation," *IEEE Trans. Sig. Proc.*, vol. 46, no. 8, pp. 2231–2235, Aug. 1998.

[56] J. J. Fuchs, "Multipath time-delay detection and estimation," *IEEE Trans. Sig. Proc.*, vol. 47, no. 1, pp. 237–243, Jan. 1999.

[57] L. Li and T. P. Speed, "Parametric deconvolution of positive spike trains," *Annals of Statistics*, pp. 1279–1301, 2000.

[58] D. L. Donoho, "Superresolution via sparsity constraints," *SIAM Journal on Mathematical Analysis*, vol. 23, no. 5, pp. 1309–1331, Sep. 1992.

[59] T. Manabe and H. Takai, "Superresolution of multipath delay profiles measured by PN correlation method," *IEEE Trans. Antennas Propag.*, vol. 40, no. 5, pp. 500–509, May 1992.

[60] E. J. Candès and C. Fernandez-Granda, "Towards a mathematical theory of super-resolution," *Communications on Pure and Applied Mathematics*, vol. 67, no. 6, pp. 906–956, Apr. 2013.

[61] K. Abed-Meraim and Y. Hua, "Blind identification of sparse multipath channels using cyclostationary statistics," in *Proc. of the European Sig. Process. Conf.*, Sep. 1998, pp. 1–4.

[62] S. F. Cotter and B. D. Rao, "Sparse channel estimation via matching pursuit with application to equalization," *IEEE Trans. Commun.*, vol. 50, no. 3, pp. 374–377, Mar. 2002.

[63] N. Dharamdial, R. Adve, and R. Farha, "Multipath delay estimations using matrix pencil," in *Proc. IEEE Wireless Comm. and Networking*, vol. 1, Mar. 2003, pp. 632–635 vol.1.

[64] S. Hernandez-Marin, A. M. Wallace, and G. J. Gibson, "Bayesian analysis of lidar signals with multiple returns," *IEEE Transactions on Pattern Analysis and Machine Intelligence*, vol. 29, no. 12, pp. 2170–2180, 2007.

[65] A. Bhandari, A. Kadambi, and R. Raskar, "Sparse linear operator identification without sparse regularization? Applications to mixed pixel problem in time-of-flight/range imaging," in *IEEE Intl. Conf. on Acoustics, Speech and Signal Processing (ICASSP)*, May 2014, pp. 365–369.

[66] A. Bhandari and R. Raskar, "Signal processing for time-of-flight imaging sensors," *IEEE Signal Process. Mag.*, vol. 33, no. 4, pp. 2–16, Sep. 2016.

[67] R. L. Stoica, P. and Moses, *Introduction to spectral analysis*. Prentice hall Upper Saddle River, 1997, vol. 1.

[68] Y. Hua, A. Gershman, and Q. Cheng, *High-resolution and robust signal processing*. CRC Press, 2003.

[69] M. Vetterli, P. Marziliano, and T. Blu, "Sampling signals with finite rate of innovation," *IEEE Trans. Sig. Proc.*, vol. 50, no. 6, pp. 1417–1428, 2002.

[70] T. Blu, P. L. Dragotti, M. Vetterli, P. Marziliano, and L. Coulot, "Sparse sampling of signal innovations," *IEEE Signal Process. Mag.*, vol. 25, no. 2, pp. 31–40, Mar. 2008.

[71] Y. Hao, P. Marziliano, M. Vetterli, and T. Blu, "Compression of ECG as a signal with finite rate of innovation," in *IEEE Engg. in Medicine and Biology*. IEEE, 2005.

[72] Y. Barbotin, A. Hormati, S. Rangan, and M. Vetterli, "Estimation of sparse MIMO channels with common support," *IEEE Trans. Commun.*, vol. 60, no. 12, pp. 3705–3716, Dec. 2012.

[73] A. Bhandari, A. M. Wallace, and R. Raskar, "Super-resolved time-of-flight sensing via FRI sampling theory," in *IEEE Intl. Conf. on Acoustics, Speech and Signal Processing (ICASSP)*, Mar. 2016.

[74] C. Chen, P. Marziliano, and A. C. Kot, "2D finite rate of innovation reconstruction method for step edge and polygon signals in the presence of noise," *IEEE Trans. Sig. Proc.*, vol. 60, no. 6, pp. 2851–2859, Jun. 2012.

[75] H. Pan, T. Blu, and P. L. Dragotti, "Sampling curves with finite rate of innovation," *IEEE Trans. Sig. Proc.*, vol. 62, no. 2, pp. 458–471, Jan. 2014.

[76] S. Mulleti and C. S. Seelamantula, "Ellipse fitting using the finite rate of innovation sampling principle," *IEEE Trans. Image Proc.*, vol. 25, no. 3, pp. 1451–1464, Mar. 2016.

[77] J. Oñativia, S. R. Schultz, and P. L. Dragotti, "A finite rate of innovation algorithm for fast and accurate spike detection from two-photon calcium imaging," *J. Neural Eng.*, vol. 10, no. 4, p. 046017, Jul. 2013.

[78] R. Tur, Y. C. Eldar, and Z. Friedman, "Innovation rate sampling of pulse streams with application to ultrasound imaging," *IEEE Trans. Sig. Proc.*, vol. 59, no. 4, pp. 1827–1842, Apr. 2011.

[79] Z. Dogan, T. Blu, and D. V. D. Ville, "Detecting spontaneous brain activity in functional magnetic resonance imaging using finite rate of innovation," in *IEEE Intl. Symp. on Biomed. Imaging*. IEEE, Apr. 2014.

[80] C. S. Seelamantula and S. Mulleti, "Super-resolution reconstruction in frequency-domain optical-coherence tomography using the finite-rate-of-innovation principle," *IEEE Trans. Sig. Proc.*, vol. 62, no. 19, pp. 5020–5029, Oct. 2014.

[81] S. Peleg and B. Porat, "Estimation and classification of polynomial-phase signals," *IEEE Trans. Inf. Theory*, vol. 37, no. 2, pp. 422–430, Mar. 1991.

[82] S. Mann and S. Haykin, "The chirplet transform: physical considerations," *IEEE Trans. Sig. Proc.*, vol. 43, no. 11, pp. 2745–2761, 1995.

[83] R. Baraniuk and D. Jones, "Shear madness: new orthonormal bases and frames using chirp functions," *IEEE Trans. Sig. Proc.*, vol. 41, no. 12, pp. 3543–3549, 1993.

[84] R. Gribonval, "Fast matching pursuit with a multiscale dictionary of Gaussian chirps," *IEEE Trans. Sig. Proc.*, vol. 49, no. 5, pp. 994–1001, 2001.

[85] G. Engen and Y. Larsen, "Efficient full aperture processing of TOPS mode data using the moving band chirp z-transform," *IEEE Trans. Geosci. Remote Sensing*, vol. 49, no. 10, pp. 3688–3693, Oct. 2011.

[86] S. Schock, "A method for estimating the physical and acoustic properties of the sea bed using chirp sonar data," *IEEE Journal of Oceanic Engineering*, vol. 29, no. 4, pp. 1200–1217, Oct. 2004.

[87] M. Martone, "A multicarrier system based on the fractional Fourier transform for time-frequency-selective channels," *IEEE Trans. Commun.*, vol. 49, no. 6, pp. 1011–1020, Jun. 2001.

[88] A. Harms, W. U. Bajwa, and R. Calderbank, "Identification of linear time-varying systems through waveform diversity," *IEEE Trans. Sig. Proc.*, vol. 63, no. 8, pp. 2070–2084, Apr. 2015.

[89] F. Gori, "Fresnel transform and sampling theorem," *Optics Communications*, vol. 39, no. 5, pp. 293–297, Nov. 1981.

[90] N. Chacko, M. Liebling, and T. Blu, "Discretization of continuous convolution operators for accurate modeling of wave propagation in digital holography," *Journal of the Optical Society of America A*, vol. 30, no. 10, p. 2012, Sep. 2013.

[91] S.-C. Pei and J.-J. Ding, "Relations between Gabor transforms and fractional Fourier transforms and their applications for signal processing," *IEEE Trans. Sig. Proc.*, vol. 55, no. 10, pp. 4839–4850, Oct. 2007.

[92] I. Yetik and A. Nehorai, "Beamforming using the fractional Fourier transform," *IEEE Trans. Sig. Proc.*, vol. 51, no. 6, pp. 1663–1668, Jun. 2003.

[93] T. Setälä, T. Shirai, and A. T. Friberg, "Fractional Fourier transform in temporal ghost imaging with classical light," *Physical Review A*, vol. 82, no. 4, Oct. 2010.

[94] G. Unnikrishnan, J. Joseph, and K. Singh, "Optical encryption by double-random phase encoding in the fractional Fourier domain," *Optics Letters*, vol. 25, no. 12, p. 887, Jun. 2000.

[95] Y. Huang, "Entropic uncertainty relations in multidimensional position and momentum spaces," *Physical Review A*, vol. 83, no. 5, May 2011.

[96] N. Wiener, "Hermitian polynomials and fourier analysis," *Journal of Mathematics and Physics*, vol. 8, no. 1-4, pp. 70–73, Apr. 1929.

[97] E. U. Condon, "Immersion of the Fourier transform in a continuous group of functional transformations," *Proceedings of the National Academy of Sciences*, vol. 23, no. 3, pp. 158–164, Mar. 1937.

[98] M. Moshinsky and C. Quesne, "Linear canonical transformations and their unitary representations," *Journal of Mathematical Physics*, vol. 12, no. 8, pp. 1772–1780, 1971.

[99] L. B. Almeida, "The fractional Fourier transform and time-frequency representations," *IEEE Trans. Sig. Proc.*, vol. 42, no. 11, pp. 3084–3091, 1994.

[100] R. Tao, B. Deng, W.-Q. Zhang, and Y. Wang, "Sampling and sampling rate conversion of band limited signals in the fractional Fourier transform domain," *IEEE Trans. Sig. Proc.*, vol. 56, no. 1, pp. 158–171, Jan. 2008.

[101] J. Shi, X. Liu, X. Sha, and N. Zhang, "Sampling and reconstruction of signals in function spaces associated with the linear canonical transform," *IEEE Trans. Sig. Proc.*, vol. 60, no. 11, pp. 6041–6047, Nov. 2012.

[102] S. Abe and J. T. Sheridan, "Generalization of the fractional Fourier transformation to an arbitrary linear lossless transformation an operator approach," *J. of Physics A: Math. and General*, vol. 27, no. 12, p. 4179, 1994.

[103] S. C. Pei and J. J. Ding, "Eigenfunctions of Fourier and fractional Fourier transforms with complex offsets and parameters," *IEEE Trans. Circuits Syst. I*, vol. 54, no. 7, pp. 1599–1611, Jul. 2007.

[104] A. Gerrard and J. Burch, *Introduction to Matrix Methods in Optics*, ser. Dover Books on Physics. Dover, 1975.

[105] J. J. Healy, M. A. Kutay, H. M. Ozaktas, and J. T. Sheridan, Eds., *Linear Canonical Transforms: Theory and Applications*, ser. Springer Series in Optical Sciences. Springer New York, 2016, vol. 198.

[106] M. J. Bastiaans and A. J. Van Leest, "From the rectangular to the quincunx Gabor lattice via fractional Fourier transformation," *IEEE Signal Process. Lett.*, vol. 5, no. 8, pp. 203–205, Aug. 1998.

[107] A. I. Zayed, "On the relationship between the Fourier and fractional Fourier transforms," *IEEE Signal Process. Lett.*, vol. 3, no. 12, pp. 310–311, Dec. 1996.

[108] L. B. Almeida, "Product and convolution theorems for the fractional Fourier transform," *IEEE Signal Processing Letters*, vol. 4, no. 1, pp. 15–17, Jan. 1997.

[109] A. I. Zayed, "A convolution and product theorem for the fractional Fourier transform," *IEEE Signal Processing Letters*, vol. 5, no. 4, pp. 101–103, Apr. 1998.

[110] Q. Xiang and K. Y. Qin, "Convolution, correlation, and sampling theorems for the offset linear canonical transform," *Signal, Image and Video Processing*, pp. 1–10, 2012.

[111] H. M. Ozaktas, D. Mendlovic, L. Onural, and B. Barshan, "Convolution, filtering, and multiplexing in fractional Fourier domains and their relation to chirp and wavelet transforms," *Journal of the Optical Society of America A*, vol. 11, no. 2, p. 547, Feb. 1994.

[112] S. Abe and J. T. Sheridan, "Optical operations on wave functions as the abelian subgroups of the special affine Fourier transformation." *Optics Letters*, vol. 19, no. 22, p. 1801, Nov. 1994.

[113] A. Bhandari and A. I. Zayed, "Shift-invariant and sampling spaces associated with the special affine Fourier transform," *Applied and Computational Harmonic Analysis*, Jul. 2017.

[114] A. Bhandari and P. Marziliano, "Sampling and reconstruction of sparse signals in fractional Fourier domain," *IEEE Signal Process. Lett.*, vol. 17, no. 3, pp. 221–224, 2010.

[115] T. I. Laakso, V. Valimaki, M. Karjalainen, and U. K. Laine, "Splitting the unit delay: FIR/all pass filters design," *IEEE Signal Processing Magazine*, vol. 13, no. 1, pp. 30–60, Jan. 1996.

[116] A. Bhandari and P. Marziliano, "Fractional delay filters based on generalized cardinal exponential splines," *IEEE Signal Processing Letters*, vol. 17, no. 3, pp. 225–228, Mar. 2010.

[117] C. Aubel, D. Stotz, and H. Bölcskei, "A theory of super-resolution from short-time Fourier transform measurements," *Journal of Fourier Analysis and Applications*, 2017.

[118] Y. C. Eldar, P. Sidorenko, D. G. Mixon, S. Barel, and O. Cohen, "Sparse phase retrieval from short-time Fourier measurements," *IEEE Signal Process. Lett.*, vol. 22, no. 5, pp. 638–642, May 2015.

[119] Z. Zalevsky, R. G. Dorsch, and D. Mendlovic, "Gerchberg-Saxton algorithm applied in the fractional Fourier or the Fresnel domain," *Optics Letters*, vol. 21, no. 12, p. 842, Jun. 1996.

[120] B.-Z. Dong, Y. Zhang, B.-Y. Gu, and G.-Z. Yang, "Numerical investigation of phase retrieval in a fractional Fourier transform," *Journal of the Optical Society of America A*, vol. 14, no. 10, p. 2709, Oct. 1997.

[121] S.-C. Pei, M.-H. Yeh, and T.-L. Luo, "Fractional Fourier series expansion for finite signals and dual extension to discrete-time fractional Fourier transform," *IEEE Trans. Sig. Proc.*, vol. 47, no. 10, pp. 2883–2888, 1999.

[122] B. N. Bhaskar, G. Tang, and B. Recht, "Atomic norm denoising with applications to line spectral estimation," *IEEE Trans. Sig. Proc.*, vol. 61, no. 23, pp. 5987–5999, Dec. 2013.

[123] E. Matusiak and Y. C. Eldar, "Sub-Nyquist sampling of short pulses," *IEEE Trans. Sig. Proc.*, vol. 60, no. 3, pp. 1134–1148, Mar. 2012.

[124] K. Jaganathan, Y. C. Eldar, and B. Hassibi, "STFT phase retrieval: Uniqueness guarantees and recovery algorithms," *IEEE J. Sel. Topics Signal Process.*, vol. 10, no. 4, pp. 770–781, Jun. 2016.

[125] P. L. Butzer and R. L. Stens, "Sampling theory for not necessarily band-limited functions: A historical overview," *SIAM Rev.*, vol. 34, no. 1, pp. 40–53, Mar. 1992.

[126] A. I. Zayed, *Advances in Shannon's Sampling Theory*. CRC Press, 1993.

[127] P. L. Butzer, M. M. Dodson, P. J. S. G. Ferreira, J. R. Higgins, G. Schmeisser, and R. L. Stens, "Seven pivotal theorems of Fourier analysis, signal analysis, numerical analysis and number theory: Their interconnections," *Bull. Math. Sci*, vol. 4, no. 3, pp. 481–525, Oct. 2014.

[128] Y. Lu and M. Do, "A theory for sampling signals from a union of subspaces," *IEEE Transactions on Signal Processing*, vol. 56, no. 6, pp. 2334–2345, Jun. 2008.

[129] M. Mishali, Y. C. Eldar, and A. J. Elron, "Xampling: Signal acquisition and processing in union of subspaces," *IEEE Trans. Sig. Proc.*, vol. 59, no. 10, pp. 4719–4734, Oct. 2011.

[130] B. Adcock and A. C. Hansen, "Generalized sampling and infinite-dimensional compressed sensing," *Foundations of Computational Mathematics*, vol. 16, no. 5, pp. 1263–1323, Aug. 2015.

[131] P. Feng and Y. Bresler, "Spectrum-blind minimum-rate sampling and reconstruction of multiband signals," in *Proc. of IEEE ICASSP*. IEEE, 1996.

[132] G. E. Pfander, "Sampling of operators," *Journal of Fourier Analysis and Applications*, vol. 19, no. 3, pp. 612–650, Apr. 2013.

[133] F. Krahmer and G. E. Pfander, "Local sampling and approximation of operators with bandlimited kohn–nirenberg symbols," *Constructive Approximation*, vol. 39, no. 3, pp. 541–572, Apr. 2014.

[134] J. Abel and J. Smith, "Restoring a clipped signal," in *Proc. of IEEE ICASSP*. IEEE, 1991.

[135] T. Olofsson, "Deconvolution and model-based restoration of clipped ultrasonic signals," *IEEE Trans. Instrum. Meas.*, vol. 54, no. 3, pp. 1235–1240, Jun. 2005.

[136] A. Adler, V. Emiya, M. G. Jafari, M. Elad, R. Gribonval, and M. D. Plumbley, "A constrained matching pursuit approach to audio declipping," in *Proc. of IEEE ICASSP*. IEEE, May 2011.

[137] S.-K. Ting and A. H. Sayed, "Mitigation of clipping in sensors," in *Proc. of IEEE ICASSP*. IEEE, May 2013.

[138] F. Esqueda, S. Bilbao, and V. Valimaki, "Aliasing reduction in clipped signals," *IEEE Trans. Sig. Proc.*, vol. 64, no. 20, pp. 5255–5267, Oct. 2016.

[139] B. F. Logan, "Signals designed for recovery after clipping–II. Fourier transform theory of recovery," *AT&T Bell Laboratories Technical Journal*, vol. 63, no. 2, pp. 287–306, Feb. 1984.

[140] L. Gopal, Y. Rong, and Z. Zang, "Tomlinson-harashima precoding based transceiver design for MIMO relay systems with channel covariance information," *IEEE Trans. Wireless Commun.*, vol. 14, no. 10, pp. 5513–5525, Oct. 2015.

[141] T. Ericson and V. Ramamoorthy, "Modulo-PCM: A new source coding scheme," in *Proc. of IEEE ICASSP*. IEEE, 1979.

[142] W. Chou and R. Gray, "Modulo sigma-delta modulation," *IEEE Trans. Commun.*, vol. 40, no. 8, pp. 1388–1395, 1992.

[143] W. Kester, "ADC architectures VI: Folding ADCs (MT-025 tutorial)," Analog Devices, Tech. Rep., 2009.

[144] J. Rhee and Y. Joo, "Wide dynamic range CMOS image sensor with pixel level ADC," *Electronics Letters*, vol. 39, no. 4, p. 360, 2003.

[145] K. Sasagawa, T. Yamaguchi, M. Haruta, Y. Sunaga, H. Takehara, H. Takehara, T. Noda, T. Tokuda, and J. Ohta, "An implantable CMOS image sensor with self-reset pixels for functional brain imaging," *IEEE Trans. Electron Devices*, vol. 63, no. 1, pp. 215–222, Jan. 2016.

[146] S. Kavusi and A. E. Gamal, "Quantitative study of high-dynamic-range image sensor architectures," in *Sensors and Camera Sys. for Sci., Industrial, and Dig. Photography Applications V*, M. M. Blouke, N. Sampat, and R. J. Motta, Eds. SPIE-Intl Soc Optical Eng, Jun. 2004.

[147] T. Yamaguchi, H. Takehara, Y. Sunaga, M. Haruta, M. Motoyama, Y. Ohta, T. Noda, K. Sasagawa, T. Tokuda, and J. Ohta, "Implantable self-reset CMOS image sensor and its application to hemodynamic response detection in living mouse brain," *Japanese J. of App. Physics*, vol. 55, no. 4S, p. 04EM02, Mar. 2016.

[148] R. Tibshirani, "Regression shrinkage and selection via the lasso," *Journal of the Royal Statistical Society (Series B)*, vol. 58, pp. 267–288, 1996.

[149] E. Candes and T. Tao, "Decoding by linear programming," *IEEE Transactions on Information Theory*, vol. 51, no. 12, pp. 4203–4215, Dec. 2005.

[150] D. Donoho, "Compressed sensing," *IEEE Transactions on Information Theory*, vol. 52, no. 4, pp. 1289–1306, Apr. 2006.

[151] E. J. Candes and T. Tao, "Near-optimal signal recovery from random projections: Universal encoding strategies?" *IEEE Transactions on Information Theory*, vol. 52, no. 12, pp. 5406–5425, Dec. 2006.

[152] A. Zymnis, S. Boyd, and E. Candes, "Compressed sensing with quantized measurements," *IEEE Signal Processing Letters*, vol. 17, no. 2, pp. 149–152, Feb. 2010.

[153] J. N. Laska, P. T. Boufounos, M. A. Davenport, and R. G. Baraniuk, "Democracy in action: Quantization, saturation, and compressive sensing," *Applied and Computational Harmonic Analysis*, vol. 31, no. 3, pp. 429–443, Nov. 2011.

[154] P. Boufounos and R. Baraniuk, "1-bit compressive sensing," in *42nd Annual Conference on Information Sciences and Systems*, Nov. 2009.

[155] L. Jacques, J. N. Laska, P. T. Boufounos, and R. G. Baraniuk, "Robust 1-bit compressive sensing via binary stable embeddings of sparse vectors," *IEEE Transactions on Information Theory*, vol. 59, no. 4, pp. 2082–2102, Apr. 2013.

[156] Y. Plan and R. Vershynin, "One-bit compressed sensing by linear programming," *Communications on Pure and Applied Mathematics*, vol. 66, no. 8, pp. 1275–1297, Feb. 2013.

[157] Y. Shechtman, A. Beck, and Y. C. Eldar, "GESPAR: Efficient phase retrieval of sparse signals," *IEEE Transactions on Signal Processing*, vol. 62, no. 4, pp. 928–938, Feb. 2014.

[158] K. Jaganathan, S. Oymak, and B. Hassibi, "Sparse phase retrieval: Uniqueness guarantees and recovery algorithms," *IEEE Transactions on Signal Processing*, vol. 65, no. 9, pp. 2402–2410, May 2017.

[159] M. Soltani and C. Hegde, "Stable recovery of sparse vectors from random sinusoidal feature maps," in *IEEE International Conference on Acoustics, Speech and Signal Processing (ICASSP)*. IEEE, Mar. 2017.

[160] Y. Plan and R. Vershynin, "The generalized lasso with non-linear observations," *IEEE Transactions on Information Theory*, vol. 62, no. 3, pp. 1528–1537, Mar. 2016.

[161] C. Thrampoulidis, E. Abbasi, and B. Hassibi, "Lasso with non-linear measurements is equivalent to one with linear measurements," in *Advances in Neural Information Processing Systems*, 2015.

[162] J. Tumblin, A. Agrawal, and R. Raskar, "Why i want a gradient camera," in *IEEE Computer Society Conference on Computer Vision and Pattern Recognition (CVPR)*. IEEE, 2005.

[163] D. R. Brillinger, *Selected Works of David Brillinger*, ser. Selected Works in Probability and Statistics. Springer link, 2011, ch. A Generalized Linear Model With "Gaussian" Regressor Variables, pp. 589–606.

[164] M. Genzel, "High-dimensional estimation of structured signals from non-linear observations with general convex loss functions," *IEEE Transactions on Information Theory*, vol. 63, no. 3, pp. 1601–1619, Mar. 2017.

[165] M. Genzel and P. Jung, "Recovering structured data from superimposed non-linear measurements," Aug. 2017, arXiv preprint.

[166] A. Agrawal, R. Chellappa, and R. Raskar, "An algebraic approach to surface reconstruction from gradient fields," in *IEEE International Conference on Computer Vision (ICCV)*, vol. 1. IEEE, 2005.

[167] A. Agrawal, R. Raskar, and R. Chellappa, "What is the range of surface reconstructions from a gradient field?" in *Computer Vision – ECCV 2006*. Springer Berlin Heidelberg, 2006, pp. 578–591.

[168] G. Tang, B. N. Bhaskar, P. Shah, and B. Recht, "Compressed sensing off the grid," *IEEE Transactions on Information Theory*, vol. 59, no. 11, pp. 7465–7490, Nov. 2013.

[169] K. Itoh, "Analysis of the phase unwrapping algorithm," *Applied Optics*, vol. 21, no. 14, pp. 2470–2470, Jul. 1982.

[170] O. Loffeld and C. Arndt, "Estimating the derivative of modulo-mapped phases," in *IEEE International Conference on Acoustics, Speech, and Signal Processing*. IEEE Comput. Soc. Press, Apr. 1997, pp. 21–24.

[171] L. Graham, "Synthetic interferometer radar for topographic mapping," *Proceedings of the IEEE*, vol. 62, no. 6, pp. 763–768, 1974.

[172] H. A. Zebker and R. M. Goldstein, "Topographic mapping from interferometric synthetic aperture radar observations," *Journal of Geophysical Research*, vol. 91, no. B5, p. 4993, 1986.

[173] R. M. Goldstein and H. A. Zebker, "Interferometric radar measurement of ocean surface currents," *Nature*, vol. 328, no. 6132, pp. 707–709, Aug. 1987.

[174] R. M. Goldstein, H. A. Zebker, and C. L. Werner, "Satellite radar interferometry: Two-dimensional phase unwrapping," *Radio Science*, vol. 23, no. 4, pp. 713–720, Jul. 1988.

[175] W. Choi, C. Fang-Yen, K. Badizadegan, S. Oh, N. Lue, R. R. Dasari, and M. S. Feld, "Tomographic phase microscopy," *Nature Methods*, vol. 4, no. 9, pp. 717–719, Aug. 2007.

[176] J. C. Estrada, J. L. Marroquin, and O. M. Medina, "Reconstruction of local frequencies for recovering the unwrapped phase in optical interferometry," *Scientific Reports*, vol. 7, no. 1, Jul. 2017.

[177] R. Kulkarni and P. Rastogi, "Matrix pencil based phase derivative estimation in digital holographic interferometry," *Journal of Optics*, vol. 17, no. 4, p. 045604, Mar. 2015.

[178] S. M.-H. Song, S. Napel, N. Pelc, and G. Glover, "Phase unwrapping of MR phase images using poisson equation," *IEEE Transactions on Image Processing*, vol. 4, no. 5, pp. 667–676, May 1995.

[179] G. H. Glover and E. Schneider, "Three-point dixon technique for true water/fat decomposition with B0 inhomogeneity correction," *Magnetic Resonance in Medicine*, vol. 18, no. 2, pp. 371–383, Apr. 1991.

[180] N. J. Pelc, M. A. Bernstein, A. Shimakawa, and G. H. Glover, "Encoding strategies for three-direction phase-contrast MR imaging of flow," *Journal of Magnetic Resonance Imaging*, vol. 1, no. 4, pp. 405–413, Jul. 1991.

[181] D. L. Fried, "Least-square fitting a wave-front distortion estimate to an array of phase-difference measurements," *Journal of the Optical Society of America*, vol. 67, no. 3, p. 370, Mar. 1977.

[182] D. Park, J. Rhee, and Y. Joo, "A wide dynamic-range CMOS image sensor using self-reset technique," *IEEE Electron Device Letters*, vol. 28, no. 10, pp. 890–892, Oct. 2007.

[183] H. Zhao, B. Shi, C. Fernandez-Cull, S.-K. Yeung, and R. Raskar, "Unbounded high dynamic range photography using a modulo camera," in *IEEE International Conference on Computational Photography (ICCP)*. IEEE, Apr. 2015.

[184] D. C. Ghiglia and M. D. Pritt, *Two-Dimensional Phase Unwrapping: Theory, Algorithms, and Software*. Wiley, 1998.

[185] B. R. Hunt, "Matrix formulation of the reconstruction of phase values from phase differences," *Journal of the Optical Society of America*, vol. 69, no. 3, p. 393, Mar. 1979.

[186] H. Takajo and T. Takahashi, "Least-squares phase estimation from the phase difference," *Journal of the Optical Society of America A*, vol. 5, no. 3, p. 416, Mar. 1988.

[187] D. C. Ghiglia and L. A. Romero, "Robust two-dimensional weighted and unweighted phase unwrapping that uses fast transforms and iterative methods," *Journal of the Optical Society of America A*, vol. 11, no. 1, p. 107, Jan. 1994.

[188] J. L. Marroquin and M. Rivera, "Quadratic regularization functionals for phase unwrapping," *Journal of the Optical Society of America A*, vol. 12, no. 11, p. 2393, Nov. 1995.

[189] H. Y. H. Huang, L. Tian, Z. Zhang, Y. Liu, Z. Chen, and G. Barbastathis, "Path-independent phase unwrapping using phase gradient and total-variation (TV) denoising," *Optics Express*, vol. 20, no. 13, p. 14075, Jun. 2012.

[190] D. C. Ghiglia and L. A. Romero, "Minimum l_p-norm two-dimensional phase unwrapping," *Journal of the Optical Society of America A*, vol. 13, no. 10, p. 1999, Oct. 1996.

[191] M. Rivera and J. L. Marroquin, "Half-quadratic cost functions for phase unwrapping," *Optics Letters*, vol. 29, no. 5, p. 504, Mar. 2004.

[192] A. Gonzalez and L. Jacques, "Robust phase unwrapping by convex optimization," in *IEEE International Conference on Image Processing (ICIP)*. IEEE, Oct. 2014.

[193] L. Ying, Z.-P. Liang, D. Munson, R. Koetter, and B. Frey, "Unwrapping of MR phase images using a markov random field model," *IEEE Transactions on Medical Imaging*, vol. 25, no. 1, pp. 128–136, Jan. 2006.

[194] J. M. Bioucas-Dias and G. Valadao, "Phase unwrapping via graph cuts," *IEEE Transactions on Image Processing*, vol. 16, no. 3, pp. 698–709, Mar. 2007.

[195] A. Collaro, G. Franceschetti, F. Palmieri, and M. S. Ferreiro, "Phase unwrapping by means of genetic algorithms," *Journal of the Optical Society of America A*, vol. 15, no. 2, p. 407, Feb. 1998.

[196] G. Nico and J. Fortuny, "Using the matrix pencil method to solve phase unwrapping," *IEEE Transactions on Signal Processing*, vol. 51, no. 3, pp. 886–888, Mar. 2003.

[197] J. Martinez-Espla, T. Martinez-Marin, and J. Lopez-Sanchez, "An optimized algorithm for InSAR phase unwrapping based on particle filtering, matrix pencil, and region-growing techniques," *IEEE Geoscience and Remote Sensing Letters*, vol. 6, no. 4, pp. 835–839, Oct. 2009.

[198] J. M. Huntley, "Three-dimensional noise-immune phase unwrapping algorithm," *Applied Optics*, vol. 40, no. 23, p. 3901, Aug. 2001.

[199] B. Osmanoglu, T. H. Dixon, and S. Wdowinski, "Three-dimensional phase unwrapping for satellite radar interferometry, i: DEM generation," *IEEE Transactions on Geoscience and Remote Sensing*, vol. 52, no. 2, pp. 1059–1075, Feb. 2014.

[200] S. M. Nikol'skii, *Approximation of Functions of Several Variables and Imbedding Theorems*. Springer Nature, 1975, vol. 205.

[201] S. Levy and P. K. Fullagar, "Reconstruction of a sparse spike train from a portion of its spectrum and application to high-resolution deconvolution," *GEOPHYSICS*, vol. 46, no. 9, pp. 1235–1243, Sep. 1981.

[202] H. Pan, T. Blu, and M. Vetterli, "Towards generalized FRI sampling with an application to source resolution in radioastronomy," *IEEE Trans. Sig. Proc.*, vol. 65, no. 4, pp. 821–835, Feb. 2017.

[203] J. Zhang, J. Hao, X. Zhao, S. Wang, L. Zhao, W. Wang, and Z. Yao, "Restoration of clipped seismic waveforms using projection onto convex sets method," *Nature Scientific Reports*, vol. 6, no. 1, Dec. 2016.

[204] N. J. Cassidy, *Ground Penetrating Radar Theory and Applications*. Elsevier Science, 2009, ch. Ground Penetrating Radar Data Processing, Modelling and Analysis, pp. 141–176.

[205] W. Yang and Y. Ben-Zion, "An algorithm for detecting clipped waveforms and suggested correction procedures," *Seismological Research Letters*, vol. 81, no. 1, pp. 53–62, Jan. 2010.

[206] C. Anderson, S. Venkatesh, J. Ibrahim, R. Buehrer, and J. Reed, "Analysis and implementation of a time-interleaved ADC array for a software-defined UWB receiver," *IEEE Trans. Veh. Technol.*, vol. 58, no. 8, pp. 4046–4063, Oct. 2009.

[207] M. Kaplan, A. Lundberg, and T. M. Duffy, "Ultrasound imaging system apparatus and method with ADC saturation monitor," U.S. Patent US8 568 319 B1, Oct., 2013.

[208] A. Bhandari, F. Krahmer, and Ramesh, "On unlimited sampling," in *Intl. Conf. on Sampling Theory and Applications (SampTA)*, Jul. 2017.

[209] A. Bhandari, A. Kadambi, R. Whyte, C. Barsi, M. Feigin, A. Dorrington, and R. Raskar, "Resolving multipath interference in time-of-flight imaging via modulation frequency diversity and sparse regularization," *Optics Letters*, vol. 39, no. 6, p. 1705, Mar. 2014.

[210] R. E. Blahut, *Algebraic Methods for Signal Processing and Communications Coding*. Springer, New York, NY, 1992, ch. Decoding of Cyclic Codes, pp. 119–134.

[211] ——, "A universal reed-solomon decoder," *IBM Journal of Research and Development*, vol. 28, no. 2, pp. 150–158, Mar. 1984.

[212] G. Beylkin and L. Monzón, "On approximation of functions by exponential sums," *Appl. Comput. Harmon. Anal.*, vol. 19, no. 1, pp. 17–48, Jul. 2005.

[213] T. Peter, D. Potts, and M. Tasche, "Nonlinear approximation by sums of exponentials and translates," *SIAM J. Sci. Comput.*, vol. 33, no. 4, pp. 1920–1947, Jan. 2011.

[214] J. Steinwandt, F. Roemer, and M. Haardt, "Generalized least squares for ESPRIT-type direction of arrival estimation," *IEEE Signal Process. Lett.*, vol. 24, no. 11, pp. 1681–1685, Nov. 2017.

[215] P. Stoica and A. Nehorai, "MUSIC, maximum likelihood, and cramer-rao bound," *IEEE Trans. Acoust., Speech, Signal Process.*, vol. 37, no. 5, pp. 720–741, May 1989.

[216] A. E. Breiholz, "The effects of clipping on linear beamforming with sinusoidal inputs," The Pennsylvania State University, mathesis TM 77–94, Feb. 1977.

[217] A. J. Weinstein and M. B. Wakin, "Recovering a clipped signal in sparseland," *Sampling Theory in Signal and Image Processing*, vol. 12, no. 1, pp. 55–69, 2013.

[218] J. B. Carruthers and J. M. Kahn, "Modeling of nondirected wireless infrared channels," *IEEE Transactions on Communications*, vol. 45, no. 10, pp. 1260–1268, Oct. 1997.

[219] V. Jungnickel, V. Pohl, S. Nonnig, and C. von Helmolt, "A physical model of the wireless infrared communication channel," *IEEE Journal on Selected Areas in Communications*, vol. 20, no. 3, pp. 631–640, Apr. 2002.

[220] D. Wu, A. Velten, M. O'Toole, B. Masia, A. Agrawal, Q. Dai, and R. Raskar, "decomposing global light transport using time of flight imaging," *International Journal of Computer Vision*, vol. 107, no. 2, pp. 123–138, Oct. 2013.

[221] J. S. Massa, A. M. Wallace, G. S. Buller, S. J. Fancey, and A. C. Walker, "Laser depth measurement based on time-correlated single-photon counting," *Optics letters*, vol. 22, no. 8, pp. 543–545, 1997.

[222] M. Hansard, S. Lee, O. Choi, and R. P. Horaud, *Time-of-flight cameras: principles, methods and applications*. Springer Science & Business Media, 2012.

[223] C. Mallet, F. Lafarge, M. Roux, U. Soergel, F. Bretar, and C. Heipke, "A marked point process for modeling lidar waveforms," *IEEE Transactions on Image Processing*, vol. 19, no. 12, pp. 3204–3221, 2010.

[224] G. S. Buller and A. M. Wallace, "Ranging and three-dimensional imaging using time-correlated single-photon counting and point-by-point acquisition," *IEEE Journal of Selected Topics in Quantum Electronics*, vol. 13, no. 4, pp. 1006–1015, 2007.

[225] J. W. Goodman, *Introduction to Fourier optics*. Roberts and Company Publishers, 2005.

[226] A. Bhandari, M. Feigin, S. Izadi, C. Rhemann, M. Schmidt, and R. Raskar, "Resolving multipath interference in Kinect: An inverse problem approach," in *IEEE Sensors*, Nov. 2014, pp. 614–617.

[227] S. Pellegrini, G. S. Buller, J. M. Smith, A. M. Wallace, and S. Cova, "Laser-based distance measurement using picosecond resolution time-correlated single-photon counting," *Measurement Science and Technology*, vol. 11, no. 6, p. 712, 2000.

[228] Y. Hua and T. K. Sarkar, "Matrix pencil method for estimating parameters of exponentially damped/undamped sinusoids in noise," *IEEE Trans. on Acoustics, Speech and Signal Processing*, vol. 38, no. 5, pp. 814–824, 1990.

[229] Y. C. Pati, R. Rezaiifar, and P. S. Krishnaprasad, "Orthogonal matching pursuit: recursive function approximation with applications to wavelet decomposition," in *Proc. 27th Asilomar Conf. Signals Systems and Computers*, Nov. 1993, pp. 40–44 vol.1.

[230] H. He, B. K. Nunnally, L.-C. Li, and L. B. McGown, "On-the-fly fluorescence lifetime detection of dye-labeled DNA primers for multiplex analysis," *Analytical chemistry*, vol. 70, no. 16, pp. 3413–3418, 1998.

[231] Y. Sun, J. Phipps, D. S. Elson, H. Stoy, S. Tinling, J. Meier, B. Poirier, F. S. Chuang, D. G. Farwell, and L. Marcu, "Fluorescence lifetime imaging microscopy: in vivo application to diagnosis of oral carcinoma," *Optics Letters*, vol. 34, no. 13, pp. 2081–2083, 2009.

[232] R. Cicchi, D. Massi, S. Sestini, P. Carli, V. De Giorgi, T. Lotti, and F. S. Pavone, "Multidimensional non-linear laser imaging of basal cell carcinoma," *Optics express*, vol. 15, no. 16, pp. 10 135–10 148, 2007.

[233] A. T. N. Kumar, S. B. Raymond, B. J. Bacskai, D. A. Boas, R. Georgescu, D. Khismatullin, R. G. Holt, J. L. Castagner, O. A'amar, I. J. Bigio *et al.*, "Comparison of frequency-domain and time-domain fluorescence lifetime tomography," *Optics Letters*, vol. 33, no. 5, pp. 470–472, 2008.

[234] A. T. N. Kumar, S. B. Raymond, A. K. Dunn, B. J. Bacskai, and D. A. Boas, "A time domain fluorescence tomography system for small animal imaging," *IEEE Transactions on Medical Imaging*, vol. 27, no. 8, pp. 1152–1163, 2008.

[235] J. Rao, A. Dragulescu-Andrasi, and H. Yao, "Fluorescence imaging in vivo: recent advances," *Current opinion in biotechnology*, vol. 18, no. 1, pp. 17–25, 2007.

[236] B. J. Bacskai, J. Skoch, G. A. Hickey, R. Allen, and B. T. Hyman, "Fluorescence resonance energy transfer determinations using multiphoton fluorescence lifetime imaging microscopy to characterize amyloid-beta plaques," *Journal of Biomedical Optics*, vol. 8, no. 3, pp. 368–375, 2003.

[237] J. Lakowicz, *Principles Of Fluorescence Microscopy*. Springer, 1982.

[238] D. R. Yankelevich, D. Ma, J. Liu, Y. Sun, Y. Sun, J. Bec, D. S. Elson, and L. Marcu, "Design and evaluation of a device for fast multispectral time-resolved fluorescence spectroscopy and imaging," *Review of Scientific Instruments*, vol. 85, no. 3, p. 034303, 2014.

[239] E. Gratton, M. Limkeman, J. R. Lakowicz, B. P. Maliwal, H. Cherek, and G. Laczko, "Resolution of mixtures of fluorophores using variable-frequency phase and modulation data." *Biophysical journal*, vol. 46, no. 4, p. 479, 1984.

[240] G.-J. Kremers, E. B. Van Munster, J. Goedhart, and T. W. J. Gadella, "Quantitative lifetime unmixing of multiexponentially decaying fluorophores using single-frequency fluorescence lifetime imaging microscopy," *Biophysical journal*, vol. 95, no. 1, pp. 378–389, 2008.

[241] A. Esposito, T. Oggier, H. Gerritsen, F. Lustenberger, and F. Wouters, "All-solid-state lock-in imaging for wide-field fluorescence lifetime sensing," *Optics Express*, vol. 13, no. 24, pp. 9812–9821, 2005.

[242] A. Squire, P. J. Verveer, and P. I. H. Bastiaens, "Multiple frequency fluorescence lifetime imaging microscopy," *Journal of Microscopy*, vol. 197, no. 2, pp. 136–149, 2000.

[243] J. C. K. Chan, E. D. Diebold, B. W. Buckley, S. Mao, N. Akbari, and B. Jalali, "Digitally synthesized beat frequency-multiplexed fluorescence lifetime spectroscopy," *Biomedical Optics Express*, vol. 5, no. 12, pp. 4428–4436, 2014.

[244] Q. S. Hanley, V. Subramaniam, D. J. Arndt-Jovin, and T. M. Jovin, "Fluorescence lifetime imaging: multi-point calibration, minimum resolvable differences, and artifact suppression," *Cytometry*, vol. 43, no. 4, pp. 248–260, 2001.

[245] H. Qiao, J. Lin, Y. Liu, M. B. Hullin, and Q. Dai, "Resolving transient time profile in tof imaging via log-sum sparse regularization," *Optics letters*, vol. 40, no. 6, pp. 918–921, 2015.

[246] S. Y. Kung, *Kernel methods and machine learning*. Cambridge University Press, 2014.

[247] S. W. Golomb and G. Gong, *Signal design for good correlation: for wireless communication, cryptography, and radar*. Cambridge University Press, 2005.

[248] I. Yamaguchi and T. Zhang, "Phase-shifting digital holography," *Optics letters*, vol. 22, no. 16, pp. 1268–1270, 1997.

[249] PMD tec. (2014) pmd PhotonICs 19k–S3: Specs and reference design.

[250] T. F. Coleman and Y. Li, "An interior trust region approach for nonlinear minimization subject to bounds," *SIAM Journal on optimization*, vol. 6, no. 2, pp. 418–445, 1996.

[251] A. Bhandari, A. Bourquard, S. Izadi, and R. Raskar, "Blind transmitted and reflected image separation using depth diversity and time-of-flight sensors," in *Computational Optical Sensing and Imaging*, 2015, pp. CT4F–2.

[252] J. Philip and K. Carlsson, "Theoretical investigation of the signal-to-noise ratio in fluorescence lifetime imaging," *Journal of the Optical Society of America A, Optics and Image Science*, vol. 20, no. 2, pp. 368–379, 2003.

[253] S. Schuon, C. Theobalt, J. Davis, and S. Thrun, "Lidarboost: Depth superresolution for tof 3D shape scanning," in *Proc. IEEE Conf. Computer Vision and Pattern Recognition*, Jun. 2009, pp. 343–350.

[254] D. Lefloch, R. Nair, F. Lenzen, H. Schäfer, L. Streeter, M. J. Cree, R. Koch, and A. Kolb, "Technical foundation and calibration methods for time-of-flight cameras," in *Time-of-Flight and Depth Imaging: Sensors, Algorithms, and Applications*. Springer, 2013, pp. 3–24.

[255] G. Satat, B. Heshmat, C. Barsi, D. Raviv, O. Chen, M. G. Bawendi, and R. Raskar, "Locating and classifying fluorescent tags behind turbid layers using time-resolved inversion," *Nature communications*, vol. 6, 2015.

[256] M. A. Digman, V. R. Caiolfa, M. Zamai, and E. Gratton, "The phasor approach to fluorescence lifetime imaging analysis," *Biophysical journal*, vol. 94, no. 2, pp. L14–L16, 2008.

[257] N. Ohnishi, K. Kumaki, T. Yamamura, and T. Tanaka, "Separating real and virtual objects from their overlapping images," in *Lecture Notes in Computer Science*. Springer Science + Business Media, 1996, pp. 636–646.

[258] A. Levin, A. Zomet, and Y. Weiss, "Separating reflections from a single image using local features," in *Proc. of IEEE Comp. Vis. and Patt. Recognition*, vol. 1, 2004, pp. I–306.

[259] A. M. Bronstein, M. M. Bronstein, M. Zibulevsky, and Y. Y. Zeevi, "Sparse ICA for blind separation of transmitted and reflected images," *Int. J. Imaging Syst. Technol.*, vol. 15, no. 1, pp. 84–91, 2005.

[260] N. Kong, Y.-W. Tai, and S. Y. Shin, "High-quality reflection separation using polarized images," *IEEE Trans. Image Proc.*, vol. 20, no. 12, pp. 3393–3405, 2011.

[261] Y. Li and M. S. Brown, "Single image layer separation using relative smoothness," in *Proc. of IEEE Comp. Vis. and Patt. Recognition*, 2014, pp. 2752–2759.

[262] P. Chandramouli, M. Noroozi, and P. Favaro, "ConvNet-based depth estimation, reflection separation and deblurring of plenoptic images," University of Bern, submitted, 2016.

[263] A. Bhandari and Y. C. Eldar, "A swiss army knife for finite rate of innovation sampling theory," in *IEEE Intl. Conf. on Acoustics, Speech and Signal Processing (ICASSP)*, Mar. 2016, pp. 3999 – 4003.

[264] Y. C. Eldar, N. Hammen, and D. G. Mixon, "Recent advances in phase retrieval [Lecture Notes]," *IEEE Signal Process. Mag.*, vol. 33, no. 5, pp. 158–162, Sep. 2016.

[265] H. Qiao and P. Pal, "Sparse phase retrieval with near minimal measurements: A structured sampling based approach," in *Proc. of IEEE Intl. Conf. on Acoustics, Speech and Sig. Proc. (ICASSP)*, Mar. 2016, pp. 4722–4726.

[266] B. Rajaei, E. W. Tramel, S. Gigan, F. Krzakala, and L. Daudet, "Intensity-only optical compressive imaging using a multiply scattering material and a double phase retrieval approach," in *Proc. of IEEE Intl. Conf. on Acoustics, Speech and Sig. Proc. (ICASSP)*, Mar. 2016.

[267] K. Huang, Y. C. Eldar, and N. D. Sidiropoulos, "Phase retrieval from 1D Fourier measurements: Convexity, uniqueness, and algorithms," *IEEE Trans. Sig. Proc.*, vol. 64, no. 23, pp. 6105–6117, Dec. 2016.

[268] Y. M. Lu and M. Vetterli, "Sparse spectral factorization: Unicity and reconstruction algorithms," in *Proc. of IEEE Intl. Conf. on Acoustics, Speech and Sig. Proc. (ICASSP)*, May 2011.

[269] P. Boufounos, "Compressive sensing for over-the-air ultrasound," in *Proc. of IEEE Intl. Conf. on Acoustics, Speech and Sig. Proc. (ICASSP)*, May 2011.

[270] A. Velten, R. Raskar, D. Wu, B. Masia, A. Jarabo, C. Barsi, C. Joshi, E. Lawson, M. Bawendi, and D. Gutierrez, "Imaging the propagation of light through scenes at picosecond resolution," *Commun. ACM*, vol. 59, no. 9, pp. 79–86, Aug. 2016.

[271] D. Shin, F. Xu, F. N. C. Wong, J. H. Shapiro, and V. K. Goyal, "Computational multi-depth single-photon imaging," *Optics Express*, vol. 24, no. 3, p. 1873, Jan. 2016.

[272] K. Hibino, B. F. Oreb, D. I. Farrant, and K. G. Larkin, "Phase-shifting algorithms for nonlinear and spatially nonuniform phase shifts," *Jour.l of the Opt. Soc. of America A*, vol. 14, no. 4, p. 918, Apr. 1997.

[273] P. Hariharan, B. F. Oreb, and T. Eiju, "Digital phase-shifting interferometry: a simple error-compensating phase calculation algorithm," *Appl. Opt.*, vol. 26, no. 13, p. 2504, Jul. 1987.

[274] D. Potts and M. Tasche, "Parameter estimation for exponential sums by approximate prony method," *Signal Processing*, vol. 90, no. 5, pp. 1631–1642, May 2010.

[275] J. Cadzow, "Signal enhancement-a composite property mapping algorithm," *IEEE Transactions on Acoustics, Speech, and Signal Processing*, vol. 36, no. 1, pp. 49–62, Jan. 1988.

[276] G. Plonka and M. Wischerhoff, "How many Fourier samples are needed for real function reconstruction?" *Journal of Applied Mathematics and Computing*, vol. 42, no. 1-2, pp. 117–137, 2013.

[277] Z. Wang, A. C. Bovik, H. R. Sheikh, and E. P. Simoncelli, "Image quality assessment: from error visibility to structural similarity," *IEEE Transactions on Image Processing*, vol. 13, no. 4, pp. 600–612, 2004.

[278] L. V. Wang and J. Yao, "A practical guide to photoacoustic tomography in the life sciences," *Nature Methods*, vol. 13, no. 8, pp. 627–638, Jul. 2016.

[279] A. G. Bell, "On the production and reproduction of sound by light," *Biophys J*, vol. s3-20, no. 118, pp. 305–324, Oct. 1880.

[280] M. Xu and L. V. Wang, "Photoacoustic imaging in biomedicine," *Rev. Sci. Instrum.*, vol. 77, no. 4, p. 041101, Apr. 2006.

[281] F. Gao, X. Feng, and Y. Zheng, "Advanced photoacoustic and thermoacoustic sensing and imaging beyond pulsed absorption contrast," *Journal of Optics*, vol. 18, no. 7, p. 074006, May 2016.

[282] L. V. Wang, *Photoacoustic Imaging and Spectroscopy*, ser. Optical Science and Engineering. CRC Press, Mar. 2009.

[283] G. J. Diebold, M. I. Khan, and S. M. Park, "Photoacoustic "signatures" of particulate matter: Optical production of acoustic monopole radiation," *Science*, vol. 250, no. 4977, pp. 101–104, Oct. 1990.

[284] E. M. Strohm and M. C. Kolios, "Classification of blood cells and tumor cells using label-free ultrasound and photoacoustics," *Cytometry Part A*, vol. 87, no. 8, pp. 741–749, Jun. 2015.

[285] E. M. Strohm, E. S. Berndl, and M. C. Kolios, "Probing red blood cell morphology using high-frequency photoacoustics," *Biophysical Journal*, vol. 105, no. 1, pp. 59–67, Jul. 2013.

[286] G. A. D. Briggs and O. Kolosov, "Experimental elastic microanalysis," in *Acoustic Microscopy*. Oxford University Press (OUP), Sep. 2009, pp. 123–159.

[287] E. M. Strohm, M. J. Moore, and M. C. Kolios, "Single cell photoacoustic microscopy: A review," *IEEE J. Sel. Topics Quantum Electron.*, vol. 22, no. 3, pp. 137–151, May 2016.

[288] P. M. Morse and K. U. Ingard, *Theoretical acoustics*. Princeton university press, 1968.

[289] G. J. Diebold, "Photoacoustic waves at reflecting interfaces," *Review of Scientific Instruments*, vol. 74, no. 1, pp. 801–804, Jan. 2003.

[290] T. J. Allen and P. C. Beard, "High power visible light emitting diodes as pulsed excitation sources for biomedical photoacoustics," *Biomedical Optics Express*, vol. 7, no. 4, p. 1260, Mar. 2016.

[291] T. P. Speed and L. Li, "Parametric deconvolution of positive spike trains," *The Annals of Statistics*, vol. 28, no. 5, pp. 1279–1301, oct 2000.

[292] J. Urigüen, T. Blu, and P.-L. Dragotti, "FRI sampling with arbitrary kernels," *IEEE Trans. Sig. Proc.*, vol. 61, no. 21, pp. 5310–5323, Nov. 2013.